Characterisation of micron sized ferromagnetic structures fabricated by focussed ion beam and electron beam lithography

By Robin W. O'Neill

UNIVERSITY
of
GLASGOW

Submitted for the degree of Doctor of Philosophy at the Department of Physics and Astronomy, University of Glasgow.

March 2007

Abstract

Traditionally electron beam lithography (EBL) has been used to fabricate micron and sub-micron sized devices, such as Γ and T gates for metal-semiconductor devices for study within the semiconductor industry. EBL is also used for the fabrication of ferromagnetic elements for use as components in magnetic random access memory (MRAM) and read/write heads in hard disk drives (HDD). MRAM is being investigated as a direct replacement to standard semiconductor RAM as it has lower power consumption and is a non-volatile memory solution, although the areal density, at present, is not as great. Smaller read/write heads are necessary for HDD as recent advances now allow for perpendicular magnetisation (as opposed to parallel magnetisation) of films and increase the areal density to 100 Gb/inch^2, four times the current value.

In this thesis, the physical and magnetic properties of such micron-sized devices that have been fabricated by focussed ion beam (FIB) lithography for comparison to those fabricated by the EBL method are discussed. In addition to this work, the physical and magnetic properties of micron-sized element that have been irradiated using the 30 keV gallium ion source are also discussed. Also in this thesis, the results of 10×10 μm^2 arrays of 50 nm thick polycrystalline cobalt elements (270×270 nm^2 with a 400 nm period) that are fabricated by EBL to determine if there is any magnetic superdomain structure present are discussed. Bright field imaging in a transmission electron microscope (TEM) is used to investigate the physical structure of the ferromagnets, such as the grain size, element roughness and dimensions. Additional information about the topography is measured by atomic force microscopy (AFM). The magnetic properties, such as the magnitude of the applied field at which irreversible events happen and the domain structure, are investigated by the Fresnel imaging and the differential phase contrast modes of Lorentz microscopy. A programme known as object orientated micromagnetic framework (OOMMF) is used to model the magnetic properties of such structures.

In the first chapter the properties of the ferromagnetic materials are discussed. The discussion encompasses the general properties of bulk ferromagnets; the main energy contributions of a ferromagnetic system and how these contributions affect the formation of domains in the system; and the main types of domain walls that form in the structures discussed in this thesis. The energy contributions and how they can be used to model the magnetisation within the structures using the OOMMF programme are also discussed. Finally, the effects of the discrete dimensions on the magnetisation of the structures are discussed and a brief review on other work in this field is given.

The discussion in the second chapter focuses on the fabrication of the structures. Initially the two deposition techniques (plasma sputter coating and thermal evaporation) are outlined. Following this is a discussion on how the structures are fabricated by EBL and FIB lithography as well as a brief description of the hardware and software used. For FIB lithography, the discussion also focuses on the optimisation of the milling conditions, including simulations of the effects of the 30 keV Ga^+ beam on different structures and the effect of differences in beam spot size. Also discussed in this chapter is the introduction of a buffer layer to protect the substrate from milling.

In the third chapter, the techniques used to characterise the structures are discussed. The TEM is discussed as well as the modes used, such as bright field imaging, Fresnel imaging and differential phase contrast (DPC). Other techniques that could also be used to investigate the magnetic properties of the elements and the array are briefly discussed. In the final section, AFM imaging, encompassing the hardware and theory is discussed.

In the fourth chapter the preliminary investigations into the fabrication of micron-sized structures by FIB lithography and OOMMF simulations are discussed. The preliminary investigations into 1×1 μm^2 trenches irradiate the into continuous, 20 nm thick, permalloy thin film using a nominal beam current of 10 pA are discussed. The investigation mainly focussed on the effects of varying the dose of the 30 keV Ga^+ used to determine a dose range for the fabrication of permalloy elements. The permalloy is supported on 50 nm thick SiN. It is found that, by increasing the dose, the milled depth and grain sizes increase as expected. Analysis of the trenches is by AFM and bright field TEM imaging. The effects of different beam currents (nominally 10 and 100 pA) on the trenches are also discussed. It is found that the 100 pA beam attracts more contamination to the surface of the permalloy than the 10 pA beam and has a less well defined edge structure. Also discussed in this chapter are OOMMF simulations of the magnetisation within the 1000×200 and 500×500 nm^2 20 nm thick, permalloy elements in an applied field. Several states are predicted for the 1000×200 nm^2 element, it is found that the near uniform S- and C-states have the lowest energy and well defined square hysteresis loops when a field is applied along the long in-plane axis. The simulation of the 500×500 nm^2 element predicts the four-domain flux structure to be the lowest energy state. Unfortunately (even for elements with roughened edge structure) the simulation predicts a square hysteresis loop in an applied field that is not observed experimentally.

In the fifth chapter, a comparison of the physical and magnetic structure of the 1000×200 and 500×500 nm^2 elements fabricated by EBL and FIB lithography on to 20 nm thick,

permalloy (supported on 50 nm thick SiN) are discussed. This includes elements that are fabricated on 20 nm permalloy on a 4 nm copper buffer layer by FIB lithography. A comparison of the grain structure (by bright field TEM imaging) reveals an increase within the elements fabricated by FIB lithography (this appears up to the centre of the element for the permalloy-only elements at high dose) compared to unaltered grain sizes in those fabricated by EBL. The edge roughness of elements fabricated by FIB lithography is significantly increased compared to those fabricated by EBL (which is of the order of the grain size). As expected, the depth of the trench surrounding the element (analysed by AFM) is found to increase with dose. A comparison of the magnetic structure reveals that the magnetisation path followed by the 1000×200 nm^2 elements fabricated by FIB lithography (for doses >0.04 $nC\mu m^{-2}$) is similar to that followed by the EBL elements although the magnitude of the switching field is reduced. The majority of 500×500 nm^2 elements fabricated by FIB lithography (again for doses >0.04 $nC\mu m^{-2}$) also follow the same path as those fabricated by EBL. In a significant minority, however, the formation of the single vortex structure from a near uniform state proceeds through an intermediate metastable twin vortex state. For the elements fabricated by the 0.04 $nC\mu m^{-2}$ dose, the elements appear not to be isolated from the film and are, therefore, still be influenced by the thin film.

In the sixth chapter the physical and magnetic characteristics of 2×2 μm^2 elements that are irradiated by several patterns are discussed. The elements are composed of a 10 nm Cu capping layer, 20 nm permalloy ferromagnetic layer and a 5 nm Cu buffer layer on a 50 nm SiN substrate. The increased dimensions are to reduce the contributions of the edge effects on the magnetisation within the bulk of the element. The patterns are irradiated using several doses, from light irradiation to light milling. It is observed that in the case of irradiated areas, grain growth is proportional to dose, whereas one-pixel wide lines do not exhibit any visible grain growth (for a nominally 10 pA beam current). DPC and Fresnel imaging are used to identify what changes, if any, result in the magnetisation within the elements that are irradiated. The irradiated sections are found to disrupt the formation of the four-domain single vortex structure within the elements in zero field and also to disrupt the magnetisation paths from that of the unirradiated element as a field is applied.

The cobalt arrays that are fabricated by EBL are discussed in the seventh chapter. Bright field TEM imaging is used to accurately measure the dimensions of the elements within the array and the dimensions are found to be close to the nominal 270×270 nm^2 expected with one in-plane dimension being marginally larger. Large saturating magnetic fields (~0.7 T) are applied to two orthogonal in-plane axes by several procedures. By analysing the vortex

chirality distributions within the remanent states, switching of the vortex chirality distributions with the applied field is found to occur. The switching is similar in nature to that of domains within discrete elements such as those discussed in previous chapters. The distribution of the vortices is found to be anisotropic with respect to the direction of the applied field along the in-plane axes, with the more uniform vortex chirality distributions along the axis with the larger dimensions. Arrays of reduced dimensions are simulated in OOMMF to try to understand the nature of the reversal within the arrays. The perfect array is found to have an even split of vortex chiralities distributions as a field is applied for both orthogonal in-plane axes with two "domains" forming. To simulate a more real array, the individual elements are displaced randomly by 1 pixel; this changes the vortex chiralities distribution within the array. To gain further insight into the magnetic behaviour of the array, the stray field of several non-flux closure structures (flower, C- and S-states) are studied.

In the final chapter, chapter 8, conclusions drawn from the work discussed in this thesis are presented as well as any possible future work.

Acknowledgements

I would like to take this opportunity to thank my supervisors Dr. Stephen McVitie and Prof. John Chapman who have provided constant advice and help throughout my PhD. Under their guidance (and almost divine patience) I have become a better person. I would also like to thank Prof. Andrew Long for his help and guidance with the work in chapter 7.

I would also like to take this opportunity to thank the technical staff of the Solid State Physics group at the University of Glasgow, Dr. Sam McFadzean, Mr. Brian Miller, Mr. Colin How and Mr. William Smith who keep the equipment working and the anecdotes coming. I would also like to thank Dr. Jamie Scott and Dr. Pat Nicholson for teaching me how to use some of techniques used in this thesis and Dr. Damien McGrouther who taught me how to use some of the simulation packages. Other members (both past and present) in the Solid State Physics Group that I would like to thank are Yingang Wang, Michelle Cushley, David Hamilton, Paula Harkins, James Wilson, Paul Robb and Craig Brownlie, to name but a few.

Personally I have a lot of people to thank, first and foremost my Gran for putting up with me, feeding me and keeping me on the straight and narrow. All she asked for in return was cups of tea. My Parents whose constant support has been immeasurable. My Sis who, like my parents supported me throughout. My Uncle Gilbert who like my Gran has done so much and asks for nothing in return. My Aunt Janey and Uncle Simson for all the help and runs to/from home. Scott who egged me on all the time. The People of Dunure, my home even after a prolonged absence, who are always asking the questions, “So when do you finish now?” and “What EXACTLY do you do?”. I would also like to thank my friends: Jamie, Leanne, Chris, Chris, Craig, Michael, Catharine and Robert who helped me through the darkest periods. A specially thank also to Andrew Freeburn and his Family, a really good and understanding friend.

A special thanks to Lucy Murray who helped me with so much and kept me sane through the worst of it.

I also wish to take this opportunity to thank the EPSRC for the funding for this project.

Declarations

This thesis is a record of the work carried out by me in the department of Physics and Astronomy, University of Glasgow, between October 2002 and March 2007. The work described here in is my own apart from the statistical theory in chapter 7 that was derived by Prof. Andrew Long.

Some of the work discussed in this thesis has been present at EMAG ’05 in Leeds. These results can be found in the following paper:

“Transmission electron microscopy characteristics of permalloy elements fabricated by focussed ion beam lithography.” R.W. O’Neill and S. McVitie, Journal of Physics: Conference Series, 26 (2006) 187.

This thesis has not previously been submitted for a higher degree.

Table of Contents

1 Nanoscale ferromagnetic thin films

In this chapter, the properties of a class of magnetic materials known as ferromagnets are discussed, with special attention given to ferromagnets of reduced dimensions. A brief description as to what defines a ferromagnetic material will be given. The energetics of ferromagnetic materials and how this results in domain formation within such materials are also discussed. From the terms used to describe the energy of a ferromagnet, simulations that model the behaviour of the magnetisation in an applied magnetic field can be implemented using a software package known as object orientated micromagnetic framework, OOMMF [1]. A programme, developed at the University of Glasgow, that can simulate the internal and external stray field from an OOMMF simulated magnetic state is also discussed. From the energetics, the behaviour of the magnetisation of ferromagnets discussed in chapters 4, 5, 6 and 7 can be interpreted for both the remanent states and those in an applied field.

1.1 Introduction

A ferromagnetic material is defined as a material that may possess a net magnetisation (***M***, S.I. units are Am^{-1}) without the application of an external magnetic field (***H***, S.I. units are Am^{-1}). The resultant induced response in the material (the magnetic induction, ***B***, S.I. units are Tesla, T) is given in equation 1.1:

$$\boldsymbol{B} = \mu_0 (\boldsymbol{H} + \boldsymbol{M}) \qquad \textbf{(1.1)}$$

where μ_0 is the permeability of free space. The magnetic induction, ***B***, is often referred to as the force that drives a magnetic field, with the magnetic field strength, ***H***, resulting from

the induction. A ferromagnet results from the exchange interaction and this can be used to describe the three main classes of the material: a ferromagnet, an antiferromagnet and a ferrimagnet. A ferromagnet has parallel ordering of the spins in the region, as shown in Figure 1.1(a). An antiferromagnet has antiparallel ordering within the region, Figure 1.1(b), giving a net magnetisation of zero. The ferrimagnet has antiparallel ordering with the moment of one greater than the other (usually a pair of different atoms or molecules); the net moment of the region is non-zero (an example of which is given in Figure 1.1(c)). Both permalloy (taken to be $Ni_{80}Fe_{20}$ in this thesis) and cobalt (the materials used for the fabrication of the arrays discussed in this thesis) are ferromagnetic and, as a result, the properties of ferromagnets are discussed. Permalloy, in bulk form, is classed as a soft magnetic material (conventionally due to it's low coercivity and high susceptibility) and cobalt is classed as a hard magnetic material (conventionally due to it's high coercivity and low susceptibility).

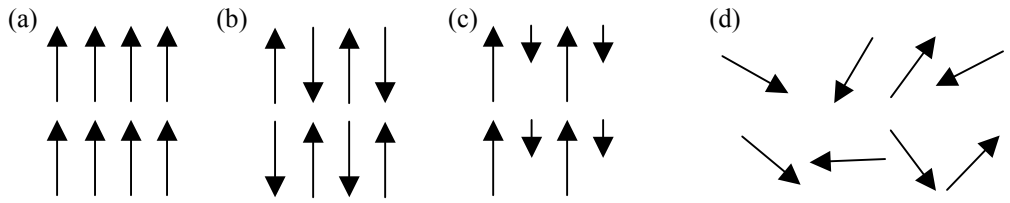

Figure 1.1: schematic of the magnetic spins in: (a) a ferromagnet, (b) an antiferromagnet, (c) a ferrimagnet and (d) a paramagnet.

The magnetisation within the ferromagnet is temperature dependent, with the magnetic ordering being destroyed above a certain temperature (known as the Curie temperature, T_C for ferromagnets; antiferromagnets have an equivalent temperature known as the Néel temperature) [2]. Above T_C the material becomes paramagnetic, in a paramagnetic material all the magnetic spins are disordered (as shown in Figure 1.1(d)). If the temperature is decreased below T_C the material becomes ferromagnetic again (although the previous ferromagnetic ordering within the material has been destroyed). Conversely the value of the saturation magnetisation, M_S, increases as the temperature is decreased, the maximum value of the saturation magnetisation, M_0 (in the absence of a field) being reached classically at absolute zero.

1.2 The energy considerations governing the magnetic properties of ferromagnetic materials

Within a ferromagnetic system there are several energy contributions that combine to give a total energy, E_{TOT}. Through a competition of the energy contributions, the system

normally minimises E_{TOT} (whether it be a global or local minima), these contributions will be outlined in this section. In a ferromagnetic system there are energy contributions from the exchange energy, E_{EX}, the anisotropy energy, E_K, the Zeeman energy (or applied field energy), E_Z, the magnetostatic energy, E_D, and the magnetostrictive energy, E_M, equation 1.2 [3].

$$E_{TOT} = E_{EX} + E_K + E_Z + E_D + E_M \quad \textbf{(1.2)}$$

1.2.1 Exchange energy

If we consider the interactions of the atomic spins, $\boldsymbol{S}$, between two nearest neighbours, i and j, of the electrons in a magnetic system (with magnetic moment, $\boldsymbol{m}$), then the exchange energy between the atoms, e_{ex}, can be expressed by equation 1.3 (derived from the Heisenberg interaction).

$$e_{ex} = -2J_{ij}\boldsymbol{S}_i.\boldsymbol{S}_j \quad \textbf{(1.3)}$$

Where J_{ij} is the exchange integral between nearest neighbours. Here "e_{ex}" is used, as opposed to "E_{EX}" to distinguish between the energy between two atoms and the global energy contribution. The minus sign arises from the convention used to define energy levels of an atom. The total exchange energy, E_{EX}, in a system that has a constant magnitude of magnetic moment ($|m_i| = |m_j| = \mathbf{m}$) is therefore the summation of the individual exchange energies between the atoms, taken over the volume, V, of the ferromagnet, equation 1.4.

$$E_{EX} = -\mu_0 S^2 J \sum_{ij}^{V} \cos\phi \quad \textbf{(1.4)}$$

Where ϕ is the angle between the nearest neighbours. From 1.4 it can be observed that the exchange energy is lowest when the angle between the moments is zero, in other words the ferromagnet is uniformly magnetised. A useful parameter often quoted is the exchange stiffness (A), given in equation 1.5. The exchange stiffness (measured in Jm^{-1}) is a measure of the exchange energy in a material and is one of the material parameters used in the OOMMF simulation package (discussed in section 1.4).

$$A = \frac{JS^2}{a} \quad \textbf{(1.5)}$$

Where a is the lattice spacing. Typical values taken for A for an OOMMF simulation of permalloy and cobalt materials are 1.3 x 10^{-11} and 3 x 10^{-11} Jm^{-1} respectively.

1.2.2 Anisotropy energy

Anisotropy energy, E_K, can arise in some ferromagnetic systems due to the direction of the magnetic moment lying off-axis relative to some structural axis of the material when the individual contributions are averaged over the volume. This form of anisotropy ultimately arises from the spin-orbit interaction of the atoms and is otherwise known as the magnetocrystalline anisotropy and the terms used to describe the energy are influenced by the symmetry of system. One of the most common forms of magnetocrystalline anisotropy results from the magnetisation vector deviating from a single common axis (known as the easy axis), this type is known as uniaxial anisotropy. An approximation for the magnetocrystalline energy for the uniaxial anisotropy is given in equation 1.6.

$$E_K \approx \int \left(K_1 \sin^2 \theta\right) dV \qquad \textbf{(1.6)}$$

where K_1 is the anisotropy constant and is measured in Jm^{-3}. K_1 is another material parameter used in OOMMF. Of the two materials discussed in this thesis permalloy has an almost zero magnetocrystalline anisotropy constant and single crystal cobalt has uniaxial anisotropy. In a continuous thin film, the variation of magnetocrystalline anisotropy from one grain to another of permalloy and cobalt gives rise to ripple contrast [4] that can be observed through techniques such as Fresnel imaging (discussed in section 3.3.1). For the micromagnetic simulations, however, the anisotropy of the polycrystalline cobalt deposited for the arrays discussed in chapter 7 when summed over the volume of the element is assumed to be zero [5].

1.2.3 Zeeman energy

The Zeeman energy, E_Z, is the energy within the whole ferromagnetic system due to an external applied field, $\boldsymbol{H}_{APP}$, and is given in equation 1.7. E_z in equation 1.7 is for a uniform external applied field applied over the volume, V, of the system.

$$E_Z = -\mu_0 M_S \int \mathbf{H}_{APP} \cdot \mathbf{n} dV \qquad \textbf{(1.7)}$$

where $\boldsymbol{n}$ is the unit vector along the direction of the magnetisation. As can be observed from equation 1.7, E_Z is at a minimum when $\boldsymbol{H}_{APP}$ is parallel to the magnetisation direction.

1.2.4 Magnetostatic energy

The demagnetisation magnetostatic field, $\boldsymbol{H}_D$, is a field that arises in a ferromagnetic material to oppose the magnetisation in a system. $\boldsymbol{H}_D$ can be either internal or external to the sample. The magnetostatic field can best be described by Maxwell's equation *"the divergence of the magnetic induction is always zero"*, in other words $\nabla.\boldsymbol{B}=\nabla.(\mu_0(\boldsymbol{H}_D+\boldsymbol{M}))=0$ [2], therefore $\nabla \cdot \mathbf{H}_D = -\nabla \cdot \mathbf{M}$. The internal field acts to oppose the magnetisation within the sample and, therefore, demagnetise the sample (hence the magnetostatic field is also known as the demagnetising field) and therefore assists the formation of domains within a ferromagnetic material (to be discussed in section 1.3). When the field is external to the sample the field is known as the stray field, which can be observed by all manner of techniques to be discussed in chapter 3. The energy associated with $\boldsymbol{H}_D$ is calculated in a similar fashion to that for the energy for electrostatic charges with the exception that because $\nabla \cdot \mathbf{B} = 0$, the magnetic charges always balance, equation 1.8.

$$E_D = \frac{1}{2}\mu_0 \int_{All\ space} \mathbf{H}_D^2 dV = -\frac{1}{2}\mu_0 \int_{material} \mathbf{H}_D \cdot \mathbf{M} dV \qquad \textbf{(1.8)}$$

The first integral term in equation 1.8 is always positive (due to the square of the magnetostatic field) and is only zero when the stray field is zero everywhere; in other words the element may form a flux closure structure to minimise the external stray field, to be discussed in section 1.3. As the second integral in equation 1.8 is integrated over the finite element size, it is therefore easier to evaluate than the first (which extends to infinity) It is the second integral that is used for the computation of the magnetostatic field in micromagnetic simulations. A value for the magnetostatic field at a point $\boldsymbol{r}'$ from a magnetic moment $\boldsymbol{M}$ whose source is at $\boldsymbol{r}$ within an element can be calculated by potential theory, equation 1.9:

$$\mathbf{H}_D = \frac{1}{4\pi}\left(\int \frac{\mathbf{M}\cdot\mathbf{n}}{|\mathbf{r}-\mathbf{r}'|^2} dS - \int \frac{\nabla \cdot \mathbf{M}}{|\mathbf{r}-\mathbf{r}'|^2} dV \right) \qquad \textbf{(1.9)}$$

where $\boldsymbol{n}$ is the outward pointing unit vector normal to the surface.

1.2.5 Magnetostrictive energy

Another magnetic property that gives rise to an energy contribution is magnetostriction. Magnetostriction is the effect whereby a change in the net magnetisation of an element that

results in a change in the dimensions of a material and visa versa. For the volume of materials discussed in this thesis, however, the changes due to magnetostriction are negligible and are therefore not considered. Typically the magnetostriction coefficient of the materials discussed in this thesis are of the order 10^{-6}. Magnetostriction, λ, is defined as the fractional change in length of the material, in other words $\lambda = \frac{\Delta l}{l}$. λ is at a maximum when the magnetisation in the sample is at a maximum, $\boldsymbol{M}_S$, this value is the saturation magnetostriction, λ_S. In an applied field the direction of λ_S is along the direction of the applied field. The magnetostriction in a material has an associated energy, E_M, that is related to the fractional change in length due to the magnetostriction of the material. For a fuller review on magnetostriction see [3].

1.3 Domains and domain wall formation

Weiss first proposed the idea of magnetic domains within a material in 1906-07 [6, 7]. This work built on the work of Ampère, Weber and Ewing. In this work the definition of a magnetic domain is taken as an area where all the magnetic moments are aligned.

The mechanism for domain formation was not proposed until 1935, however, when Landau and Lifschitz [8] proposed that domains form in order to minimise the total energy in the system (be it a local or global minimum). The minimisation of the total energy is a result of an equilibrium being reached between the energies. For the polycrystalline permalloy and cobalt elements and arrays discussed in this thesis it is mainly a competition between the exchange energy (which favours uniform magnetisation, section 1.2.1) and the magnetostatic energy (which favours multiple domains typically flux closure structures, section 1.2.4) in zero applied field. Landau and Lifschitz calculated that for a ferromagnetic material of finite dimensions, a uniform domain (Figure 1.2(a)) has a low exchange energy but a high magnetostatic energy. If the same element forms a 180^o domain wall (Figure 1.2(b)), the exchange energy increases but the magnetostatic energy decreases. The magnetostatic energy is further decreased if the ferromagnet was to adopt a series of 180^o domains walls, although this would increase the exchange energy (shown in Figure 1.2(c)). The magnetostatic energy of the system can be minimised by what is termed a flux closure structure. A flux closure structure is a magnetic structure with a closed path of magnetisation (such as a circle or a vortex) and has no magnetostatic stray field emanating from the system when in bulk form (although there is a small leakage from the thin film flux closure structure as will be discussed in section 1.3.1), Figure 1.2(d). Due to the low anisotropy constant, permalloy elements would be more likely to form a

flux closure structure than single crystal cobalt elements with a strong uniaxial anisotropy. Polycrystalline cobalt, however, is expected to form a flux closure structure, as there should be no global defining anisotropy direction [5].

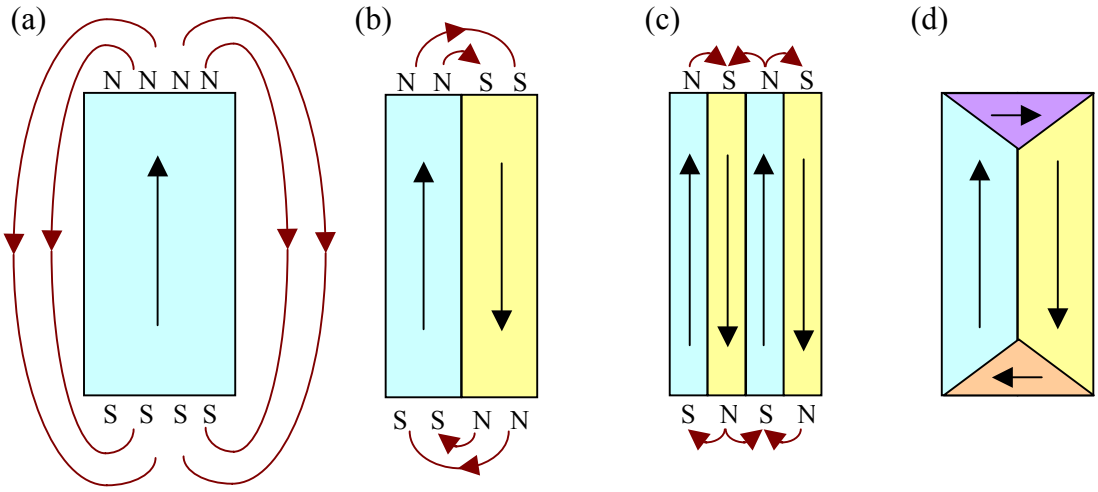

Figure 1.2: schematic of ordered domains inside a magnetic material, (a) is uniform, (b) two domains with a 180° domain walls, (c) four-domains with 180° and (d) flux closure structure. Red lines indicate stray field emanating from the material.

1.3.1 Classifications of domain walls in thin ferromagnetic films

It is important here to define what is classed as a magnetic thin film. A magnetic thin film is a film that has a thickness thinner than, or equivalent to, the width of a domain wall. Domain walls can range from a few nanometres to several hundred nanometres.

A domain wall is not considered an abrupt discontinuous change in the orientation of the spins in the ferromagnet, as the name could suggest, instead it is a progression of the orientation of the magnetic spins. There are two main types of one-dimensional domain walls, the Bloch and Néel walls, shown in Figure 1.3. A Bloch wall forms when the progression of spins rotates around an in-plane rotation axis, shown in Figure 1.3(a). If the Bloch wall forms in a bulk ferromagnet, where the progression of spins results in a divergence free domain wall, no stray field will be associated with the wall. If, however, the Bloch wall forms in a thin film of finite dimensions then the out-of-plane rotation creates surface magnetic charges at the point where the wall intersects the surface of the ferromagnet, stray field is then generated from the surface. The width of a Bloch wall, δ, is often defined as $\sqrt{A/K}$ [3].

The Néel wall (Figure 1.3(b)) forms when the progression of spins rotate around an out-of plane rotation axis. A result of the in-plane rotation in a ferromagnet of finite

dimensions is that there is always a build up of magnetic charge at the in-plane edge and, therefore, a stray field component in always produced. A Néel wall becomes favourable in a thin film when the thickness is less than the wall width. At this point, the separation of the magnetic charges is greater when the spins rotate in-plane as opposed to out-of-plane (in a Bloch wall the magnetic charge is on the surface of the thin film and becomes closer together as the thickness is reduced). The point at which a Néel wall becomes more energically favourable is dependent upon the domain wall width. For example, for 20 nm thick permalloy of the same composition to that discussed in this thesis, Néel domain walls widths have been measured as ~49 nm for 180° and ~123 nm for 90° domain walls [9]. For 6.4 nm thick cobalt, domain wall widths of 19 nm for a 180° wall have been recorded [10].

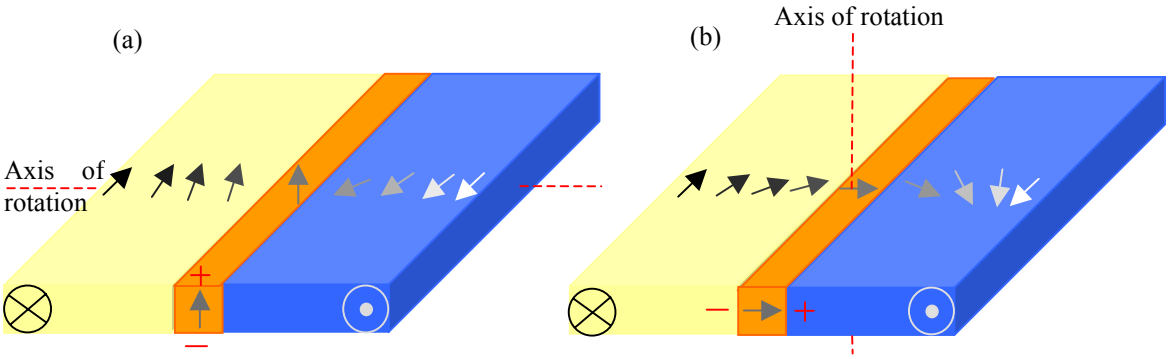

Figure 1.3: schematic of the direction of the rotation of spins to form a 180° domain wall, with magnetic charge shown. (a) is a Block wall, (b) is a Néel wall. Red lines and crosses indicate the edges where stray field is generated due to the progression of spins. The magnitude of magnetisation does not change.

Another domain wall type of particular interest here is the cross-tie wall, shown in Figure 1.4. The cross-tie wall is a combination of both the Bloch and Néel walls. The cross-tie wall arises due to the 90° Néel wall being lower in energy than the 180° Néel wall (an order of magnitude less [3]) and that opposite polarity 180° domain walls are symmetrical. The 180° Néel wall can therefore be replaced by a series of 90° walls to form a cross-tie wall (Figure 1.4). Although the size of the domain wall is significantly increased, the energy of the domain wall is reduced. Cross-tie walls usually form in the intermediate thickness between Néel and Bloch walls. For permalloy this is in the region between ~20 and ~80 nm. At the wall intersections in the cross-tie wall, Bloch lines are produced; these are singularities where the magnetisation direction is, in theory, undefined (however in practice the magnetisation points either into or out of the plane of the paper). The red circles represent cross Bloch lines and the blue circles represent circulating Bloch lines. The circulating Bloch lines are similar to those observed within the flux closure structures (called magnetic vortices) such as the elements with square in-plane dimensions discussed in this thesis (chapters 5, 6, and 7).

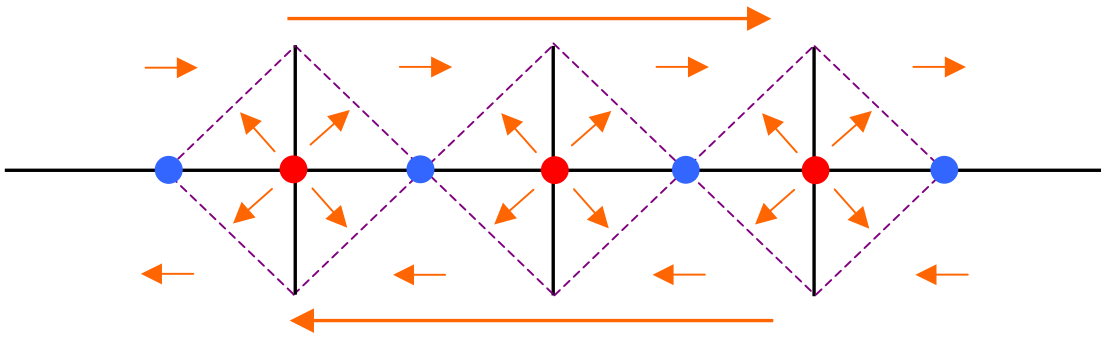

Figure 1.4: schematics of the magnetisation distribution around cross-tie walls. Orange arrows indicate the local magnetisation direction, purple dotted lines represent areas of continuous rotation, black lines indicate domain walls, red and blue circles represent Bloch lines.

1.3.2 Two dimensional domain walls

For films with larger thicknesses, walls that resemble Néel walls at the surface and Bloch walls in the centre of the material can exist (for example the vortex walls shown in Figure 1.5). The thickness region at which these walls exist is greater than a cross-tie (>80 nm, usually 100 nm in permalloy). The vortex wall is a complex structure and is not expected to be observed frequently, if at all, in this thesis. Therefore only a brief description will be given. The two types of intermediate walls show in Figure 1.5 are a symmetric Bloch wall (also known as a C-type domain wall, Figure 1.5(a)) and an asymmetric Néel wall (also known as S-type domain walls, Figure 1.5(b)). Due to the divergence of the magnetic moments within the material being non zero a charge builds up on the surface of the element in similar fashion to the Bloch wall in a thin film, except there is a region of magnetic charge at the centre of the wall on the surface that is zero (similar to a Néel wall). The symmetric Bloch wall is more favourable in low and zero applied field and the Néel wall is more favourable in high applied field. For a fuller review see [3].

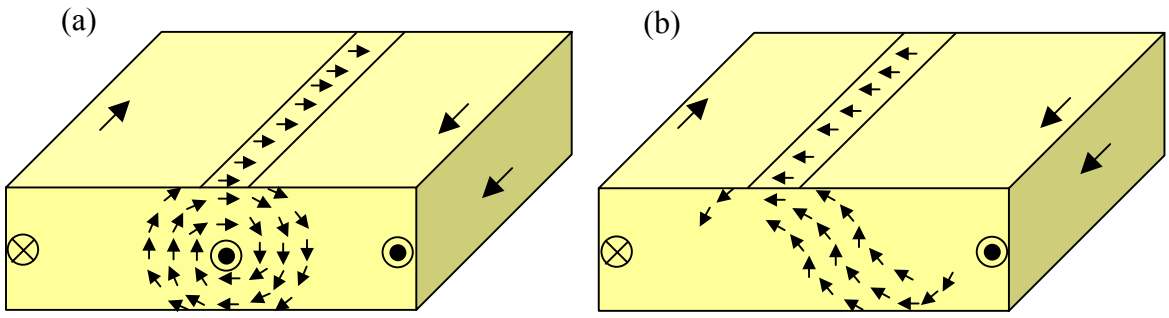

Figure 1.5 two-dimensional vortex walls, (a) symmetric Bloch wall (C-type) and (b) asymmetric Néel wall (S-type). Black lines indicate the direction of the magnetisation.

1.4 Micromagnetic Simulations

The increase in computing power in recent years has allowed computers to become powerful and fast enough to provide solutions to the micromagnetic equation governing the magnetic distributions within discrete structures and thin films in a realistic time frame. Micromagnetic simulations use ordinary differential equations (ODEs) associated with the energies of the competing contributions described in section 1.2 (in other words minimising E_{TOT} in equation 1.2). There are several methods for solving the ODEs associated with the energy to find the magnetisation distribution within a given system; Fidler and Schrefl [11] give a review on the subject and methods employed.

Computational simulations are used as a guide to the switching behaviour and field values of the elements characterised within this thesis, as the solutions provided, in general, do not take the imperfections of real systems into consideration. Introducing imperfections to the system can be labour and time intensive and serves to increase computation time. Therefore a balance between real and perfect systems has to be maintained. It has been found that the fields at which irreversible magnetic events take place in micromagnetic simulations are generally higher in magnitude to those obtained through experiment. This idea is developed further in chapters 4, 5, 6 and 7.

1.4.1 Object orientated micromagnetic framework

Object orientated micromagnetic framework (OOMMF) [1] is a micromagnetic simulation package released by the National Institute for Standards and Technology (NIST) [12]. The OOMMF simulation package uses a finite cell model to find solutions to a heavily damped version of the Landau-Lifschitz Gilbert ODE, Equation 1.10. The OOMMF simulation package sets $\boldsymbol{M}$, defined in the Landau-Liftschitz Gilbert equation (equation 1.10), as the magnetisation vector in the system and M_s as the saturation magnetisation scalar. Other variables in the Landau-Lifschitz equation include: time, t, gyromagnetic ratio ($mA^{-1}s^{-1}$), γ, damping coefficient, α, and the pointwise effective magnetic field strength vector, $\boldsymbol{H}_{eff}$.

$$\frac{\partial \mathbf{M}}{\partial t} = -\gamma \mathbf{M} \times \mathbf{H}_{eff} + \frac{\gamma \alpha}{M_s} \mathbf{M} \times (\mathbf{M} \times \mathbf{H}_{eff}) \qquad \textbf{(1.10)}$$

$\boldsymbol{H}_{eff}$ is defined in OOMMF by equation 1.11. Here e_{TOT} is the average energy density (Jm^{-3}) as a function of $\boldsymbol{M}$ as specified in Brown's equations on micromagnetics [13]. e_{TOT} (the total energy density) is similar to E_{TOT} (the total energy) that is defined in equation 1.2.

$$\mathbf{H}_{eff} = -\mu_0^{-1} \frac{\partial e_{TOT}}{\partial \mathbf{M}} \quad \textbf{(1.11)}$$

There are currently two versions of OOMMF available: the two-dimensional and three-dimensional models. In this thesis, version 1.1b (the two dimensional version) was preferred as the magnetisation was not expected to vary significantly through the thickness of the materials discussed in this thesis. In addition, version 1.2a (the three dimensional version) was newly released as an alpha version and experience using the programme was limited. Version 1.1b is discussed in section 1.4.2.1, with an example of the output given.

1.4.1.1 Two dimensional model of OOMMF

The two dimensional version of OOMMF finds solutions for the Landau-Lifschitz Gilbert equation by relaxing the projection of the three-dimensional magnetic spins onto a discrete two dimensional mesh that runs through the volume of the system. The magnetic spins are positioned at the centre of the 2D cells and are distributed evenly throughout the shape to be modelled. The discretization of the shape can be a source of problems for micromagnetic simulations. If care is not taken and the ratio of shape to cell dimensions is not an integer number, the program will resize the dimensions of the whole element to fit the cell sizes. For each stage of the micromagnetic simulation, a solution is found when the Landau-Lifschitz equation has approached a convergence value for the $|\mathbf{M} \times \mathbf{H}|$ term. The user can preset the convergence value in the software before the commencement of the simulation; the recommended value is 1×10^{-5}.

The OOMMF simulation package allows the user complete control over the simulation, including material properties such as M_s, A, $K1$ (both A and $K1$ (= K_1) are assumed to be constant over the extent of the simulation), the initial magnetisation configuration and simulation requirements such as α (recommended value = 0.5) and the demagnetisation type. The default demagnetisation (used for all the simulations discussed in this thesis) setting is a constant magnetisation through out the system and the average demagnetisation for each cell is then computed. In the simulation, a field can be applied along any, or a combination, of the three axes of the system (as defined in Figure 1.6). From this the guide to the fields at which irreversible events (and their nature) can occur. The results of the OOMMF simulations for the permalloy elements are discussed in chapters 4, 5 and 6 and the results for the cobalt elements and arrays are discussed in chapter 7.

An example of the magnetisation distribution in a $500 \times 500 \times 20$ nm^3 permalloy element, in zero field, as solved by OOMMF is given in Figure 1.6 and Table 1.1. The individual

cell sizes for the simulation are 5×5×20 nm^3. These dimensions, which have been selected as the in-plane dimensions, are approximately the calculated exchange length for permalloy (5.9 nm) [14] and allow for an integer number of cells in a simulated element. Unfortunately the two-dimensional version of OOMMF does not allow for more than one cell through the thickness of the material. This does not allow for elements that have random changes in the magnetisation vector through the thickness to be modelled. Due to the thickness of the material discussed, however, the magnetisation is not expected to vary greatly. This cell size is the standard dimension for all simulations in the thesis except the arrays, which have been increased to 10 nm to decrease computation times. Figure 1.6 is a visual representation of the magnetisation distribution along all the axes within the system. Here the arrows indicate the direction of the magnetisation in the element and the colours indicate the direction and amplitude of the magnetisation. Visible is the four-domain vortex structure discussed later in section 1.5. In this thesis only the x-axis magnetisation component is shown. The accompanying table, Table 1.1, is the global data for the system. This includes the number of iterations to minimise the energy (Iteration), the applied field (B_x, B_y and B_z), overall fractional magnetisation in the x, y and z direction (M_x/M_s, M_y/M_s and M_z/M_s) and the total energy density of the system (Energy). It is possible to obtain local data for each point in the system and this can be used to calculate the stray field from the element (section 1.4.2).

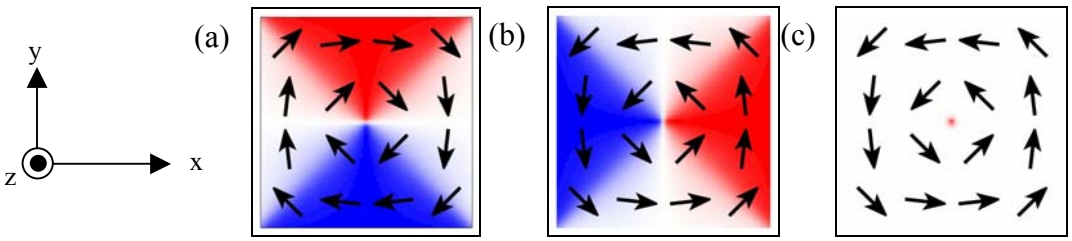

Figure 1.6: visual represention of the (a) x-axis, (b) y-axis and (c) z-axis magnetisation distributions within a 500×500×20 nm^3 permalloy element as modelled by OOMMF. Included are the simulation defined axes, z is out of the plane of the paper. The arrows indicate the direction of the magnetisation within the element and the colours indicate the direction and amplitude of the magnetisation.

Field #	Iteration	B_x (mT)	B_y (mT)	B_z (mT)	M_x/M_s	M_y/M_s	M_z/M_s	Energy (J/m^3)
0	325	0	0	0	0	0	-0.0002	1647.2693

Table 1.1: the outputed global data for the OOMMF simulation of 500×500×20 nm^3 permalloy element shown in Figure 1.6.

1.4.2 Magnetostatic field calculations for a two dimensional structure

A programme (developed by McVitie et al, [15], based on work by Beardsley [16]) has been developed to calculate the stray field associated within the element if the magnetisation distribution is known (such as the magnetisation distribution of an element simulated using the OOMMF programme discussed in the previous section). The stray field, at a user defined height, is calculated by the inverse Fourier transforms of the components of the magnetisation, which in turn have been transformed into reciprocal space by Fourier transforms, provided the thickness of the magnetic layer and cell size are known. Due to the nature of the Fourier transforms used to calculate the stray field the output has a real and imaginary component that can be separated by the programme used.

1.5 Ferromagnetism of discrete micron sized thin films

The restriction of the in-plane dimensions of thin films to dimensions of <5 μm (that is to say the creation of elements by the lithography methods discussed in chapter 2) introduces another factor in the determination of the formation of the domains, the element shape. As stated in section 1.3, domain formation is mainly a competition between the exchange energy and the magnetostatic energy but the element shape can also dictate the magnetisation distribution. This is in the absence of an applied field, a training field during deposition [17] or a strong net magnetocrystalline anisotropy energy. For example, the polycrystalline permalloy and cobalt discussed in this thesis, which are assumed to have no net magnetocrystalline anisotropy when summed over the volume of the element [5]. The individual grains within the elements still have an associated anisotropy. By introducing a shape to the thin film a magnetic boundary is introduced in the system. This is known as the shape anisotropy. To help minimise the stray field energy in the system, the magnetisation will rotate to lie along the edge of the boundary, for example, the configuration shown in Figure 1.7. The minimisation of the stray field at the boundary shows that shape anisotropy is actually a magnetostatic energy effect. The arrows

represent the progression of spins towards the boundary, the colours are to help identify the line of rotation.

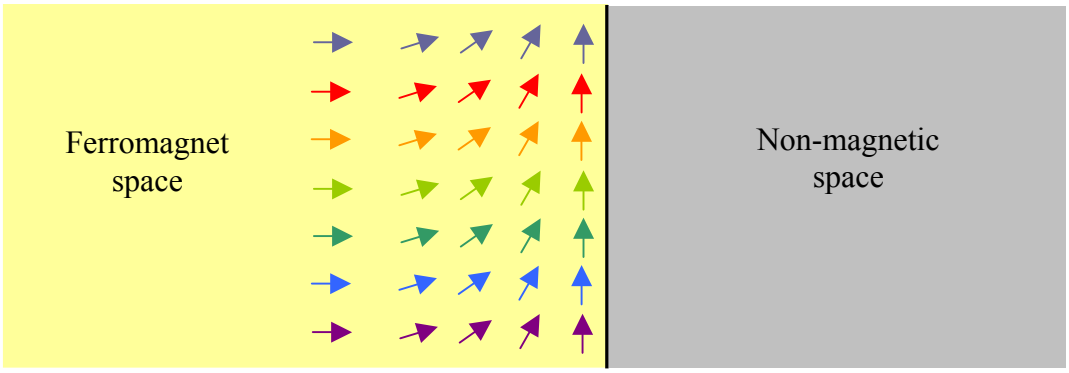

Figure 1.7: schematic of the rotation of magnetisation from the bulk to an edge of a thin film to illustrate the minimising of the stray field due to the shape (shape anisotropy). The colours indicate the line of rotation.

The shape anisotropy was a factor in the determination of the two aspect ratios of the elements considered in this thesis (a rectangle with an aspect of 5:1 and a square with an aspect ratio of 1:1). The rectangle and square structures (where the in-plane dimensions are no less than 0.2 and no greater than 2 μm for permalloy and 270 nm for cobalt) have been chosen as they are relatively simple to fabricate and reproduce by electron beam lithography (section 2.2) and focussed ion beam lithography (section 2.3). The rectangle and the square structures have also been chosen as they result in different magnetic states in zero field. For the materials and dimensions chosen, the 5:1 element is expected to form a near uniform magnetic state (such as that shown in Figure 1.8(a)) and the 1:1 element is expected to form a flux-closure state (such as that shown in Figure 1.8(b)) in the absence of strong anisotropy or a training field. In zero applied field, the near uniform state of the rectangular structure has a large net in-plane component of magnetisation (the remanent magnetisation, M_R) along the easy axis indicated in Figure 1.8(a). In contrast the flux closure structure of the square has no net in-plane component but a small leakage out-of-plane.

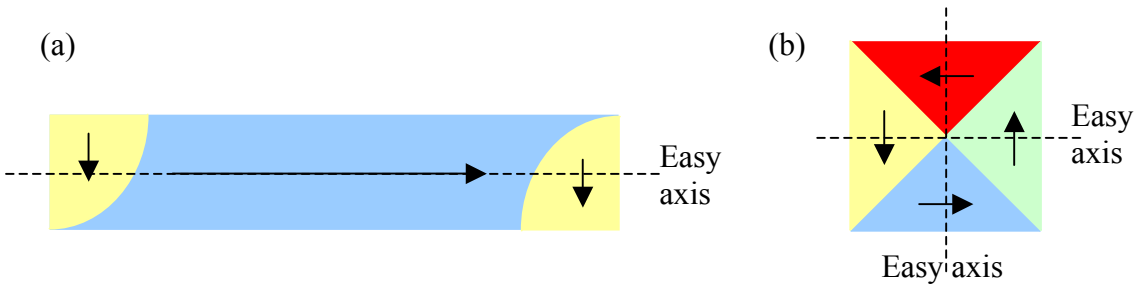

Figure 1.8: (a) a micron sized rectangular element (with in-plane aspect ratio of 5:1) in the S-state magnetisation: (b) a micron sized square element (with in-plane aspect ratio of 1:1) in a four-domain flux closure state. Shown in (a) and (b) are the easy axes of the structure. The arrows indicate the direction of magnetisation.

The magnetic properties of the structures also differ upon the application of a field. As a cyclic field is applied to the rectangular element along the easy axis (shown in Figure 1.8(a)) the domains within the structure rotate by an irreversible path to align with the field, the switching field: as a result there is always an in-plane component of magnetisation along the easy axis. The applied field at which the irreversible event within the structure occurs is known as the coercive field, H_C. The resultant hysteresis loop, Figure 1.9(a), is a well defined square. In contrast as a cyclic field is applied to the square element along an easy axis (shown in Figure 1.8(b)), the vortex of the flux closure structure is expelled and reformed in the applied field by domain contraction and expansion. The vortex formation is at a lower field than the vortex expulsion but, in general, with the same sign: as a result there is no in-plane component of magnetisation at remanence. The resultant hysteresis loop is shown in Figure 1.9(b).

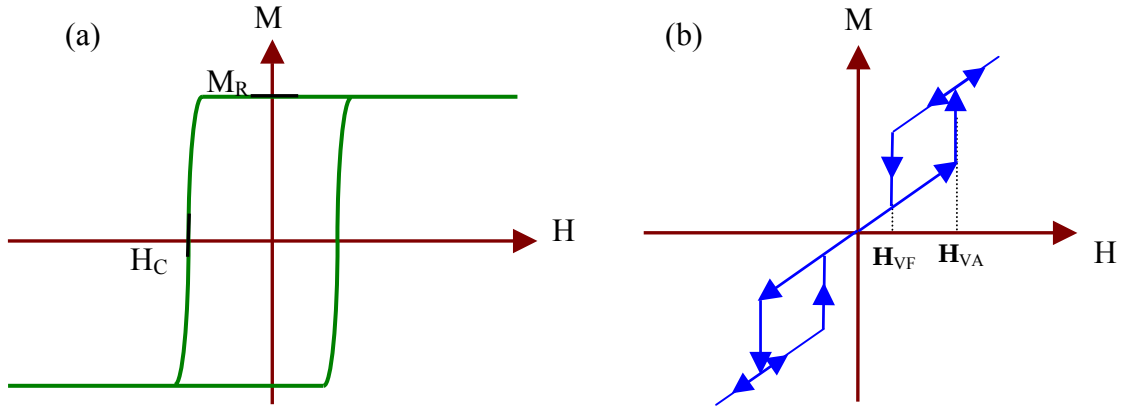

Figure 1.9: the schematic of a hysteresis loop (with arbitrary units) for the easy axis cycle of an element with aspect ratio (a) 5:1 and (b) 1:1. The elements have micron sized dimensions.

A more complete description of the magnetics of the rectangular and square structures (as simulated by the OOMMF programme) is given in chapter 4. The descriptions include the simulated energies of different remanent states and the behaviour of the elements in a

cyclic magnetic field, including magnetisation states. Rave and Hubert [18] have simulated various magnetic states for a permalloy element with similar dimensions.

1.5.1 Other factors that can effect the magnetisation of discrete submicron thin films

Discrete ferromagnetic elements fabricated by and electron beam lithography (EBL), for use in magnetic sensors, memory and storage, have been extensively studied. In this section, a selection of work pertaining to discrete elements is presented. This previous work helped define the geometry, dimensions and material of the elements discussed in this thesis. Other work, such as roughness and periodic edge structure contributed to ideas on the structures fabricated by focussed ion beam (FIB) lithography.

There are several factors that affect the behaviour of magnetisation within elements in an applied field, $\boldsymbol{H}_{APP}$ (including zero field). Dimensions, overall shape, orientation to $\boldsymbol{H}_{APP}$, previous $\boldsymbol{H}_{APP}$, time, etc. all affect the behaviour of the magnetisation within an element. There have been many studies carried out on what effect the shape has on the behaviour of elements in $\boldsymbol{H}_{APP}$ from basic ellipses with varying aspect ratios [14, 19, 20], through rings [21, 22], squares, triangles, pentagons [23] and rectangles [24, 25]. The shape of the element has been found to affect the coercivity of the element as well as the magnetisation distribution within the element. Schneider et al, [14] found that the reversal of sub-micron elliptical permalloy elements proceeds by vortex free or vortex heavy paths depending on in-plane aspect ratios (vortex free is for large aspect ratios). Uhlig and Zweck [21] found that a permalloy ring (with dimensions of 0.75 and 2 and 1.5 and 3 μm respectively) can support a flux closure (following the circumference of the ring) or an "onion" state at remanence. The "onion" state is a state where bulk of the magnetisation follows the applied field and creates two domains in a ring with a "head to head" domain wall in one half.

The end shape, temperature and time of the applied field on the switching mechanisms within elements have been investigated by Yi et al, [26]. Yi et al, found that by curving the end of 10 nm thick permalloy elements, there was a reduction in the switching field of the element when compared to an element with a squared end. This was due to the differing magnetisation states supported by the two types of element. The switching field for both types of elements was found to decrease with temperature. By varying the time that it takes to cycle an element through the hysteresis cycle, different magnetisation states were found at intermediate stages in the cycle, especially before reversal of the magnetisation occurred.

Studies of the effects of edge structure on magnetic properties have been investigated. Herrmann et al, [27] discovered that for periodic edge structures within an element, the magnetic microstructure varied from a similar element with a smooth edge structure. The magnetic states also varied with the periodicity, dimensions and edge structure. The switching field was also found to decrease with the period of the structure. Bryan et al, [28] also discovered that, in general, increased edge roughness increased the coercivity of the permalloy elements of several widths that were 5 nm and 7.6 nm long. Lim et al, [29] found that the switching fields for 400 nm wide, 12 nm thick permalloy elements increased with the angle between $\boldsymbol{H}_{APP}$ and the long axis of the element. This dependence decreased, however, as the width of the element is decreased. Cowburn [30] estimated that for a permalloy element used as part of magnetic random access memory (MRAM) technology [31], the minimum size is limited by superparamagnetism. This is related to the areal footprint of the element. Cowburn ultimately concluded that the difficulty in writing the data would be the greatest difficulty.

1.5.2 Arrays of discrete submicron ferromagnetic thin films

Previously in the discussion of the magnetic material in this chapter, only isolated thin films and elements have been considered. The magnetisation within these systems has been assumed to be allowed to relax without the presence of additional stray fields associated with other elements. When a second element is brought in to close proximity, if there is a component of stray field emanating from one element, the magnetisation within another element will be affected. If there is an array of elements then, from equation 1.9, all the elements contribute to the magnetisation state of the other elements within the array, although, as will be shown in chapter 7, only the first nearest neighbours significantly contribute.

Previous investigations into ferromagnetic arrays have shown that cobalt has a fractional spread of switching values with respect to the switching field that is smaller than that of permalloy elements with similar dimensions to those discussed in chapter 7 [32]. Kundrotaite et al, [33] established that the mean switching field of cobalt arrays were independent of the gap size between the elements of similar dimensions but the spread of the switching field did vary. For a square cobalt array of 7.5×7.5 μm^2 sized elements studied by Lau et al, [34] the reversal takes place by two mechanisms: either by the formation of a four-domain flux closure structure or by the formation of a seven-domain flux closure structure. The four-domain flux closure state is thought to originate from a state with one vortex nucleation site, for example a C-state, while the seven-domain flux

closure structure is thought to originate form a state with two nucleation sites, for example an S-state. An investigation into elliptical permalloy elements by Liu et al, [35] with similar dimensions to the elements within the array discussed in chapter 7, shows that the antiparallel C-state forms a four-domain flux closure structure. In contrast, the S-state, due to the parallel end domains, forms a uniform state. The formation of the C- and S-state are thought to be related to the rate of change of the applied field with respect to time. An investigation into 7.5×7.5 μm^2 arrays by Volkov et al, [36] discovered a relationship that is inversely proportional between thickness of the cobalt elements and their coercivity.

The magnetisation of 10×10 μm^2 cobalt arrays with 270×270 nm^2 elements and a periodicity of 400 nm has been investigated by bright field, Lorentz and differential phase contrast imaging and the results are discussed in chapter 7.

Bibliography

[1] OOMMF simulation package available for download at NIST (URL active 16/02/06): http://math.nist.gov/oommf/

[2] Jiles D., *"Introduction to magnetism and magnetic materials"* Chapman and Hall 1998, ISBN 041279850.

[3] Hubert A., Schäfer R., *"Magnetic domains: the analysis of magnetic microstructures"*, Springer-Verlag Berlin Heidelberg, 1998, ISBN 3540641084.

[4] Harte K.J., J. Appl. Phys. 39(3) (1968) 1503.

[5] Dunin-Borkowski R.E., McCartney M.R., Kardynal B., Smith D.J., Scheinfein M.R., Appl. Phys. Lett. 75(17) (1999) 2641.

[6] Weiss P., Compt. Rend., 143 (1906) 1136.

[7] Weiss P., J. Phys., 6 (1907) 661.

[8] Landau I.D., Lifschitz E.M., Physik Z. Sowjetunion 8 (1935) 153.

[9] McVitie S., Chapman J.N., J. Magn. Magn. Mat. 83 (1990) 97.

[10] Crew D.C., Stamps R.L., J. Appl. Phys. 93(10) (2003) 6483.

[11] Fidler J., Schrefl T., J. Phys D: Appl. Phys. 33 (2000) R135.

[12] National Institute for Standard and Technology: http://math.nist.gov/ (active as of 27th March 2007)

[13] Brown W.F. Jr., Micromagnetics, Wiley & Sons, New York Press.

[14] Schneider M., Hoffmann H., Zweck J., J. Mag. Mag. Mat. 257 (2003) 1.

[15] McVitie S., White G.S., Scott J., Warin P., Chapman J.N., J. Appl. Phys. 90(10) (2001) 5220.

[16] Beardsley I.A., IEEE Trans. Magn. 35(1) (1989) 671.

[17] Gentils A., Chapman J. N., Xiong G., Cowburn R. P., J. Appl. Phys. 98 (2005) 053905.

[18] Rave W., Hubert A., IEEE Trans. Mag. 36(6) (2000) 3886.

[19] Schneider M., Liszkowiski J., Rahm M., Wegscheider W., Weiss D., Hoffmann H., Zweck J., J Phys D: Appl Phys 36 (2003) 2239.

[20] Felton S., Gunnarsson K., Roy P. E., Svedlindh P., Quist A., J. Mag. Mag. Mat. 280(2-3) (2004) 202.

[21] Uhlig T., Zweck J., Phys. Rev. Lett. 93(4) (2004) 047203-1.

[22] Zhu F.Q., Chern G.W., Tchernyshyov O., Zhu X.C., Zhu J.G., Chien C.L., Phys. Rev. Lett. 96(2) (2006) 027205.

[23] Kirk K.J., McVitie S., Chapman J.N., Wilkinson C.D.W, J. Appl. Phys. 89(11) (2001) 7174.

[24] Kirk K.J., Scheinfein M.R., Chapman J.N., McVitie S., Gilles M.F., Ward B.R. Tennent J.G., J. Phys. D: Appl. Phys. 34 (2001) 160.

[25] Kirk K.J., Chapman J.N., Wilkinson C.D.W., Appl. Phys. Lett. 71(4) (1997) 539.

[26] Yi G., Aitchison W.D., Chapman J.N., Wilkinson C.D.W., J. Appl. Phys. 92(10) (2002) 6087.

[27] Herrmann M., McVitie S., Chapman J.N., J. Appl. Phys. 87(6) (2000) 2994.

[28] Bryan M.T., Atkinson D., Cowburn R.P., Appl. Phys. Lett. 85(16) (2004) 3510.

[29] Lim C.K., Yi G., Chapman J., Nicholson W.A.P., McVitie S., Wilkinson C.D.W., J. Phys. D: Appl. Phys. 36 (2003) 3099.

[30] Cowburn R.P., J. Appl. Phys. 93(11) (2003) 9310.

[31] Prinz G. Science (Washington D.C. U.S.) 282 (1998) 1660.

[32] Kirk K.J., Chapman J.N., McVitie S., Aitchison P.R., Wilkinson C.D.W., Appl. Phys. Lett. 75(23) (1999) 3683.

[33] Kundrotatie A., Chapman J.N., Rahman M., IEEE Trans. Mag. 39(5) (2003) 2672.

[34] Lau J.W., Beleggia M., Schofield M.A., Neumark G.F., Zhu Y., J. Appl. Phys. 97 (2005) 10E702.

[35] Lui X., Chapman J.N., McVitie S., Wilkinson C.D.W., J. Appl. Phys. 96(9) (2004) 5173.

[36] Volkov V.V., Zhu Y., Malac M., Phil. Mag. 84(25-26) (2004) 2607.

2 Deposition and fabrication of magnetic thin film structures

In this chapter the deposition and fabrication techniques that are used in this project are discussed. The two deposition techniques (discussed in section 2.1) are plasma sputter coating and thermal evaporation, both in zero applied magnetic field and with no substrate heating or cooling. Plasma sputter coating is a deposition technique that gives smoother films and finer grains than thermal evaporation. Reported grain sizes for permalloy are <5 nm for plasma sputter coating [1] and 7-10 nm for thermal evaporation [2]. The systems for both deposition techniques are housed at the University of Glasgow.

The magnetic thin film structures investigated in this project were fabricated by two techniques: i) electron beam lithography (EBL, section 2.2); and ii) focussed ion beam (FIB) lithography (section 2.3). For EBL, the process of the fabrication on a bulk substrate and on an electron transparent substrate (~50 nm thick SiN), is discussed. The majority of the EBL fabrication stages on a bulk substrate and on an electron transparent substrate are the same (spinning a bilayer, obtaining an inverted "T" profile and the development conditions), with the exception of cleaning, electron beam dose and lift-off. FIB lithography is a relatively new technique in which nanostructures are being fabricated for a direct comparison to EBL. In this section a discussion will be given on aspects of FIB lithography such as: machine hardware, gallium implantation simulations (using a simulation package), scanning techniques, the relationship between depth and dose and other factors.

2.1 Deposition Techniques

2.1.1 Plasma sputter coating

The term sputtering applies to a system where fast heavy particles bombard a target and erosion of the target takes place [1]. The sputter system (Emitech K575x peltier cooled twin head system) uses argon for the fast moving particles as argon is a gas that has a large atomic number and is inert when used to sputter material. The fast moving argon ions are generated in a way similar to that of a cathode gas tube where the free ions and electrons are attracted to the opposite electrodes and a small current is produced. The glow discharge region (so called because of the associated luminous glow) is where self-sustaining ionisation of the argon takes place in the presence of an applied electric field. This occurs after the ionisation potential for one electron has been exceeded. In the glow discharge region, the current density and voltage drop between the cathode (metal target) and anode (behind the sample) is constant, Figure 2.1.

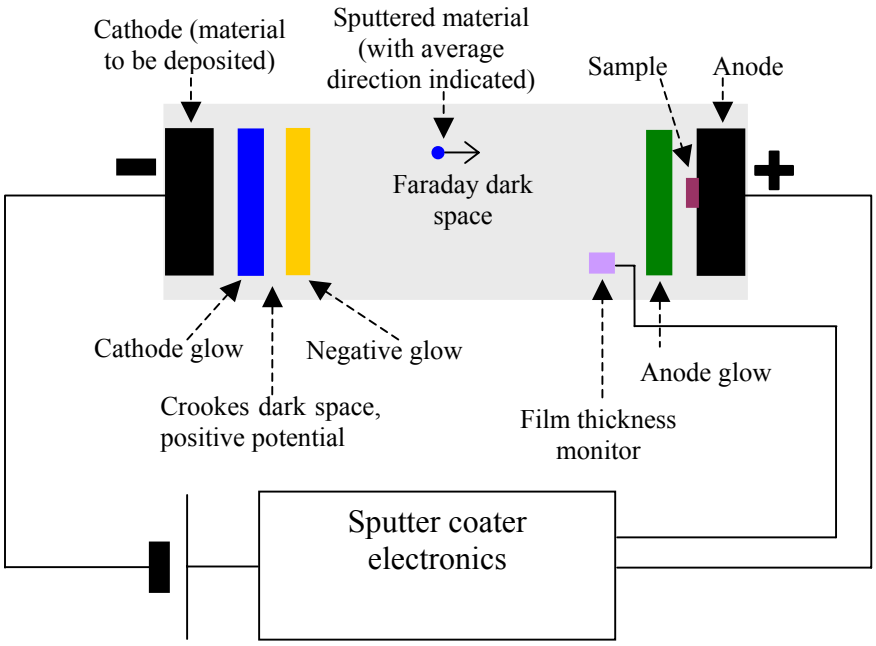

Figure 2.1: the physical appearance of the glow in the sputter coater chamber from cathode (metal target) to anode (behind the sample). Also shown are the positions of the power source, sample and film thickness monitor (FTM). Not to scale.

In the glow discharge region, the discharge is self-sustaining as the positive ion bombardment of the cathode produces secondary electrons that are accelerated towards the anode causing ionisation, with the resultant ion being attracted to the cathode. As the resulting ions move towards the cathode they pass through an area of space, know as Crookes dark space, located just after the cathode glow and before the negative glow,

Figure 2.1. The space has very large positive ion density which results in a significant voltage drop that accelerates the ions into the target. When the ion bombardment of the cathode occurs the cathode material (i.e. the material to be deposited) is eroded (through secondary scattering events) and redeposited in an omni-directional manner in the sputter coater, this forms a film of the cathode material on the substrates.

The sputter coater system is fully automated (the system will not sputter unless an evacuation pressure of $<5.25 \times 10^{-5}$ Torr and a sputter pressure for the Argon gas of ~517 Torr are obtained) and this gives good reproducibility between samples. Unfortunately, however, the metallic source in the sputter coater is extended, ~5.4 cm in diameter, and the working distance is small, ~4 cm. The extended source and small working distance leads to the omni-directional nature of the sputter coater. This omni-directional sputtering can create problems for the nanoscale dimensions of the elements fabricated by electron beam lithography (EBL), as illustrated in Figure 2.2(a) shown in section 2.1.2. From Figure 2.2(a) metal can be observed to coat the sidewall of the resist thus causing problems during the lift-off process, this process is discussed further in section 2.2.1.

2.1.2 Thermal evaporation

In contrast to plasma sputter coating, thermal evaporation is an almost unidirectional deposition system. The metal to be deposited in the thermal evaporator is placed in a ceramic crucible that is attached by wire to the electrodes. A current is passed through the wire surrounding the crucible. This heats the metal above its melting point and metal vapour then travels upwards towards the sample where the vapour cools and coats the sample. The magnitude of the current through the crucible regulates the deposition rate, with the evaporation current threshold equivalent to the melting point of the metal. The sample is ~20 cm from a source ~0.25 cm in diameter, giving a divergence angle at the sample of ~0.36^{o}. This system is more suited for coating nanoscale structures fabricated by EBL as the near unidirectional beam is less likely to coat the sides of the resist, Figure 2.2(b). In comparison to other systems (a modified evaporator ($<3 \times 10^{-6}$ Torr) or a Plassis deposition system ($\sim 3.75 \times 10^{-7}$ Torr)) the thermal evaporation system used has a relatively poor vacuum pressure (deposition is initiated when the pressure is $<4 \times 10^{-6}$ Torr on an analogue Pirani gauge). Both the modified evaporator and Plassis deposition systems relative new systems that are housed in a cleanroom. The relatively poor pressure increases the probability of the metal vapour scattering off a contaminant (such as a hydrocarbon from the pumping system) before reaching the specimen thus increasing

directionally in the beam deposition. This system is used, however, as it can readily deposit permalloy.

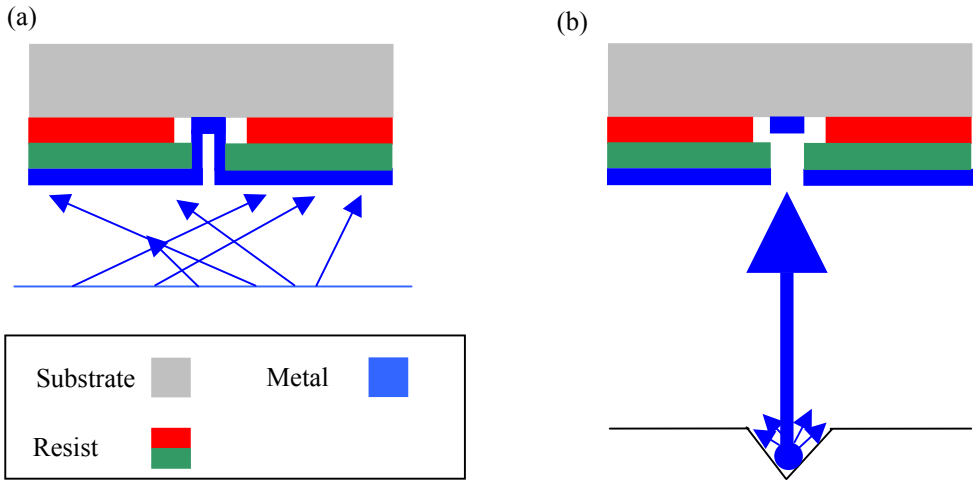

Figure 2.2: deposition of a nanoscale element by a) plasma sputter coating and b) thermal evaporation, not to scale.

2.2 Electron beam lithography and lift-off of electron transparent substrate

The conventional method for fabricating nanoscale elements is by electron beam lithography (EBL). EBL is a process that uses electrons to change the chemical bonds in a resist to create a pattern. The electron microscope system used in this project to fabricate EBL structures is the Leica Microsystems Lithography LTD EBPG 5-HR100 (henceforth known as the beam writer) located at the University of Glasgow. The EBL system used in this project has a minimum spot size of 12 nm (although through novel techniques, features as little as ~3 nm can be written [3]) and can write an area up to 126 mm^2. The electron beam writer is housed in a class 10 cleanroom (a class 10 cleanroom is a room that has less than 246 particles (greater than 0.5 μm) per m^3; class 10 cleanrooms are also known as ISO class 4 cleanrooms [4]).

The method for fabricating nanoscale structures by EBL is well established and consequently the process has been well refined. For this report, the fabrication process has been broken down into three steps, pre EBL processing, EBL and post EBL processing. The EBL process for this thesis is based on the methods developed by Khamsehpour et al [5] with additional work by Yi et al [6]. Details of the practical issues learned in this project are included in the description below.

2.2.1 Overview of electron beam lithography processing

A schematic of the complete EBL process is shown in Figure 2.3. Before the sample can be placed in to the electron beam writer it has to be cleaned and the bilayer of resist is then spun onto the sample. To clean the sample, Figure 2.3(a), the following steps were observed:

1. Place in warm acetone (and ultrasonic bath if fabricating on a bulk substrate) to degrease and remove contaminants from the surface of the substrate.

2. Then place into isopropanol (IPA) to remove the acetone. Acetone has a low boiling point and evaporation leaves drying marks (caused by impurities in the cleaning solution for example) on the surface of the substrate.

3. The substrate is then placed into methanol which has a higher boiling point. Little evaporation occurs reducing the chances of leaving drying marks on the surface of the substrate.

4. The sample is then dried in pure nitrogen and baked in an oven at 180 ^{o}C for 5 minutes to remove any remaining water vapour that may be present on the surface of the substrate.

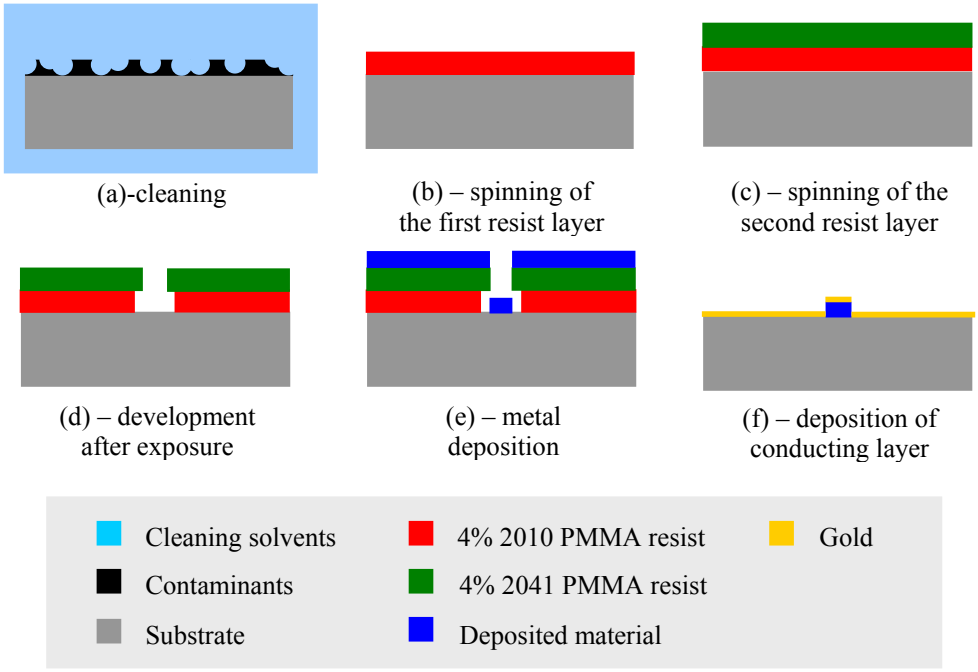

Figure 2.3: schematic, with key, highlighting the important steps in electron beam lithography. Descriptions of individual steps are in the text.

After the substrate has been cleaned a bilayer of polymethyl methacrylate (PMMA) resists is spun on to the sample. The PMMA resists are molecules of PMMA that are

dissolved in solvents (mainly ortho-xylene). The two PMMA resists used in this project were 4% 2041 (molecular weight of 345 amu) and 4% 2010 (molecular weight of 90 amu) [7]. Both of the PMMA resists were spun at 5000 rpm for 60 s to give each resist a uniform thickness of 100 nm across the surface for the electron beam writer. After the 4% 2010 was spun the sample was baked at 180 ^{o}C for 45 mins, Figure 2.3(b). This was then repeated for the 4% 2041 layer, Figure 2.3(c). To achieve the inverted "T" profile during EBL the 4% 2010 resist is spun on as the bottom layer, as this resist has a higher sensitivity with respect to electron-resist interactions than the 2041 4% resist top layer. The inverted "T" profile is used to fabricated elements as it has been found that this gives better edge profiles than a single layer resist. The resist-covered substrate can now be submitted to the electron beam writer to have the relevant areas of resist exposed.

After exposure to the electron beam writer, the developer removes PMMA chains that have been cross-linked by exposure to the electron beam by dissolving them in a solvent, Figure 2.3(d). The developer is a 2.5:1 mixture of methyl isobutyl ketone (MIBK) to IPA. The development time and temperature are essential for good definition of elements. For this project the developer solution was kept at 21^{o}C and the resist is immersed in the solution for 60 s then immediately immersed in fresh IPA to stop development. The specimen is now ready for metal deposition, Figure 2.3(e). After deposition the sample is immersed in warm (~40 ^{o}C) acetone to remove the remaining resist, this is known as lift-off. It is essential that lift-off is allowed to go to completion as when the sample is removed from the solution any resist left on the sample cannot easily be removed. It is also important not to leave the sample in the acetone solution any longer than necessary, as the acetone has been known to attack and deform the metal, Figure 2.4. When the sample has been removed from the acetone solution, it is then cleaned in fresh acetone. This removes fragments of metal that have become loosely attached to the surface. The sample is then cleaned in a similar manner to the first step described in Figure 2.3(a). After lift-off the sample has to be coated with a thin layer of conducting material to avoid charge build-up in the electron microscope due to the poor conduction of the silicon nitride (Si_3N_4, denoted in the project SiN), Figure 2.3(f). The preferred coating layer for the samples discussed in this thesis was ~4 nm gold as the sputtered gold layer is sufficiently thin to still allow reasonable imaging of magnetic structures. Other materials of various thickness, such as carbon and chromium, can be used.

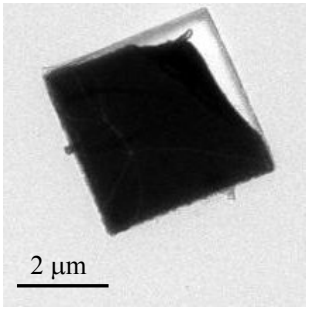

Figure 2.4: TEM image of a 4×4 μm^2 cobalt element damaged during the lift-off process after being submerged in acetone for 26 hrs.

The complete EBL process, from the initial cleaning of the substrate to having a sample ready to analyse, can take between 2 to 3 days if all equipment is available and in proper working order, for the majority of this time the sample remains in a cleanroom. Of the 2 to 3 days the electron beam writing process usually takes <2 hours (for most patterns discussed in this thesis a write time of ~30 minutes was possible).

2.2.2 Electron beam lithography

To create structures using the electron beam writer, the relevant areas that are to be exposed first have to be defined using a CAD programme. In this project, L-edit (manufactured by Tanner EDA) was used to design the patterns. For example, a screen shot of the cobalt arrays discussed in chapter 7, as designed in L-edit, is shown in Figure 2.5. In L-Edit, up to 64 layers can be designed at one time and the results can be observed on screen, this allows for complete registration between multilayer devices. The L-edit programme stores the patterns in integer co-ordinates scaled to a user defined base unit, allowing for shapes with irregular spacing, such as waveguides, to be designed. For the example shown in Figure 2.5 the base unit used was 1 nm. Everything designed in the L-edit programme is contained in cells. These cells can be inserted into other cells and repeated to create arrays. The advantage is that designs can be changed in one cell and this propagates through the other cells. Figure 2.5 is a collection of such cells. Unfortunately certain shapes are hard to reproduce, due to the pixelation caused by the electron beam probe, for example circles, shapes with crossovers, etc. The L-edit output (.gds) has to under go several programming levels before the file is compatible with the Unix based system that controls the electron beam writer. This process is summarised in Figure 2.6.

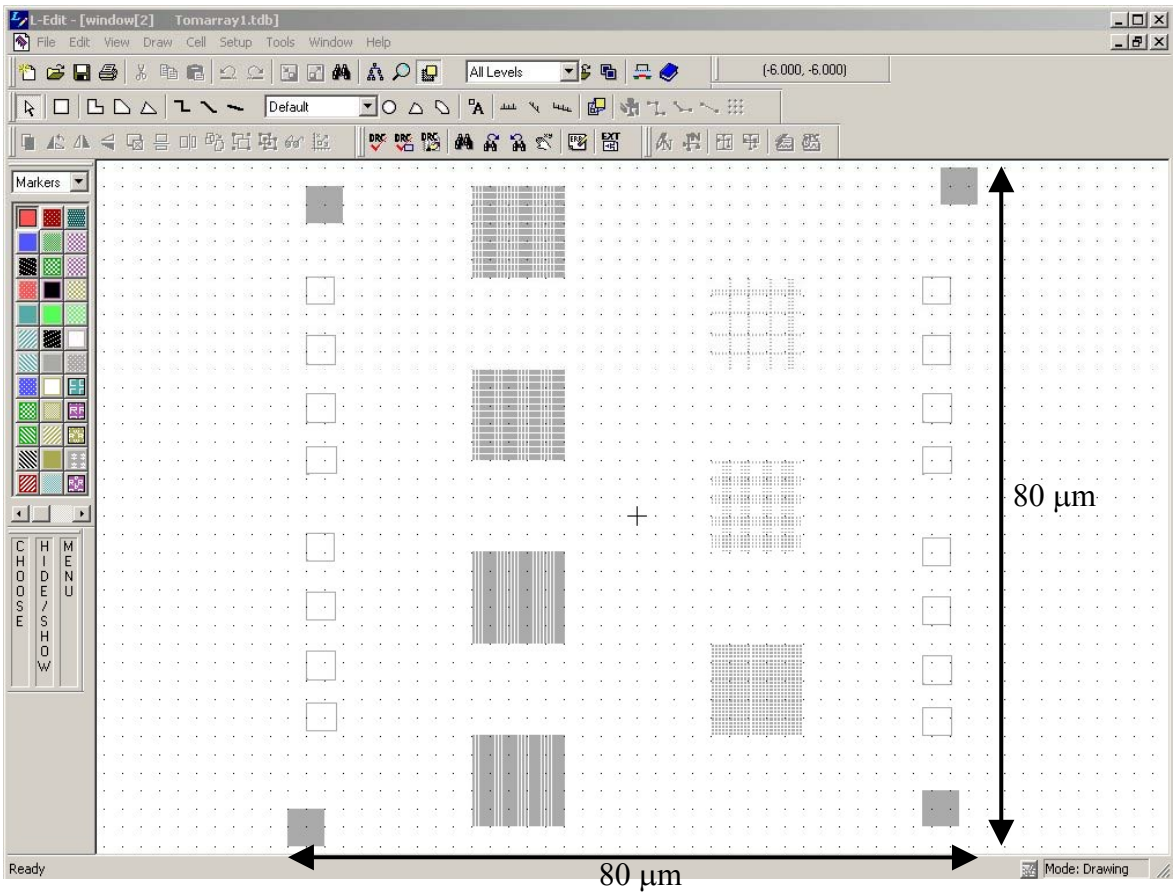

Figure 2.5: L-edit screen shot for cobalt arrays to be patterned on a 100×100 µm² electron transparent substrate.

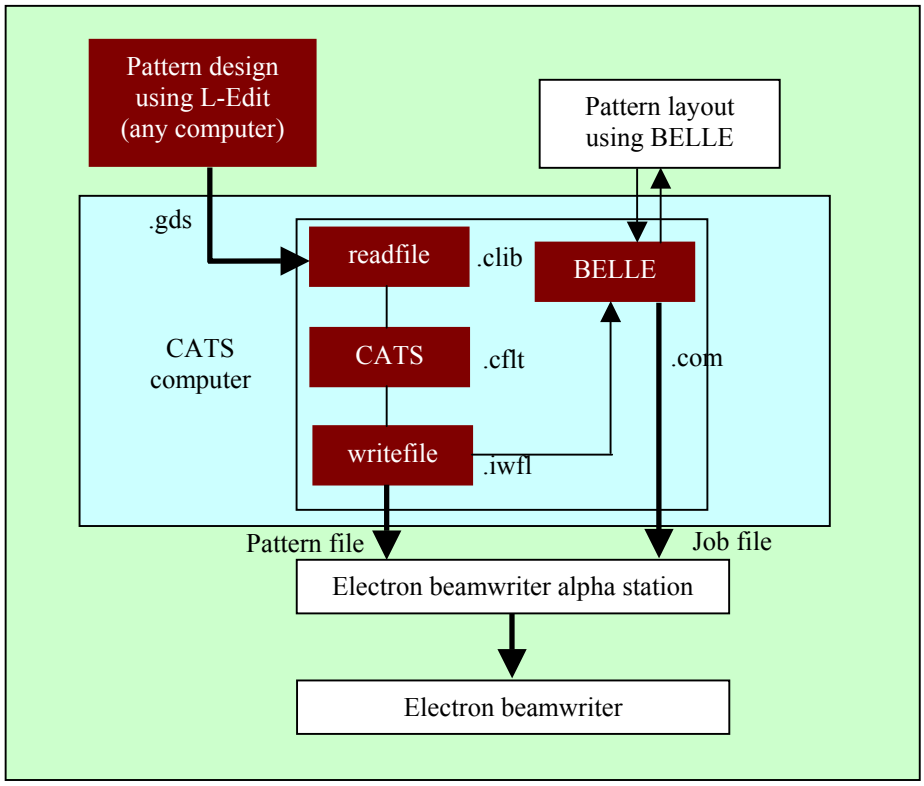

Figure 2.6: Summary of data flow for the control programmes for the electron beam writer, programme steps are in red boxes.

The important steps to note in Figure 2.6 are the CATS programme and BELLE programme steps. The CATS programme (computer aided transcription system

manufactured by Los Gatos) is used to fracture the CAD design into a series of primitive shapes that removes the unnecessary stage movements from the electron beam writer (this is to minimise stage movements for better pattern registration). In addition to removing overlap in shapes (fracturing) the CATS programme is used to set the resolution, beam step size, etc, for the electron beam writer. The beam step size is usually set equal to the resolution although multiples can be used; the exact parameters used are unique to the sample. For example, for the cobalt arrays shown in Figure 2.5, the resolution and the beam step size are set to 0.01 μm whereas the larger permalloy elements discussed in chapter 5 had a resolution and a beam step size of 0.05 μm. By setting the beam step size equal to the resolution, the pattern can be accurately written by the microscope on the sample.

The BELLE (Beamwriter Exposure Layout for Lithographic Engineers, developed by the University of Glasgow Electronics and Electrical Engineering Department) programme is the final step in the calibration of the beam writer. It is the BELLE programme where: i) the electron beam energy; ii) the dose to be received; iii) beam spot size and iv) any other relevant parameters are set. The electron beam energy can be set to 20, 50 or 100 keV for low, medium and high resolution lithography respectively. The beam spot size is usually set to be twice the pattern resolution and between a quarter and a tenth the smallest feature size and is selected from a predefined range. For example, as the smallest feature in the cobalt arrays shown in Figure 2.5 is 60 nm, 100 keV electron beam energy with a high dose of 1800 $\mu C/cm^2$ and the beam spot size 15 nm was selected. As the permalloy elements discussed in chapter 5 have larger dimensions (minimum feature size is 200 nm), the dose is approximately half that used for the cobalt arrays (60 nm minimum feature size) and the lower energy 50 keV beam was used (which has lower resolution); this decreases the irradiation time and stage movement (which could result in registration difficulties).

To create the pattern inputted in L-edit, the electron beam probe (formed by a three condenser lens system and focussed by an objective lens, to be discussed in section 3.2) is scanned, in a raster fashion (left to right, bottom to top) using the deflection coils shown in Figure 2.7. The electron source used by the electron beam writer is a LaB_6 filament.

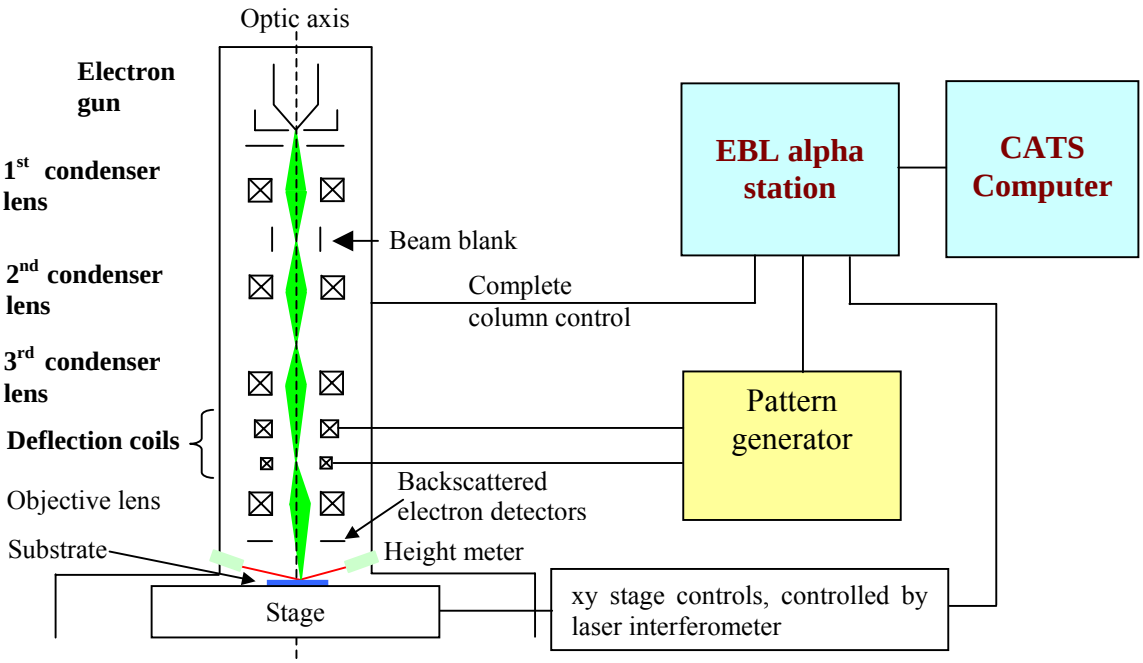

Figure 2.7: schematic of the column and control mechanisms of the beam writer.

The electron beam writer is controlled via a master computer where the pattern and substrate information is stored. The electron beam, when it interacts with the resist, cross-links the relevant chains in the PMMA resist so that they can be dissolved by the developer solution. Due to the energy that the electrons have entering the resist there are relatively few of these events and normally backscattering from the substrate accounts for the majority of the patterning process. For transmission electron microscopy (TEM) imaging, however, the substrate has to be electron transparent. Therefore a higher dose is necessary. From the Klein-Nishina cross section for a free electron, σ_{KN} [8], it can be shown that as the velocity (proportional to the square root of the accelerating voltage) is increased the probability of the electron interacting with the PMMA molecules decreases. The advantage of not having backscatter from the substrate is that it is not necessary to perform proximity correction [9, 10] on the shapes to be exposed. Proximity correction exists to give a lower dose at the edge of the elements to correct for the effects of the increased dose caused by backscatter and is introduced in the CATS programme. As the backscatter is dependent on the type and thickness of both the resist and substrate different proximity correction algorithms exist. Backscattering in a thick substrate would also result in imaging problems within the TEM by producing inelastically scattered electrons, see sections 3.1-3.3.

2.3 Focussed ion beam lithography on bulk and electron transparent substrates

2.3.1 The focussed ion beam microscope

The focussed ion beam (FIB) microscope, shown schematically in Figure 2.8, is similar in construction to an SEM with the difference being the use of liquid metal ions as the source instead of electrons. The most commonly used liquid metal ion source (LMIS) is gallium as the metal is almost a liquid at room temperature (gallium melts at 16^{o}C) and, therefore, requires little heating to achieve emission from the tip. The FIB microscope used in this project is a FEI Strata FIB200TEM focussed ion beam system (henceforth known as the FIB microscope) located in the University of Glasgow. The FIB microscope has a liquid metal gallium ion (Ga^{+}) source that uses an ion extractor voltage of 12 kV [11]. The FIB system has two separate chambers, the ion column and the specimen chamber, that are connected by the column isolation valve. The ion column is mounted on top of the specimen chamber and consists of an LMIS (which is positioned over the central axis of the column), two electrostatic lenses, one set of beam blanking plates, a beam acceptance aperture (BAA), an automatic variable aperture (AVA) and an octupole deflector lens. The ion column operates under high vacuum (<9.33×10^{-7} Torr) to avoid interference to the beam from atmospheric gas molecules and to reduce contamination of the tip.

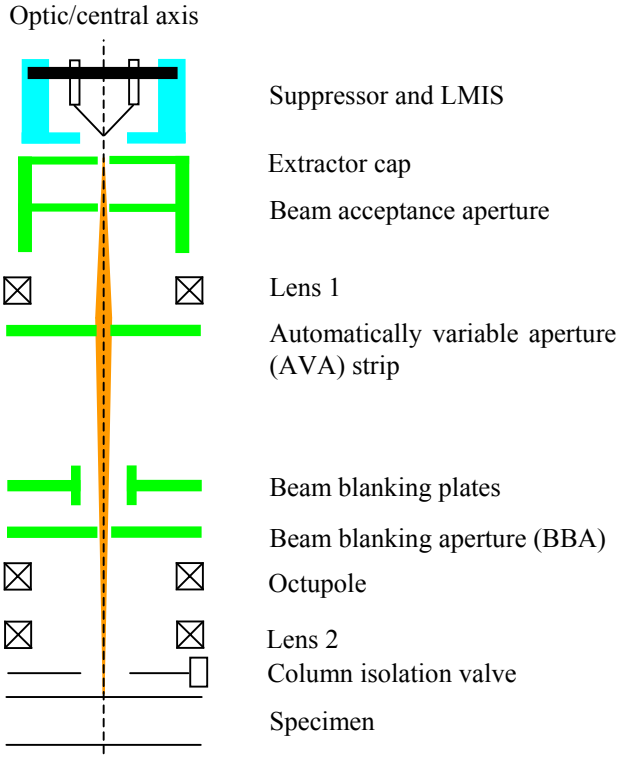

Figure 2.8: the column components of a FIB microscope components [11].

The LMIS has a tungsten tip, Figure 2.9, with a radius of curvature of 1 μm, that has been wetted by gallium and provides the system with a bright source (~10^6 A cm^{-2} sr^{-1}) and has a high angular current density (~17 μA sr^{-1}). By applying an electric field of ~10^8 V cm^{-1} to the ion source the potential barrier holding the electrons to the ions is reduced. In the deformation of the potential barrier the probability of electron tunnelling increases and thus leaving behind a positive ion. When a large negative electric field is applied to the extractor cap a Taylor cone [12] is produced on the LMIS tip. It is upon the formation of the Taylor cone that emission of the ions occurs, giving a current density on the surface of the LMIS of ~10^8 A cm^{-2} and it is from the tip of the Taylor cone (radius ~2 nm) where emission takes place. The ions are then accelerated though an accelerating voltage of 30 kV. The limiting factor of the FIB is chromatic aberration that is the result of a 5 eV spread in the Ga^+ emitted from the source.

Figure 2.9: image of the gallium wetted tungsten tip used as a LMIS for the FIB microscope [13].

Below the LMIS/suppressor assembly and Lens 1 is the AVA. This is the probe-forming aperture strip, Figure 2.8. The aperture strip acts to blank the outer regions of the beam and decrease the number of ions incident on the surface of the specimen (i.e. the ion current). To do this the aperture physically limits the number of ions passing through it. As a result of interacting with the beam, the size of the aperture increases (due to milling, the aperture strip is replaced approximately ever 1–2 years). The beam current also increases with the aperture area but the change in the beam current is easier to measure. It is, therefore, more convenient to quote aperture sizes as the original beam currents incident on the specimen. The aperture sizes (of an unused strip) range from 1 pA (spot size 6 nm) to 7000 pA (spot size 150 nm) [11]. In this project, the 10 pA beam current aperture (spot size 10 nm) has been used unless otherwise stated. The current in Lens 1 varies according to aperture selected. To stop any unnecessary milling or irradiation of samples, the FIB system contains a beam blanking assembly, located between the AVA and Lens 2, Figure

2.8. During blanking, the blanking plates deflect the beam into a Faraday cup [14] in the blanking aperture plate.

In the final section of the column the beam passes through the octupole stigmator/deflector assembly and Lens 2. The octupole/deflector assembly consists of eight metal sectors in precisely machined dielectric tube elements that are used to stigmate the beam and scan it over the surface of the sample. Lens 2 is used to focus the beam onto the surface of the sample.

The specimen stage is housed in the specimen chamber. The stage can move 75 mm in x and y, a working distance in z of 10 mm, tilt from -15^{o} to +51^{o} (the asymmetry is a result of the position of the detectors and other electronics within the chamber) and rotate through 360^{o}. An additional feature of the FIB stage is eucentric tilt and rotation, i.e. the stage can tilt and rotate around an area of interest defined by the user. Also in the specimen chamber are the detectors, a secondary ion detector and a secondary electron detector. To help the user identify topographical information in images, the detectors are positioned off the central axis.

An additional feature of the FIB system is the gas injection system (GIS). The GIS allows the user to inject gas onto the surface of the sample for either etching or deposition and up to four GIS units can be installed on the FIB system. At the University of Glasgow, a platinum GIS has been installed to deposit protective platinum films on the surface of samples. This is commonly used during the process for manufacturing TEM samples prepared by the lift-out method [15]. The ability to easily define and irradiate areas using a range of beam currents and beam movements (as opposed to stage movements), as well as the small beam spot sizes quoted for the FIB microscope [11] warrants investigation into the possible use as a lithography tool for pattering micron-sized elements.

2.3.1.1 Simulated gallium ion implantation

When the gallium ions are incident on the vacuum-sample interface, there are some interactions with the atoms in the sample. The interactions with the atoms in the sample can lead to backscattered ions, secondary ions, secondary electrons, atom vacancies, photon emission, and other such events. A simulation programme, known as stopping and ranges of ions in matter (SRIM) [16], can be used to model these effects. SRIM is "a group of programmes which can calculate the stopping and range of ions (10 eV-2 eV/amu) into matter using a full quantum mechanical treatment of ion-atom

collisions…" [17]. In the SRIM programme atomic effects, such as the screened Coulomb collisions and long-range interactions are taken into account.

The sub-programme of SRIM that calculates the effects of ions in a solid is the TRIM (transportation of ions in matter) programme. The TRIM programme uses a Monte Carlo method [18] in the calculation of the events for the interaction between ions and atoms. From the TRIM calculations, simulated information on the penetration of the gallium ions into the sample can be obtained for three dimensions (the xy-axis (ion straggle) and the z-axis (ion penetration)) for a point impact, Figure 2.10.

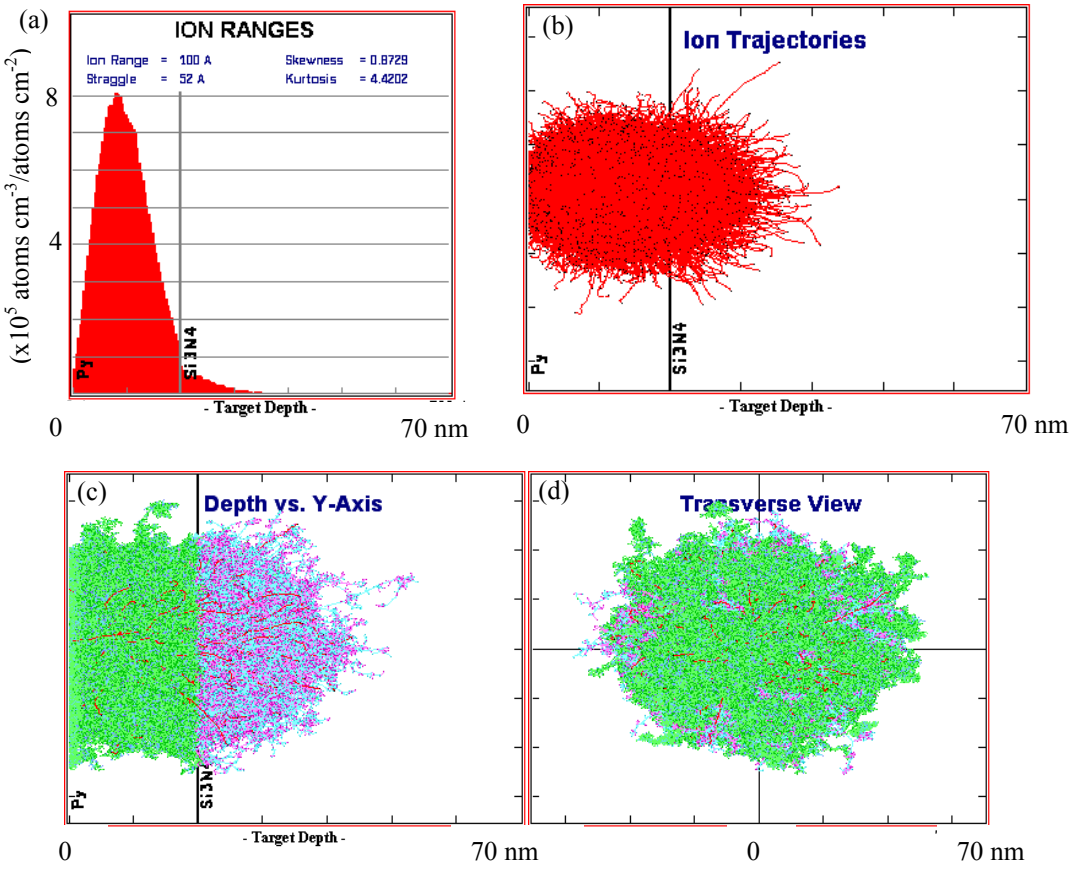

Figure 2.10: simulation of the implantation of 30 keV gallium ions into 20 nm thick permalloy on 50 nm thick SiN. a) is a plot of the ion ranges, b) is a plot of the ion trajectories and c) and d) are the plots of the secondary events through the depth and transveres planes respectively. Red indicates ions, green/dark blue events in permalloy and purple/light blue events in silicon nitride.

Shown in Figure 2.10(a) is the simulated penetration depth obtain for 100,000 ions (the standard number of ions used for this project, shown in red) into 20 nm of permalloy (green/dark blue) on 50 nm of SiN (purple/light blue) substrate. From the simulation it can be observed that the majority of ions are stopped within the first 10 nm of the permalloy, although some do travel through to the SiN layer. Figure 2.10(b) is the primary ion spread tracking the ions from first entering the sample until the ion has lost sufficient energy that

it can no longer perturb an atom in the target by one lattice spacing or more (in this case it is assumed that the energy of the atom returning to its site is dissipated via photonic emission). Figure 2.10(c) is the simulated penetration of the ions and (predominantly) the secondary events (photons, phonons, scattered ions, electron/hole pairs and such like) as the ions moves through the sample. Figure 2.10(d) is the transverse straggle of the ions and secondary events as the ions move through the sample. From the plots a 3D model of how the ions interact with the sample can be built up. The TRIM programme can also calculate the energy imparted by the ions as they collide with the atoms in the sample. Subsequent events such as recoils, vacancy creation, photons produced, etc., can be obtained from simulations. The simulations of the Ga^+ implantation into the materials are used as a guide to the extent of the interaction of the FIB lithography with the samples during milling/implantation.

2.3.2 Milling of continuous thin films

When irradiating continuous films by a FIB system, several factors have to be considered: the dose to be imparted into the material, the sputter rate of the material, the beam current used for irradiation, the area irradiated on the film and the pixel spacing of the beam. In the FIB microscope, milling is only achieved in the materials studied in this thesis after a threshold dose has been reached. Before milling, however, the ions are implanted into the material, as will be shown in chapters 4 and 6. The dose ($nC\mu m^{-2}$) delivered to the material is directly proportional to the sputtered depth, z, (μm after the threshold has been reached) and inversely proportional to the sputter rate, sr, ($\mu m^3 nC^{-1}$) of the material (material dependent), equation 2.1.

$$Dose = \frac{z}{sr} \qquad \textbf{(2.1)}$$

Implantation of ions can affect the properties of the material. For example, in the case of permalloy, the magnetic and structural properties are changed. Generally, the magnitude of the magnetisation decreases as the administered dose increases [19, 20]**.** This phenomena is not restricted to permalloy. Other magnetic materials, such as CoFe/IrMn [21], experiences interesting changes in magnetic properties due to ion beam irradiation and intermixing. Physically the grain structure can be altered by using different beam overlaps [22, 23]. The beam overlap in the irradiated area is determined by spacing between irradiated pixels, when the pixel spacing is equal to the beam spot size, 2r, this is known as 0% overlap, Figure 2.11(a). If the pixel spacing is decreased and the beam spot size stays the same then the overlap increases, Figures 2.11(b) and (c).

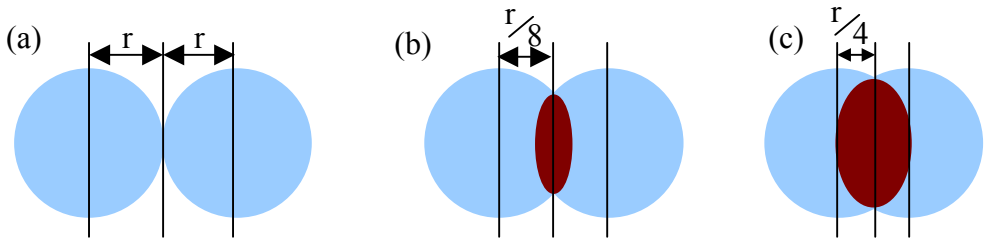

Figure 2.11: (a) 0%, (b) 25% and (c) 50% overlap of FIB pixels. The blue area indicates the beam spot and bugendy area in (b) and (c) indicate the overlap.

To administer the user defined dose, the gallium ion beam is positioned at the relevant pixel for an allotted time, known as the dwell time. The dwell time has a lower and upper limit imposed by the machine. If doses greater than the upper dwell time limit are required then the beam is cycled through the pattern to achieve this. Unfortunately for large dwell times mechanical drift in the FIB stage can be a problem. Also, when there is a large number of repeats in the pattern, registration with the location of the pattern on the specimen and beam position can shift, again due to mechanical drift. A compromise is therefore necessary between long dwell times and repeats, for patterns with long irradiation times. Another way to decrease the dwell time is to increase the beam current by using a larger aperture size, this too can introduce problems that will be discussed in section 2.3.3.

The units used to denote the gallium ion dose received by the sample are usually quoted in either ions cm^{-2} or $nC\mu m^{-2}$. The conversion factor from ions cm^{-2} to $nC\mu m^{-2}$ is $1\ ions\ cm^{-2} = 6.24 \times 10^{17}\ nC\mu m^{-2}$. The units $nC\mu m^{-2}$ are used in this project.

There are several different methods used to pattern thin films using the FIB microscope. One is to manually input the image via the computer terminal. The second is via computer scripting, and the third is via the creation of a stream file. The stream file contains information about the coordinates to be irradiated, the number of repeats for each coordinate, the order of coordinates to be milled, the time the gallium beam has to spend over the coordinate and the total number of coordinates in the stream file. Caution needs to be exercised when using the FIB system due to memory limitation, the total number of points per loop that can be milled has to be less than 750,000.

The standard method for milling in a FIB system is a raster scan, Figure 2.12(a) starting in the top left of screen, travelling left to right, to the bottom right. This method can be detrimental to the shape milled by the beam in the sample due to the finite blanking ability in the system allowing the beam to enter areas that are not to be irradiated (known as flyback). To achieve a higher quality of patterning the beam direction, via the octupole lenses, can be altered, this is known as vector scanning, Figure 2.12(b). Vector scanning serves to remove/reduced flyback from the area of interest. Vector scanning increases the

programming and fabrication time, however, and it is only necessary when the unirradiated area is essential.

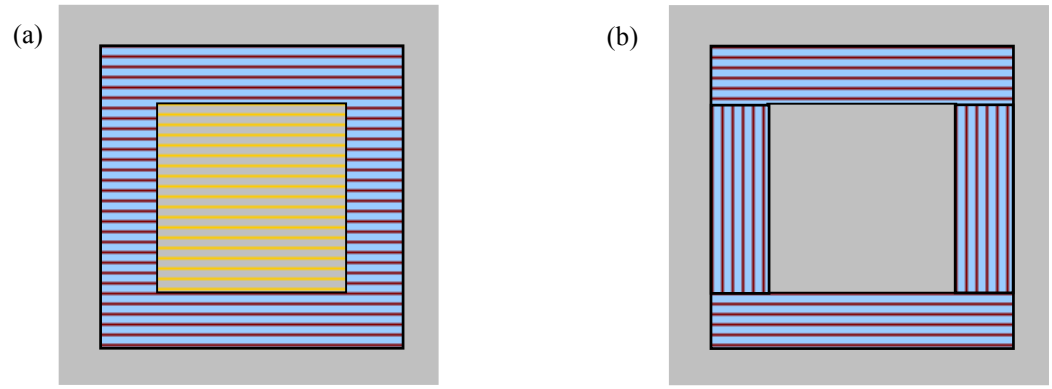

Figure 2.12: schematic of an element fabricated by (a) raster and (b) vector scanning in the FIB microscope. The motion of the ion beam is shown in each figure (red in cut and yellow in element). Blue indicates the areas to be milled/irradiated and grey the areas to be left (not to scale).

2.3.3 Optimisation of the milling conditions

When milling 20 nm thick permalloy on 50 nm thick SiN it is important to ensure that the milling ceases when the gallium ions broach the permalloy/SiN boundary. There are numerous reasons to stop milling at the permalloy/SiN boundary, these include: the SiN having a higher sputter rate than the permalloy (see sections 4.1 and 5.1) and the SiN support membrane being milled faster than the permalloy material; and the SiN being non-conducting of the Ga^+, this will lead to being a build up of charge that could damage the substrate. From equation 2.1 the one factor that determines the sputtered depth is the dose administered to the material. To determine the correct range of doses (and hence the *sr* of the material) a series of squares were milled into 20 nm thick permalloy and their depth measured by atomic force microscopy (AFM), the results of which are be discussed in chapters 4 and 5.

Using different beam currents to mill the same area changes the effective dose that the adjacent areas receive, due to the profile of the beam (believed to be Gaussian in profile [24]). As the beam current is increased the tails of the beam increase thus irradiating the surrounding pixels, Figure 2.13. In addition to the larger tails in the beam the increased number of ions can cause an increase in the number of secondary ion atom interactions, this can increase the effective dose received by the material.

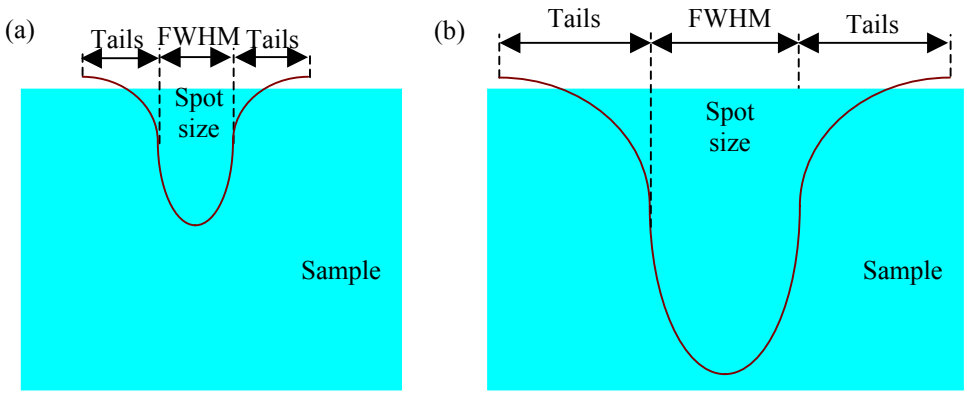

Figure 2.13: beam profile for the gallium ion beam as the beam current is increased from (a) small to (b) large, not to scale.

2.3.3.1 Simulations on gallium ion implantation into permalloy on silicon nitride substrate

The SRIM simulation programme, described in Section 2.3.1, can be used as a reference to calculate the depth the gallium ions penetrate as the permalloy is milled away and hence the effects the ions have on the different layers. Figure 2.14 shows the implantation of gallium ions (red in the upper images) into varying depths of permalloy. In all SRIM simulations, the permalloy (green/dark blue in the lower image) is on 50 nm thick SiN (purple/light blue in the lower image) and gallium ions have an initial energy of 30 keV. In Figure 2.14(a), 20 nm thick permalloy, the majority of gallium ions have been stopped within 10 nm of the permalloy although the secondary events do penetrate into the SiN layer. For Figure 2.14(b), 10 nm thick permalloy, a significant minority of ions stop in the SiN layer and the majority of secondary events occur in this layer. In Figure 2.14(c), 0 nm thick permalloy, in which all the permalloy has been milled away the gallium ions (upper image) travel through the SiN layer which has very little stopping power in comparison. The simulation in Figure 2.14 can be used as a guide to the damage that results in the non-conducting SiN layer during milling, this is shown to produce milling of the substrate, see section 5.1. From the secondary event plot (lower images in Figure 2.14(c)), a number of secondary ion events pass through the adjoining SiN/vacuum boundary, as shown by the abrupt change in the plot. From the simulations it can be shown that as the permalloy is milled the penetration depth increases to the point that the number of secondary events increases in the SiN layer, Figure 2.14(b). This, as mentioned previously (section 2.3.2), will affect the properties of the SiN, eventually the SiN will be milled away.

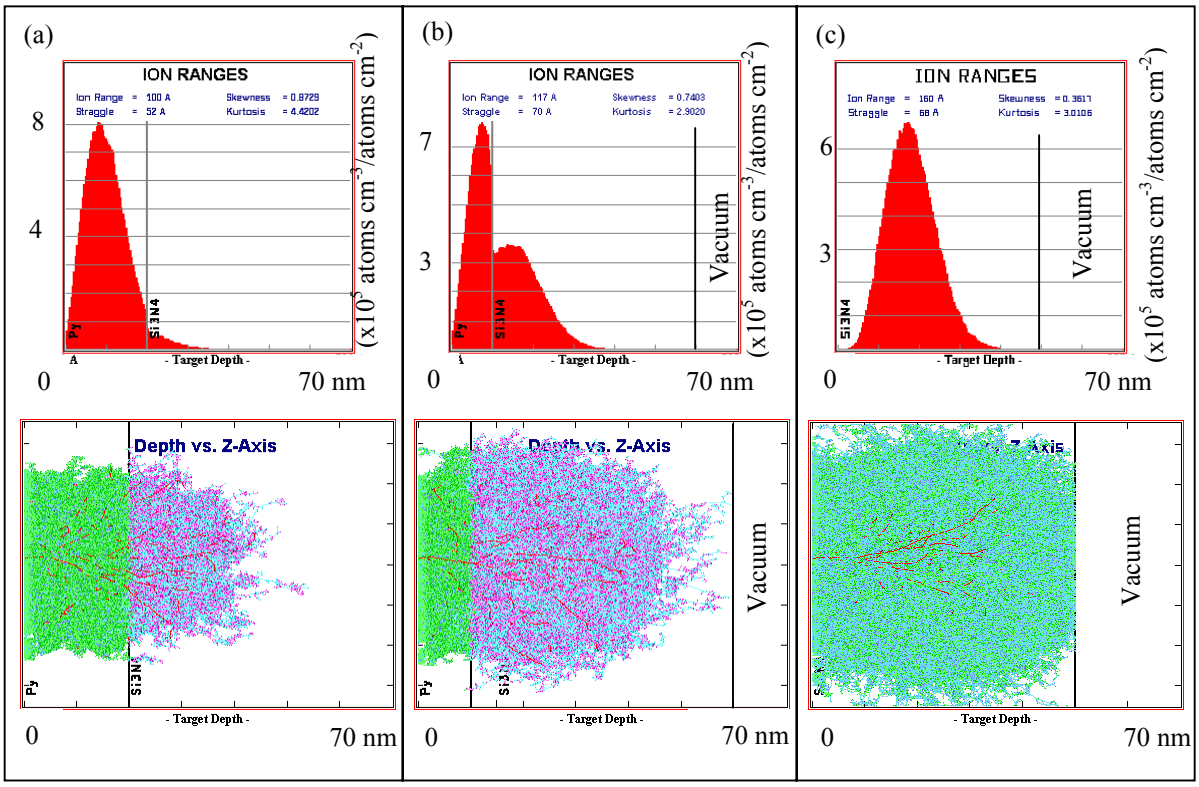

Figure 2.14: SRIM simulated 30 keV gallium ion implantation depths (and secondary events) into (a) 20 nm thick permalloy, (b) 10 nm thick permalloy and (c) 0 nm thick permalloy on 50 nm thick SiN. Red indicates ions, green/dark blue secondary events in the permalloy and purple/light blue secondary events in the SiN.

2.3.4 The introduction of a non magnetic metal layers

From the experiments on the FIB milling of permalloy and the TRIM simulations of gallium ion implantation into the permalloy it became apparent that a protective layer between the permalloy and the SiN layers could be beneficial to stop milling of the SiN substrate. The protective layer had to fill three criteria, it had to be: i) non magnetic; ii) conductive; and iii) introduce manageable extra scattering of the electron beam when imaged by TEM. To meet the three criteria a 4 nm thick copper was chosen.

2.3.4.1 Simulations of gallium ion implantation into permalloy on silicon nitride substrate with a copper buffer layer

To gauge the effectiveness of the ~4 nm copper layer TRIM calculations were run for the layer with different thickness of permalloy (green/dark blue) on 50 nm thick SiN (beige/light blue), this is shown in Figure 2.15. The TRIM calculations were for gallium ions (red) with 30 keV implanted into the aforementioned materials. The upper images in Figure 2.15 are of the ions only implanted into the material and the lower images are of the secondary events that result from ion implantation into the material. Initially, Figure

2.15(a), the copper layer reduces the number of gallium ions (and secondary events) that breech the SiN substrate when compared to simulations with no copper layer, Figure 2.14(a). Upon milling to a depth of 10 nm, Figure 2.15(b), the copper layer acts to decrease the number, and penetration, of gallium ions in the SiN, again the number of secondary events has been decreased. Finally when all the permalloy has been milled from the sample, Figure 2.15(c), the copper layer, unfortunately, offers the thin supporting substrate little protection from the gallium ions except to diffuse the penetration of the ions over tens of nanometres and absorb some of the gallium ions.

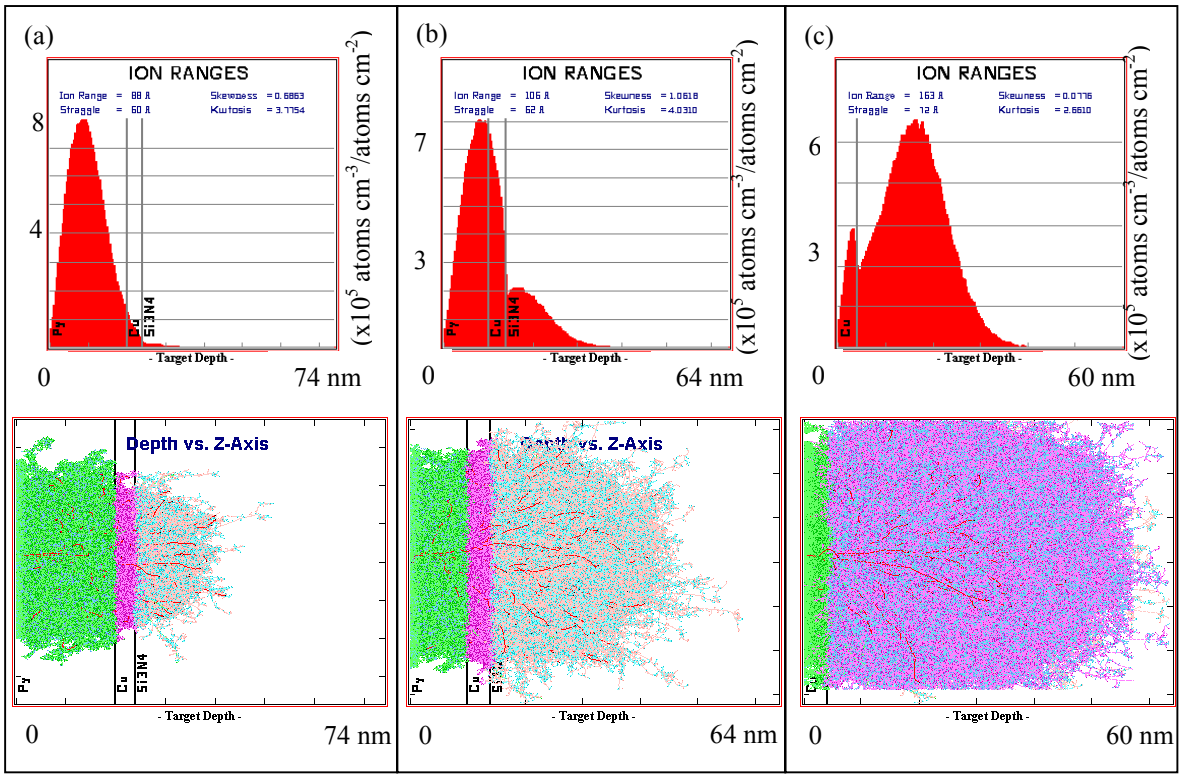

Figure 2.15: SRIM simulated gallium ion implantation depths (upper images) and secondary events (lower images) into (a) 20 nm thick permalloy, (b) 10 nm thick permalloy and (c) 0 nm thick permalloy on 4 nm thick copper and 50 nm thick SiN. Red indicates ions, green/dark blue secondary events in the permalloy, purple secondary events in the copper and beige/light blue secondary events in the SiN.

2.3.4.2 Simulations of gallium implanted into a copper/permalloy/copper system

In chapter 6 the results of the irradiation, with varying doses of Ga^+, on 20 nm thick 2×2 μm^2 permalloy elements on a 5 nm thick copper buffer layer (green) capped by a 10 nm thick copper layer (a schematic is shown in Figure 2.16) are discussed. It is expected that the Ga^+ beam imparts sufficient energy to diffuse the copper capping layer (green) into the permalloy layer (blue and purple) and thus alter the magnetic properties of the system. The copper buffer layer (green) and SiN substrate (beige and aqua) are expected to remain intact. To this end TRIM simulations of Ga^+ implanted into this structure have been implemented. The results are shown in Figure 2.17. The 10 nm copper cap reduces the penetration depth of the ions and secondary events, with the majority of the ions stopping at the Cu cap and permalloy layer (Figure 2.17(a)). Also visible in Figure 2.17(a) is a slight intermixing of the permalloy layer with both copper layers, visible as transitions of the atoms across the boundaries. The copper cap also acts to decrease the lateral straggle of the ions and the subsequent secondary events, Figure 2.17(b). This is compared to the uncapped simulations (Figures 2.14 and 2.15) and is also true of the vertical spread of the ions (Figure 2.17(c)). The majority of the primary ions are stopped within the copper capping layer and the first 10 nm of the permalloy layer (Figure 2.17(d)), with the subsequent 10 nm stopping the majority of the remaining ions. Using a range of doses similar to that of Kaminsky et al, [19], 2×2 μm^2 elements (that were fabricated by FIB irradiation) were irradiated with different doses and patterns and the characteristics of such elements are discussed in chapter 6.

Figure 2.16: schematic of the sample used in chapter 6. 10 nm copper capping layer, 20 nm permalloy ferromagnetic layer, 5 nm copper buffer layer and 50 nm electron transparent silicon nitride layer.

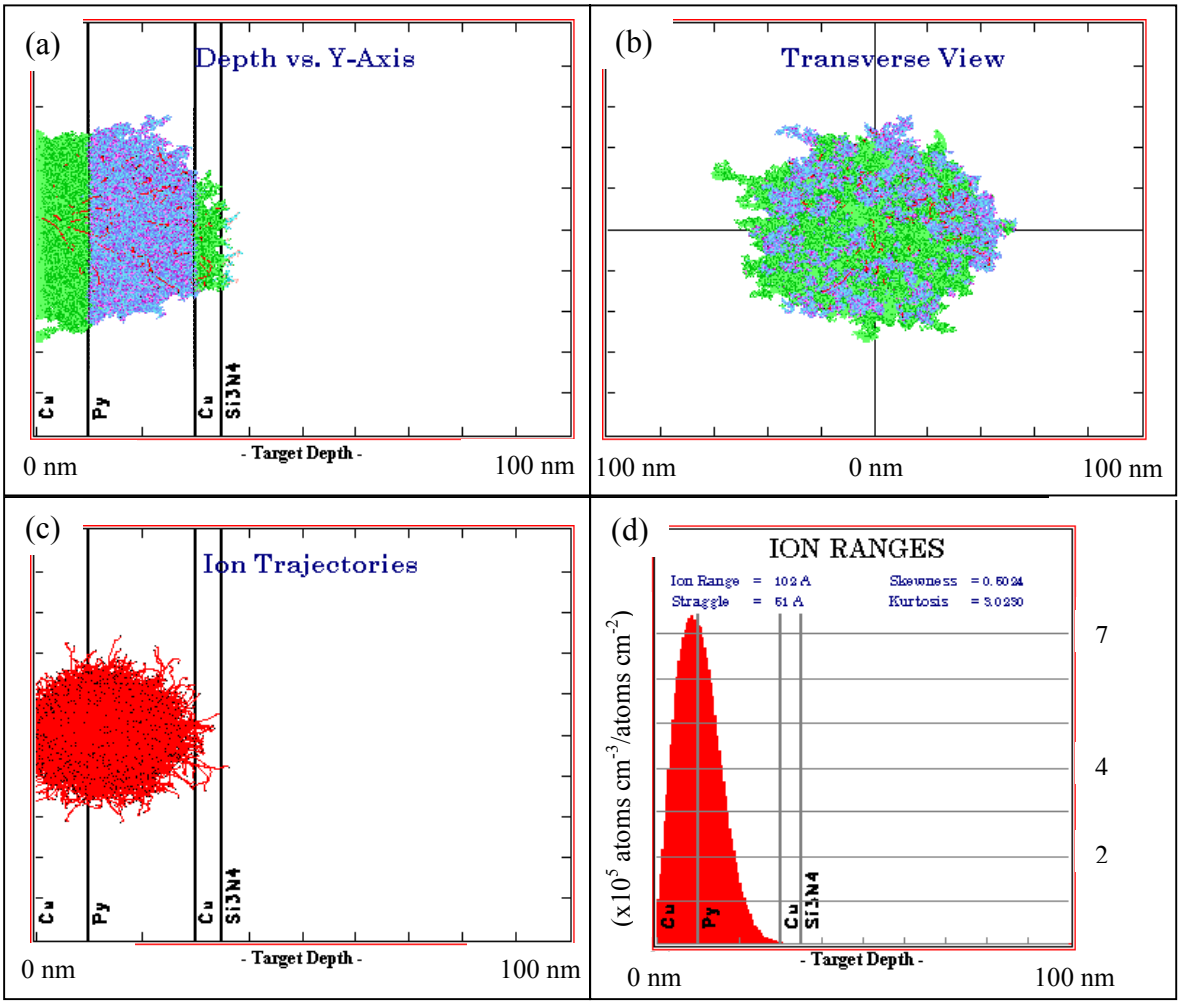

Figure 2.17: simulations of 30 keV Ga^+ implanted into a 20 nm permalloy thin film on a 5 nm copper film capped by a 10 nm copper layer. Supported on 50 nm thick SiN layer. Red indicates ions, green secondary events in the copper, purple/light blue secondary events in the permalloy and beige/aqua secondary events in the SiN. (a) Is the vertical straggle of the ions and secondary events, (b) is the horizontal straggle of the ions and secondary events in the material, (c) is the vertical ion straggle and (d) is the ion ranges through the material.

The simulation of the ferromagnetic permalloy layer with a copper capping layer shows little intermixing of layers and a decrease in the straggle of the ions and secondary events. The stopping range of the ions show that the majority of the ions are stopped at the Cu /permalloy interface, in reality this would probably lead to intermixing as the ion/atom collisions would knock the atoms either side of the boundary (this is assuming there has been no intermixing during deposition). The TRIM simulations, however, do not allow for other effects that could be caused by the interaction of the beam with the sample. Beam/sample interaction effects such as milling (chapters 4, 5 and 6), magnetostriction within the magnetisation or heating of the sample, if there are any.

Bibliography

[1] Emitech technical brief for Emitech K575x peltier cooled twin head system sputter coater.

[2] Schneider M., Hoffmann H., Zweck J., J. Magn. Magn. Mater. 257 (2003).

[3] Cumming D.R.S., Thoms S., Beaumont S.P., Weaver J.M.R., Appl. Phys. Lett. 68(3) (1996) 322.

[4] Cleanroom classifications found at the following URL. URL active on 27th Mar. 2007: http://www.mssl.ucl.ac.uk/www_cleanroom/cleanroom/cr_standards.html#iso_s

[5] Khamsehpour B., Wilkinson C.D.W., Chapman J.N., Johnston A.B., J Vac. Sci. Tech. B. 14(5) (1996) 3361.

[6] Yi G., Aitchison P.R., Doyle W.D., Chapman J.N., Wilkinson C.D.W., J. Appl. Phys. 92(10) (2002) 6087.

[7] Internal Electrical Engineering training document.

[8] Woan G., "*The Cambridge Handbook of Physics Formulas"*, Cambridge University Press 2000, ISBN 0521575079. Page 155, equation 7.243.

[9] Chang T.H.P., J. Vac. Sci. Tech B. 12(6) (1975) 1271.

[10] Kyser D.F., Ting C.H. J. Vac. Sci. Tech. B. 16(6) (1980) 1759.

[11] FEI technical manual on operation of FIB microscope PN 20486-B

[12] Information on a Taylor cone can be found at the following URL, URL active on 27th Mar. 2007: http://en.wikipedia.org/wiki/Taylor_cone

[13] LMIS source image available at: http://www.feibeamtech.com/pages/liquid.html URL active 27th Mar. 2007.

[14] Information on the Faraday cup can be found at the following URL, URL active on 27th Mar. 2007: http://www.casetechnology.com/implanter/faraday.html

[15] For a review on the subject: Kato N.I., J. Elec. Micros. 53(5) (2004) 451.

[16] SRIM programme available for download at: http://www.srim.org/ (active as of 27th Mar. 2007).

[17] Zieger J.F., SRIM manual, available for download at: http://www.srim.org/

[18] For a description of the Monte Carlo method see Mathworld at: http://mathworld.wolfram.com/MonteCarloMethod.html (active as of 27th Mar. 2007).

[19] Kaminsky W.M., Jones G.A.C., Patel N.K., Booij W.E., Balmire M.G., Gardiner S.M., Xu Y.B., Bland J.A.C., Appl. Phys. Lett 78(11) (2001) 1589.

[20] Woods S.I., Ingvarsson S., Kirtley J.R., Hamann H.F., Koch R.H. Appl. Phys. Lett. 81(7) (2002) 1267.

[21] McGrouther D., Chapman J.N., Vanhelmont F.W.M., J Appl Phys 95(12) (2004) 7772.

[22] Park C. -M., Bain J.A. J. Appl. Phys. 91(10) (2002) 6830.

[23] Voegeli W., Able K., Hahn H., Nucl. Inst. & Meth. Phys Res B 202 (2003) 230.

[24] McGill R.A., Vizir A., Brown I.G., Rev. of Sci. Inst. 71(2) (2000) 672.

3 Imaging techniques used to characterise micron sized ferromagnetic elements and arrays

In this chapter, the instrumentation used for characterisation of micron sized ferromagnetic elements and arrays is discussed. Initially a brief history of the TEM is given, then the hardware used in a transmission electron microscope (TEM), more specifically, the Philips CM20FEG TEM and the modifications made to allow magnetic imaging to occur, are discussed in section 3.1. Following the description of the TEM, in sections 3.2 and 3.3 the imaging techniques employed for the characterisation of the physical and magnetic properties of the array and elements by TEM are discussed. The imaging techniques include bright field TEM imaging, Fresnel imaging and differential phase contrast (DPC) imaging.

Also discussed in this chapter (section 3.4) is a surface profiling technique known as atomic force microscopy (AFM). The discussion on AFM encompasses a brief history, the hardware of the machinery, the physics governing tip-specimen interactions and how a surface profile can be determined from this.

3.1 The transmission electron microscope

In 1925 Louis de Broglie formulated that matter has a wave-particle duality [1]. The de Broglie postulate states that matter travelling with a momentum, p, has an associated wavelength, the de Broglie wavelength, λ, with the relationship given in equation 3.1.

$$p = \frac{h}{\lambda} \tag{3.1}$$

where *h* is Planck's constant. From the de Broglie principle, the concept of an electron microscope was developed, with Knoll and Ruska demonstrating the first working version in 1932 [2]. Using the de Broglie relationship it can be shown that for an electron with a rest mass of 9.109 $x10^{-31}$ kg and a charge of 1.602 $x10^{-19}$ C accelerated through a potential difference of 200 kV (the accelerating voltage of the Philips CM20FEG used in this project) has a relativistic wavelength of ~2.5 pm. Comparing the wavelength of TEM to the wavelength of blue light (~400 nm), it can be seen why TEM microscopy is useful for high resolution imaging. However, other problems (such as transmission of the electron beam through the specimen and properties of the lenses) limit the resolution of the TEM. Thinner specimens increase the number of electrons that are transmitted through the specimen (<100 nm in thickness for a good signal level). The physical construction of the microscope gives rise to the largest contributions to the reduction of the resolution. The lenses of the microscope have a diffraction limit associated with them (similar to the limit imposed on an optical system) and aberrations (spherical aberration) due to the physical construction. Even for a perfectly constructed system there is still a spherical aberration associated with it that is always positive and non-zero, this is known as Scherzer's theorem. The electron source limits the resolution by not being a point source and having an energy spread in the electrons emitted (this results in a chromatic aberration). The extended source size, source coherence, brightness and microscope lenses limit the resolution to >5 nm in the modified Philips CM20FEG STEM (hereafter referred to as the CM20).

A schematic of the CM20 that is used for the majority of the imaging in this thesis is shown in Figure 3.1. The CM20 is located at the University of Glasgow. This CM20, with scanning coils after the electron source, varies from a standard CM20 TEM by having a super mini (or Lorentz) lens fitted above and below the objective lens to enable magnetic imaging in field free conditions [3]. This is explained in greater detail later in this section. The CM20 uses a Schottky emitter type of field emission gun (FEG) as an electron source and can scan a small electron probe across the surface using the built in scanning coils; this allows the TEM to be used as a scanning TEM (STEM). By having the STEM, imaging modes such as DPC can be implemented in the microscope in addition to bright field and Fresnel imaging that can readily be implemented in a conventional TEM. The Schottky emitter is a truncated tetrahedral tungsten tip that is orientated along the <100> crystallographic axis, see insert to Figure 3.1, with a suppressor to reduce contributions to the beam from the edges. By a combination of applying a voltage across the emitter (~4 kV), to lower the work function, and heating the tungsten tip, to thermally excite the

electrons, electrons can be removed and accelerated towards the specimen. A brightness, at the tip, of ~10^{13} $Am^{-2}sr^{-1}$ can be achieved using a Schottky emitter as a source [4].

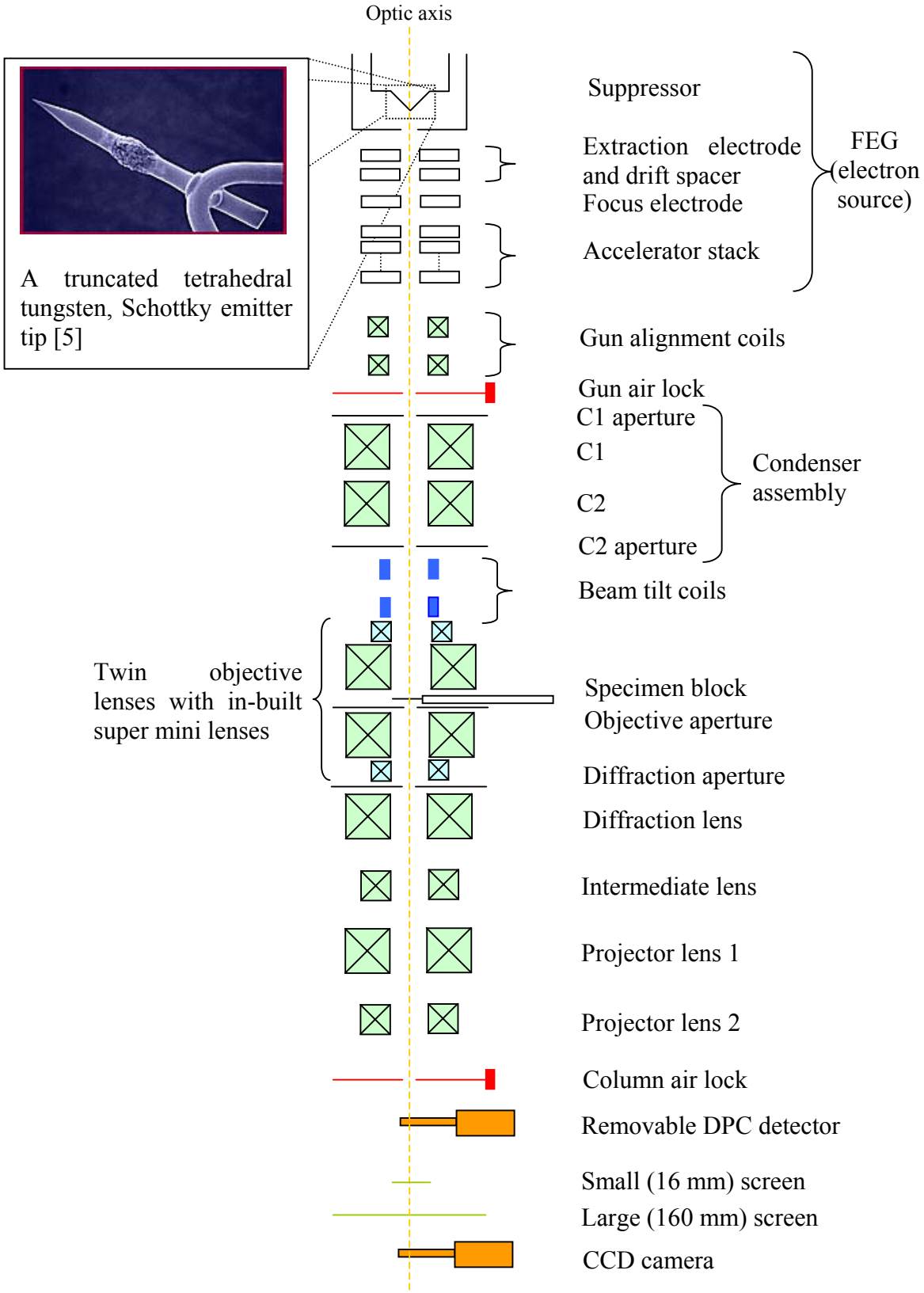

Figure 3.1: cross sectional schematic of the modified Philips CM20FEG with the detectors used in this project.

The condenser assembly is located after the gun assembly in the TEM, with the CM20 having a twin condenser lens system. Condenser lens 1, C1, is used to select the desired

beam spot size for the imaging mode. Condenser lens 2, C2, is the lens that can be used to create (almost) parallel illumination for bright field imaging (by under focusing the crossover), or by transferring the C1 beam crossover to the specimen, for scanning over the surface of the specimen using the scan coils. The C2 aperture is used to control the convergence of the electron beam when the beam is focussed.

The objective lens (with super mini lens assembly) is located below the condenser lens assembly with the specimen mount being at the centre of the objective lens. For studying magnetic structures the super mini lenses have been added to act as a field free objective lens system when the specimen is at the eucentric height and the objective lens is switched off. By placing the specimen into the centre of objective lens (or the super mini lenses) the lens can act as a pre- and post-specimen lens. The pre-specimen lens can be strongly excited and therefore can be used as a third condenser lens for STEM modes.

As mentioned previously the objective lens produces a large magnetic field (~0.7 T, although a weaker field used to image the specimen) when it is used to focus the electron beam. Therefore, the super mini lens assembly has been added above and below the object lens assembly to allow magnetic field free imaging. As the super mini lens assembly is further away from the specimen and operates at a reduced current, the resolution is reduced. The spherical aberration of the super mini lenses is also greater than that of the objective lens. In addition to the field free imaging, by passing a current through the objective lens a magnetic field, $\boldsymbol{B}$, can be induced along the optical axis of the TEM giving a local field at the specimen of up to ~0.7 T. Components of the magnetic field can be induced in the plane of the specimen by tilting, as shown in Figure 3.2. The in-plane component of the field ($\boldsymbol{B}\ sin\ \theta$) is at a minimum and the out-of-plane field component ($\boldsymbol{B}\ cos\ \theta$) at a maximum when the specimen is perpendicular to the direction of the applied field. Although the goniometer can be tilted to 90^{o} in one direction (electrical connections limit the tilt in reverse direction), viewing is usually limited to $\pm\sim35^{o}$ by the profile of the opaque support silicon substrate obscuring the transparent viewing membrane. Through time, the zero tilt position of the goniometer can be misaligned from the magnetic field zero and therefore the magnetic field zero should be calibrated for each specimen, if possible. The specimen was imaged in a tilt-rotate rod unless otherwise specified.

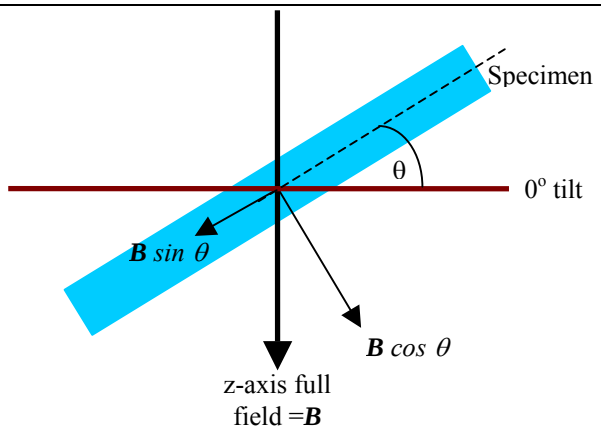

Figure 3.2: schematic defining the magnetic field components applied to a specimen in the CM20.

The condenser lenses, objective lens (including the super mini lenses) and diffraction lens all have associated apertures. The purpose of the aperture is mainly to limit the collection angle of the electrons for the associated lens. The objective lens aperture can be used at different areas of the electron beam to obtain different information about the specimen. For example, the objective lens aperture can be used to control the resolution of the image, the depth of field and the depth of focus, the image contrast and other such properties. By off-centring the objective aperture from the straight through beam, at the appropriate position in diffraction space, the contributions from the electrons elastically scattered by that particular crystallographic axis can be imaged (this is known as dark field imaging) [4].

As mentioned previously, the electron wavelength is not the current limit of transmission electron microscopy. One of the limiting factors is specimen thickness, the specimens have to be electron transparent and these are always optically transparent. Specimens prepared for TEM analysis have stringent requirements for the dimensions that can fit in the pole gap in the imaging lens and electron transparency. For example for high resolution imaging (sub-nanometre resolution) the specimen requirements are very stringent as the inelastic scattering of the electron beam with the specimen can obscure the information to be gathered (especially from thicker specimens). In general high resolution specimens are prepared by thinning down bulk specimen by a number of processes (see chapter 10 in [4]). Recent advances in technology have allowed specimens to be fabricated though the lift out technique implemented in focussed ion beam lithography [6].

The ferromagnetic elements and arrays (to be discussed in the subsequent chapters of this thesis) are deposited on specially designed substrates, a schematic of which is shown Figure 3.3. The substrates are designed to have a surface area of ~4 mm^2, with a thickness of ~450 μm in the bulk, to allow the specimen to be tilted in the pole gap of the objective

lens in the CM20. They have an electron transparent section, 50 nm thick, in the centre for imaging. The substrates are composed of ~400 μm thick single crystal silicon with an ~50 nm thick layer of amorphous silicon nitride (Si_3N_4, denoted SiN) deposited on top. During processing, a section, that measures 100×100 μm^2 at the SiN face, is wet etched from the silicon side to reveal the ~50 nm thick electron transparent SiN layer. It is in this 100×100 μm^2 window where the structures to be analysed are deposited. To help fabricate structures on the electron transparent section without exposing the window to unnecessary irradiation, alignment markers have been etched into the substrate at a position of (400,400) μm from the electron transparent section.

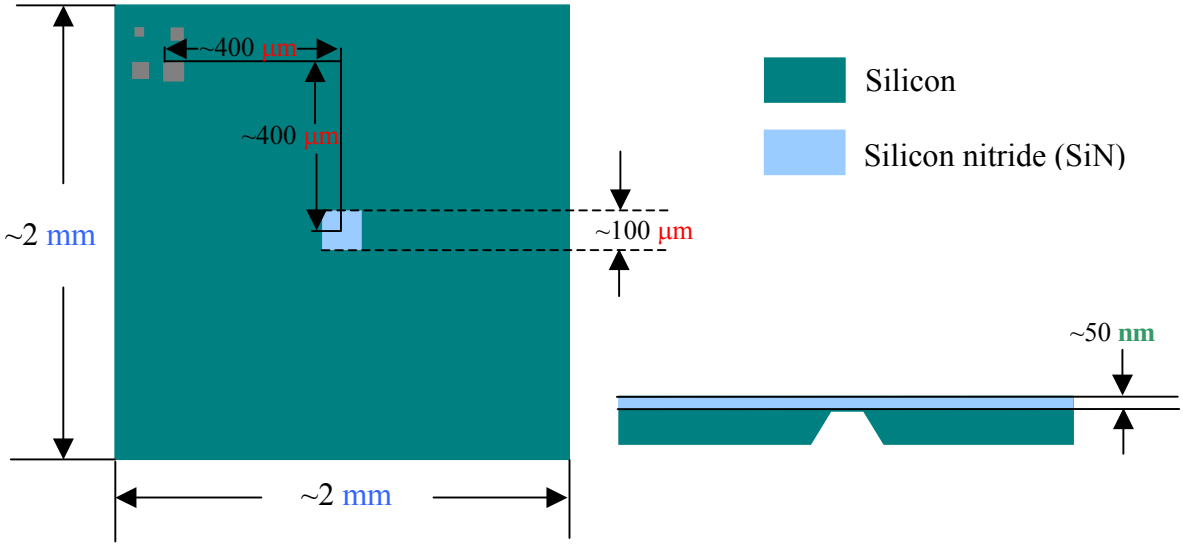

Figure 3.3: schematic of a TEM support membrane (with cross-section) used for the fabrication of nanoscale structures and thin films with alignment markers (grey squares). The electron transparent window is centred on the substrate (blue). Not to scale.

3.2 Bright field imaging using the transmission electron microscope

Bright field TEM imaging derives its name from the similarity, in nature, it has to optical bright field imaging. An (almost) parallel beam of electrons is incident on the specimen and the majority of these electrons remain unscattered as they pass through the specimen. It is the unscattered electrons from the beam that are used to form the bright field images discussed in this thesis. As stated previously, to help the formation of a bright field image the objective aperture can be used to remove unwanted scattered electrons that can decrease the image contrast, as shown in Figure 3.4. The unscattered electrons are then magnified through a series of post specimen lenses to form an image on a detector (whether that be a CCD camera, photographic film or phosphorescent plate). Bright field

TEM imaging in the CM20 using the Lorentz lenses can achieve the >5 nm resolution discussed in the previous section. When the objective lens is used for imaging the resolution can be increased to the <5 nm range. An example of a bright field TEM image taken using a 30 μm C2 aperture (standard for this thesis unless otherwise stated) is shown in Figure 3.5. Figure 3.5 is an image of a 500×500 nm^2 permalloy element that has been fabricated by using focussed ion beam lithography. The image was taken with a C1 aperture of 150 μm, a C2 aperture of 30 μm and no aperture. These are the standard conditions for the bright field images discussed in this thesis. Clearly visible within the image are the grain structure (~7 nm) and the edge roughness of the element, to be discussed in greater detail in the subsequent chapters.

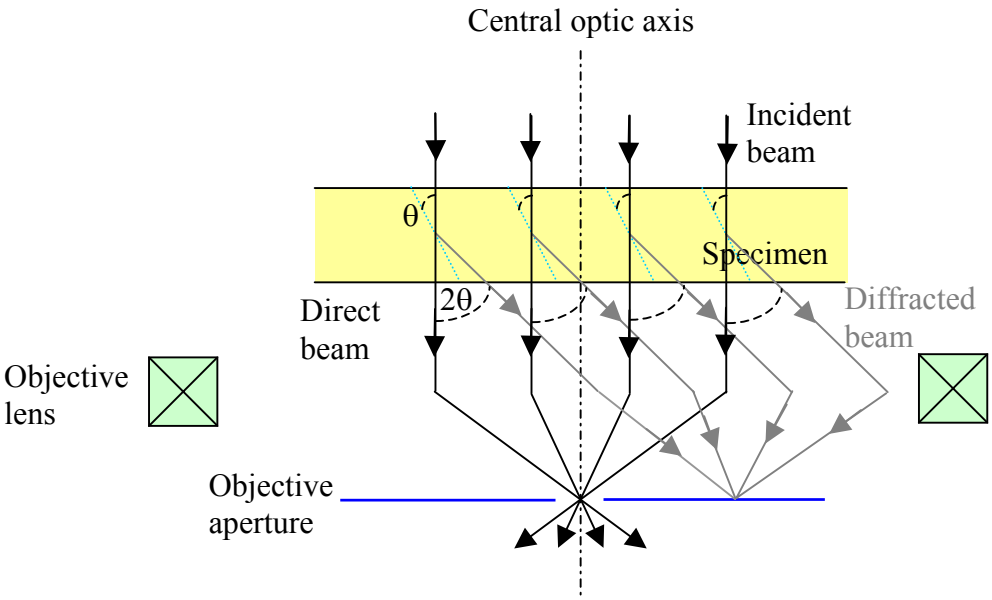

Figure 3.4: schematic of the beam contributions to a bright field image.

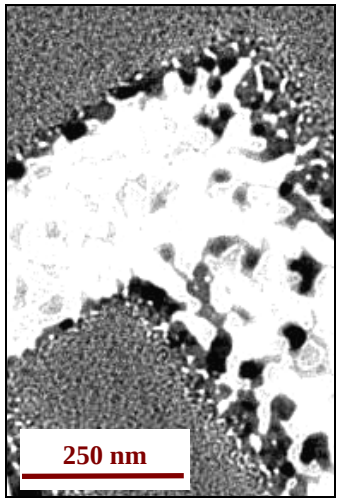

Figure 3.5: bright field TEM image of the corner of a 500×500 nm^2 permalloy milled by a focussed ion beam microscope with a 1 pA beam current taken using the CM20.

3.3 Magnetic imaging using the transmission electron microscope

The imaging of the magnetic structure of materials in a TEM is accomplished by use of a set of imaging techniques known as Lorentz microscopy. There are several techniques that are encompassed by the term Lorentz microscopy [7]. The two used in this project are Fresnel imaging and differential phase contrast (DPC). The name Lorentz microscopy is derived from the Lorentz equation that describes the relationship between the resultant force on a particle (an electron in this case), $\boldsymbol{F}$, due to the electric field, $\boldsymbol{E}$, and magnetic induction, $\boldsymbol{B}$, that can be both internal and external to a specimen, equation 3.2.

$$\boldsymbol{F} = -e(\boldsymbol{E} + \boldsymbol{v} \times \boldsymbol{B}) \qquad \textbf{(3.2)}$$

where e = charge of the electron and $\boldsymbol{v}$ = velocity of the electron. From the Lorentz equation, it can be shown, that for an electron travelling along the z-axis that is incident on a variable component of magnetisation, there is an associated local angle of deflection, $\beta_L(x,y)$, using the coordinate system defined in Figure 3.6 in section 3.3.1. Therefore, for a magnetic specimen with a domain whose magnetisation varies, the local angle of deflection (due to the component of the local magnetic induction, $\boldsymbol{B}$)f that is perpendicular to the beam, is given in equation 3.3.

$$\beta_L(x,y) = \frac{e\lambda}{h} \int_{-\infty}^{\infty} \mathbf{B} \times \hat{\mathbf{n}} dz \qquad \textbf{(3.3)}$$

Where $\hat{\mathbf{n}}$ is the unit vector parallel to the direction of the beam. Typical values for the CM20 are λ=2.5 pm for an accelerating voltage of 200 kV; with e=1.602 x 10^{-19} C and h=6.63 x 10^{-34} Js being fundamental constants. The resultant typical magnetic deflection from such values is ~0.02 mrad for 20 nm thick permalloy (compared to a typical Bragg scattering angle of ~10 mrad) [8].

3.3.1 Magnetic structures as viewed by Fresnel imaging

Fresnel imaging is an out-of-focus technique that was first demonstrated by Hale et al, in 1959 [9]. The technique was used to obtain images of domains walls in $Ni_{50}Fe_{50}$ and $Ni_{80}Fe_{20}$ by turning the objective lens off and defocusing the projector lens (that was used as the imaging lens instead) in a conventional TEM (hence giving the technique the other name of the "defocus technique"). A schematic of the imaging technique for a three-domain magnetic system with 180° in-plane domain walls is shown in Figure 3.6. By

defocusing the imaging lens, to a value ±Δz, the specimen plane is no longer coincident with the object plane. The deflection of the electrons due to the integrated magnetic induction of the specimen therefore either converges or diverges where there is a change in the direction of in-plane magnetisation associated with the specimen (such as domain walls). Areas of convergent contrast appear as light bands and areas of divergence appear as dark bands. The convergent or divergent bands reverse as the focus value is reversed. For example, a magnetic wall that appears white when underfocussed (a weakened imaging lens) will appear dark when overfocussed (a strengthened imaging lens).

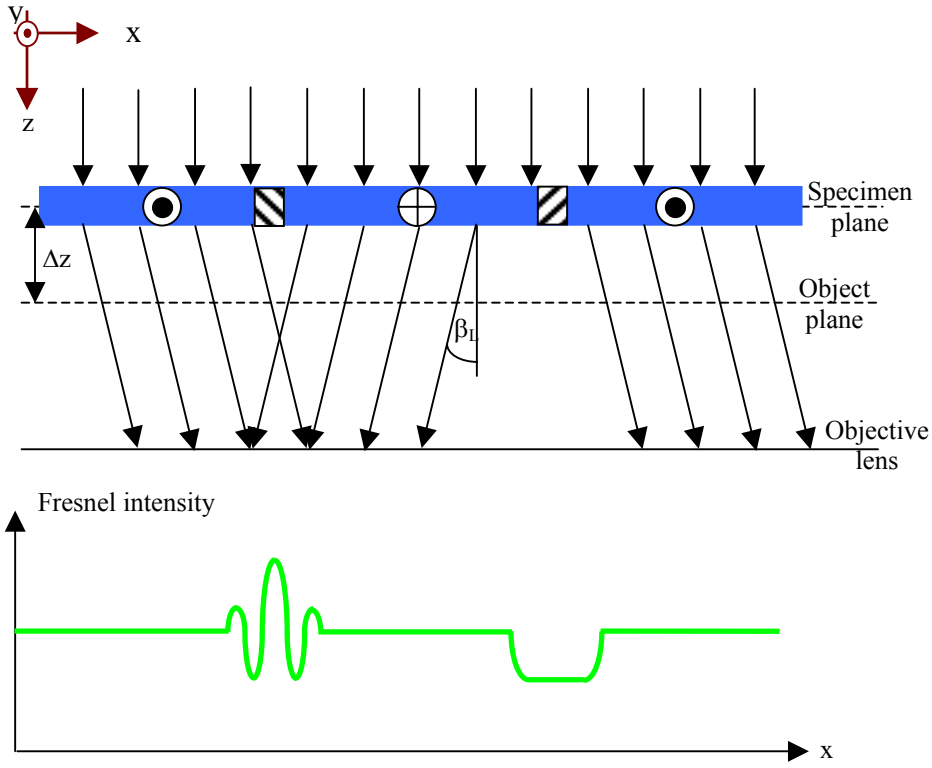

Figure 3.6: schematic of the Fresnel imaging technique as the electrons leave the specimen to the objective lens. Also shown is the image intensity as a function of position.

Using Abbe theory for a conventional TEM and making the assumption that the electron wave incident upon the specimen is of a planar nature then the initial electron wave incident on the specimen shown in Figure 3.6 can be expressed as $\Psi_0(x,y)$ which is proportional to $e^{2\pi ikz}$, where k is the wavenumber and $k=1/\lambda$. As the wave travels through the specimen, the phase of the wave is altered by the quantity, known as the specimen transmittance $f(x,y)=e^{i\varphi(x)}$. The phase shift, $\varphi(x)$, of an electron wave between two coordinates in x, x_1 and x_2, is defined as $\varphi(x)=\frac{2\pi et}{h}\int_{x_1}^{x_2} B_y(x)dx$ [8], where $B_y(x)$ is the y component of the magnetic induction as it varies along the x-axis. Therefore the emergent wave, S_T, has the form shown in equation 3.4.

$$S_T = f(x,y)\Psi_0(x,y) = f(x,y)e^{2\pi ikz} \quad \textbf{(3.4)}$$

The electron wave then propagates into the back focal plane, where it is more convenient to think of the electron in terms of the Fourier transform, $\Im$, of S_T, $g(k_x,k_y)$ as given in equation 3.5. In Fourier space it is easier to separate out the individual component of the equation.

$$g(k_x,k_y) = \Im\big(f(x,y)\Psi_0(x,y)\big) \quad \textbf{(3.5)}$$

The wave is subsequently altered as it emerges from the back focal plane due to the finite size and aberrations of the imaging lens. The effect of the microscope on the electron wave as the wave travels to the imaging plane can also be more readily included in reciprocal space. The lens transfer function, $T(k_x,k_y)$, is given in equation 3.6.

$$T(k_x,k_y) = A(k_x,k_y)e^{-2\pi i\left[\frac{C_s\lambda^3(k_x^2+k_y^2)^2}{4} - \frac{\Delta z\lambda(k_x^2+k_y^2)}{2}\right]} \quad \textbf{(3.6)}$$

$A(k_x,k_y)$ is a pupil (or aperture) function which is unity unless an aperture is used and C_s is the spherical aberration coefficient of the lens (the Lorentz lens in this case). In the case of Fresnel imaging, the transfer function of the imaging lens can be simplified due to the term containing C_s being negligible in this mode and $A(k_x,k_y)$ being unity. Therefore equation 3.6 simplifies to:

$$T(k_{\mathbf{r}}) = e^{\pi i\Delta z\lambda(k_x^2+k_y^2)} \quad \textbf{(3.7)}$$

At the imaging plane, x',y', the wave expression can be calculated, in real space for the image intensity, $I(x',y')$, by taking the inverse Fourier transform. Using the simplification in equation 3.7, $I(x',y')$ can be written in terms of a convolution between $e^{i\varphi(\mathbf{x'})}$, and inverse Fourier transform of equation 3.7 which becomes $e^{\frac{\pi i(x'^2)}{\lambda\Delta z}}$, this is a Fresnel propagation factor. The image intensity for a Fresnel image is given in equation 3.8.

$$I(x',y') = \left| e^{i\varphi(x')} * e^{\frac{\pi i(x'^2+y'^2)}{\lambda\Delta z}} \right|^2 \quad \textbf{(3.8)}$$

where * denotes the convolution integral. From equation 3.8, the image intensity is linear over a small range of Δz and can be used to calculate an image for any known specimen and microscope conditions. However, the magnetic induction due to a specimen cannot be easily recovered from an image. The image intensity varies non-linearly with phase of the

material outside the small range of Δz and, unfortunately, the range at which the defocus becomes visible to the user in the TEM is out of the linear range. As is shown, obtaining information on the magnetic induction due to the specimen is often problematic and difficult (see [10, 11, 12] for one possible avenue). Fresnel imaging however, can be quickly and easily implemented to obtain the domain structure (via the domain wall contrast) and the fields at which magnetic events take place.

An example of an image taken using Fresnel microscopy with a 150 μm C1 aperture, 30 μm C2 aperture and no objective aperture (the standard conditions for the images discussed in this thesis) is shown in Figure 3.7(a). The image is of a 4×0.8 μm^2, 20 nm thick, permalloy element fabricated on a 50 nm silicon nitride substrate in a (-12 ± 6) Oe field. Visible within the element are both areas of convergent (light lines) and divergent (dark lines) contrast, as well as contrast at the edge of the element that is associated with the magnetisation of the specimen. The physical edge can be thought of as a domain wall where the deflected beam is convergent or divergent with the straight through beam. The edge contrast (the band around the element) can also be used to say when an element has reversed even when the internal magnetic contrast has been obscured. Using Fresnel images, it has been possible to construct a schematic of the magnetisation distribution within the element, as shown in Figure 3.7(b). Visible are the 90^o and the 180^o domain walls that result in the rotating Bloch lines (magnetic vortices) that are mentioned in section 1.3.1.

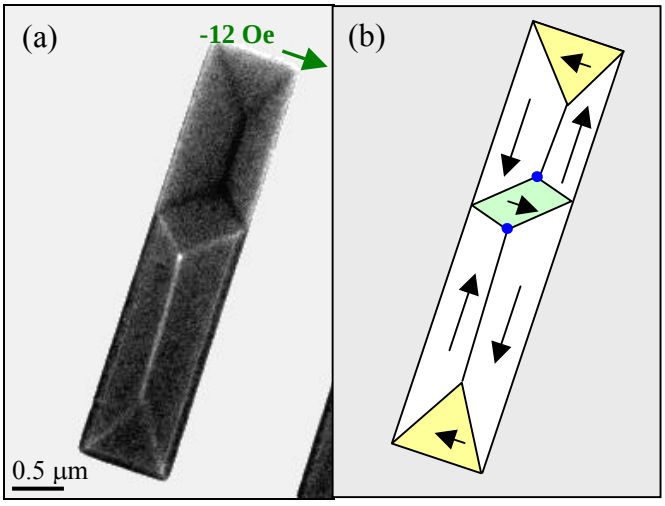

Figure 3.7: (a) Fresnel image of 4×0.8 μm^2 permalloy element in a field of (-12 ± 6) Oe, (b) a schematic of the magnetic induction distribution within the element based on the previous magnetic history. The blue circles indicate rotating Bloch lines.

3.3.2 Differential phase contrast imaging

Differential phase contrast (DPC) is an imaging technique that was first applied by Chapman et al, [13] in 1978 for the direct imaging of the magnetic domains in thin film specimens. In addition to direct domain structure imaging, quantitative information about the domain orientation and magnetic induction within the specimen can be obtained. The DPC technique requires a scanning probe TEM (STEM), such as the modified CM20, to raster scan a focused probe (with convergent half angle α) over the surface of the specimen and a solid state split detector (situated in the far field) to measure the Lorentz deflection, β_L (defined in equation 3.3), that results from the specimen, shown in Figure 3.8. The deflection due to β_L, which in turn is due to the integrated magnetic induction over the path of the electron, is measured from the difference in signal in the opposing segments of the detector. The sum signal of the number of electrons incident on the total detector can be used to construct a bright field image of the scanned area, thus allowing parallel acquisition between magnetic and physical images of the specimen. The acquisition of the images can take seconds to minutes to complete; this depends on the scan rate of the probe and the signal to noise level in the detector. FEG emission sources are most commonly used, as they are bright sources with high spatial resolution. The resolution of DPC is limited by two factors, the incoherent and coherent limits. The incoherent limit arises from the probe having a finite size and not being able to be demagnified to a zero point probe. The coherent limit is imposed by the spherical aberration ($C_S\alpha^3$ where C_S is the spherical aberration) of the equipment and the diffraction limit (λ/α) that is imposed by the electron wavelength and the equipment. Of the two limitations the incoherence limitation has the largest contribution, giving a probe size of <10 nm [8].

A schematic of the DPC scanning mode from scanning coils to the detector for a two domain magnetic specimen with a 180^o domain wall is shown in Figure 3.8. The first set of scanning coils in the STEM are used to raster scan the beam across the specimen and the second set are used to rectify the beam to a position perpendicular to the specimen. A similar arrangement is used by the de-scan coils to re-centre the beam onto the detector in the absence of a magnetic specimen. Upon insertion of a magnetic specimen, the beam becomes deflected. The deflection moves the beam off the centre of the detector and the position, with respect to the centre of the detector, is used to form the DPC image. After the beam has been rectified, the post specimen lenses are used to select the diameter of the cone that falls on the DPC detector. To negate the dead zones between the separate quadrants and to ensure no signal is lost at the edge of the detector a cone diameter of

approximately half the detector diameter is required (although this is not always achieved in reality).

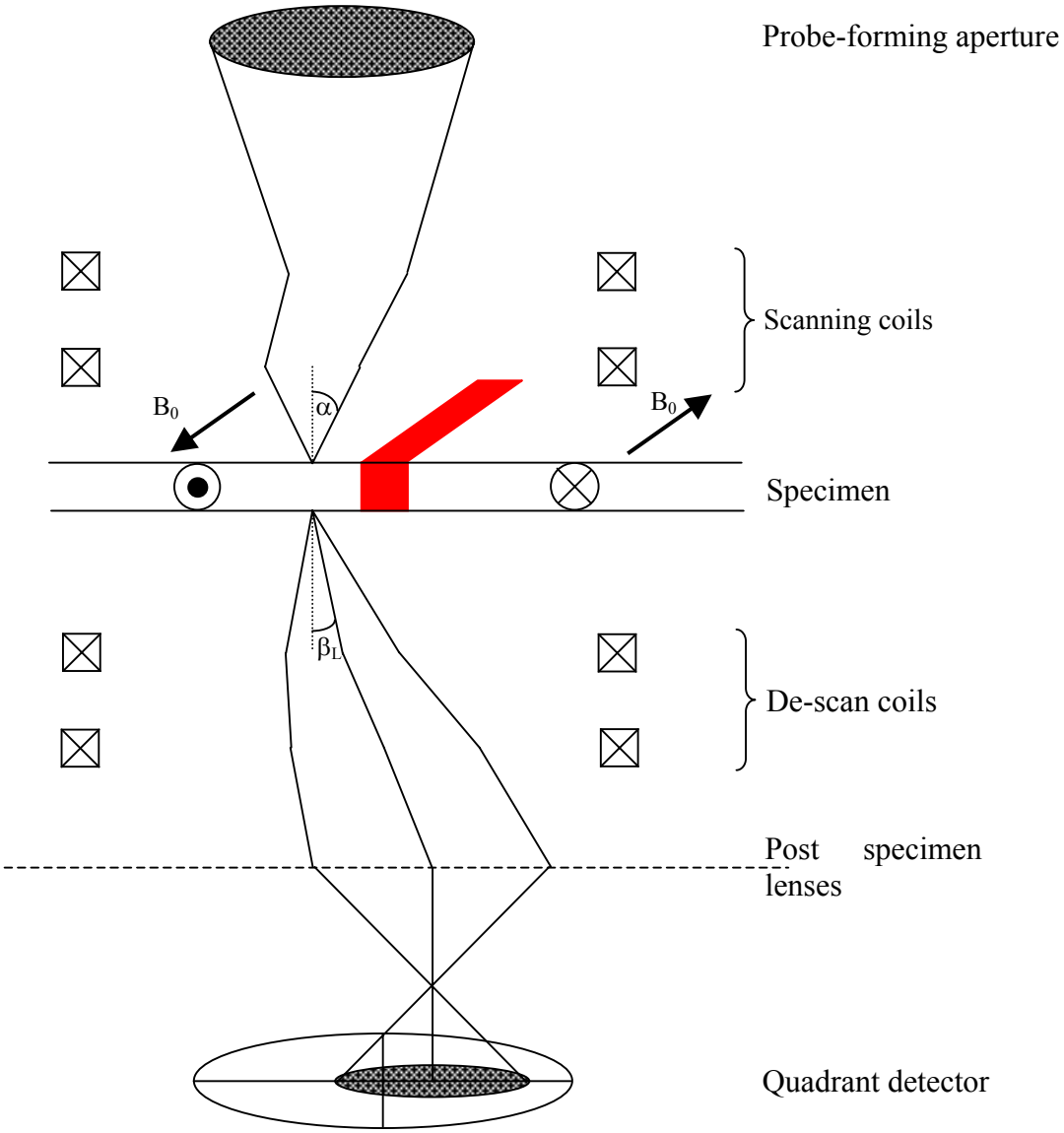

Figure 3.8: schematic of DPC scanning of a magnetic specimen from scanning coils to detector, showing the deflection due to the specimen. Red indicates a domain wall.

The pre-specimen electron optics of the CM20 can result in two separate DPC modes, low magnification (LMS) and high magnification scanning (HMS), although the physics governing the image formation is the same. For both LMS and HMS the probe size is governed by the beam spot size (spot sizes 5–9 are generally used) and the size of the C2 aperture. The probe size decreases but so too does the intensity (hence the signal to noise ratio) as the scanning spot size and the size of the C2 aperture decrease. Therefore a compromise between the probe size and intensity has to be made. For this thesis, a spot size of 7 and a C2 aperture of 30 μm is used unless otherwise stated. In LMS only the C2 lens is used to form the probe on the specimen, by doing this α is small, α_L say, and the

probe size is large (~38 nm for spot size 7 and a C2 aperture of 30 μm [14]). This set-up allows for a large scan area and increased sensitivity to the integrated magnetic induction because of the small probe angle. The probe size can be decreased, resulting in an increase in α, by using the upper Lorentz lens as a third condenser lens (that has a fixed current to minimise thermal drift due to its proximity to the specimen [15]). The C2 lens is used to focus the scanning probe instead of the objective lens. The increased α, α_H say, allows for a finer probe to be achieved (<10 nm, mentioned previously, for spot size 7 and a C2 aperture of 30 μm [14]). Unfortunately the trade-off with the increased α of the HMS is a reduction in the sensitivity to the integrated magnetic induction and scan area of the technique. Both LMS and HMS modes are shown schematically in Figure 3.9.

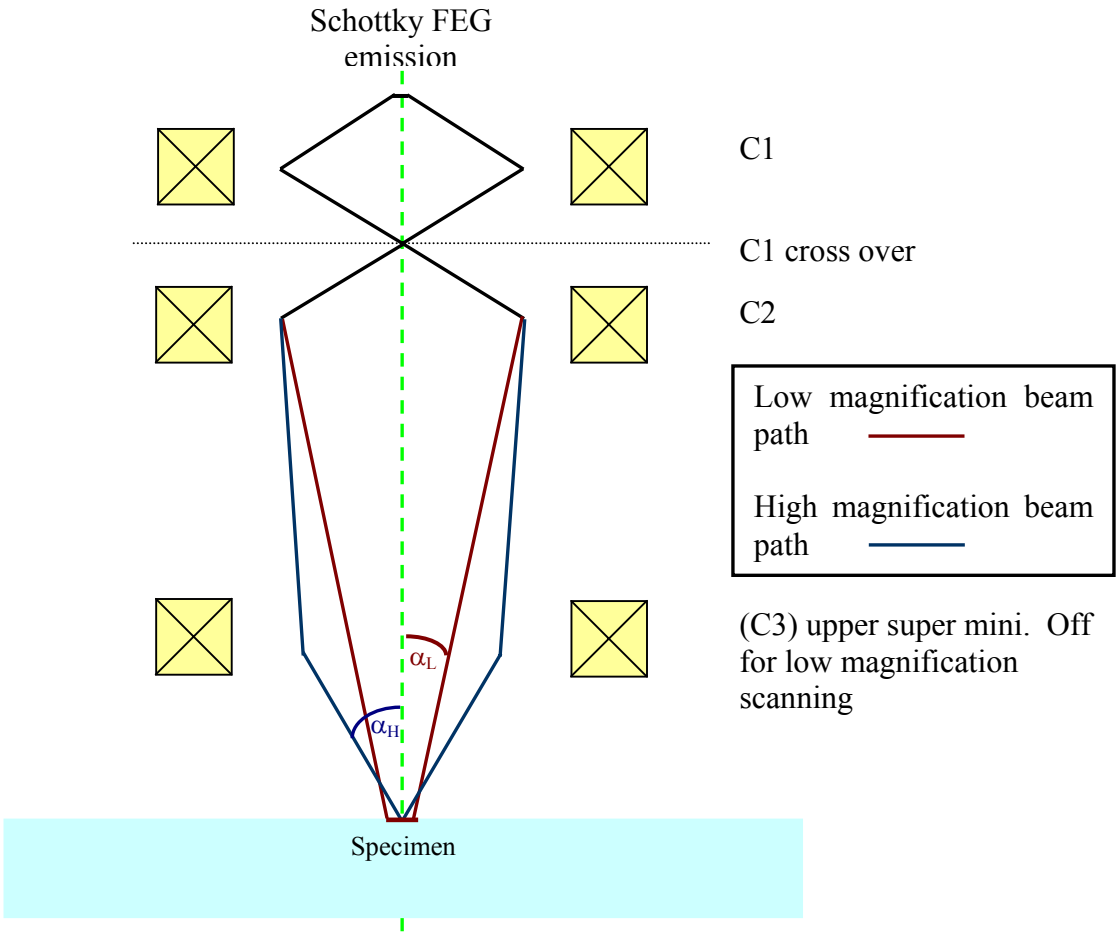

Figure 3.9: schematic of the beam paths for low magnification (red) and high magnification (blue) DPC scanning, with angle of incidence, α, at the specimen. Not to scale.

So far the description of the DPC imaging mode has focussed entirely on the effect of the magnetic induction to the electron beam. From equation 3.3, the Lorentz force also has a contribution from the electrostatic potential of the structure within the specimen. Chapman, McFadyen and McVitie [16] have shown that the addition of an annular detector can help suppress the physical signal due to the differential elastic scattering from many

crystalline specimens. The suppression of the physical structure is due to the spatial frequencies of the diffraction contrast generated by the physical strucutre, in general, being higher than the spatial frequencies of the magnetic signal, thus resulting in a smaller scattering of the electron beam. The hole in the detector helps remove the majority of the smaller deflections due to the physical structure. The scattering due to the physical structure is only visible within the image when a probe size around the grain size being investigated is used; otherwise the physical contribution is averaged out in the large probe signal. Thus the annular detector is only necessary for the HMS that is used in this thesis. The use of the annular detector is often referred to as modified DPC and the annular detector is incorporated into the existing solid detector (a schematic of which is shown in Figure 3.10) allowing both modes to be implemented on the same DPC system.

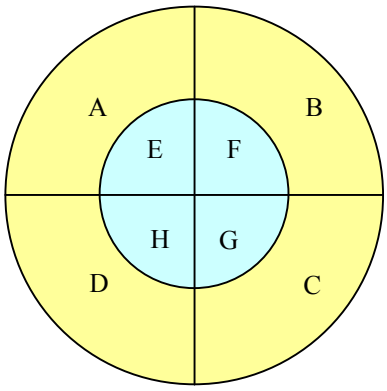

Figure 3.10: schematic of the modified DPC detector with inner circular detector (E, F, G and H) and outer annular detector (A, B, C and D).

Given the dimensions of the specimens discussed in this thesis, HMS is primarily used and therefore only the modified DPC set-up is used. An example of HMS images taken using the modified DPC technique is shown in Figure 3.11(a)-(e) with a schematic of the magnetisation shown in Figure 3.11(f). The images are of a 1×1 μm^2, 20 nm thick permalloy element fabricated by electron beam lithography. Figures 3.11(a)-(b) are of sections (A-C) and (B-D) respectively and Figures 3.11(c)-(d) are of sections ((A+B)-(D+C)) and ((A+D)-(B+C)) respectively. The sections of the DPC detector are shown in Figure 3.10. The images in Figure 3.11 show the in-plane components of **B** integrated along the path of the electron with the direction of sensitivity for the image indicated by the arrows. Shown in Figure 3.11(e) is the sum image (which, as noted above, is equivalent to the bright field image). Visible at the centre of the difference images is the magnetic vortex core. The individual permalloy grains can be identified in the sum image. A comparison of the difference images and the sum image show signal variation generated by the polycrystalline grain structure has been reduced, although not completely suppressed. A schematic of the magnetisation within the permalloy is shown in Figure

3.11(f), this shows the rotation of the magnetisation (green arrows) to form four-domains separated by 90° domains walls (red lines), also deduced from the images is the direction of the rotation (anticlockwise).

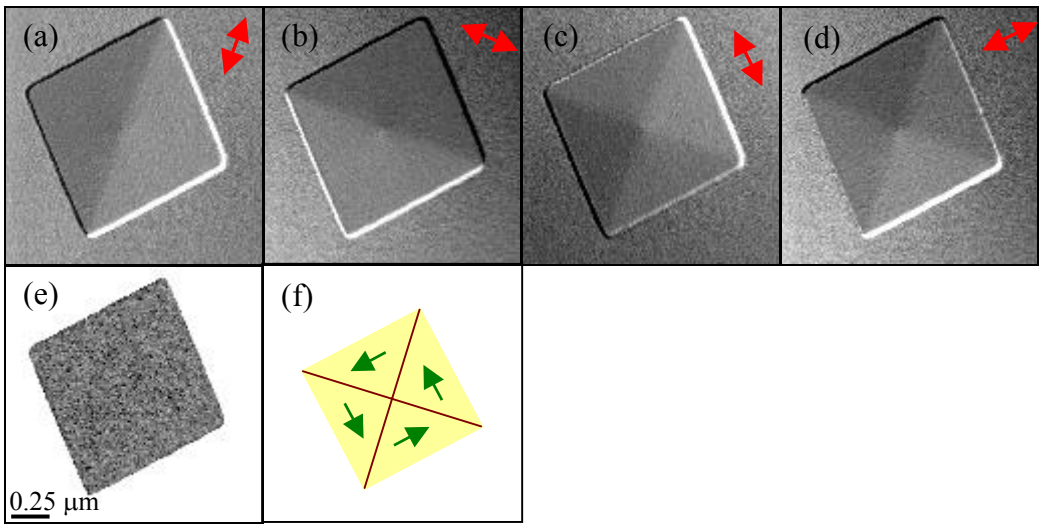

Figure 3.11: (a)-(e) an example of a 1×1 μm², 20 nm thick, permalloy element fabricated by EBL imaged using the HMS DPC imaging mode. The arrows in the image show direction of the sensitivity to B. (f) A schematic of the magnetisation within the element. Taken in zero applied field.

3.3.3 Other magnetic imaging techniques

The magnetic properties of a material can be examined by a number of other techniques, for example the Bitter method. Here the surface of the specimen is covered by small magnetic particles; these particles tend to congregate around areas of high stray field. The disadvantage of this technique is that it is limited by the particle size and the ability to resolve them. Two other techniques that are related to each other are the Faraday and Kerr techniques. For both techniques, a laser is focussed on the surface of the specimen and information on the magnetisation within the specimen is obtained from the polarisation of the transmitted beam (the Faraday effect, if the specimen is thin enough) or from the reflected beam (Kerr effect). Both these techniques can be used to obtain an average hysteresis loop for materials from large numbers of samples over short time frames. A review of the three techniques mentioned above is given by Hubert and Schäfer [17]. A technique, similar in principle to the Kerr technique, that images the polarised electrons produced by the magnetisation within the specimen when an electron probe is scanned across the surface of the specimen and then analysed in a specially modified scanning electron microscope (SEM), can also be used to study magnetic materials. This technique is known as scanning electron microscopy with polarisation analysis (SEMPA) [18]. Neutron and x-ray diffraction can also be used to investigate the magnetic properties of a

specimen. Neutron diffraction, however, only returns the phenomenal component of the magnetic ordering of the specimen but no information on the domain walls and x-ray diffraction cannot reveal 180^{o} domain walls. The technique cannot distinguish between the x-rays that have been scattered by magnetic spins that are orientated parallel and antiparallel [8].

One other magnetic imaging technique that belongs to the force microscopy group of techniques known as scanning probe microscopy (section 3.4) is magnetic force microscopy (MFM) [19, 20]. MFM involves scanning a sharpened silicon tip coated with a magnetic material (that can be tailored to the specimen imaged) over the surface of the specimen. The magnetic stray field of the tip interacts with the stray field of the specimen and a suitable two-dimensional plot can be obtained about the stray field gradient with respect to the surface. The disadvantages of this technique are the resolution is limited by the tip radius, the stray field from the tip can influence the magnetisation of the material, the acquisition time is usually in tens of minutes and the information obtained is limited to the surface of the material.

3.4 Atomic force microscopy

Among the many surface-profiling techniques available, scanning probe microscopy (SPM) is one of the most versatile and widely used. SPM encompasses several techniques including scanning tunnelling microscopy (STM), MFM and atomic force microscopy (AFM). The last is the surface profiling method used to investigate the elements discussed in this thesis. The definition of an SPM technique used in this thesis is one where a solid probe is scanned over the surface of a specimen. AFM is implemented on a Digital Instruments Dimension 3100 SPM microscope located at the University of Glasgow (hereafter referred to as the DI3100). The DI3100 can accommodate specimens with a diameter of up to ~20 cm in the specimen plane and over 1 cm in height. When the probe is engaged with the specimen the area the probe can scan is ~80×~80 μm^2 in the specimen plane and ~6 μm in height.

3.4.1 A brief history of force microscopy

Force microscopy (and in particular AFM) is a development of the first SPM technique, (STM), to overcome certain disadvantages of the technique. STM was invented by Binning et al, in 1982 [21]. The STM is a microscope that uses a piezoelectrical stack to control the movement of the probe over the surface of the specimen to within several Angstroms and is kept under vacuum. A potential difference is then applied between to the probe and the

sample and by a phenomenon know as quantum tunnelling the resulting current can be detected on the specimen. As the distance between the specimen and probe increases the current decreases and the reverse is true. Coupled with the knowledge of the position on the specimen provided by the piezoelectrical stack, a map of the surface can be developed. The main disadvantage of STM imaging is the necessity of the specimen to be conducting. To overcome this disadvantage, another mode of SPM, know as atomic force microscopy (AFM) was invented by Binning et al, [22] in 1986.

3.4.2 The atomic force microscope

An AFM works by scanning a sharpened probe, at the end of a cantilever (that is attached to a piezoelectric stack) across the surface of the specimen, a schematic of which is shown in Figure 3.12. The probe is either in contact with or close to the surface of the specimen. When scanning, any change in the position of the probe due to the surface forces of the specimen are recorded by the deflection sensor. A quadrant detector to receive a photodiode laser is used for the DCI3100. In Figure 3.12 an angle of 10^{o} from the horizontal is noted between the cantilever and the piezoelectric stack, this is to allow for the probe mounting mechanism of the DCI3100.

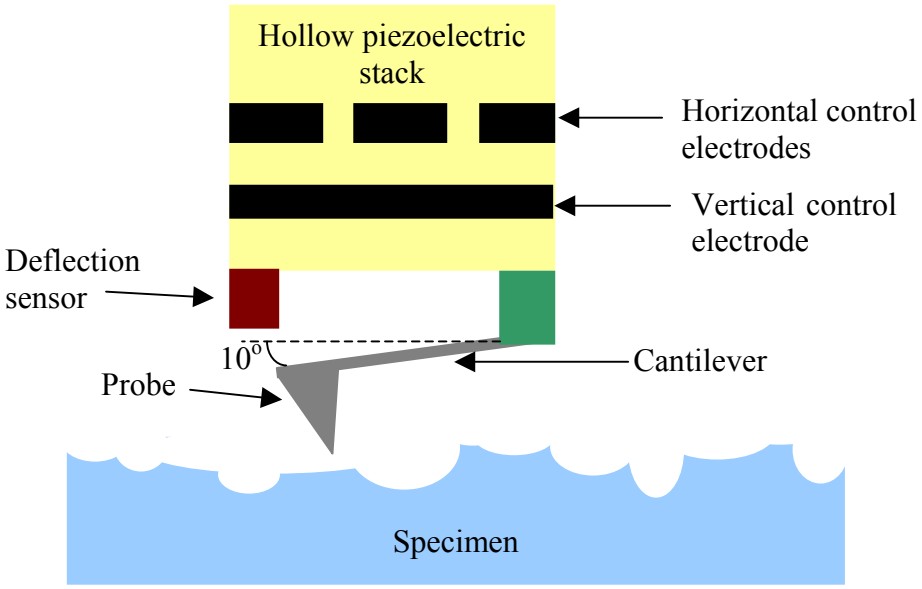

Figure 3.12: schematic of the basic controls for the DCI3100 AFM, not to scale.

The main surface forces that affect the probe of the AFM are atomic shell repulsion and Van der Waals forces. Atomic shell repulsion arises from the interaction of the overlap of the electron clouds when the atoms in the tip are brought into close contact with the atoms of the specimen and are repulsed (due to the Pauli exclusion principle). Atomic shell repulsion is a short-range force (~1 Å) that rapidly increases with decreasing interatomic distances. Van der Waals forces, conversely, are long ranging forces that arise due to

dipole, dipole interactions of the molecules in the probe and the specimen [23]. A graph, with arbitrary units, shown in Figure 3.13, is of the two regions of force, the atomic shell repulsion ("contact mode") and the Van der Waals force ("non-contact mode").

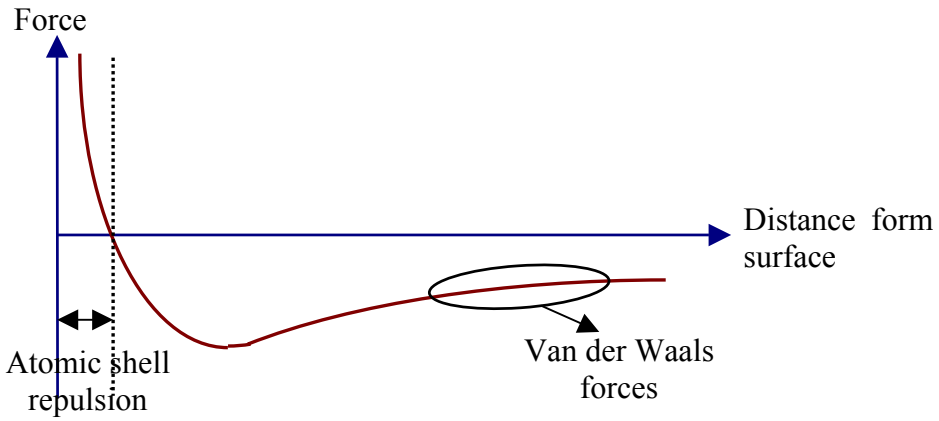

Figure 3.13: plot of force experienced for AFM probes against distance from surface (axes have arbitrary units).

The main AFM imaging mode used in this project was TappingMode™. TappingMode™ imaging is where the cantilever is vibrated at or near the resonance frequency, $f_0 = \frac{1}{2\pi}\left(\frac{k}{m_0}\right)^{\frac{1}{2}}$, and brought close to the surface of the specimen so that when the cantilever is vibrated near the specimen the probe is in "contact" at the bottom of the arc. k is the spring constant associated with the cantilever and the m_0 is the effective mass that loads the spring (the probe on a cantilever). As the probe approaches the surface of the specimen, the atomic shell repulsion of atoms present in the surface is sensed. As a result the resonance frequency is changed and the height can be calculated accordingly. The height and in-plane position for each pixel is stored and the surface map is produced. An example of a surface map obtained by TappingMode™ AFM is shown in Figure 3.14(a) and a line profile of the element is shown in Figure 3.14(b). This image is of 20 nm thick, square permalloy element (500 nm in length) that have been created by FIB milling the surrounding thin film with a gallium ion dose of 0.07 nCμm^{-2} (the result of which are to be discussed in chapter 5).

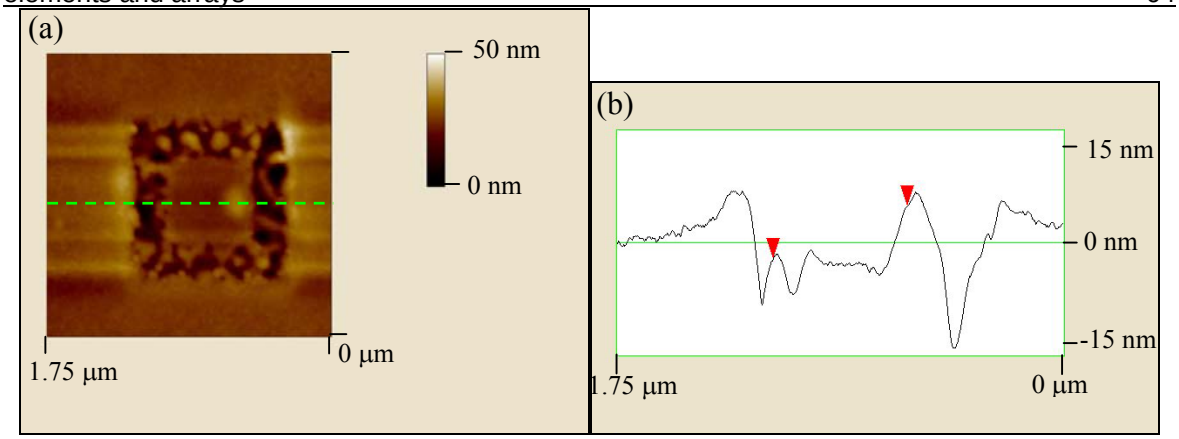

Figure 3.14: (a) a TappingMode™ AFM image of a 500×500 nm² permalloy element created by FIB milling and (b) the surface profile of the element (the green line indicated in (a)).

The probe at the end of the cantilever is a sharpened tip, usually fabricated from single crystal silicon for TappingMode™ imaging. Standard AFM TappingMode™ probes [24] have a radius of curvature of 5-10 nm, 17° angles on the sidewalls, a forward angle of 25° and a rear angle of 10°, Figure 3.15. Both the radius of curvature and the aspect ratio of the features on the surface of the specimen with respect the probe walls, limits the resolution of the microscope.

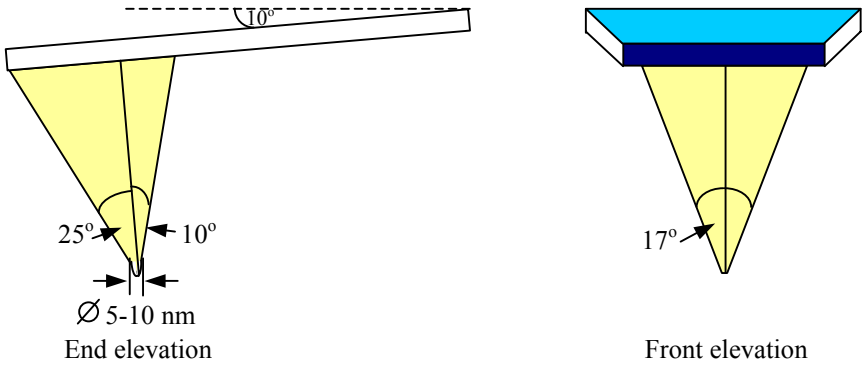

Figure 3.15: schematic of a standard silicon nitride AFM probe used for TappingMode™, not to scale.

Acoustical and vibrational noise acts to limit the sensitivity of any AFM system and can interfere with imaging. To decrease the noise, the majority of AFM systems are mounted on air tables and are encased in a protective hood. The ultimate resolution of the AFM probe, however, is still the probe size; to improve this resolution FIB sharpened AFM TappingMode™ probes are available. The FIB probes have a smaller radius of curvature (2-5 nm) and sidewall angles. The standard single crystal silicon probes are used in this thesis as the average depth is important and not the surface map as TEM imaging is used for this.

Bibliography

[1] de Broglie L., Ann de Physiques 3 (1925) 22.

[2] Knoll M., Ruska E., Z. Physik 78 (1932) 318.

[3] Chapman J.N., Johnston A.B., Heyderman L.J., McVitie S., Nicholson W.A.P., Bormans B., IEEE Trans. Mag. 30(6) (1994) 4479.

[4] Williams D.B., Carter C.B., *"Transmission electron microscopy"*, Plenum Press 1996, ISBN 030645324X.

[5] Tungsten Schottky emitter source image available at: http://www.feibeamtech.com/pages/schottky.html URL active 27th Mar. 2007.

[6] For a review on the subject: Kato N.I., J. Elec. Micros. 53(5) (2004) 451.

[7] Chapman J.N., Scheinfein M.R., J. Magn. Magn. Mat. 200 (1999) 729.

[8] Chapman J.N., J. Phys. D: Appl. Phys. 17 (1984) 623.

[9] Hale M.E., Fuller H.W., Rubinstein H., J. Appl. Phys. 30 (1959) 789.

[10] De Graef M., Zhu Y., J. Appl. Phys. 89(11) (2001) 7177.

[11] Volkov V.V., Zhu Y., Ultramicroscopy 98 (2004) 271.

[12] McVitie S., Cushley M., Ultramicroscopy 106(4-5) (2006) 423.

[13] Chapman J.N., Batson P.E., Waddell E.M., Ferrier R.P., Ultramicroscopy 3 (1978) 203.

[14] Lindsay R, *"TEM Investigation of Silicon Devices"*, Thesis (1998), University of Glasgow.

[15] Scott J., *"Characterisation of MFM Tip Stray Fields using Lorentz Electron Tomography"*, Thesis 2001, University of Glasgow.

[16] Chapman J.N., McFadyen I.R., McVitie S., IEEE Trans. Magn. 26(5) (1990) 1506.

[17] Hubert A., Schäfer R., *"Magnetic domains: the analysis of magnetic microstructures"*, Springer-Verlag Berlin Heidelberg, 1998, ISBN 3540641084.

[18] Scheinfein M.R., Unguris J., Kelley M.H., Pierce D.T., Celotta R.J., Rev. Sci. Instrum 61(10) (1990) 2501.

[19] Martin Y., Wickramasinghe H.K., Appl. Phys. Lett. 50(20) (1987) 1455.

[20] Sáenz J.J., Garciá N., Grütter P., Meyer E., Heinzelmann H., Wiesendanger R., Rosenthaler L., Hidber H.R., Güntherodt H.-J., J. Appl. Phys. 62(10) (1987) 4293.

[21] Binning G., Rohrer H., Gerber C.H., Weibel E., Phys. Rev. Lett. 49 (1982) 57.

[22] Binning G., Quate C.F., Gerber Ch., Phys. Rev. Lett. 56(9) (1986) 930.

[23] Kittel C., *"Introduction to Solid State Physics"*, 7th edition J. Wiley and Sons, Inc., 1996, ISBN 0471111813.

[24] Standard AFM probe data available at: https://www.veecoprobes.com/probe_detail.asp?ClassID=20 URL active 27th Mar. 2007

4 Preliminary results for the fabrication of nanoscale elements

In this chapter the preliminary results from the investigation into the characteristics of micron and sub-micron ferromagnetic elements fabricated by focussed ion beam milling are presented. Firstly, the initial investigations into the effect of the variation in the dose on the film are presented and discussed. Secondly, an investigation into the effects of varying the beam current is discussed. From these results a beam current and range of doses was determined to optimise a range of milling conditions for the elements.

Lastly the results of OOMMF simulations [1] for the 1000×200 nm^2 and 500×500 nm^2 elements are discussed in this chapter. These results include simulations for ideal elements and elements that have been artificially roughened to break the symmetry of the system.

4.1 The effect of varying dose on 20 nm thick permalloy thin film

In order to observe the effects of varying the dose of a 30 keV Ga^+ beam on 20 nm thick, permalloy ($Ni_{80}Fe_{20}$) thin film (deposited on 50 nm thick silicon nitride substrate), a series of trenches were milled into the film using the focussed ion beam (FIB) microscope described in section 2.3. The trenches were fabricated by milling the pattern shown in Figure 4.1 in three columns into the permalloy, with black pixels indicating the highest dose (0.025 $nC\mu m^{-2}$) decreasing in nine even steps to the lowest dose (0 $nC\mu m^{-2}$), white. The nine steps are due to the programme using 256 shades of grey to signify a dose range and the nine steps give a good range from the highest to lowest doses. Using a beam

current of 12 pA, the trenches were fabricated with nominal in-plane dimensions of 1×1 μm^2. The pattern was originally designed for a 10 pA beam current (the upper dose in Figure 4.1) with corresponding spot size ~10 nm [2] but through time the aperture size increases by milling from Ga^+ beam (section 2.3.1), this alters the corresponding doses (the lower dose in Figure 4.1). The permalloy film was deposited by the plasma sputter coating method described in section 2.1.1.

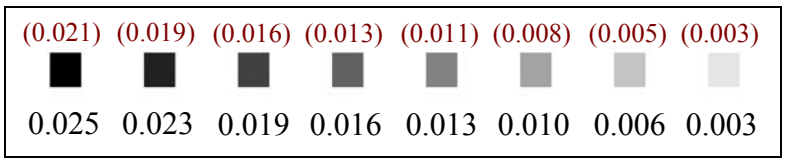

Figure 4.1: schematic of the input for the 1×1 μm^2 milled trenches. Shown above, in brackets, are the expected doses for a 10 pA beam current and below are the corrected doses for a 12 pA beam current. The doses are measured in $nC\mu m^{-2}$.

After fabrication of the 1×1 μm^2 trenches the physical structure was initially imaged using the DI3100 AFM described in section 3.4 and surface profiles were obtained. An overview of the trenches has been obtained and is shown in Figure 4.2. From the overview it can be observed that the pattern defined in Figure 4.1 has been milled into the 20 nm thick permalloy, although higher resolution images are necessary for more accurate depth measurements. Also visible around the trench situated first left on the second row is beam contamination due to the imaging in the CM20 TEM described in section 3.1.

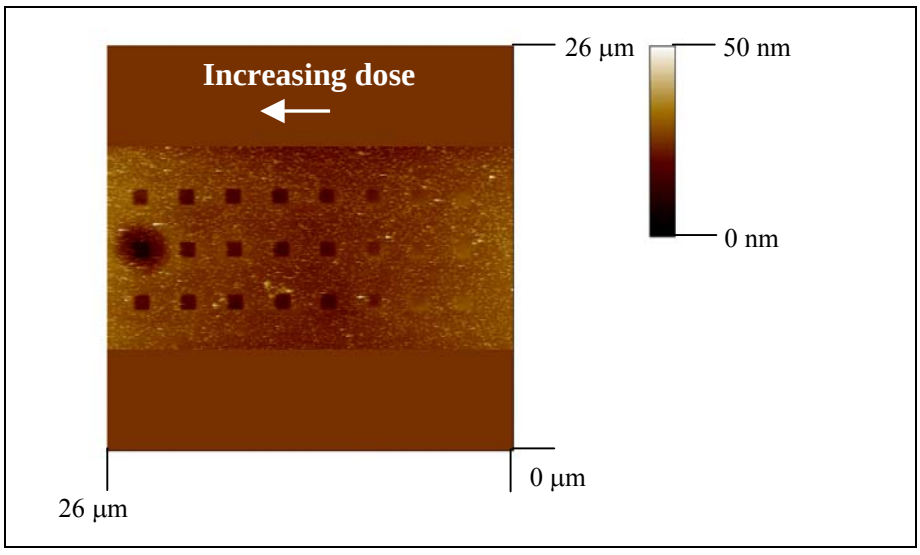

Figure 4.2: AFM image of the 1×1 μm^2 trenches fabricated in 20 nm thick permalloy thin film using increasing Ga^+. Doses increases from right to left.

In Figure 4.3 higher resolution images of the 1×1 μm^2 trenches are shown. Higher resolution AFM images of the three trenches most heavily irradiated (0.025, 0.023 and

0.019 $nC\mu m^{-2}$ doses) are shown in Figure 4.3(a), in this figure beam damage due to the TEM is clearly visible. Since the beam damage has occurred on the second line, line traces of the first row of trenches were used (dotted black box). The line trace is averaged over 30 lines to reduce the noise within the scan and allow the profile of the trench to be more accurately measured. From the line trace the edge of the trenches can be observed to have a definite width as opposed to a discontinuous change. This can probably be attributed to the profile of the beam believed to be Gaussian in nature [3]. The asymmetry of the trench sidewalls is due to the nature of the scanning in the AFM. In Figure 4.3 the scanning of the image by the tip is on the retrace (right to left), therefore the measure of the left sidewalls is more accurate. On average the sidewall width between the continuous film and the bottom of the trenches is ~250 nm. Bowing in the image has not been completely removed by the computer algorithms: this is most probably a result of a large hysteresis in the piezoelectric stack that is due to the rapidly changing depths. Also, from the line trace, the depth of the trenches can be calculated to be (9.5 ± 0.5) nm for the three trenches after normalizing to the reference level for the image.

The higher resolution AFM image of the three trenches irradiated with mid-range doses (0.016, 0.013 and 0.010 $nC\mu m^{-2}$) reveals a map of the trenches that has a visible change in the depth within the three trenches, Figure 4.3(b), the line trace confirms the decrease in depth of (9.0 ± 0.5) nm, through (8.0 ± 0.5) nm to (4.0 ± 0.5) nm. In the highest dosed trench in Figure 4.3(b) the slope of the sidewall is ~250 nm on the left edge, in the other two trenches in Figure 4.3(b), however the curving of the sidewalls has increased to ~500 nm. The increased curving within the sidewalls of the two lower dose trenches in Figure 4.3(b) is due to the decrease in the relative dose received by the trench which does not mill as much of the material. A change in film height (and subsequently the focus conditions) has been discounted, as there is no step in the AFM contrast around the trenches. A change in the Ga^+ beam is also discounted as the contrast and profiles of the trenches milled after (the trenches are milled by the raster fashion described in section 2.3.2) are similar to those milled before, i.e. the first, second and third columns are similar. Bowing can, again, be observed in the line trace (again due to the piezoelectric hysteresis), although it is not as pronounced as the change in depth is not as pronounced.

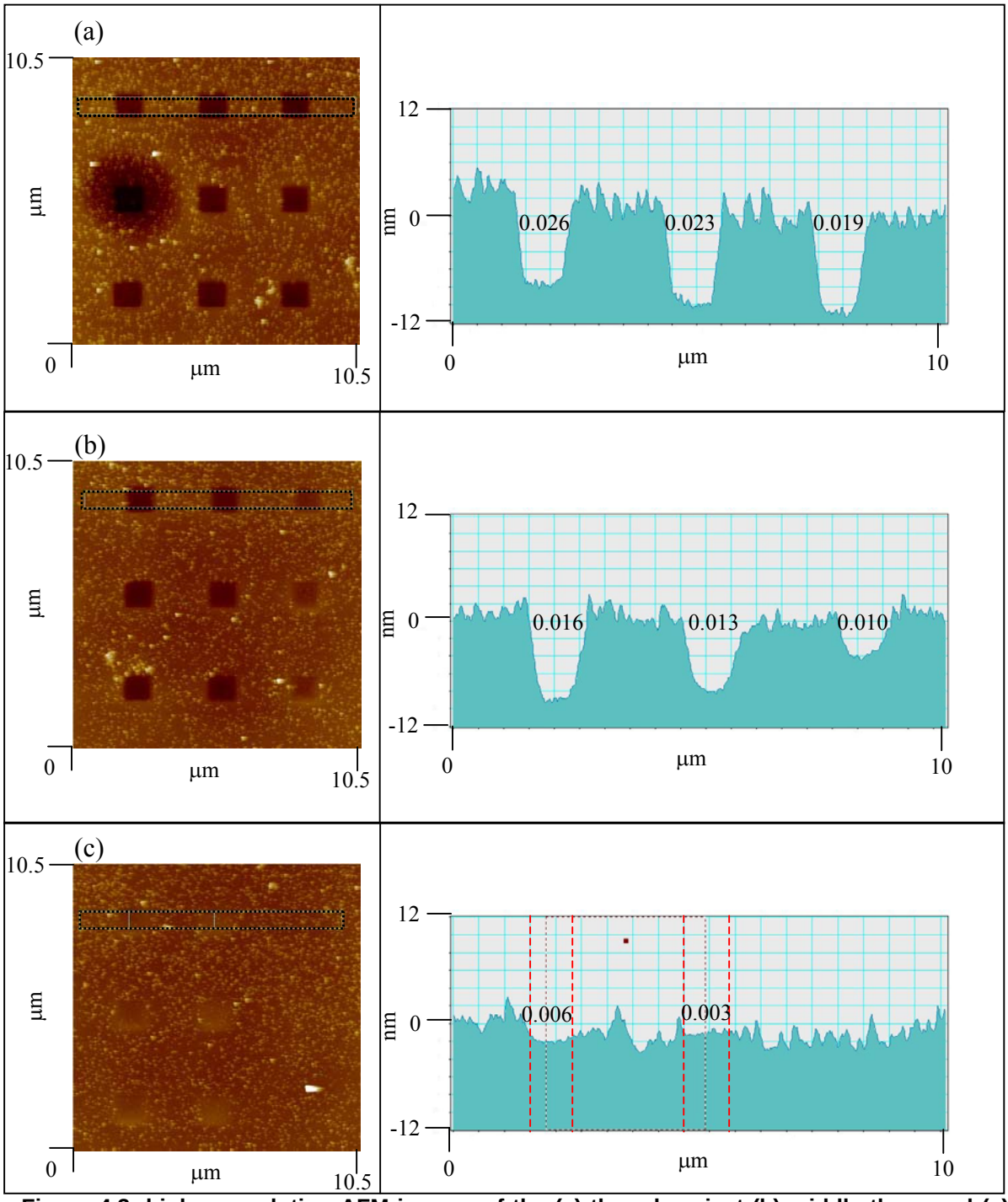

Figure 4.3: higher resolution AFM images of the (a) three heaviest (b) middle three and (c) two lightest 1×1 µm^2 irradiated trenches in Figure 4.2. The corresponding line traces (boxed in the left images and averaged over 30 lines) is shown in the right image with the relevant corrected doses (in nCµm^{-2}). The red lines in the depth profile in (c) indicate the approximate position of the irradiated areas.

A higher resolution AFM image of the two lowest dosed trenches revealed little depth changes in the irradiated areas, Figure 4.3(c). The two lowest doses (0.006 and 0.003 nCµm^{-2}) have acted to smooth the surface of the thin film, this is confirmed by the line trace in Figure 4.3(c). The areas that have been milled by the FIB are highlighted in Figure 4.3(c) with red dotted vertical lines. At the low doses, it is suspected that the Ga^+ has only been implanted into the material and that there is not the sufficient ion dose for

milling. Some of the energy from the 30 keV beam has also been dissipated by creation and destruction of secondary events (such as phonons and photons, see TRIM [4] calculations in section 2.3.1.1) with little milling occurring. To confirm this, imaging using electron energy loss spectroscopy (EELS) [5] or a similar technique could be used to measure the relative level of Ga^+ due to the implantation of the 30 keV beam.

From the AFM images and line profiles of the 1×1 μm^2 trenches, non uniform depths can be observed within the trenches as well as a definite width associated with the sidewall. The highest dose (0.025 $nC\mu m^{-2}$) is too low to mill completely through 20 nm thick permalloy. The average depths of trenches against the dose administered have been plotted in Figure 4.4. For the average depth, an uncertainty of ±1 nm has been assumed, although as shall be shown by bright field TEM imaging, the true uncertainty is greater. This discrepancy highlights a limitation of the AFM imaging technique due to the probe geometry. From the plot a general trend of an increase with the dose can be observed, as expected. A sputter rate of 0.43 ± 0.03 $\mu m^3 nC^{-1}$ has been measured.

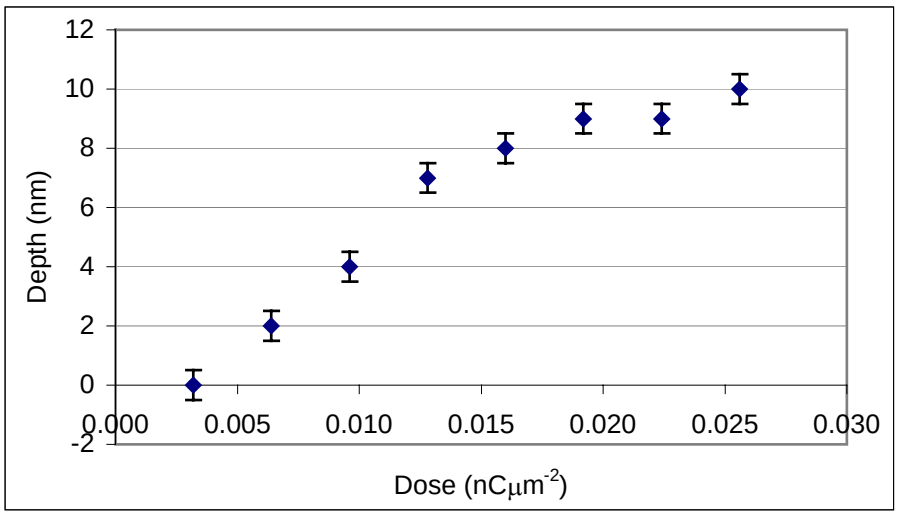

Figure 4.4: plot of depth (nm) against dose ($nC\mu m^{-2}$) for the 1×1 μm^{-2} trenches milled out of 20 nm thick permalloy film. An uncertainty of ±0.5 nm has been assummed for each value.

To observe the effects of the 30 keV Ga^+ on the grain structure of the permalloy thin films, bright field images (as described in section 3.2) have been obtained for the irradiated areas. Low magnification bright field images of the irradiated areas are shown in Figure 4.5. The lowest dose is in Figure 4.5(a) and the highest dose is in Figure 4.5(h). As can be observed in the images, there is an overall grain growth for the irradiated areas with respect to the as-deposited grains in the surrounding film. The grain growth increases with the dose received. Higher magnification images are necessary to obtain an estimate of the increase in grain growth within the trenches. The low magnification images also reveal

areas of non-uniform milling which are more visible at higher doses (but still evident at low doses) where the Ga^+ has milled through sections the supporting silicon nitride membrane in addition to the permalloy thin film. This is not readily observable in the AFM line traces. The areas of non-uniform milling appear as differing contrast levels (either different grain sizes or milled depths). The greatest non-uniformity can be observed for the bright white areas where both the permalloy and silicon nitride have been completely milled away, such as the area highlight with a dotted blue circle in Figure 4.5(h). This non-uniform milling appears greater in the higher doses than is observed in the AFM imaged samples. As such the deviation associated with the average depth should increased to reflect this. The increased deviation in depth (hence roughness) that is observed in Figure 4.5 thus alters the plot of depth against dose (Figure 4.4); the uncertainty should increase with dose. As the increased deviation is observed phenomenologically in bright field TEM imaging, no estimate can truly be made of the increase (a measure could be made if a sharpened AFM tip, section 3.4.2. The non-uniform milling is a result of preferential milling received by certain grain orientations [6]. The non-uniform milling is confirmed by the higher magnification images in Figure 4.6.

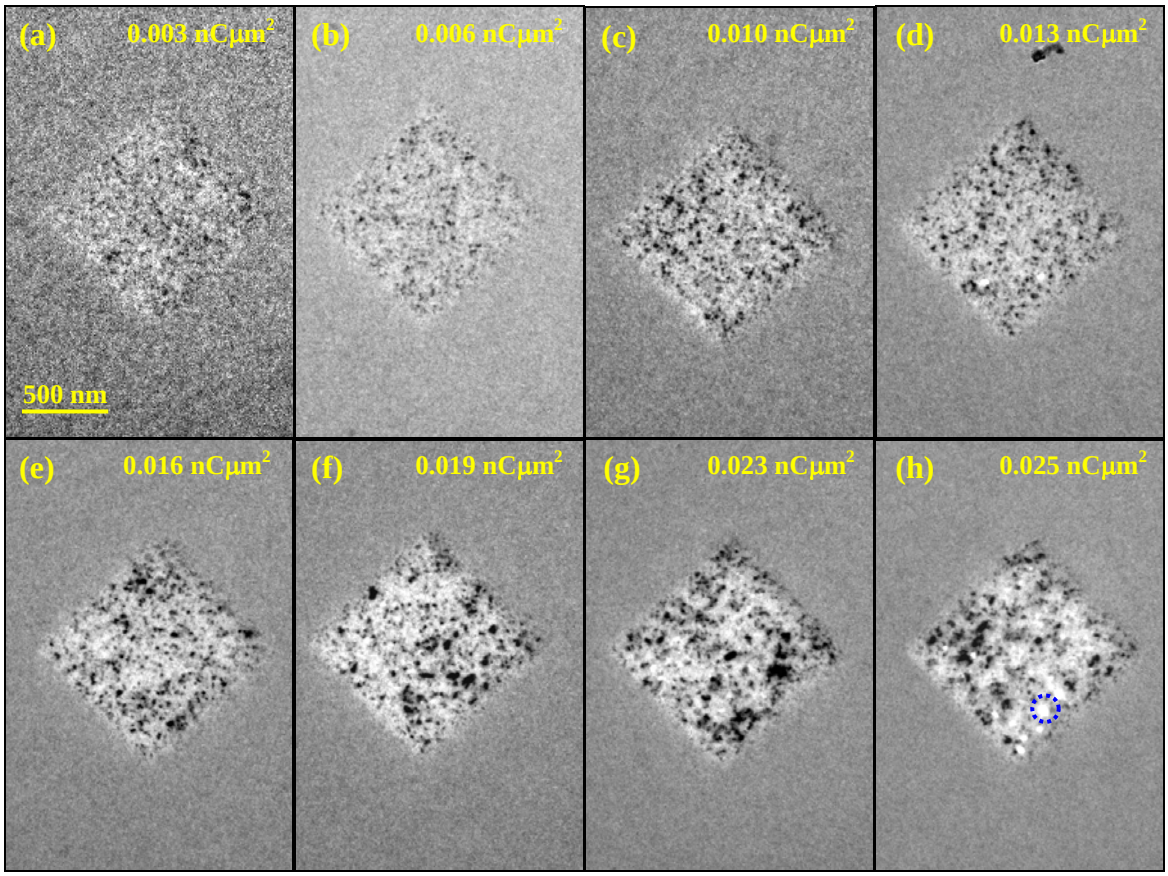

Figure 4.5: low magnification bright field images of 1×1 μm² trenches milled into 20 nm thick permalloy film and the remaining surrounding films with various doses (indicated in the individual images). The blue dotted circle indicates areas where the 30 keV Ga^+ beam has milled through both the permalloy and SiN substrate.

Higher magnification bright field images, Figure 4.6, have been obtained in order to estimate the increase in the grain size in the trenches. Evident in Figure 4.6 but not from Figure 4.5 is the affect the Ga^+ irradiation has on the surrounding thin film. Within the trenches shown in Figure 4.6, a spread of grain sizes can be observed (with respect to the deviation of the grain size) that varies with dose and a measure of the increase of grain size with dose can be made, Figure 4.7. For comparative purposes, the size of the grains of the unirradiated continuous thin permalloy film is shown in Figure 4.7 as zero dose. There is a variable spread in the grain sizes within the individual trenches with respect to dose that can also be observed in Figure 4.7. This reflects the binomial type grain distribution that can be observed in the images. The spread of the size is due to certain preferred grain orientations growing faster from the imparted energy of the 30 keV Ga^+ than other orientations. In Figure 4.6 there appears to be a definite change in the grain sizes at the trench/continuous thin film boundary (red dotted line), suggesting the tails of the Ga^+ beam for this beam current do not greatly affected the surrounding continuous thin film.

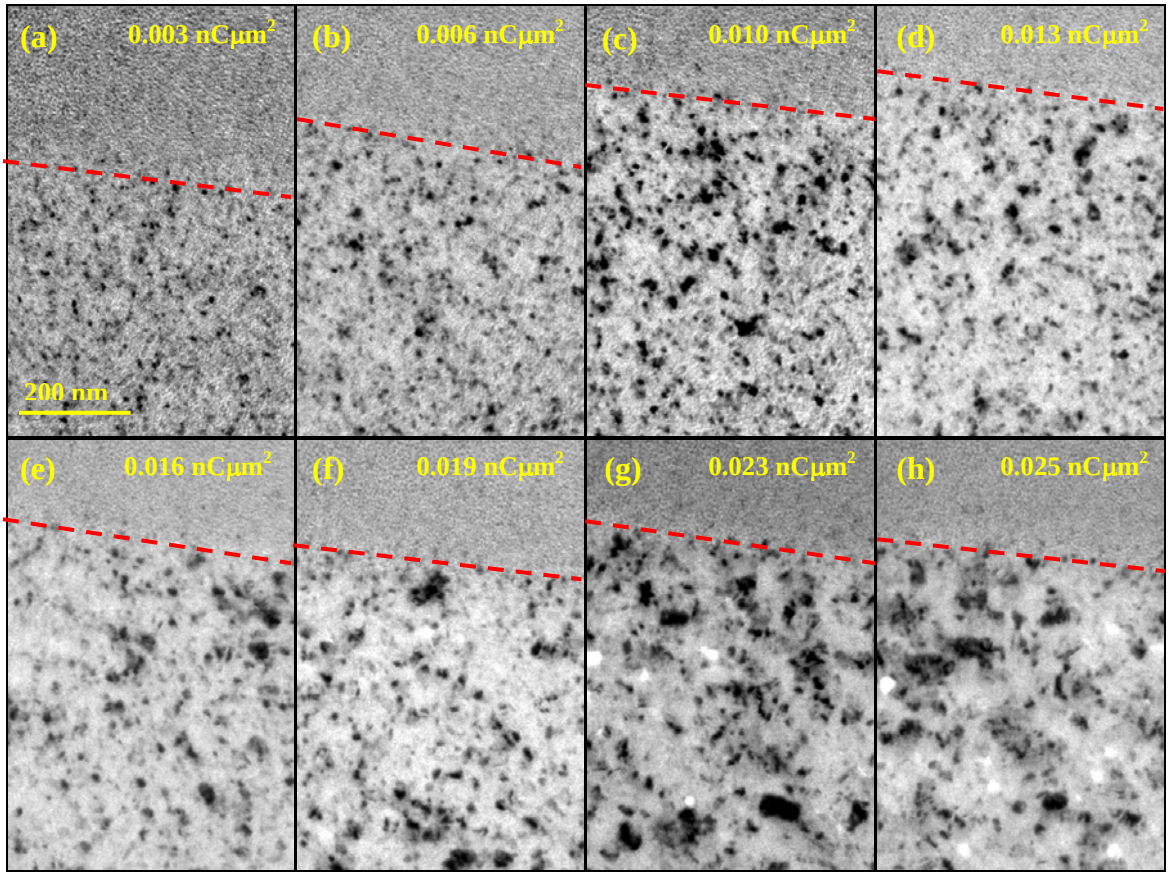

Figure 4.6: high magnification bright field images of 1×1 μm^2 trenches milled out of 20 nm thick permalloy thin film with various doses (indicated). The red line indicates the approximate boundary of the trench.

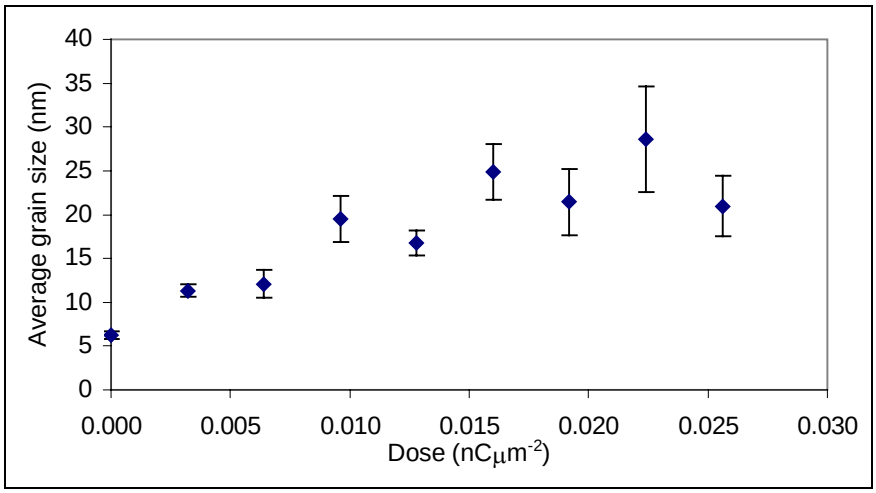

Figure 4.7: a plot of the average grain size against the corrected Ga^+ dose in the trenches. Included is the as depostied grain size, indicated at zero dose.

4.2 The effect of beam current on the structure of 1×1 μm² trenches

To observe what difference a change in beam current, if any, has on the milling of structures the 1×1 μm^2 trench pattern has been milled into 20 nm thick permalloy thin film, deposited under the same conditions as in section 4.1, using the 100 pA Ga^+ beam in the FIB microscope are discussed. A beam current ten times the previous beam current (section 4.1) is used as this has a spot size double the 10 pA aperture (20 nm for the 100 pA and 10 nm for the 10 pA beam current) [2] this should help highlight any discrepancies due to the beam current. The pattern in Figure 4.1 has been adjusted appropriately to maintain the nominal size of 1×1 μm^2 of the trenches. Before the trenches were imaged by bright field TEM, the surface profiles were measured by AFM. An overview of the 100 pA fabricated trenches, as imaged by the AFM, is shown in Figure 4.8(a) with the depth versus dose relation shown in Figure 4.8(b). The AFM images show areas of milling and areas where the trenches have grown (as confirmed by the plot of depth against dose shown in Figure 4.8(b)). The sputter rate has been calculated to be 0.5 ± 0.1 $\mu m^3 nC^{-1}$. Although there is a large uncertainty in the calculated sputter rate, this sputter rate is similar to the sputter rate calculated for the 10 pA beam current (0.43 ± 0.03 $\mu m^3 nC^{-1}$ section 4.1). The growth in the film is most probably due to contamination of hydrocarbons from the vacuum system in the FIB chamber attracted to the surface by energy imparted by the 30 keV Ga^+ beam. This has been observed by Kong [7]. Another reason for the difference in depths between the 100 pA and the 10 pA fabricated trenches could be the change in the aperture size with time (as discussed in section 2.3.1). For example, the increase of 2 pA for the "10 pA" beam current aperture is the 20 % dose

increase reported in the previous section, where as the similar increase in the "100 pA" aperture is a 2 % increase in the dose (a beam current of 102 pA was observed). The 2% increase in dose does not increase the overall dose greatly (for the highest dose 0.021 nCμm^{-2}, the calculated increase is 0.0004 nCμm^{-2}).

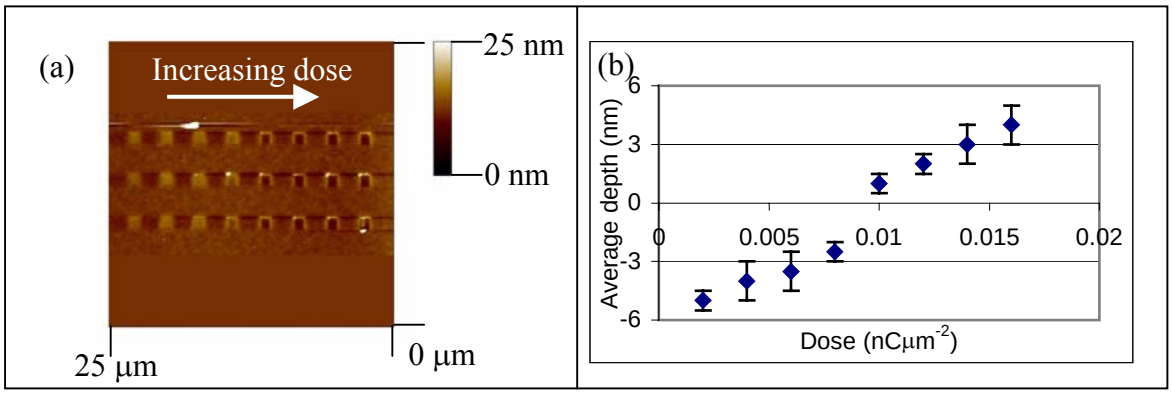

Figure 4.8: (a) AFM image of the trenches fabricated using a 102 pA beam current, (b) plot of depth against dose for the 102 pA trenches.

A selection of low magnification bright field images of the trenches milled using the 102 pA beam are shown in Figure 4.9. As with the trenches milled using the 12 pA beam (Figure 4.5 and 4.6) grain growth and preferential milling can be observed within the trenches, Figure 4.9.

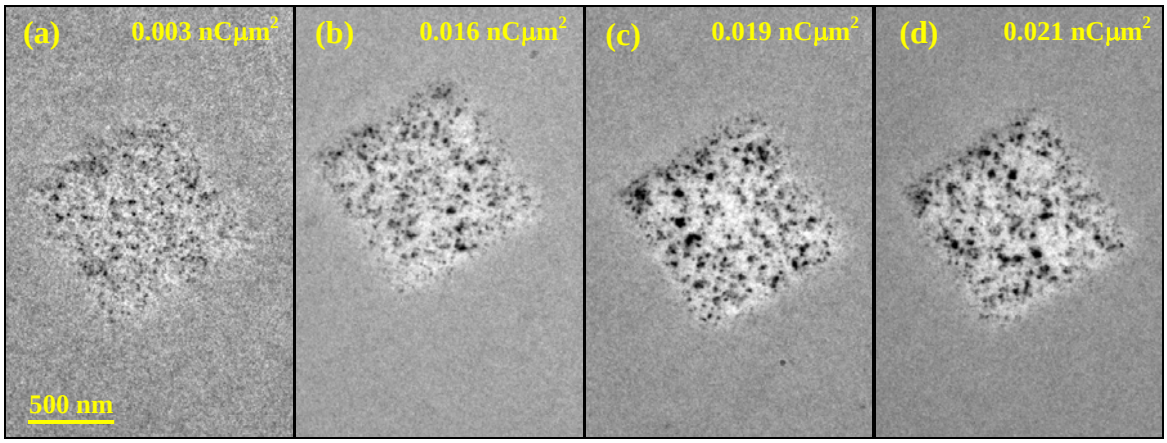

Figure 4.9: low magnification bright field images of 1×1μm^2 trenches milled out of 20 nm thick permalloy using various doses irradiated with a 102 pA beam current.

As with the 12 pA milled trenches, higher magnification bright field TEM image have been taken to obtain information on the grain structure within the trenches milled using the 102 pA beam current, Figure 4.10. For the lowest dose there appears to be a ~35% increase in the average grain size compared to the surrounding continuous film ((8.1 ± 1.0) nm compared to (6.0 ± 1.0) nm respectively). Here grain growth has taken place along with an increase in the height of the film due to contamination; this is probably due to the beam clearing contaminants while milling and grain growth continuing during this.

Again the magnitude of the grain growth increases with the received dose, shown in Figure 4.11, the relationship is similar to the trenches irradiated with the 12 pA beam current (red markers in Figure 4.11). A comparison of the grain size of the trenches irradiated with similar doses shows a similar increase for the different beam currents with dose. This indicates that the grain increase is dose dependent and not greatly related to the beam spot size, as would be expected.

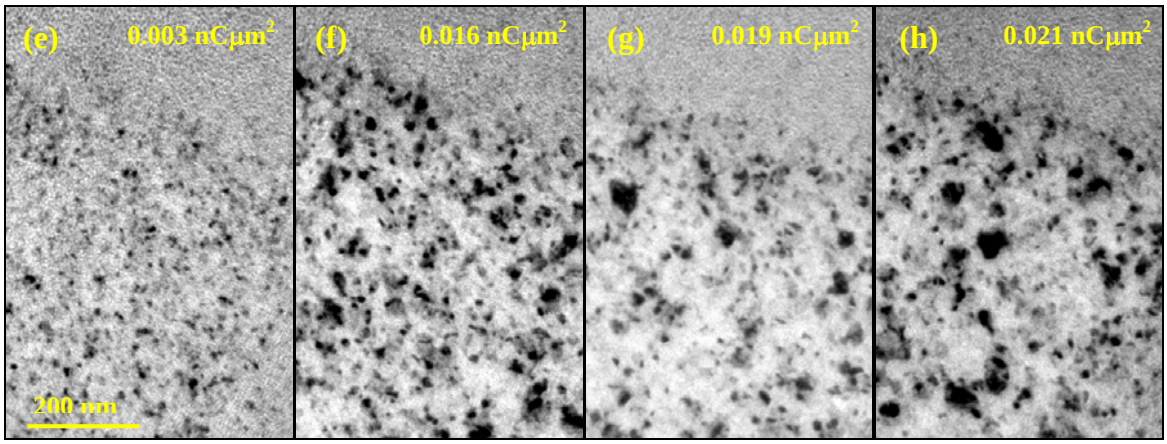

Figure 4.10: high magnification bright field images of 1×1 μm^2 trenches milled out of 20 nm thick permalloy with various doses, irradiated using a 102 pA beam current.

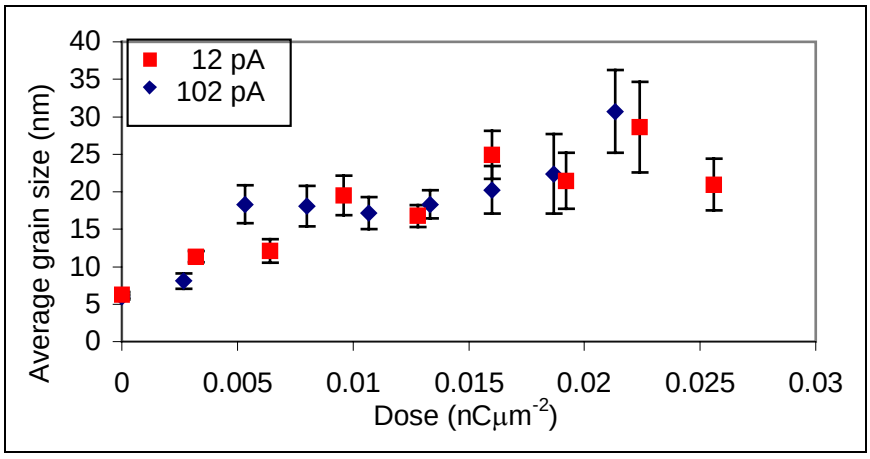

Figure 4.11: a plot of the average grain size against the Ga$^+$ dose in the trenches milled using a 100 pA beam current.

It can also be observed from the 102 pA milled trenches, in comparison to the 12 pA milled trenches, that the edge structure of the trench is diffused. An example of the edge structure in a 12 pA trench milled with a dose of 0.016 nCμm^{-2} is shown in Figure 4.12(a) and the edge structure in a 102 pA trench irradiated with the same dose is shown in Figure 4.12(b). From the images there appears to be a more diffuse boundary at the 102 pA irradiated trench (red to blue dotted line) in comparison to the 12 pA trench (red line). Also visible in the image is an apparent step in the boundary of the 102 pA trench (a kink

in the dotted lines in Figure 4.12(b)) compared to the straight line at the boundary of the 12 pA trench (red dotted line in Figure 4.12(a)).

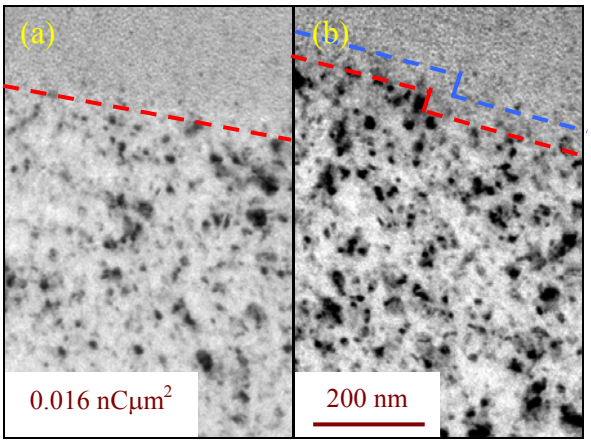

Figure 4.12: bright field image of the trench milled using (a) 12 pA and (b) 102 pA beam currents. Red and blue dotted lines indicate the approximate position of the boundary between the irradiated trench and the surrounding film.

In this thesis there has been no attempt made to model the grain growth mechanisms in the 1×1 μm^2 trenches. It is thought, however, that the grain growth arises from the heat imparted due to the change in the momentum of the Ga^+ as they interact with the sample. The imparted heat allows certain grain orientations to grow at the expense of others. The grain growth and milling of the permalloy film within the trenches increases with the dose, this, in turn, increases the overall roughness within the trenches. The clearing of the trenches also appears to be related to the beam current. There is better average clearing for the low beam currents (12 pA) compared to high beam currents (102 pA); this is due to the reduction in contaminants attracted to the surface by the smaller beam spot size.

4.3 Simulations of geometrically perfect permalloy elements

As a guide to the nature of the reversal of the elements discussed in chapter 5, OOMMF simulations have been performed and are presented in this section. The OOMMF simulation package can model remanent (static) states that are very similar to those observed experimentally. As has been observed by Kirk et al, [8], however, the event fields provided by the simulations are, in general, found to be higher than the experimental fields, this is discussed in greater detail later in this section.

4.3.1 Simulated states of the 1000×200 nm^2 permalloy element in zero field

Several states have been simulated for the 1000×200 nm^2 element using the initial conditions setting in the OOMMF programme and a selection are given in Figure 4.13. A table of the components of magnetisation and the energy density of each of the simulated states shown in Figure 4.13 is given in Table 4.1. The simulation has assumed the permalloy elements have an anisotropy constant (K_1, defined in section 1.2.2) of zero and therefore the anisotropy energy density is zero and as there is no applied field the Zeeman energy densities is also zero. In the table the exchange (e_{EX}), magnetostatic (e_D) and total (e_{TOT}) energy densities are given. Shown in Figures 4.13 (a) and (b) are the so-called C- and S-state respectively; these states, while essentially the same uniform state along the x-axis, have different total magnetisation vectors in the y-axis due to the orientations of the magnetic spins at the short edges of the element. As the magnetostatics of the C- and S-state are essentially the same, the elements have the same energy densities. The so-called flower state, shown in Figure 4.13(c), has an energy density slightly higher than that of the C- and S-state, as shown in Table 4.1. From Table 4.1 a slight increase in the total energy density can be observed due to an increase in both the exchange and magnetostatic energy densities. Although the flower state is similar to the C- and S- state in energy, this state is never observed in a real system due to the high symmetry of the perfect element necessary to support it (as assumed by the OOMMF simulation).

A state that has a higher energy density than the flower state is the four-vortex state (shown in Figure 4.13(d)). The four-vortex state is a flux closure state that, unlike the three previous states (Figure 4.13(a)-(c)), has no net in-plane component of magnetisation, although a very small out-of-plane component is observed due to the vortex cores. The twin vortex state shown in Figure 4.13(e) has a lower exchange energy density than the four vortex state, Figure 4.13(d). The increased demagnetisation energy associated with the increased length of 180^o domain walls, however, increases the total energy density above that of twin vortex state. This increase in the demagnetisation energy density raises the total energy density above that of the four-vortex state. For similar reasons, the single vortex state (four-domain, Figure 4.13(f)) has a higher total energy density still. Another state where the magnetisation is not circulating around the core is shown, this is known as a cross-tie state, Figure 4.13(g). Here the magnetisation is pointing in opposite directions at the vortex core, by adopting such a state there is a significant increase in the demagnetisation energy density and thus the overall energy of the system is increased as a result, as shown in Table 4.1. The end domains of the non-uniform structures can be used

to categorise the structures in a fashion similar to the C- and S-states for the near uniform states. For example, due to the parallel end domains, the four and twin vortex states can be classed as S-type and, due to the antiparallel end domains, the single vortex and cross-tie states can be classed as a C-type state.

Included to show a limitation of the software is a simulated element where the initial, field free, state has all the magnetic spins out-of-plane, Figure 4.13(h). The energy for this state is approximately twenty times any of the other states (~401 kJm^{-3}, as magnetostatic energy), as shown in Table 4.1. This state reflects the perfect symmetry of the element inputted to the OOMMF software.

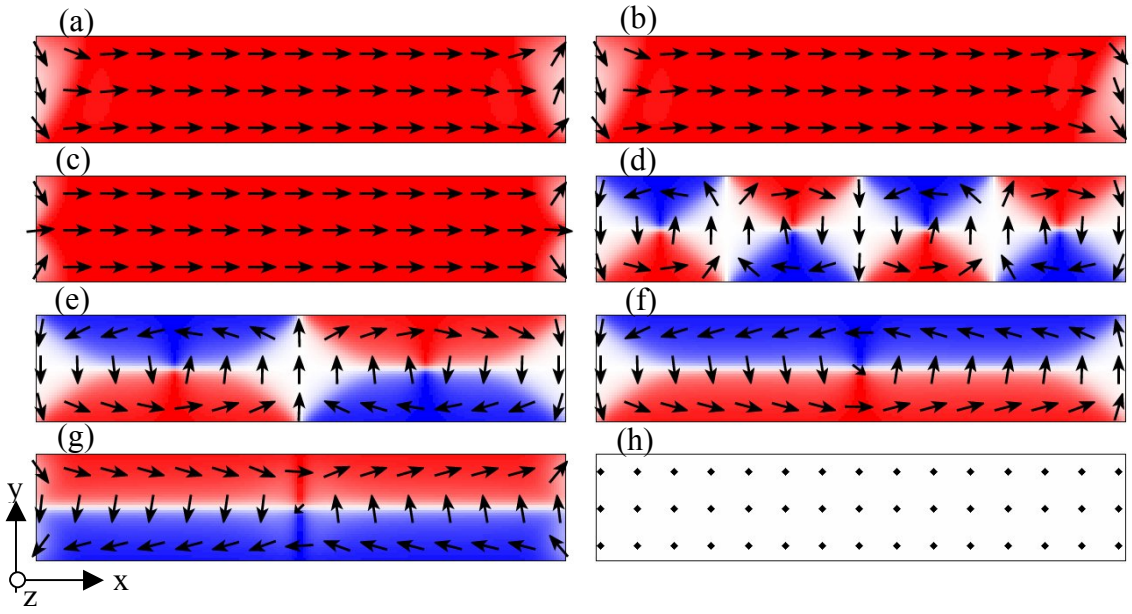

Figure 4.13: OOMMF simulations (with simulation defined coordinates shown) of different field free states for a 1000×200 nm^2 permalloy element. (a) is the C-state, (b) the S-state, (c) the flower state, (d) the four-vortex state, (e) the twin vortex state, (f) the single vortex state, (g) the cross-tie state and (h) the uniform in the z-axis state.

State	M_x/M_s	M_y/M_s	M_z/M_s	e_{EX} (kJ/m^3)	e_D (kJ/m^3)	e_{TOT} (kJ/m^3)
C-state	0.9594	0.0000	0.0000	0.63	7.25	7.88
S-state	0.9594	-0.0708	0.0000	0.63	7.25	7.88
Flower	0.0000	-0.0072	0.0000	0.66	7.84	8.50
Four vortices	-0.0001	0.0072	0.0019	7.20	7.26	14.46
Twin Vortex	0.0000	-0.0223	0.0020	6.40	9.10	15.50
Vortex	0.0000	0.0000	0.0010	6.15	11.46	17.61
Cross-tie	0.0000	0.0000	-0.0013	6.67	20.00	26.67
Uniform in z-axis	0.0000	0.0000	1.0000	0.00	401.02	401.02

Table 4.1: table detailing the components of magnetisation (M_X, M_y and M_Z), the exchange (e_{EX}), magnetostatic (e_D) and total (e_{TOT}) energy density for the states shown in Figure 4.13.

Several of the initial magnetics states for the 1000×200 nm^2 simulated element using the OOMMF micromagnetic simulation software have been discussed in this section. The C- and S-state states have been found to have the lowest total energy densities (and hence

energies) of the magnetic states simulated here and are assumed to be the ground states of this particular element. The simulations show that for the 1000×200 nm^2 element, flux closure structures have higher energies than the near uniform states and are, therefore, metastable states.

4.3.2 Simulated 1000×200 nm^2 permalloy cycled through magnetic fields

The OOMMF package has been used to simulate the response of the element in a magnetic field. A typical magnetisation cycle for a 1000×200 nm^2 permalloy element is shown in Figure 4.14 for a magnetic field with steps of 40 Oe. This size of step has been chosen as the magnetisation is not expected to vary a lot over this range and it should be adequate to highlight the important events. Upon the application of an ~80 Oe field along the easy axis (as shown in Figure 4.14), the magnetisation within the simulated elements shown in Figures 4.13(d)-(h) revert to a lower energy state that is effectively a C- or S-states, an example of this is shown in Figure 4.14. Initially the magnetisation is in a double vortex state (Figure 4.14(a)). As a magnetic field is applied along the easy axis the vortices are driven to the edges as the domains orientated along the direction of the field grow, Figure 4.14(b). At a higher field the vortices are driven out and the magnetisation reverts to an S-type state within the element, Figure 4.14(c). This state persists as the field is increased to 600 Oe, Figure 4.14(d) (a further increase in the field could drive the magnetisation into a flower type state). As the applied field is further reduced the end domains grow prior to reversal, Figure 4.14(e). The reversal of the magnetisation with the simulated element occurs after the applied field is reduced past remanence, Figure 4.14(f). This state persists as the applied field is increased, Figure 4.14(g). As the field is reduced to zero and then increased in the opposite direction the reversal of magnetisation occurs in a similar fashion to before, Figures 4.14(h)-(j). The hysteresis loop for this simulation, Figure 4.14(k), confirms the symmetry of the reversal of the element. The element has a simulated coercivity between 400 and 440 Oe. This is determined by the simulation step size.

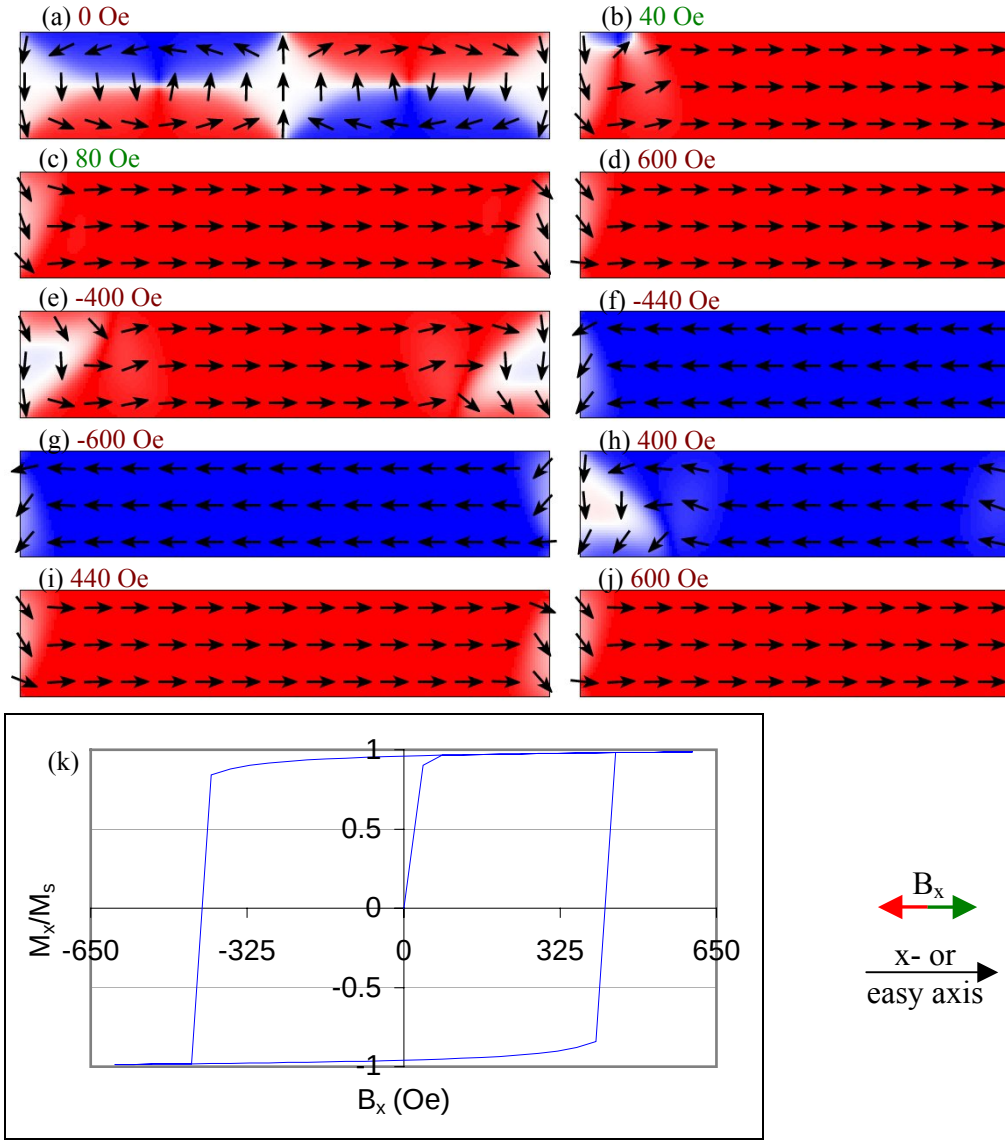

Figure 4.14: (a)-(j) the OOMMF simulation of vortex expulsion from a 1000×200 nm^2 permalloy element to an S-state and the subsequent reversal. (k) the simulated hysteresis loop.

A comparison of the hysteresis loops for the S- and C-states (Figure 4.14(k) and Figure 4.15, starting the cross-tie state (Figure 4.13(g)) shows that both loops have the same coercivity (between 400 and 440 Oe) and the same magnetisation behaviour after the magnetisation in the initial states has been destroyed. The only difference in hysteresis loops is the path taken to drive out the initial states. When the magnetisation is in either the C- or S-state, the magnetisation is inclined to remain in that orientation unless the field is increased and the magnetisation is driven into a flower state. The simulated 1000×200 nm^2 element show has the square hysteresis loop that has been predicted (section 1.5) for this element.

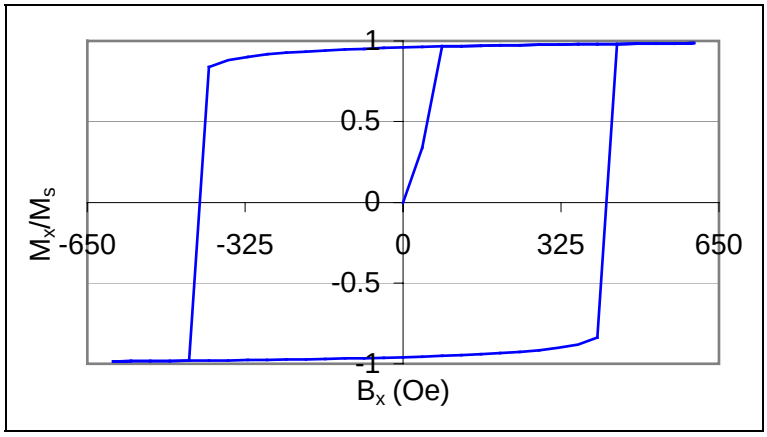

Figure 4.15: the simulated hysteresis loop for an element whose magnetisation is in a C-type state after the application of ~80 Oe to a cross-tie wall, Figure 4.13(g).

4.3.3 Simulated states of the 500×500 nm² permalloy element

OOMMF simulations have been performed for a 500×500 nm^2 element to investigate the remanent states and the behaviour of the element in an applied field. The simulations predict that the four-domain flux closure structure has the lowest energy, this is for an element allowed to relax with no constraints from numerous magnetisation orientations in zero field, as shown in Figures 4.16(a) and (b). The four-domain flux closure state can support both clockwise, Figure 4.16(a), and anticlockwise rotation, Figure 4.16(b). There is an equal probability of any particular isolated element adopting either sense of rotation as both magnetic configurations have identical magnetisation distributions and total energy densities (4.21 kJm^{-3}). Other magnetisation states were only observed when the simulated elements were cycled through an applied magnetic field large enough to driven out the vortex, for example the C-state shown in Figure 4.16(c). This C-state, Figure 4.16(c), has a total energy density of 16.1 kJm^{-3}, approximately four times the vortex state. This metastable state could be produced by the simulation because of the step size, the perfect symmetry of the element, the convergence parameter of $|\mathbf{M} \times \mathbf{H}|$ or a combination of the three.

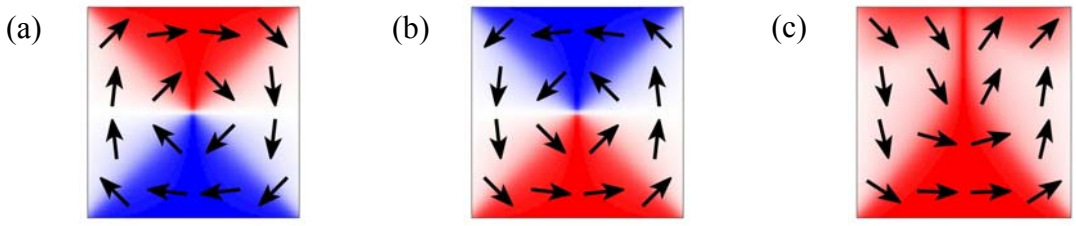

Figure 4.16: OOMMF simulations of the ground state of a 500×500 nm^2 permalloy element with (a) clockwise and (b) anticlockwise rotation. (c) is a C-state created after application of a field sufficiently large to drive out the vortex in (b) and then relaxed in zero field.

Upon the application of a magnetic field along the easy x-axis (as defined by the shape (section 1.5) shown in Figure 4.17) of the element (Figure 4.17(a)), the domain orientated along the field direction grows at the expense of the other three, this moves the vortex at the centre towards an edge, Figure 4.17(b). A similar event occurs of the field is applied in the y-axis (the orthogonal in-plane axis to the x-axis) with the vortex being driven into a perpendicular edge. The vortex is eventually driven out and a C-state is formed, Figure 4.17(c). This state persists as the field is increased to 600 Oe, Figure 4.17(d) (at a higher field of ~800 Oe the magnetisation can be forced to form a flower state). As the field is reduced the domains perpendicular to the field grow and the C-state is maintained through remanence, Figure 4.17(e). The remanent C-state has a total energy density of 12.8 kJm^{-3} and has 60.53% of the magnetisation along the x-axis. The magnetisation within the element almost forms a flux closure state just prior to the reversal of C-state (Figure 6.17(f)) to the mirror C-state, Figure 4.17(g). This C-state persists as the field is increased to –600 Oe, Figure 4.17(h), and as the field is decreased to zero and then increased in the opposite direction switching between C-states is observed again.

The hysteresis loop, Figure 4.17(i), shows the element starting in a state with zero net magnetisation in the direction of the applied field and then transforming into a state where a large fraction of the magnetisation is aligned with the direction of the applied field. As the field is reduced and reversed the magnetisation almost reforms the original flux closure structure before reversing, Figure 4.17(f). The same is true as the field is reversed in the opposite direction with magnetisation distribution along the field direction being mirrored. This switching behaviour is not observed experimentally for isolated elements (as discussed in section 5.2.2). A reason for such behaviour could be due to the energy difference between the C- and vortex state being too large for the simulated element with these dimensions to overcome. Other reasons could include the large field step size, the convergence value of the $|\mathbf{M} \times \mathbf{H}|$ could be too large, the cell size could be too large and the perfect structure input to the OOMMF simulation.

The simulation of the 500×500 nm^2 permalloy element highlights the care that should be taken when processing simulations. The predicted experimental behaviour for an element of this type is discussed in section 1.5. The element is expected to reform the four-domain flux closure state before remanence (such that the net magnetisation is zero), which does not happen in the simulation.

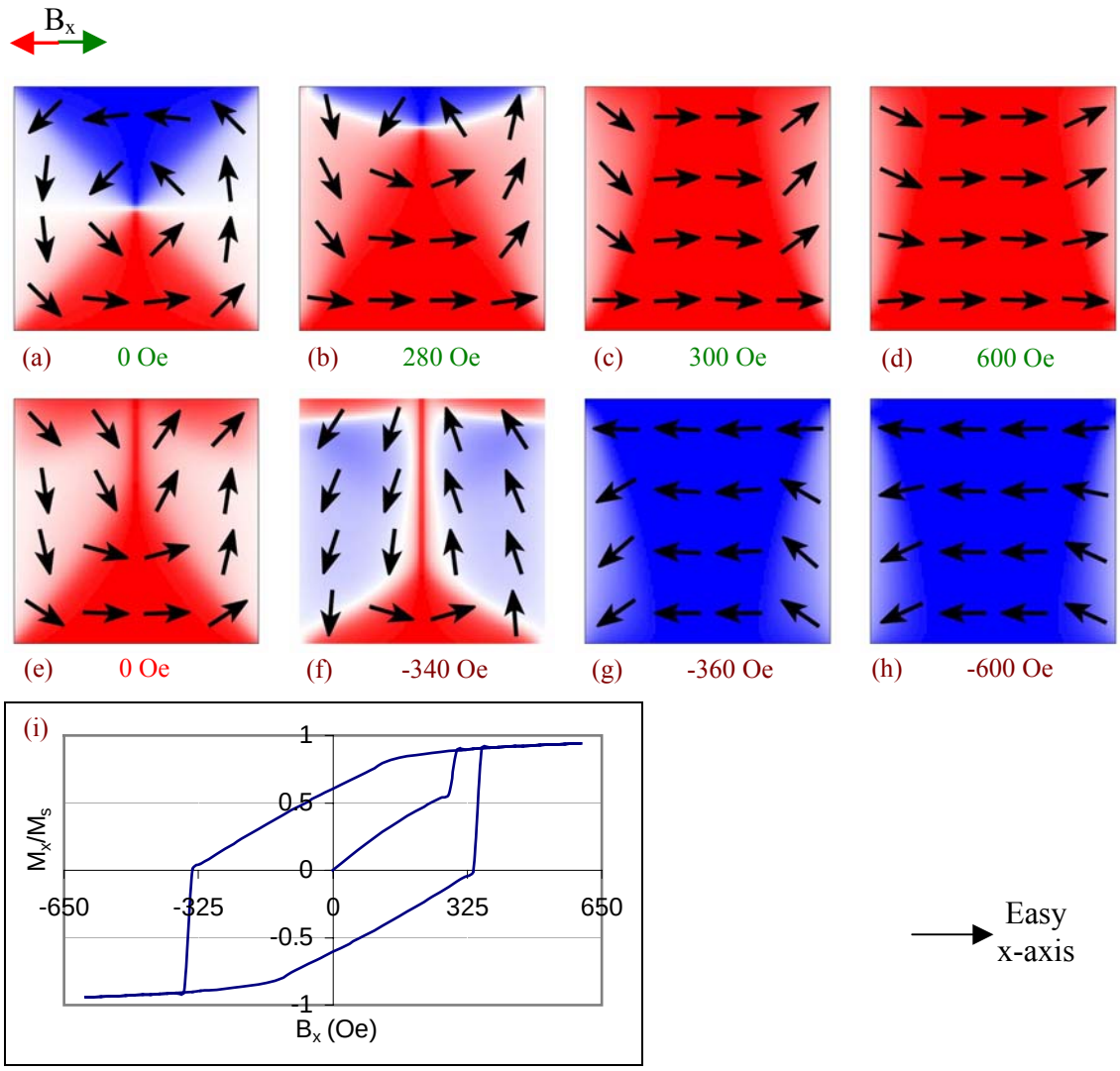

Figure 4.17: (a)-(j) the OOMMF simulation the magnetisation distribution within a 500×500 nm^2 permalloy element as the element is cycled through a magnetic field. (k) the simulated hysteresis loop.

4.4 Simulations of 500×500 nm^2 permalloy elements with irregular edges

In an attempt to create a simulation that may better resemble the experimental results of the 500×500 nm^2 permalloy element, templates that have had their symmetry broken were input into the OOMMF programme. The symmetry was broken in the elements by two processes: the first was pixelation caused by rotation within a computer programme, the second was by manually altering the symmetry by deletion and addition of pixels.

4.4.1 Masks input to OOMMF simulation package

To break the symmetry of the simulated element and in an attempt to make a more real element (such as those fabricated by electron beam lithography (EBL) and FIB lithography), templates were constructed for the 500×500 nm^2 permalloy element. Two masks have been created through pixelation using a computer programme. The pixelation occurs when the perfect square has been rotated through a) 45^o (mask C1) and b) 22.5^o (mask C2) and then rotated back to zero. By doing this, the image becomes pixelated due to a bug in the programme. The computer programme used to break the symmetry in this fashion was Paint Shop Pro version 6.02 manufactured by Jasc Software. Two other templates were constructed: one where one pixel had been manually added/removed along the edges of the mask (mask M1) and another where up to five pixels had been added/removed from the edges (mask M2). The images in Figure 4.18 are of the four different mask types: (a) is C1, (b) is C2, (c) is M1 and (d) is M2. As there have been pixels added and removed from the elements there is a slight increase in the volume of the elements. As the values of the magnetisation components and total energy are given in relative terms, however, a like for like comparison can be made.

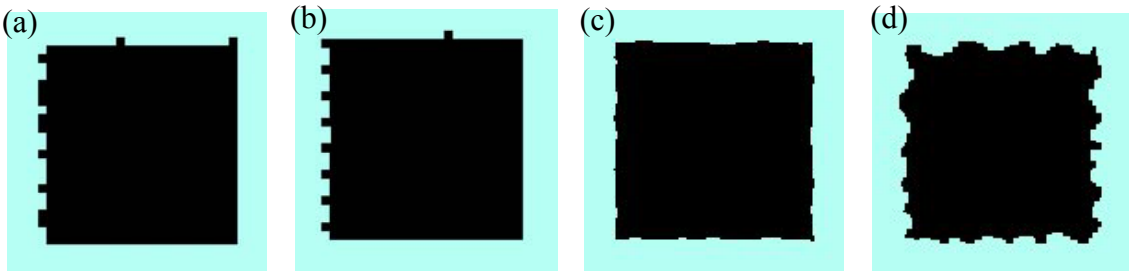

Figure 4.18: the input masks for simulations that have had their symmetry broken, black is the magnetic section and blue the non-magnetic. (a) is mask C1, (b) is mask C2, (c) is mask M1 and (d) is mask M2 where descriptions of C and M are given in the text.

The initial states modelled by the OOMMF simulation package for all the masks predicts a four-domain flux closure structure for the simulation as the element is allowed to relax from a random orientation, as shown in Figure 4.19. Aside from localised rotation at the edge of the simulated element and the C2 mask adopting a clockwise rotation, there are few differences in the remanent states.

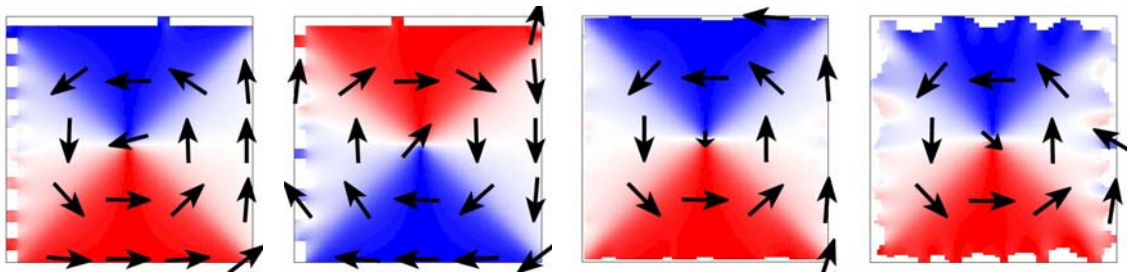

Figure 4.19: the initial states for masks (a) C1, (b) C2, (c) M1 and (d) M2 in a remanent field.

As a simulated field is applied along the x-axis (in-plane left to right), the vortices are driven into an edge parallel to the field and the magnetisation within the element forms a C-state. The magnitude at which the vortex is driven out varies for each mask and is shown in Figure 4.20. From the plot in Figure 4.20 it can be observed that the exit fields for the vortices within the two computer generated masks (C1 and C2) are lower than the perfect element; which in turn is lower than the two manually generated elements (M1 and M2).

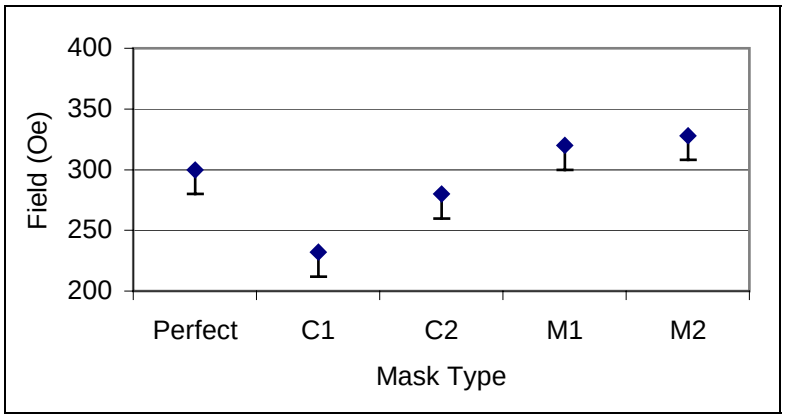

Figure 4.20: plot of simulated vortex annihilation field for the 500×500 nm^2 permalloy element against mask type, including the ideal element. Uncertainty is -20 Oe (the field step).

After the field is increased to 600 Oe and then decreased to zero, the simulated elements do not reform the vortices (as shown in Figure 4.21), which is similar to the perfect element. The computer generated masks, C1 and C2, form S-states (Figures 4.21(a) and (b)) and the manually generated masks, M1 and M2, form C-states (Figures 4.21(c) and (d)). With M2 the left side-wall is pinned along the left edge and not in the corner. The pixelated edge almost certainly causes increased magnetostatic energy and may result in reorientation of the domains, forcing the magnetisation of the C1 and C2 elements into an S-state.

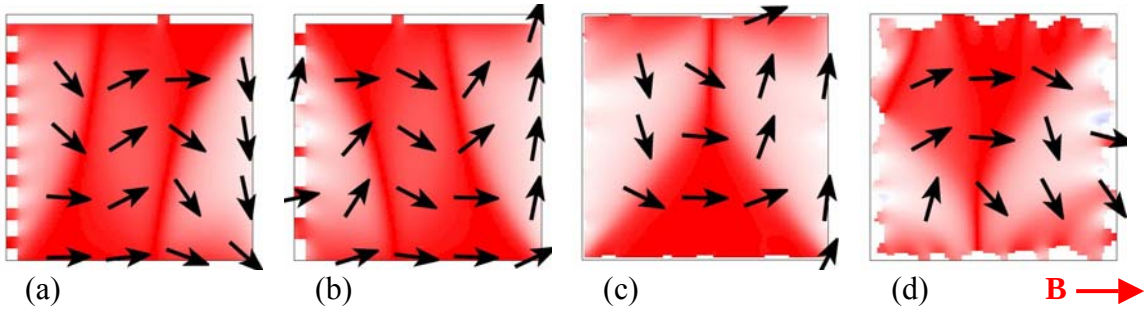

Figure 4.21: the remanent state of the (a) C1, (b) C2, (c) M1 and (d) M2 after the application of a 600 Oe magnetic field in the direction shown.

The total energy densities of the elements for the initial remanent state, after the application of a forward field and after the application of a reverse field are shown in Table 4.2. From the table of the total energy densities, Table 4.2, an increase in the total energy densities for the remanent states after the application of a field can be observed. The lowest and highest increases in the energy densities are for M1 (~195%) and M2 (~274%) respectively. Although there is such a large difference in the total energy densities between the vortex and the C-states the energy for the formation of a vortex is obviously too great for the OOMMF simulation to overcome for these step sizes (40 Oe) for permalloy elements with dimensions of 500×500 nm^2.

Mask	Total energy density (kJm^{-3})		
	Initial remanent state	After forward 600 Oe field	After reverse 600 Oe field
C1	6.35	14.93 (~235%)	14.93 (0%)
C2	6.23	14.76 (~237 %)	14.76 (0%)
M1	4.82	13.19 (~274 %)	13.16 (0%)
M2	9.10	17.77 (~195 %)	17.77 (0%)

Table 4.2: total energy densities of the remanent states for masks (a) C1, (b) C2, (c) M1 and (d) M2 in the initial remanent field and after a field of ± 600 Oe has been applied. The value in brackets shows the percentage difference from the previous value.

4.5 Conclusions

The basis of this chapter is to establish the conditions for the fabrication of 1000×200 and 500×500 nm^2 permalloy elements that have been milled out of 20 nm thick permalloy film (on a 50 nm thick silicon nitride substrate) by FIB lithography. To establish the effects of the beam on such a film, trenches with an area of 1×1 μm^2 were milled into the film using varying doses and beam currents and then imaged using the AFM and TEM microscopes. The varying beam current produces trenches that increase in depth as the dose is increased. The edge profiles of such trenches are not a discontinuous step but have a slope between 250 and 500 nm associated with them instead. It is thought this gradient is related to the beam profile that is Gaussian in nature.

Non-uniform milling has been observed within the trenches, especially at higher doses, the non-uniform milling is evidence of preferential milling of certain grain orientations. Also observed within the trenches was grain growth of the permalloy crystallites. The grain size increases with dose reaching a plateau at higher doses. When the dose is corrected to account for the milling of the aperture the grain growth for the 12 and 102 pA beam currents (from 10 and 100 pA) are observed to be similar. There is, also, a variation in the spread of grain sizes as the dose is increased. The variation in the spread of sizes is again linked to the preferential milling mentioned previously. The increase in the total dose of the tails of the Ga^+ beam are observed as the beam current is increased form 12 to 102 pA. From the initial results of the gallium milling of permalloy thin film, it has been decided to fabricate both the 1000×200 and 500×500 nm^2 elements using a nominal dose range of 0.03–0.11 $nC\mu m^{-2}$ and to use the nominally sized 10 pA beam current. The results are to be presented in chapter 5.

OOMMF simulations have been used to simulate possible initial configurations of the magnetisation within the elements and how they behave as a magnetic field is applied along the easy axis. Several possible states were modelled for the perfect element 1000×200 nm^2, the two lowest identical energy states were the C- and S-state. The other simulated states collapsed to either the C- or S-type state after a field was applied along the easy axis, dependent on the orientation of the end domains. The simulated coercivity of the perfect element 1000×200 nm^2 permalloy element is between 400 Oe and 440 Oe and the simulated hysteresis loop was the square type predicted for this element.

The magnetic ground state of the 500×500 nm^2 permalloy element was simulated to be the four-domain flux closure state that is observed experimentally. As a magnetic field is applied to this state the vortex moves to the edge of the element, as happens experimentally although the expulsion occurs at a higher field. As the field is reduced, however, the vortex does not reform, as expected from experiments, instead the element reverses in a manner similar to that of the 1000×200 nm^2 element. The high symmetry of the element input to OOMMF and step sizes appear to be the cause for the vortex not reforming, another being the large energy barrier created by the exchange energy within the near uniform system. To combat this, elements with their symmetry broken were simulated. The magnitude of the vortex expulsion field of the roughened elements fluctuates with respect to the ideal element field. It is found that the roughened elements do not reform the vortex state either; instead they form either a C- or S-type state. A comparison of the energies shows that the C- and S-type states are over two times larger than the vortex state. There are several reason why the vortex does not reform in the system: i) the vortex

formation energy barrier is too great for the OOMMF simulation to overcome for the 500×500 nm^2 permalloy elements, ii) the field step size could be too large to allow the reformation of the vortex, iii) the convergence value of the $|\mathbf{M} \times \mathbf{H}|$ could be too large and therefore allowing the metastable C-state to exist, iv) the cell size could be too large or v) a mixture of the previous four.

The OOMMF simulations illustrate the topic discussed in section 1.5 about the shape anisotropy influencing of the element. The simulations highlight the difference between the two chosen shape of permalloy, the 1000×200 nm^2 element has the near uniform ground state and the 500x500 nm^2 element has the flux closure structure. Both structures behave differently in an applied field (as discussed in section 1.5).

Bibliography

[1] OOMMF simulation package available for download at NIST (URL active 16/02/06): http://math.nist.gov/oommf/

[2] Aperture spot sizes from FEI technical manual on operation of FIB microscope PN 20486-B.

[3] McGill R.A., Vizir A., Brown I.G., Rev. of Sci. Inst. 71(2) (2000) 672.

[4] SRIM programme available for download at: http://www.srim.org/ (active as of 27th Mar. 2007).

[5] Williams D.B., Carter C.B., *"Transmission electron microscopy"*, Plenum Press 1996, ISBN 030645324X.

[6] Moore K.T, Howe J.M., Csontos A.A., Ultramicroscopy 76(4) (1999) 195.

[7] Private communicate with X. Kong.

[8] Kirk K.J., Scheinfein M.R., Chapman J.N., McVitie S., Gillies M.F., Ward B.R., Tennant J.G., J Phys D: Appl. Phys 34 (2001) 160.

5 The characterisation of nanoscale elements fabricated by electron beam lithography and focussed ion beam milling

In this chapter the results for 20 nm thick permalloy ($Ni_{80}Fe_{20}$) elements with dimensions 1000×200 and 500×500 nm^2 that have been fabricated by both electron beam lithography (EBL) and focussed ion beam (FIB) lithography are discussed. Small-scale structures (< 10 μm in length) are conventionally fabricated by EBL, structures such as T and Γ gates for field effect transistors [1], 23 nm period gratings [2], 3 nm wide NiCr wires [3] and ferromagnetic elements of various dimensions [4, 5 and 6]. EBL has been chosen as it is a well established technique and permalloy elements have been fabricated by EBL for comparison to those fabricated by FIB lithography using 30 keV Ga^+. Some of the physical and magnetic characteristics of the EBL fabricated permalloy elements are discussed in this chapter.

The EBL elements were fabricated by the technique described in section 2.2 and the FIB milled elements were fabricated by the technique described in section 2.3. The EBL elements were deposited on a ~50 nm thick, electron transparent, SiN substrate. Whereas the elements fabricated by FIB milling have been deposited on both 50 nm thick SiN and 50 nm thick SiN with a 4 nm Cu buffer layer deposited on top. The addition of the 4 nm copper layer is hoped to act as a buffer layer between the relatively hard permalloy and soft amorphous SiN layer during milling and avoid charging problems associated with the insulating SiN. The metal layers were deposited by thermal evaporation (as described in section 2.1.2) and in the same vacuum, when possible, for both fabrication

techniques. The physical and magnetic structures of both sets of elements have been characterised by atomic force microscopy (using the AFM discussed in section 3.4), bright field, Fresnel and differential phase contrast (DPC) imaging, as described in sections 3.2 and 3.3.

5.1 The physical characterisation of the nanoscale sized permalloy elements

The physical structure of the elements has been analysed by bright field imaging. Examples of the elements fabricated by EBL are shown in Figure 5.1. The image in Figure 5.1 (a) is a 1000×200 nm^2 permalloy element and in Figure 5.1(b) is a 500×500 nm^2 permalloy element. Both elements are 20 nm thick. The most noticeable feature of the EBL fabricated elements is the rounded corners in both the 1000×200 and 500×500 nm^2 structures. This feature is common in structures fabricated by EBL (as can be observed in [5, 7]). A measure of the radius of curvature for the corners of the EBL fabricated elements reveals a radius between 20 and 25 nm for the elements, this is approximately ¼ to ⅓ the beam spot size used for writing (~80 nm). This is consistent with the raster scanning technique of the writing process. Grain structure is visible within the elements (with the average grain size being (8 ± 1) nm), which is of the order of the edge roughness.

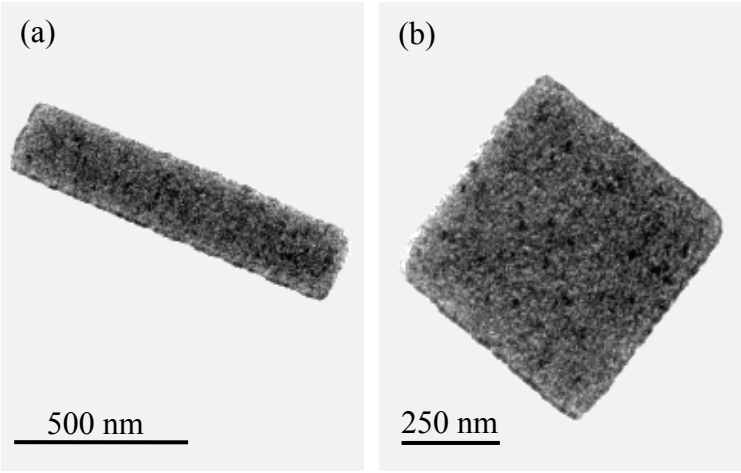

Figure 5.1: bright field images of 20 nm thick permalloy elements with dimensions of (a) 1000×200 and (b) 500×500 nm^2.

The clearing of the FIB lithographed trenches for the 1000×200 and the 500×500 nm^2 permalloy elements at the same doses are very similar, hence only the 500×500 nm^2 elements need be shown at lower magnifications. Examples of low magnification bright field TEM images of the 500×500 nm^2 permalloy element fabricated on both samples with varying doses (with a 12 pA beam current) are shown in Figure 5.2. From the bright field

images it can be observed that the quality of clearing of the remaining film within the trenches surrounding the elements decreases with dose, as would be expected. In the bright field TEM images there appears to be areas of lighter and darker contrast in the trenches surrounding the same element. The differing contrast levels can be attributed to differences in milling depths (to be discussed later in this section), which in turn can be attributed to non-uniform milling. The non-uniform milling can be attributed to preferential milling of certain grain orientations within the polycrystalline film [8]. Although there are islands of materials in the trenches it is thought that the large doses with which they have been irradiated have destroyed the magnetic properties of the material, with the exception of the lower dose elements [9]. Irregular edge structure can also be observed in the images, although the quality of the edge structure of the elements with a copper buffer layer appears more regular than those milled on the permalloy-only film. In the lower dose images (0.08 and 0.04 nCμm^{-2} are shown in Figure 5.2(d) and (e)), remnants of the permalloy (or permalloy on copper) film are clearly visible in the milled trenches surrounding these elements. The grain sizes within the elements of the permalloy on copper sample does not appear to be as greatly affected as that of the elements fabricated from the permalloy-only film, although higher magnification images are necessary to obtain a quantitative values. This is done later in this section.

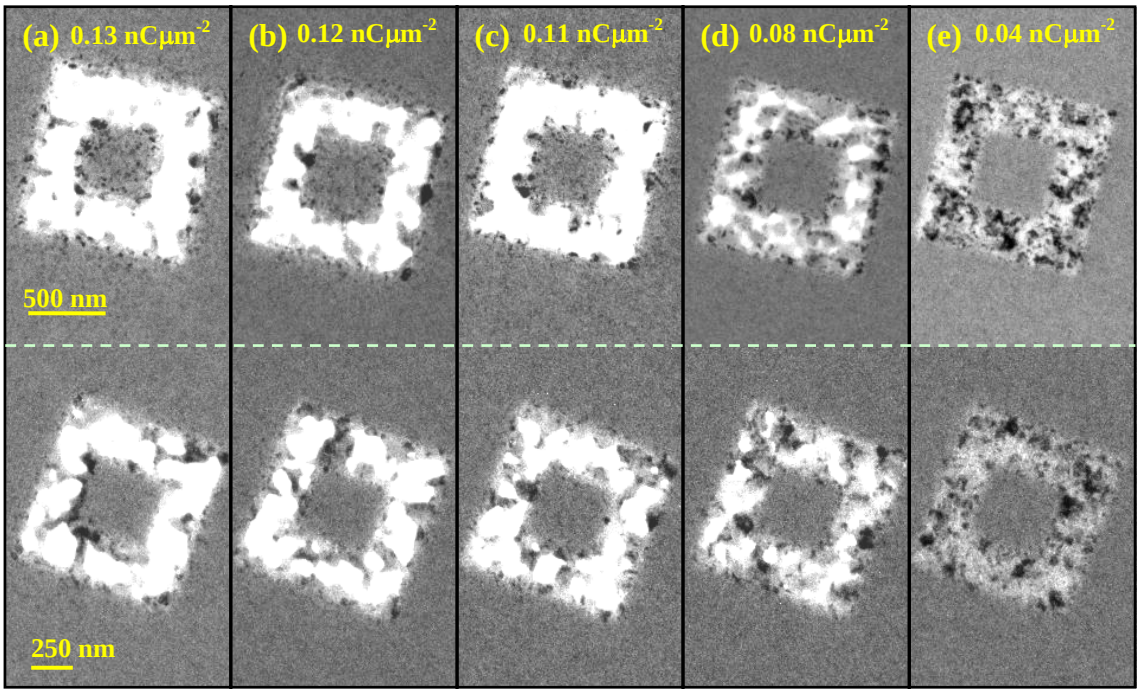

Figure 5.2: low magnification images of 500×500 nm^2 permalloy-only (top) and permalloy on copper (bottom) elements milled using varying doses (indicated).

Higher magnification bright field TEM images of the 1000×200 nm^2 elements are shown in Figures 5.3.4. These images show areas of preferential milling in greater detail. Islands

of permalloy are visible in the trenches surrounding the elements fabricated by higher doses (Figure 5.3(a)-(c)). The amount of material milled from the trenches visibly decreases with dose, as expected. Visible in the second highest dose (Figure 5.3(b)) is complete milling of the SiN substrate (a hole in trench), as indicated by the blue dotted circle. In the higher magnification images, a difference in edge structure of the 1000×200 nm^2 permalloy elements can be observed. In the lowest dose element (Figure 5.3(e)) the edge roughness is comparable to the grain structure, where as at the higher dose an edge roughness of ~50 nm can be observed.

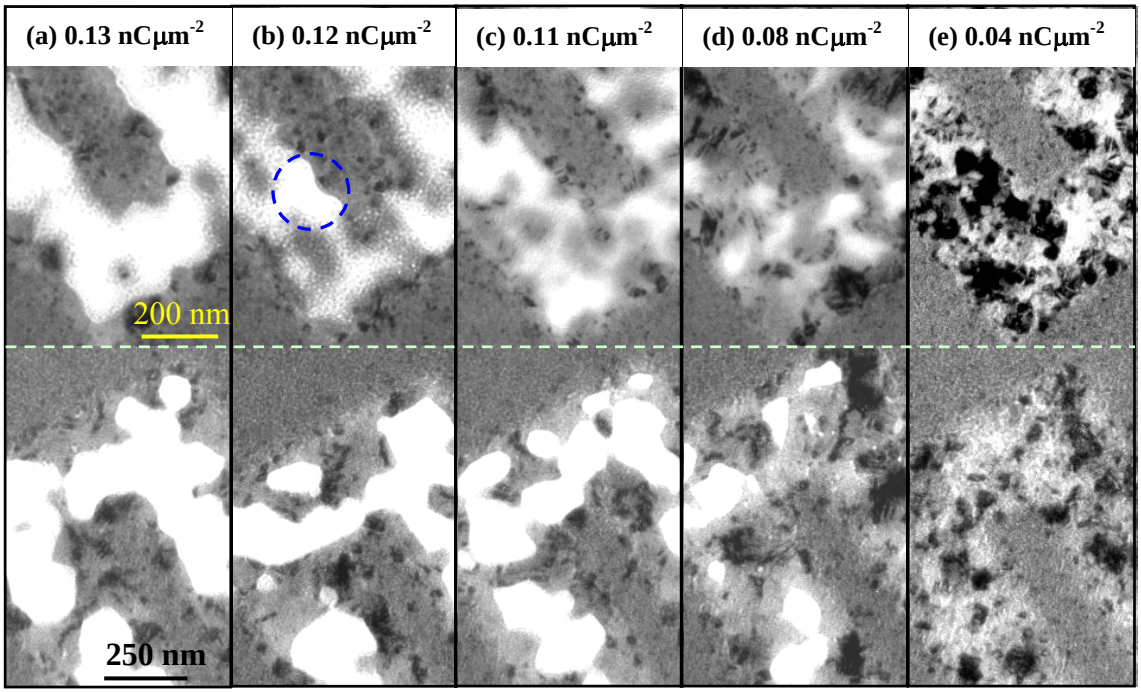

Figure 5.3: (a)-(e) high magnification bright field images of 1000×200 nm^2 permalloy (top) and permalloy on copper (bottom) elements fabricated by FIB milling (doses are indicated in the images).

By focusing on, first the permalloy-only and then the permalloy on copper 500×500 nm^2 elements, the effects of the beam on the grain size can be observed over a larger distance into the element. For the elements fabricated from the permalloy-only thin film (upper images in Figure 5.4), there is an unexpected increase in the average grain size (grains averaged over 15 samples, plotted in Figure 5.5) within the element, especially those fabricated with the two highest doses (Figures 5.4(a) and (b)). The majority of grains appear to be equiaxial in nature. An increase of ~25 nm (compared to the as deposited grain size (8 ± 1) nm) has been measured. For lower doses (0.11 and 0.08 $nC\mu m^{-2}$, Figure 5.4 (c) and (d)) the increase in grain size does not penetrate into the centre of the elements and is confined mainly to the edge (up to ~100 nm in from the edge). The increase at the edge of the element in the grain size is again ~25 nm. The unexpected grain growth within

the elements is most probably due to the tails in the beam profile and the energy imparted by the 30 keV Ga^+ beam interacting with the continuous film and the subsequent creation of the secondary events (modelled by the TRIM simulations in sections 2.3.3.1 and 2.3.4.1). There is no visible sign of an increase in grain size within the 0.04 nCμm^{-2} permalloy element.

Similarly to the 1000×200 nm^2 elements, the edge roughness of the 500×500 nm^2 elements increases with dose from roughness comparable to the grain size (0.04 nCμm^{-2}) to an edge roughness of ~50 nm (0.13 nCμm^{-2}). As with the 1000×200 nm^2 elements, the edge roughness of the 500×500 nm^2 elements could be a result of the Ga^+ beam profile and grain growth due to the imparted energy.

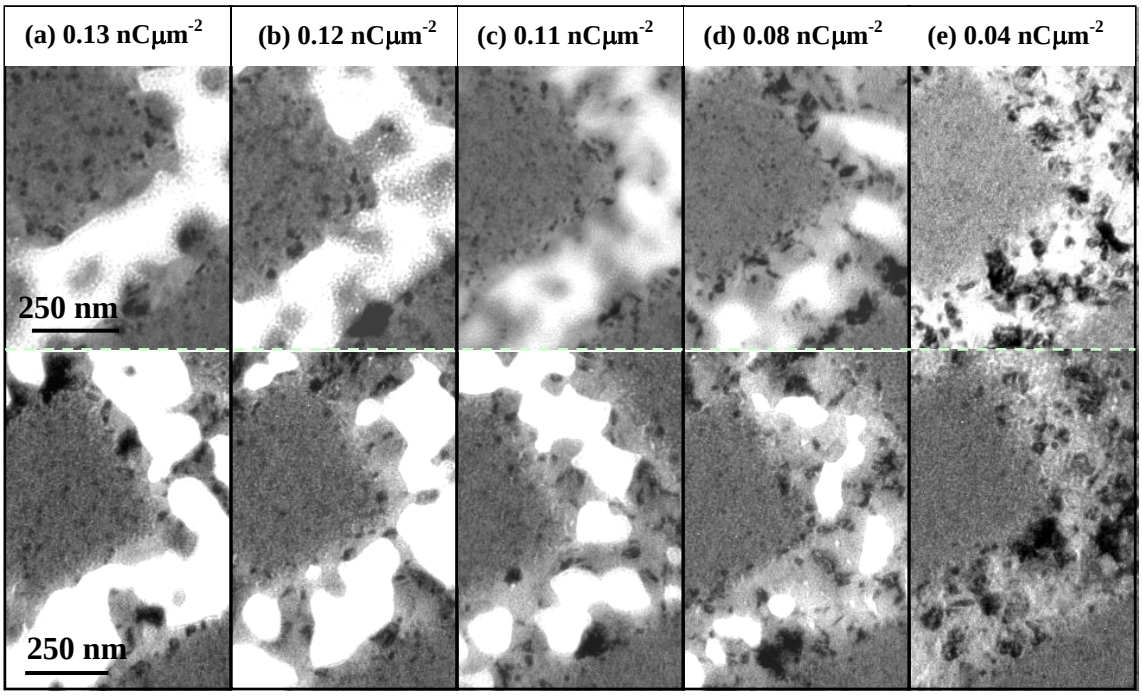

Figure 5.4: (a)-(e) high magnification bright field images of 500×500 nm^2 permalloy (top) and permalloy on copper (bottom) elements fabricated by FIB milling (the doses are indicated in the images).

From the higher magnification images obtained of the permalloy elements on copper and surrounding area (lower images in Figure 5.4), islands of remaining material (the composition of the material (it could be Cu, Cu/Ni/Fe alloy or permalloy/Cu for example) has not been determined) can be observed within the trenches for the higher doses. Due to the addition of the 4 nm copper layer, the clearing within the trenches is not as comprehensive as the permalloy-only elements. The preferential milling of grains unfortunately results in both the permalloy and copper being left in the trenches, as shown later by the AFM images in this section. The copper layer has acted to disperse some of

the energy associated with the beam; this is evident from the reduction in the grain growth within the elements. Grain growth is observed at the edge of the permalloy on copper elements (Figure 5.5(a)) and not at the centre (Figure 5.5(b)) as with the permalloy-only element. From the plot of the average grain size at the edge against dose (Figure 5.5(a)) the grain size for the irradiated trenches and elements appears to fluctuate around ~35 nm for the permalloy on copper sample, this is approximately three and a half times the as deposited value of ~10 nm.

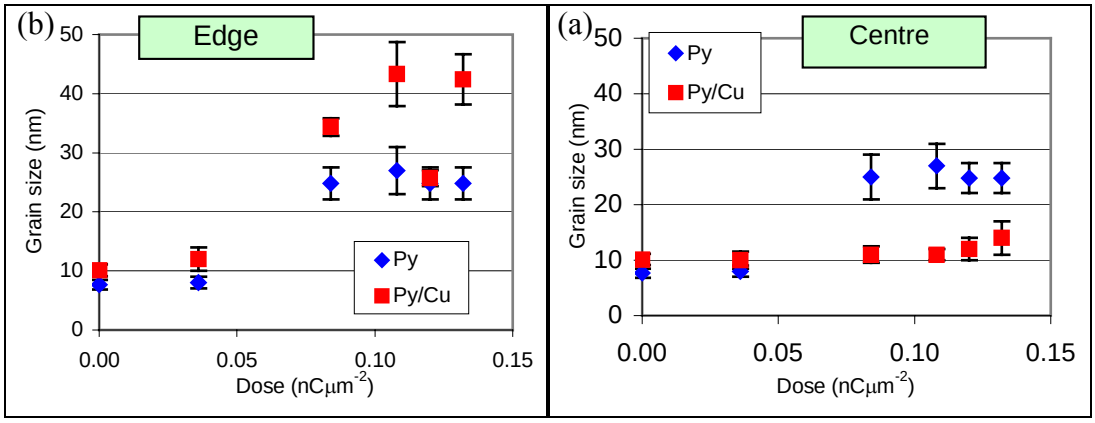

Figure 5.5: plot of average grain size against dose at the (a) the centre and (b) the edge of the element for both permalloy and permalloy/copper 500×500 nm^2 elements fabricated by FIB lithography. Shown is the average as deposited (zero dose) grain size.

After the elements fabricated by FIB lithography had been imaged by bright field TEM imaging, the surface profiles were measured by AFM profiling (the DI3100 AFM described in section 3.4). Shown in Figures 5.6(a) and (b) are example AFM images of the 500×500 nm^2 elements fabricated out of the permalloy-only sample milled using a low dose (0.04 nCμm^{-2}) and a high dose (0.12 nCμm^{-2}). Shown in Figures 5.6(c) and (d) are similar AFM images of 1000×200 nm^2 elements fabricated from the permalloy with copper buffer layer for the same doses. In the AFM images (the elements are ringed by white boxes) the non-uniform, preferential milling in the trenches (observed in the bright field images) can again be observed. The preferential milling is more pronounced in the Figures 5.6(b) and (d) and the edge of the element is more irregular than that of the lower doses, Figures 5.6(a) and (c). From the change in the visible contrast levels there appears to be little difference in the overall depth of the elements fabricated using the same doses. The islands in the trench show little difference in contrast (and hence depth) to that of the element and the surrounding trench. The white lines are scan artefacts most probably due to hysteresis in the piezoelectric stack.

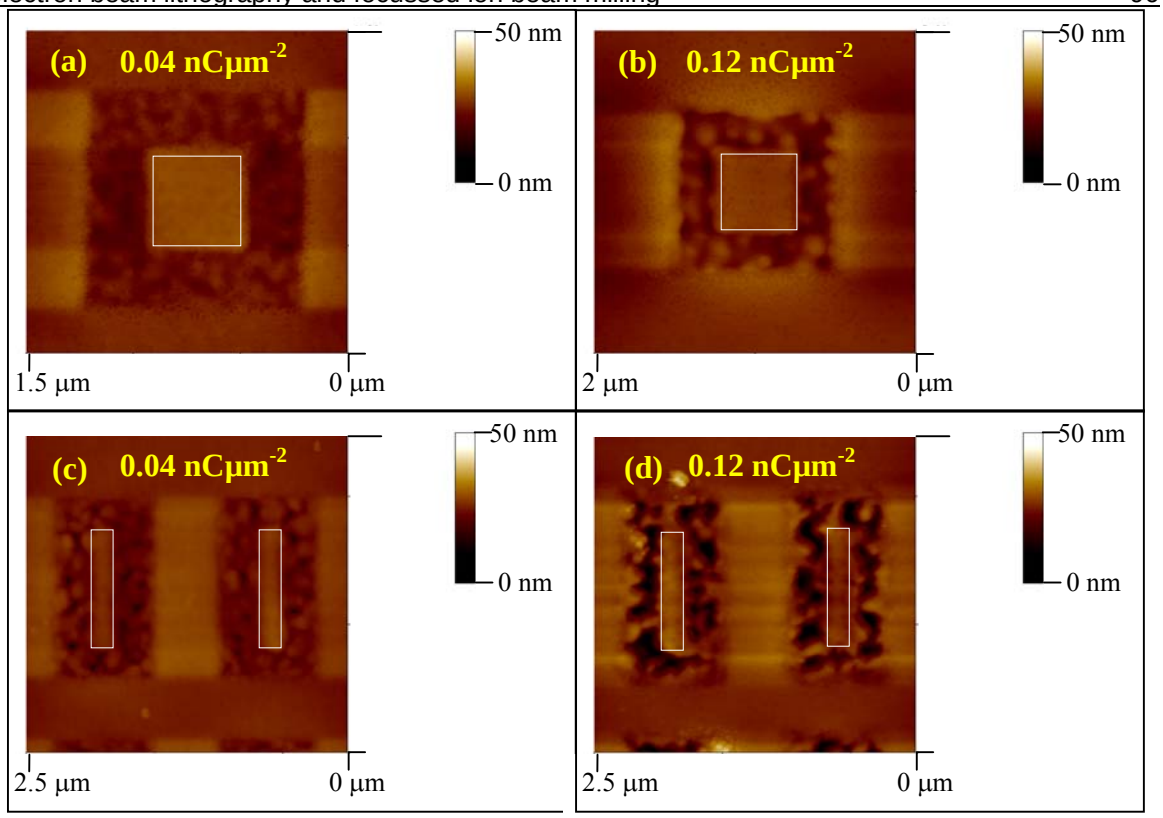

Figure 5.6: AFM images of 500×500 nm^2 permalloy-only element (white box) ((a) and (b)) and 1000×200 nm^2 permalloy on Cu elements (white boxes) ((c) and (d)) milled with various doses (indicated). The permalloy layer is 20 nm thick and the copper layer is 4 nm thick, supported on a 50 nm thick SiN substrate.

From the surface profiles of the elements fabricated by FIB lithography using varying doses, a more accurate sputter rate (with respect to the conditions used to fabricate these elements on these substrates) can be determined for both FIB lithographed samples, with the results presented in Figure 5.7. From the plot in Figure 5.7 it is evident that there are two sputter rates corresponding to the different layers milled through for both samples. In the low dose region (i.e. up to the 0.08 nCμm^{-2}) where the material milled is mainly permalloy the sputter rate is calculated to be (0.15 ± 0.05) μm^{3}nC^{-1} for both samples. The value of the sputter rate for $Ni_{80}Fe_{20}$ calculated here is similar to that quoted by Park and Bain (0.1 μm^{3}nC^{-1}) [10]. This was for 560 nm thick permalloy deposited on a Al_2O_3-TiC substrate of unspecified thickness. The sputter rate is lower than that calculated of the irradiated trenches in sections 4.1 and 4.2 (~0.43 μm^{3}nC^{-1}). The difference could be the different dose regions. In sections 4.1 and 4.2 the dose region was just above the threshold for milling and lower than the range of doses discussed here, Ga^+ is implanted and little permalloy is milled. In the higher dose regions, the sputter rates differ slightly. For the permalloy on silicon nitride sample the sputter rate has been calculated to be (0.41 ± 0.05) μm^{3}nC^{-1} (for milled depths >20 nm, when silicon nitride only is being milled) and for the permalloy on copper and silicon nitride (again after the permalloy has been milled

away) the sputter rate has been calculated to be slightly higher at (0.42 ± 0.05) $\mu m^3 nC^{-1}$. The slight difference in the sputter rates is most probably due to the thin copper layer.

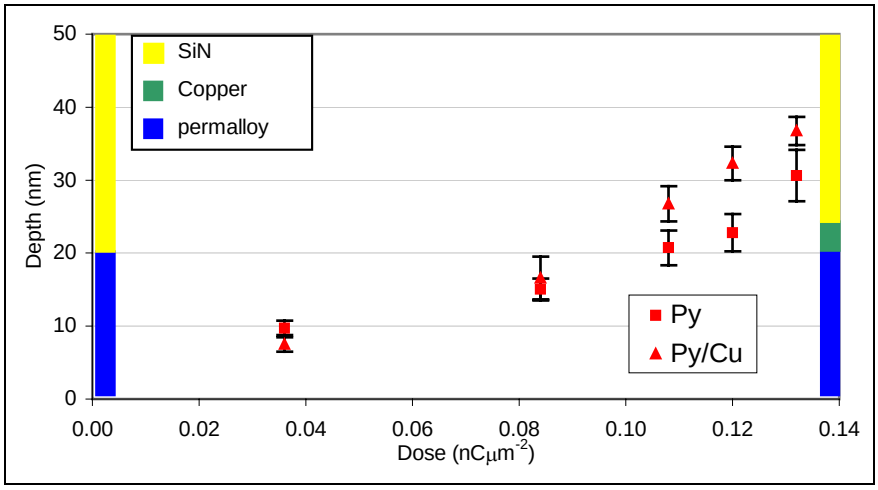

Figure 5.7: plot of average depth milled against dose for trenches surrounding the elements fabricated out of the permalloy and permalloy on copper films by FIB milling using a 12 pA beam current. Shown in the plot are keys for the two different thin films, blue indicates permalloy, green copper and yellow silicon nitride.

5.2 The magnetic characterisation of the nanoscale sized permalloy elements

In the following section, the details of the response of the magnetisation within the elements fabricated by EBL and FIB lithography on permalloy and permalloy on copper upon the application of a magnetic field is discussed. Through the use of Fresnel imaging and DPC, the reversal of the domain structure of the elements as well as the magnitude of the field at which these events take place have been investigated. The magnetic field values for the elements discussed in this chapter have been averaged over several cycles.

5.2.1 The magnetic structure of the 1000×200 nm² elements

When in zero applied field, the 1000×200 nm^2 permalloy element fabricated by EBL are in a near uniform magnetic state such as an S-state (discussed in sections 1.5 and 4.3), this state can be observed by DPC, Figure 5.8. The two orthogonal DPC images (Figures 5.8(a) and (b)), taken in zero field, shows the main domain in the element and the 90° rotation at the ends that form the end domains. Also visible outside the element in the DPC image of Figure 5.8(a) is stray field emanating from the end domains of the element, circled. The direction of sensitivity to the magnetic induction is indicated by the red arrows in Figures 5.8(a) and (b). In Figure 5.8(c) a schematic of the S-state is shown. This

schematic shows approximately the position of the 90° domain walls that form the end domains.

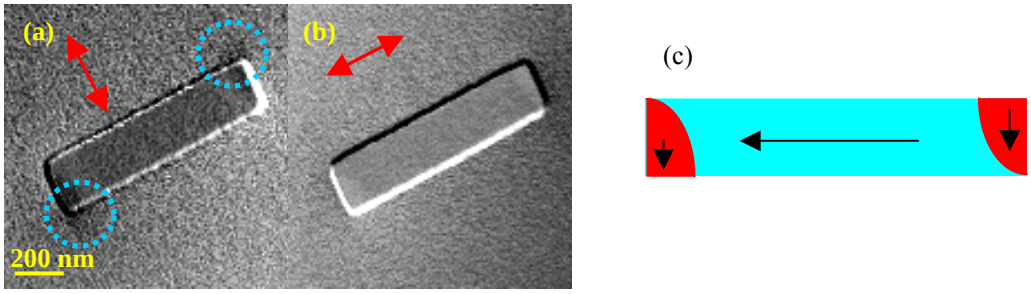

Figure 5.8: (a) and (b) orthogonal DPC images of a 1000×200 nm^2 permalloy element with the direction of sensitivity shown, the blue dotted circles highlight stray field emanating from the element. (c) schematic of the magnetisation distribution within the element.

As shown in section 4.3, an element with these dimensions can support both an S-state and C-state as the states have the same energy and will remain in that orientation when a field is applied along the easy axis. The elements fabricated by EBL exhibit this behaviour. For example when a magnetic field is applied along the easy axis of the element, the element remains in a C- (or S-) state configuration with the main domain aligned parallel to the field, Figure 5.9(a). As the applied field is reduced to zero, the end domains grow at the expense of the main domain, Figure 5.9(b). The end domains continue to grow, Figure 5.9(c), up to the reversal of the magnetisation within the element to the direction of the applied field of (140 ± 6) Oe, Figure 5.9(d). Increasing the field further, the main domain lengthens at the expense of the smaller end domains, Figure 5.9(e). When the applied field is reduced to zero and subsequently applied in the opposite direction the magnetisation within the element follows a similar path as before (Figures 5.9(f)–(h)). The nature of the reversal of the elements fabricated by EBL are similar to that shown for the OOMMF [11] simulation in section 4.3.1 but the coercive field is three times lower. The discrepancy is most probably due to the perfect symmetry and cells input into the simulation.

In the Fresnel images (Figure 5.9) the light and dark bands (discussed in section 3.3.1) can be observed at the opposing edges of the element (shown by the yellow and orange arrows respectively). The bands arise from the deflection of the beam, due to the magnetisation, either converging (light) or diverging (dark) with the straight through undeflected beam. If the bands are followed from image to image it can be observed that the contrast of the bands reverse with the reversal of the magnetisation within the element. The reversal of the dark and light bands at the edge of the element with the magnetisation

within the element allows us to determine when an element has reversed if the internal magnetic structure has been obscured by the physical contrast.

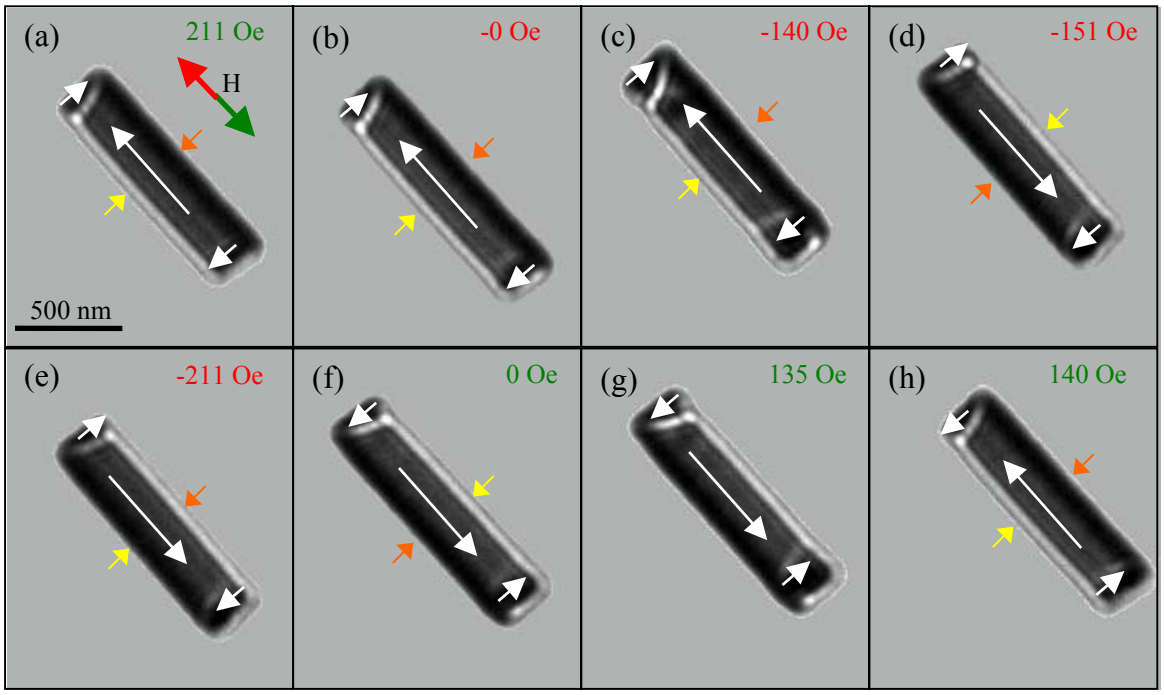

Figure 5.9: Fresnel images of a 1000×200 nm^2 permalloy element as it is cycled through a magnetic field ± 211 Oe. All images have an uncertainty in the field value of ± 6 Oe. The white arrows indicate the direction of magnetisation and the yellow and orange arrows indicate light and dark bands respectively.

The physical edge structure resulting from the 1000×200 nm^2 rectangular elements fabricated by FIB lithography for both the permalloy and permalloy on copper elements generates a large amount of non-magnetic contrast in the image therefore a large defocus is necessary for Fresnel imaging. For both the permalloy and permalloy/Cu elements milled using a high dose (>0.08 nCμm^{-2}), the magnetisation reversal proceeds in a similar manner to the EBL elements (Figure 5.9) as shown in Figure 5.10. For example, a 1000×200 nm^2 element fabricated using a dose of 0.11 nCμm^{-2}, in a high enough magnetic field the elements will have a nearly uniform magnetisation state, Figure 5.10(a). In this state the majority magnetisation is aligned along the direction of the field indicated. Unlike the EBL element, there appears to be no end domain contrast that can be observed within the element, although just visible are dark and light bands (indicated by yellow and orange arrows) that indicate that the magnetisation is parallel (or almost) to the edge of the element, as can be observed in the EBL samples (Figure 5.9). Reducing the applied field to zero (Figure 5.10(b)) does not increase end domain contrast. An end domain appears within the right side upper element prior to switching (blue dotted circle) but is not observed within the lower element which has already switched (Figure 5.10(c)). After

switching has taken place in both elements, the dark and light bands have reversed position, Figure 5.10(d). Reducing the field to zero after reversal (Figure 5.10(e)) does not increase the visible magnetic contrast within the elements, although end domains do appear in both elements when the applied field is increased in the opposite direction prior to switching (blue dotted circles), Figure 5.10(f). The end domains in these elements appear to form vortex structures due to the roughened edge structure. This is has been reported in similar elements previously by Hermann et al, [12] for elements fabricated by EBL with artificially induced edge structure. Both of the elements then switch at the same field value, Figure 5.10(g).

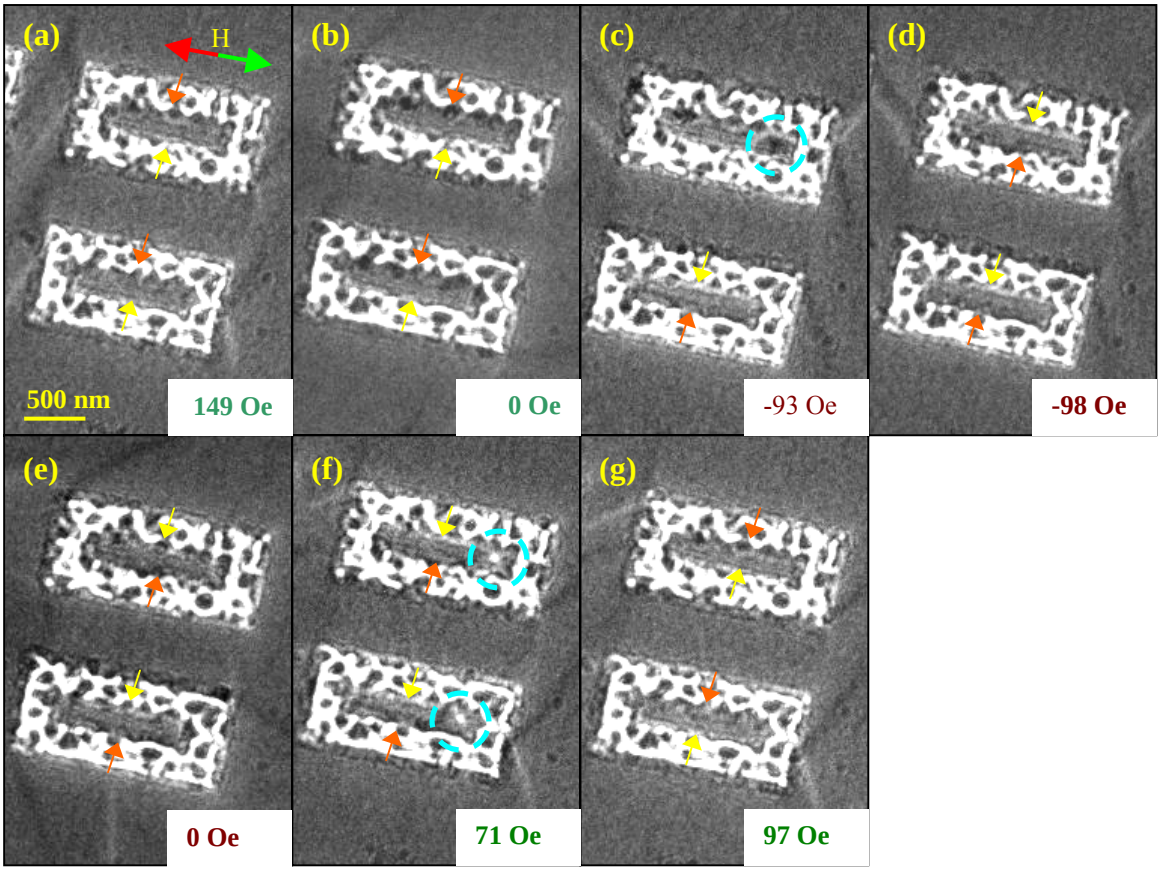

Figure 5.10: switching in a 1000×200 nm^2 permalloy element fabricated by FIB milling with a dose 0.11 nCμm^{-2}. Yellow and orange arrows indicate light and dark edge structure and the blue dotted circle indicate vortices. The field is cycled between ± 146 Oe, uncertainity of the field value is ± 2 Oe.

From the Fresnel images of the permalloy elements fabricated by EBL (Figure 5.9) and FIB lithography (Figure 5.10) two mechanisms can observed. The reversal of the EBL permalloy elements is a symmetrical reversal by domain growth and eventually reversal of the main domain. The reversal of the FIB lithography fabricated element is asymmetric; certain parts of the reversal cycle are similar to those of the EBL elements. In other parts of the cycle, the reversal is aided by the formation of a vortex (most probably due to the

roughened edge structure). The coercivity of all the 1000×200 nm^2 elements discussed in this section are given in Figure 5.11 as a function of dose. From the graph it can be observed that the coercivity of the FIB lithography fabricated elements is lower than the EBL fabricated elements, which is, in turn, lower than the OOMMF simulated coercivity (between 400 and 440 Oe, section 4.3.1). Also observable from the graph (Figure 5.11) is a general decrease in the coercivity with the dose for the permalloy on copper sample. This differs from the permalloy-only sample that appears to have a steady coercive value over this range of doses. The decrease in the coercivity of the elements fabricated by FIB lithography is possibly linked to the stray field influence of the remaining surrounding film, although the physical contrast obscures the stray field.

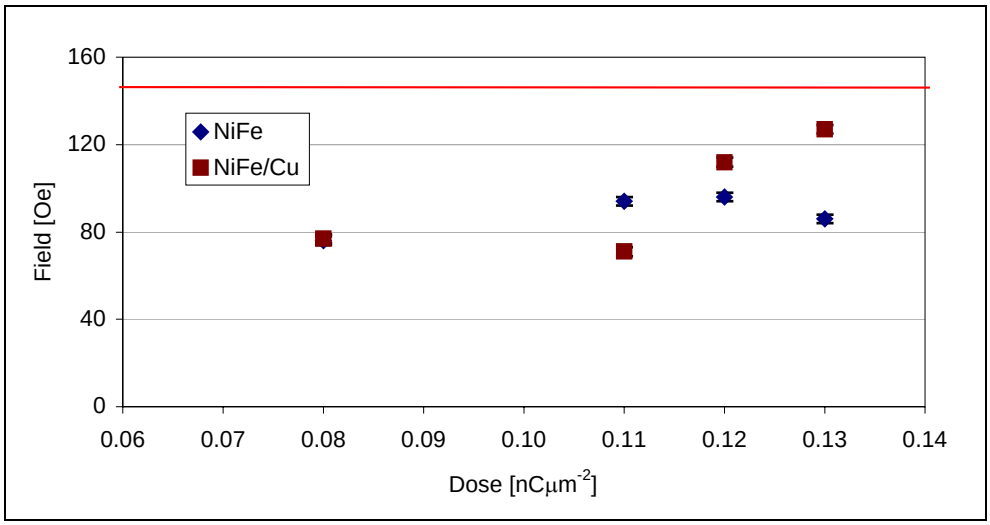

Figure 5.11: plot of the coercivity against dose of 1000×200 nm^2 permalloy-only and permalloy on copper elements fabricated by FIB milling. Shown as a red line is the value of the average coercivity of the EBL fabricated elements.

5.2.2 The magnetic structure of the 500×500 nm^2 elements

The most common remanent state (the single vortex state) for the 20 nm thick 500×500 nm^2 permalloy/permalloy on copper element fabricated by both EBL and FIB lithography has been imaged using DPC and is shown in Figure 5.12. In Figure 5.12 (an EBL fabricated element), the four-domain flux closure structure is visible. From the two sets of orthogonal images (Figures 5.12(a)-(b)) the anticlockwise rotation of the magnetic induction within the element can be observed, Figure 5.12(c).

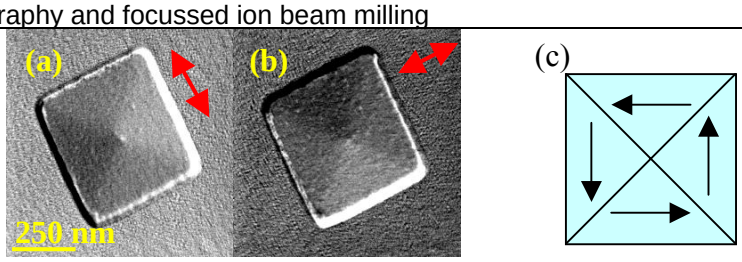

Figure 5.12: (a) and (b) orthogonal DPC images of a 500×500 nm^2 permalloy element. (c) schematic of the rotation of the magnetisation within the element. Red indicates the direction of sensitivity to the magnetic induction.

The typical behaviour of the 500×500 nm^2 permalloy element upon the application of a magnetic field for the EBL and the majority of the FIB lithography fabricated elements (85%) is shown in Figure 5.13. In an applied magnetic field (which has been applied along one of the easy axes of the element), the magnetisation within the element is in a C-state (Figure 5.13(a)). As the applied field is decreased the vortex reforms (Figure 5.13(b)), a further reduction in the applied field to zero moves the vortex continuously into the centre of the element (Figure 5.13(c)). The motion of the vortex is due to the expansion of the domain that is aligned parallel to the applied field and contraction of the domain that is aligned antiparallel. As the applied field is increased in the opposite direction the vortex moves to the opposing wall from where it formed (Figure 5.13(d)) and is expelled to form the reverse C-state as the applied field is further increased (Figure 5.13(e)). The magnitude of the applied field for the vortex expulsion (~±280 Oe) is greater than that of the vortex formation (~±70 Oe). As the applied field is decreased and increased in the opposite direction the element follows a similar magnetisation path, with the vortex reforming (Figure 5.13(f)) and moving to the centre as the applied field is reduced to zero (Figure 5.13(g)). The vortex then move into the opposite wall as the applied field is increased in the opposite direction (Figure 5.13(h)) and expelled as the applied field is further increased (Figure 5.13(i)), again this occurs at an applied field higher than the formation field. Shown in Figure 5.13(j) is the schematic of the hysteresis loop associated with the magnetisation cycle. In Figure 5.13(j) the formation of the flux closure structure at remanence has altered the experimental hysteresis cycle from the simulated cycle, Figure 4.17(j), which has a near uniform state at remanence.

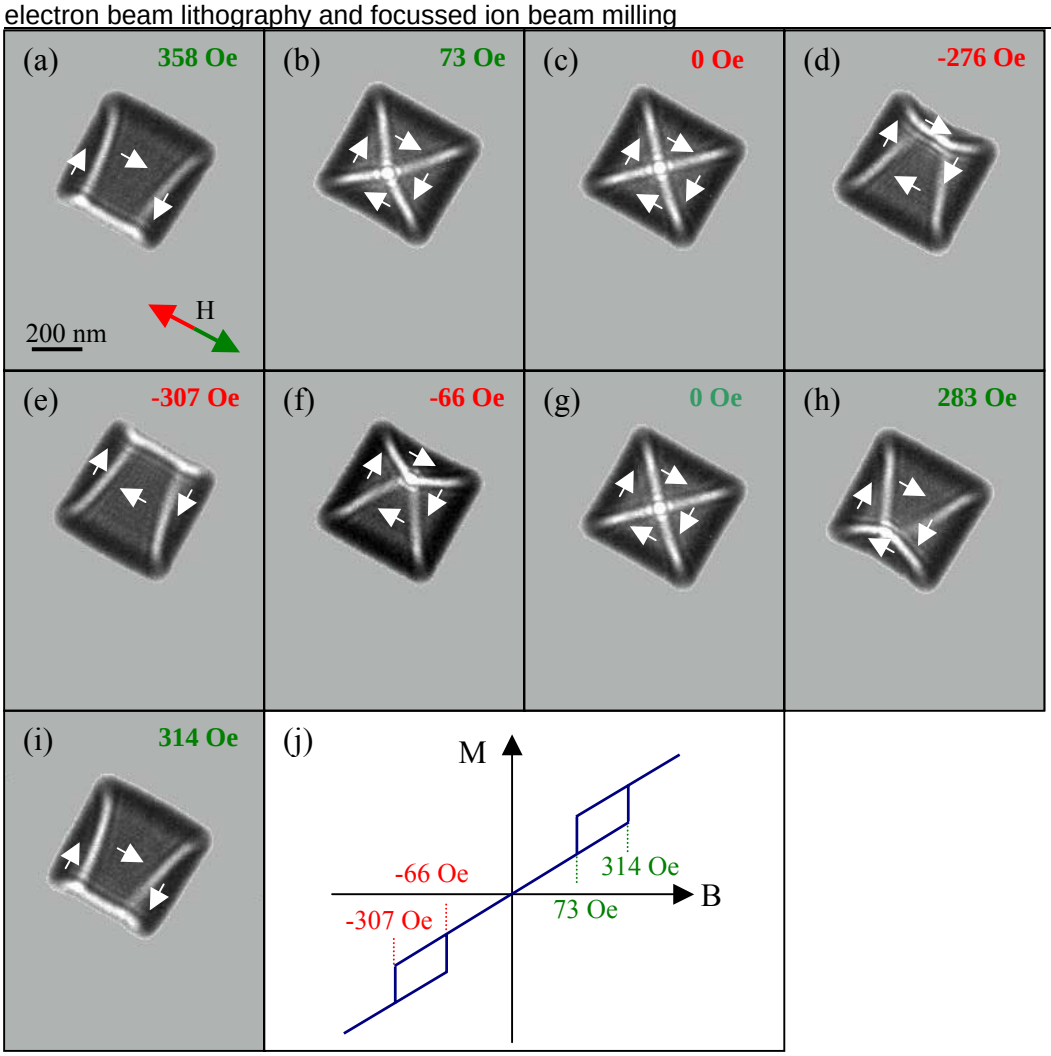

Figure 5.13: (a)–(i) Fresnel images of a 500×500×20 nm^3 permalloy element cycled through a magnetic field. All image have an uncertainity in the field value of ± 4 Oe. (j) a schematic of the hysteresis loop associated with the element.

As mentioned previously, the path of the magnetisation within a cyclic applied field for the majority of the elements fabricated by FIB lithography and with a dose >0.04 nCμm^{-2} is similar to that for the EBL samples detailed in Figure 5.13. In a significant minority of cases (15%), however, the magnetisation follows a different path. The two different paths can be observed in Figure 5.14. In the lower right element (ringed in blue) the magnetisation can be observed to follow the typical path (the black vortex in the element). In the other elements the magnetisation path is different, most noticeably in the upper left element (ringed in burgendy). In this element the chirality of the four-domain vortex state can be observed to reverse through an intermediate state.

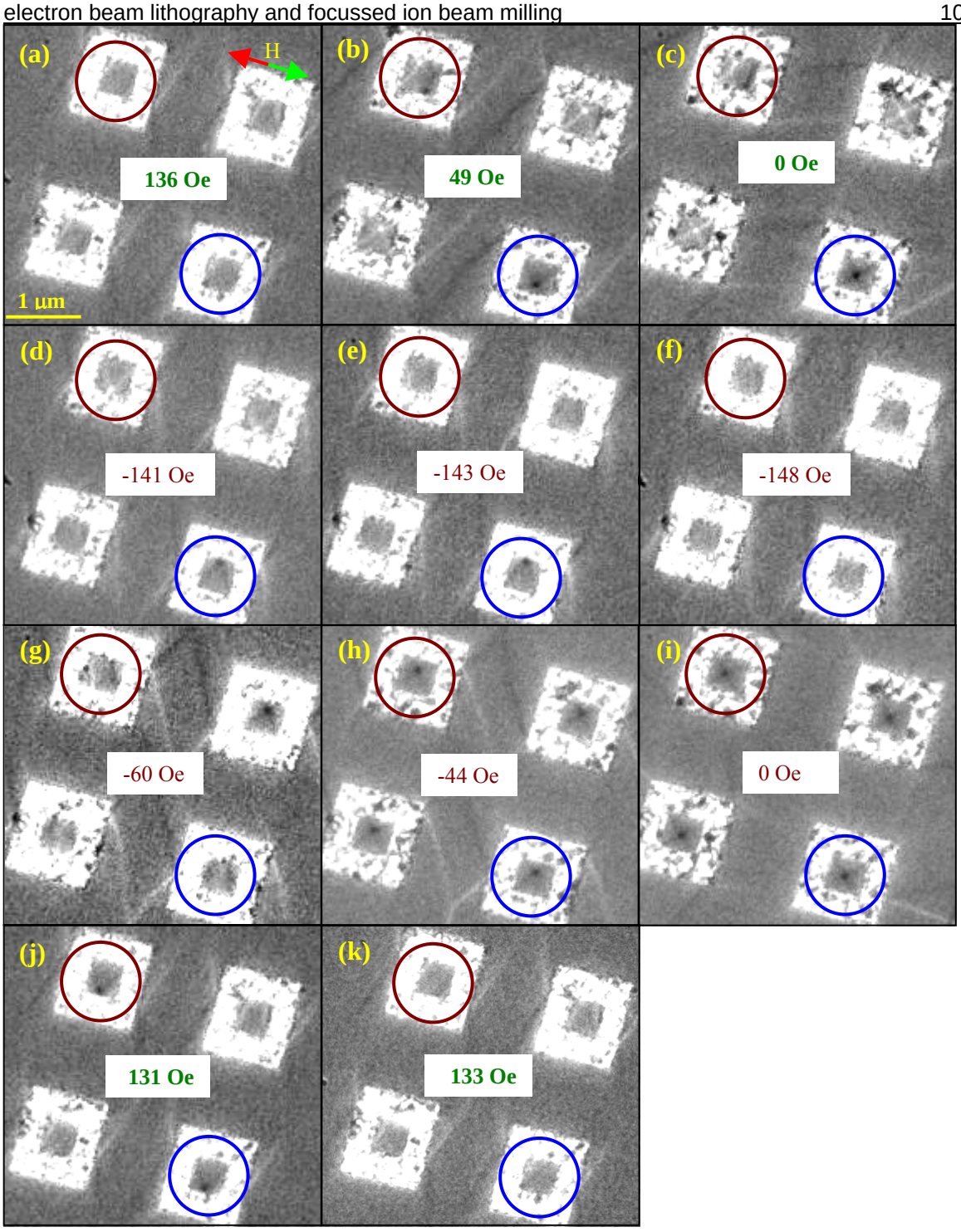

Figure 5.14: the motion of vortices in a 500×500 nm^2 permalloy element on a copper layer fabricated by FIB milling using a 0.11 nCμm^{-2} dose. The field is cycled through ± 148 Oe, with the uncertainty in each field values is ± 1 Oe. The burgendy circle show an element that forms a four domain state via a metastable state, and the blue circle shows an element that follows a conventional path.

A series of higher magnification Fresnel images of the upper left element, shown in Figure 5.15, reveals that the element forms a twin vortex state (Figure 5.15(b)) before collapsing to a four-domain state at a lower applied field. The chirality of the vortex within the element changes too, as seen by a comparison of Figures 5.15(c) and (f) shows. There are a couple of reasons why the higher energy double vortex state could form from a S-state in this element, Figure 5.15(a). One could be influence of the surrounding film on the magnetisation within the element; another could be the edge roughness of the element influencing the magnetisation. As the applied field is reduced further and the energy in the system is reduced, the vortices collapse to form one vortex. The collapse of the vortices is probably due to the reduced dimensions of the element being unable to support both vortices at the low applied field and, therefore, expelling one. As there is a change in chirality of the vortex, the edge roughness must make the formation of this vortex preferable as opposed to the one forming from the C- type state as typically occurs. The vortex is expelled as the applied field is increased in the opposite direction, Figure 5.15(d). As the applied field is reduced an S-state can be observed in the element, Figure 5.15(e). Unlike the previous S-state, the magnetisation forms a single vortex state without going through the metastable state, Figure 5.15(f) and expelled as the applied field is increased, Figure 5.15(g).

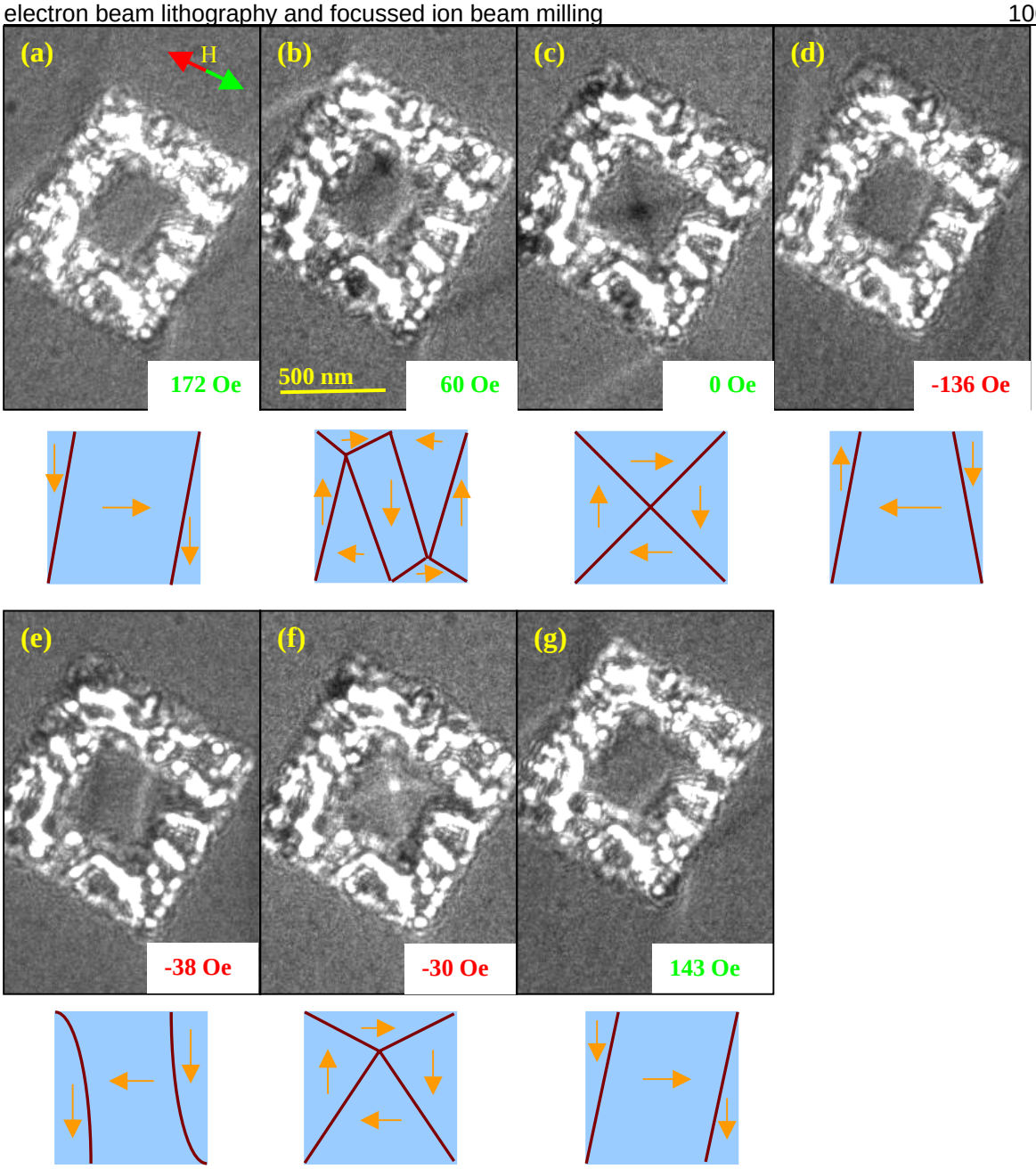

Figure 5.15: High magnification Fresnel images the top left 500×500 nm^2 permalloy element on copper in Figure 5.23 as it is cycled through a magnetic field, with schematics. Uncertainty in the field value is ± 2 Oe.

A plot of the vortex formation and expulsion fields against dose is shown in Figure 5.16. From the plot it can be observed that the average values of the vortex formation and expulsion fields are constant with the exception of the 0.08 nCμm^{-2} expulsion field, which has decreased to be of the same magnitude as the formation fields. The overall formation and expulsion fields for the FIB lithography elements are lower than that for the EBL fabricated elements. The EBL expulsion field is of the order of the OOMMF simulated expulsion field (sections 4.3.3 and 4.4.1).

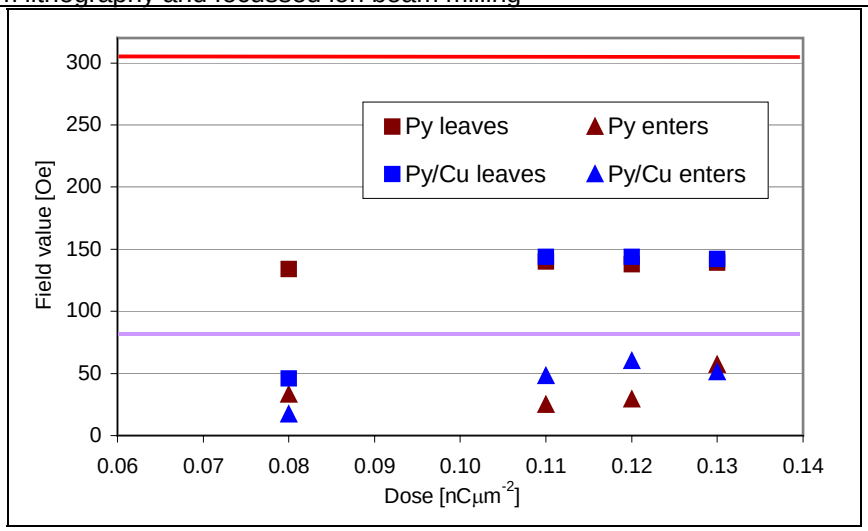

Figure 5.16: plot of the vortex expulsion and formation with respect to dose for 500×500 nm^2 permalloy-only and permlloy on copper elements fabricated by FIB milling. Shown as lines are the values for the EBL formation (purple) and expulsion (red) field values.

5.2.3 The magnetic structure of the elements fabricated by low dose

So far, only the behaviour of the elements fabricated with high doses has been considered. This is because the behaviour and magnitudes of field values of the elements fabricated above 0.04 nCμm^{-2} are quite similar. For the elements fabricated with a dose of 0.04 nCμm^{-2} the behaviour of the magnetisation within the elements differs as well as the field values at which the events take place. Examples of the low dose elements are shown below.

Shown in Figure 5.17 is the magnetisation cycle of the 1000×200 nm^2 permalloy-only element fabricated with the 0.04 nCμm^{-2} dose. The majority of the magnetisation within the element is aligned along the direction of the applied field at a field lower than the elements fabricated using doses <0.04 nCμm^{-2} (-41 Oe, as opposed to ~-80 Oe for >0.04 nCμm^{-1}), Figure 5.17(a). As the applied field is decreased to zero and then increased in the opposite direction, domain wall contrast is visible at the end immediately before switching (most probably a vortex, circled in gold), Figure 5.17(b). The switching of the lower element in Figure 5.17 is more visible in the first half of the cycle due to the end domain wall contrast. However, a change in the contrast along the major edges of the element (indicated by the blue and orange arrows) shows the switching of the upper element. On the second half of the cycle both elements are observed to switch through domain growth at the end of the elements prior to reversal (circled in gold), Figures 5.17(e)-(g).

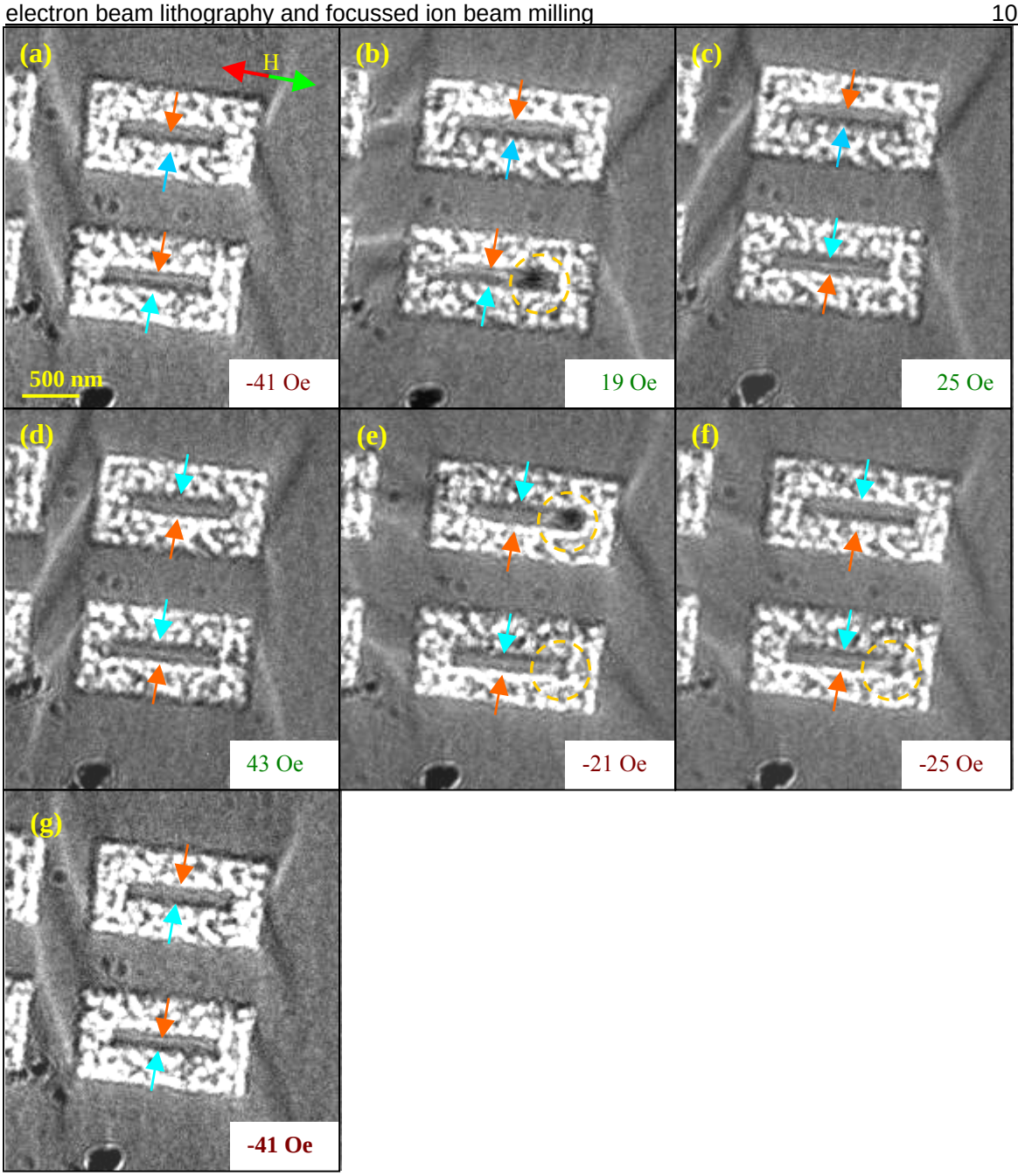

Figure 5.17: switching in a 1000×200 nm^2 permalloy element fabricated by FIB milling with a dose 0.04 nCμm^{-2}. The field is cycled between ± 41 Oe, uncertainity in each image is ± 1 Oe. The gold circles indicate areas where edge domains appear and the blue and orange arrows indicate edge contrast within the elements.

The 500×500 nm^2 permalloy and permalloy on copper elements fabricated by the low, 0.04 nCμm^{-2} dose do not follow either path described for the 500×500 nm^2 previously shown (Figures 5.13 and 5.14), as shown in Figure 5.18. The magnetisation within the element switches in a fashion similar to that of the elements with dimensions of 1000×200 nm^2. In a large enough applied magnetic field, the elements are in a C-type state with the largest domain in the direction of the field (Figure 5.18(a)), as the field is reduced the elements stay in this orientation and do not form a vortex, Figure 5.18(b). Reversal in

the elements (identifiable by the change in the position of the domain walls, indicated by the red and green arrows) coincides with the reversal of the surrounding continuous film (blue and yellow arrows), Figure 5.18(c), a further increase in the field has little affect on the elements, Figure 5.18(d). It is the change in ripple contrast [13, 14] that indicates the reversal of the surrounding continuous film. As the field is reversed the magnetisation within the elements follow a similar path with the exception of the lower right element, Figures 5.18(e)-(h). Upon reversal, the lower right element appears to form a vortex (Figure 5.18(f)), this vortex exists at the edge of the element and is expelled as the applied field is increased. The expulsion field occurs at a lower field than that of the elements fabricated using a higher dose (>0.04 $nC\mu m^{-2}$).

The similarity in reversal fields between the surrounding permalloy on copper film and the 500×500 nm^2 element fabricated using a Ga^+ dose of 0.04 $nC\mu m^{-2}$ could be due to the element not being isolated from the film and (as shown in Figure 5.19) which is confirmed by the average depth profile shown in Figure 5.7. In a case such as this, the element could no longer be considered an isolated element; it is more a topographical feature of the film and, as a result, the feature is exchanged coupled to the film. The feature is, therefore, heavily influenced by the magnetic properties of the film and has the local magnetic properties of an element. DPC images taken at certain points of a forward cycle similar to that of Figure 5.18 are shown in Figure 5.20. These images show correlations between the magnetic induction distribution within the element and that in the surrounding thin film. For the following DPC images (Figure 5.20) the 500×500 nm^2 element and film are represented by the green square and the milled trench by the yellow region. The burgundy arrows and lines represent the magnetic induction direction and domain walls respectively.

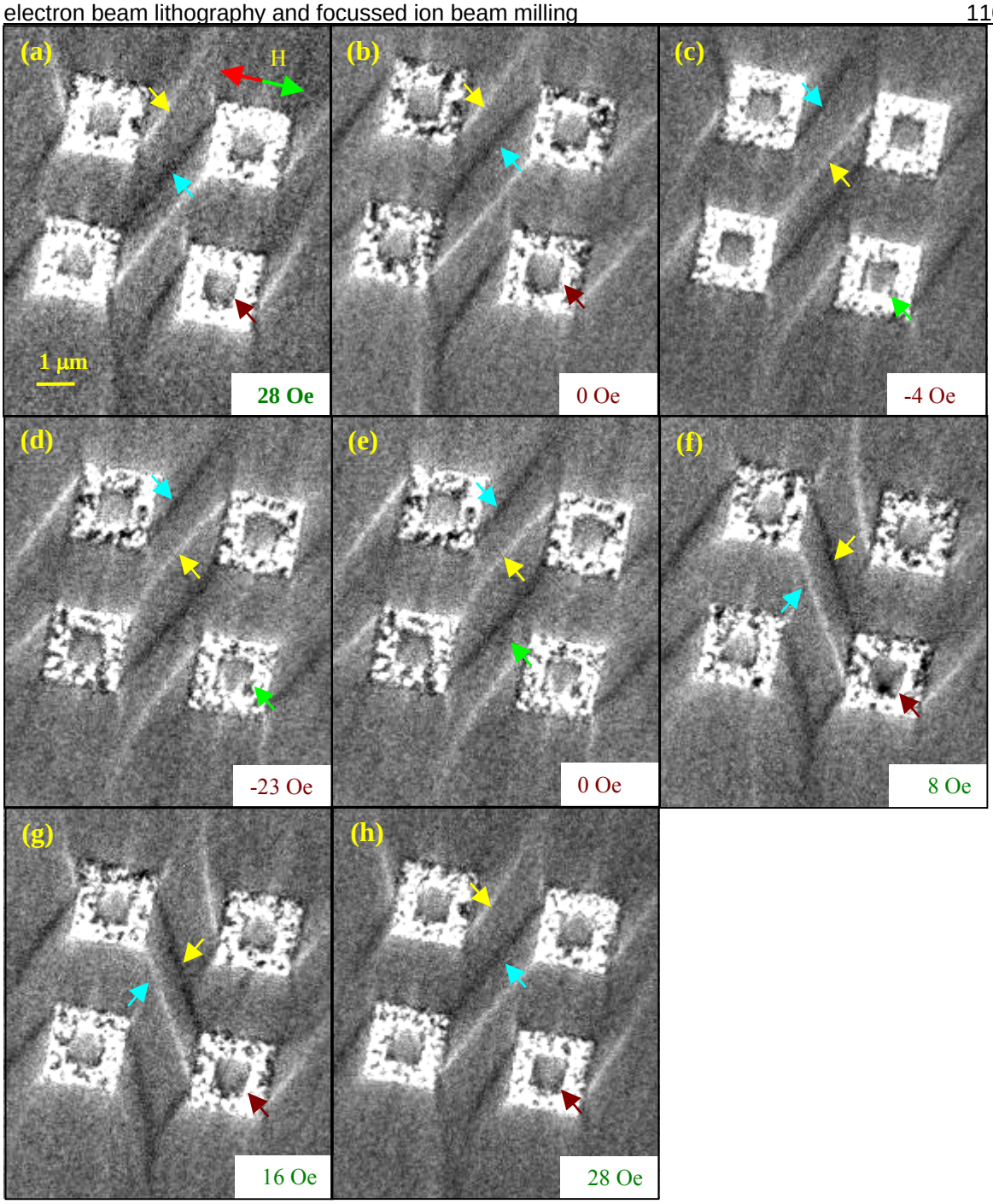

Figure 5.18: Fresnel images of a 500×500 nm^2 permalloy on copper element fabricated by FIB milling using a 0.04 nCµm^{-2} dose. The field is cycled through ± 28 Oe, the uncertainty in the field value is ± 1 Oe. Blue and yellow arrows indicate changes in the magnetic ripple of the continous film and red and green arrows indicate changes in the magnetic contrast in the element.

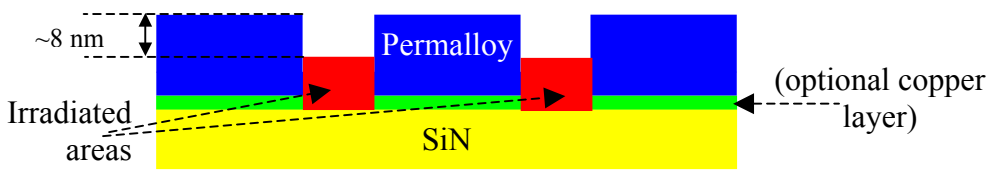

Figure 5.19: cross sectional schematic of a 20 nm thick permalloy on 4 nm copper element, supported by 50 nm SiN, fabricated with the 0.04 nCµm^{-2} dose.

The magnetic induction within the element in Figure 5.20(a) has the majority of the magnetisation within the element saturated along the direction of the field, with slight rotation at the corners of the element. The change in contrast (due to changes in the magnetic induction) appear to flow through the element and the film continuously although this is not certain due to the large physical changes in trench obscuring any magnetic detail in this region. As the field is reduced, Figure 5.20(b), contrast grows in the area surrounding the element but not within the element. At remanence, Figure 5.20(c), the magnetic induction in the element and surrounding area is still in the same orientation. As the field is increased in the opposite direction the magnetisation of the film and the element reverses, Figure 5.20(d), this is indicated by a reversal of the contrast in the DPC images. The magnetisation within the element forms a four-domain vortex state. This state has a vortex core and a small fourth domain. The field has then been decreased after reversal to zero field in an attempt to detach the vortex from the edge of the element and form the four-domain flux closure structure, Figure 5.20(e), but the vortex remains at the edge of the element, further indication of the influence of the surrounding film. The field is then increased in the opposite direction and the vortex is expelled, Figure 5.20(f). The majority of the domains throughout the field series, within the elements and the surrounding continuous thin film appear to align.

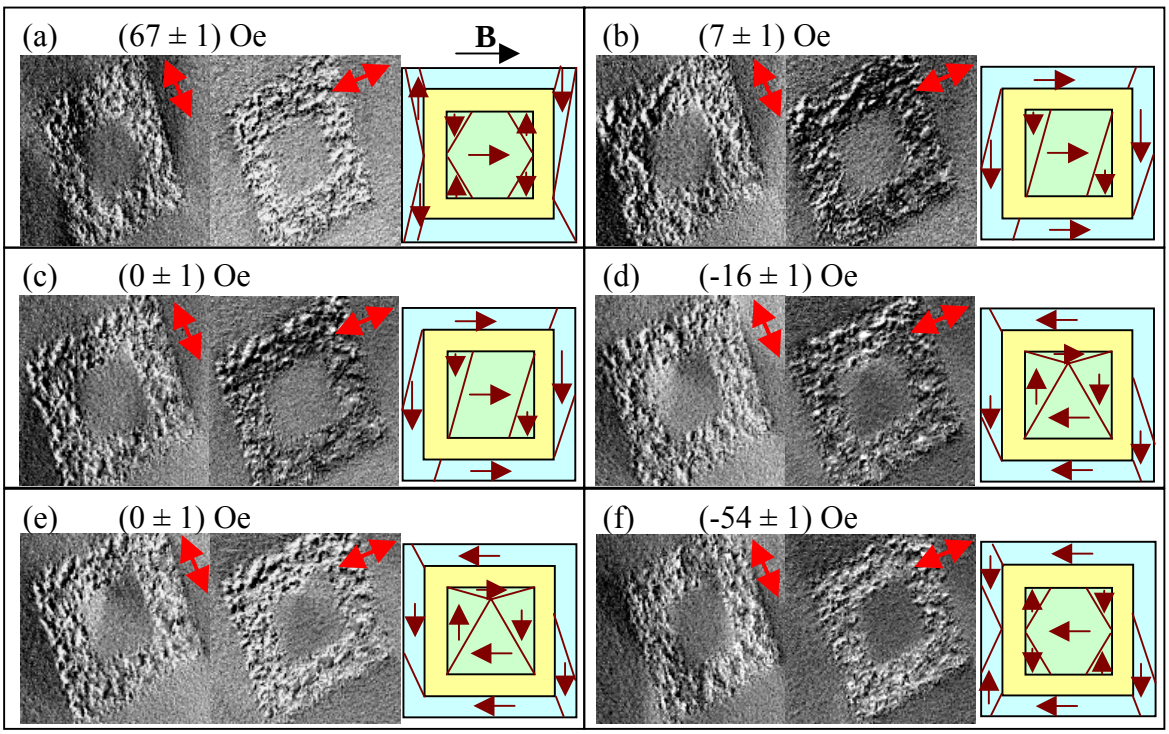

Figure 5.20: DPC image of a 500×500 nm^2 permalloy on copper element fabricated using a 0.04 nCμm^{-2} dose. The red arrows in the DPC image represent the direction of sensitivity, the burgundy arrows/lines represent the direction of B/domain walls, the blue represents the permalloy and the yellow represents the milled trench.

5.3 Conclusions

The elements fabricated by EBL have an edge roughness comparable to the as deposited grain sizes (~8 nm) with rounding of the corners approximately one quarter to a third the beam spot size (~80 nm). In comparison the average size of the grains within the FIB lithography fabricated elements vary with dose and composition. For high doses there is grain growth of up to ~32 nm, although this is for permalloy on copper and this grain growth is limited mainly to the edge of the element. For the permalloy-only sample a grain growth of up to ~25 nm is observed over the entire element, although this is for doses >0.11 $nC\mu m^{-2}$. For doses of 0.11 $nC\mu m^{-2}$ and lower, grain growth was confined to the edge of the element. It is thought that the grain growth is induced by the energy in the tails of the Ga^+ beam infringing on the element and the secondary events produced by the Ga^+ beam. Within the trenches milled to create the elements, preferential milling can be observed. This is confirmed by AFM profiles of the surface of the elements, trenches and surrounding area. The surface profiles measured by the AFM show that there is an average depth associated with the trenches. From the surface profiles the average sputter rates of the materials have been calculated. For the 20 nm thick permalloy layer deposited on 50 nm thick SiN a sputter rate of $(0.15 \pm 0.05)\ \mu m^3 nC^{-1}$ was calculated; after the permalloy was milled away on the silicon nitride specimen a sputter rate of $(0.41 \pm 0.05)\ \mu m^3 nC^{-1}$ was calculated and after the permalloy was milled away on the copper and silicon nitride specimen a sputter rate of $(0.43 \pm 0.05)\ \mu m^3 nC^{-1}$ was calculated. There is a slight difference in the sputter rate of the two samples that can be attributed to the 4 nm thin copper layer.

In general the magnetisation of both the 1000×200 nm^2 and the 500×500 nm^2 elements fabricated using doses <0.04 $nC\mu m^{-2}$ from both FIB lithography samples behave in a similar fashion to the elements fabricated by EBL, although the fields at which these events take place are lower in magnitude. The experimental fields are lower than those of the elements simulated by the OOMMF simulation package discussed in section 4.3. The lower field magnitudes are probably due to the influence of the surrounding continuous thin film, induced roughness and the increased grain sizes in the real elements. In certain cases the magnetisation within the 500×500 nm^2 elements proceeds through a metastable twin vortex state from the C-type state to single vortex state. The intermediate double vortex state probably arises due to the element roughness and the influence of the surrounding film. The vortex chirality is, as a result, reversed in all such cases. The extent of the influence of stray field emanating from the surrounding film on the elements could be estimate using the programme described in section 1.4.2. By setting the component of

magnetisation in the film to lie parallel to the easy axis of the element this would give the largest stray field to impinge on the element.

In the case of the lower dose elements (<0.04 $nC\mu m^{-2}$) it appears that these elements are more topographical features of the film than isolated elements given the average depth in the trenches being 12 nm. As a result the magnetostatics of the films and the trenches reduce the event fields dramatically for the elements. For the 500×500 nm^2 elements, the magnetostatics effects hinder the formation of the magnetic vortex structure within the element and pin the vortex core to an edge so it does not form. The three dimensional model of the OOMMF programme (section 1.4.1) could be used to model several scenarios to observe any influence of the surrounding film on the elements: i) the element is complete detached from the surrounding film: ii) the element is a topographical feature of a thin film (created by milling) where the connecting trenches have the same magnetic properties as the film and element and iii) the trench connecting the element and film has altered magnetic properties. The stray fields due to each scenario could also be calculated (section 1.4.2) from the OOMMF simulations.

Although the elements fabricated by EBL still have better definition, with respect to edges and corners, than those fabricated by FIB lithography, improvements in the machinery could lead to improvements in the elements. For example, in section 4.2 it was shown that a finer beam decreases edge roughness of trenches. The problem with a lower beam current to sharpen the edges (and decrease the tails of the beam) is the increased milling time and a combination of beam currents requires a realignment of the beam between beam current changes. The accuracy of the stage movements does not allow for good registration between beam currents and the TEM windows are too fragile to image using the FIB microscope. The new dual beam FIB microscope (a FIB microscope that has a Ga^+ and e^- source) will allow elements fabricated using multiple beam currents to be fabricated on TEM membranes. The use of this technology may allow for better clearing of the trenches and more regular edge structure giving an element of similar quality to that fabricated by EBL with decreased fabrication times.

Bibliography

[1] Chen Y, Macintyre D., Thoms S., J. Vac Sci Tech B 17(6) (1999) 2507.

[2] Lister K. A., Casey B.G., Dobson P.S., Thoms S., Macintyre D.S., Wilkinson C.D.W., Weaver J.M.R., Microelec. Eng. 73-74 (2004) 319.

[3] Cumming D.R.S., Thoms S., Beaumont S.P., Weaver J.M.R., Appl. Phys. Lett 68(3) (1996) 322.

[4] Schneider M., Hoffmann H., Zweck J., J. Mag. Mag. Mat. 257 (2003) 1.

[5] Lui X., Chapman J.N., McVitie S., Wilkinson C.D.W., Appl. Phys. Lett 84(22) (2004) 4406.

[6] Kirk K.J., Chapman J.N., Wilkinson C.D.W., J. Appl. Phys. 85(8) (1999) 5237.

[7] Kirk K.J., Scheinfein M.R., Chapman J.N., McVitie S., Gillies M.F., Ward B.R., Tennant J.G., J Phys D: Appl. Phys 34 (2001) 160.

[8] Moore K.T, Howe J.M., Csontos A.A., Ultramicroscopy 76(4) (1999) 195.

[9] Kaminsky W.M., Jones G.A.C., Patel N.K., Booji W.E., Blamire M.G., Gardiner S.M., Xu Y.B., Bland J.A.C., Appl. Phys. Lett. 78(11) (2001) 1589.

[10] Park C.-M., Bain J.A., IEEE Trans Mag. 38(5) (2002) 2337.

[11] Hermann M., McVitie S., Chapman J.N., J. Appl. Phys., 87(6) (2000) 2994.

[12] OOMMF simulation package available for download at NIST (URL active 16/02/06): http://math.nist.gov/oommf/

[13] Harte K.J., J. Appl. Phys. 39(3) (1968) 1503.

[14] Lim C.K., Chapman J.N., Rahman M., Johnston A.B., O'Donnell D.O., J. Phys. D: Appl. Phys. 35 (2002) 2344.

6 The characteristics of gallium ion irradiated, square, micron sized ferromagnetic elements

In this chapter the results for 2×2 μm^2 elements fabricated from a multilayer system composed of 10 nm Cu/20 nm permalloy ($Ni_{80}Fe_{20}$)/5 nm Cu on a 50 nm thick silicon nitride substrate are presented. The elements are fabricated by focussed ion beam (FIB) lithography and subsequently have been irradiated with a selection of patterns at various doses using a 30 keV Ga^+ beam in the FIB microscope. The physical and magnetic characteristics of the elements have been imaged by bright field TEM (section 3.2), Fresnel and, mainly, differential phase contrast (DPC) imaging (section 3.3), with the results discussed in this chapter. The 10 nm copper cap is hoped to alter the magnetic properties after irradiation by intermixing with the permalloy layer similar to McGrouther et al, [1]. To reduce the contributions of the edge effects on the magnetisation within the elements as they are cycled through an applied field (as discussed in chapter 5), the in-plane dimensions of the elements have been increased to 2×2 μm^2. Deposition of all the layers upon the 50 nm thick, silicon nitride substrate was done continuously using the thermal evaporation system discussed in section 2.1.2.

OOMMF simulations [2] have been implemented for each of the patterned elements. In the simulations (due to the limitations of OOMMF version 1.1b2), it has been assumed that irradiation has deadened the magnetisation (a valid assumption for high doses [3]) and that all the remaining magnetic material has the magnetic properties of unirradiated permalloy. The OOMMF 1.1b2 programme (section 1.4.2) can only model one magnetic layer per simulation. The results of the simulations are discussed along with the elements modelled.

6.1 30 keV gallium ion irradiation of 2×2 μm² elements fabricated by focussed ion beam lithography

The FIB microscope was used to both fabricate and irradiate, 2×2 μm² $Cu/Ni_{80}Fe_{20}/Cu$ elements with a total thickness of 35 nm using the method described in section 2.3. The 10 nm Cu capping layer was added to observe the effects of intermixing between the copper and 20 nm permalloy layers caused by the energy imparted by the Ga^+ beam. The second copper layer (5 nm) is a buffer layer to reduce charge build-up in the elements, similar to that discussed in chapter 5. The use of the FIB for lithography and irradiation allows the beam shifts to be used to reduce mismatch between the irradiated patterns and elements to <5 nm [4]. Elements with an in-plane aspect ratio of 1:1 and with dimensions greater than those discussed in chapter 5 were fabricated to give an element with a predictable magnetisation path in an unirradiated state (four-domain vortex state, section 1.5). The element size was increased to 2×2 μm² to allow for a larger element that would reduce the contribution of the edge on the bulk of the magnetisation within the element. The irradiated patterns of the 2×2 μm² $Cu/Ni_{80}Fe_{20}/Cu$ elements can be divided into two sections: i) lines (Figures 6.1 (a) and (b)), for example a one pixel (~10 nm) wide cross: and ii) areas (Figures 6.1 (c) and (d)), for example an area (~500 nm wide in the centre). The patterns illustrated in Figure 6.1 were irradiated using nine doses ranging from 0.001 nCμm^{-2} to 0.096 nCμm^{-2}. This range of doses was chosen to range from light irradiation up to slight milling of the element (given the doses discussed in chapters 4 and 5).

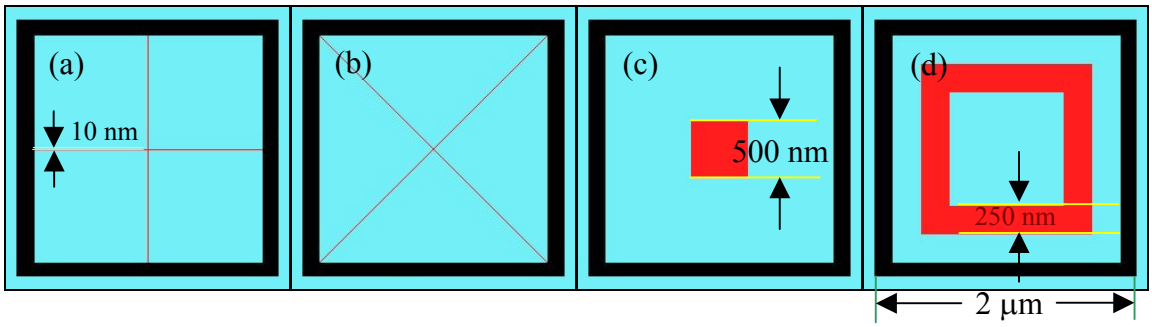

Figure 6.1: (a) and (b) line patterns; (c) and (d) area pattern. Blue indicates the copper/permalloy/copper element/thin film, black the milled trench and red the irradiated section.

6.1.1 The physical structure of elements irradiated by 30 keV gallium ions

The technique used to create the trenches to isolate the 2×2 μm^2 elements in the continuous film is the same as that used to create the FIB milled elements in chapter 5. As the film was thicker than the elements discussed in chapter 5 the dose was increased to 0.14 $nC\mu m^{-2}$ to ensure the trench surrounding the element was cleared. To illustrate the effect of the change in physical structure with respect to dose, Figure 6.2 shows a series of low magnification bright field TEM images of elements irradiated with the pattern shown in Figure 6.1(d) using various doses. From Figure 6.2, there is no obvious grain growth within the elements for the lower doses elements (Figures 6.2(b) and (c)) compared to the zero dose (Figure 6.2(a)); however, with the high doses (Figures 6.2(d) and (e)) grain growth due to the Ga^+ beam can be observed within the element. Figure 6.2(f) is the same image as Figure 6.2(e) with the exception that the contrast within the element has not been expanded: this is to show that there is still material present in the trench surrounding the element but the majority of the film has been cleared. Some asymmetry can be observed within the trenches surrounding the elements in Figure 6.2 although the elements themselves do not exhibit the asymmetry. The asymmetry within the trenches is a product of the pattern used to mill the trenches surrounding the element being asymmetric in construction but still giving the element square dimensions.

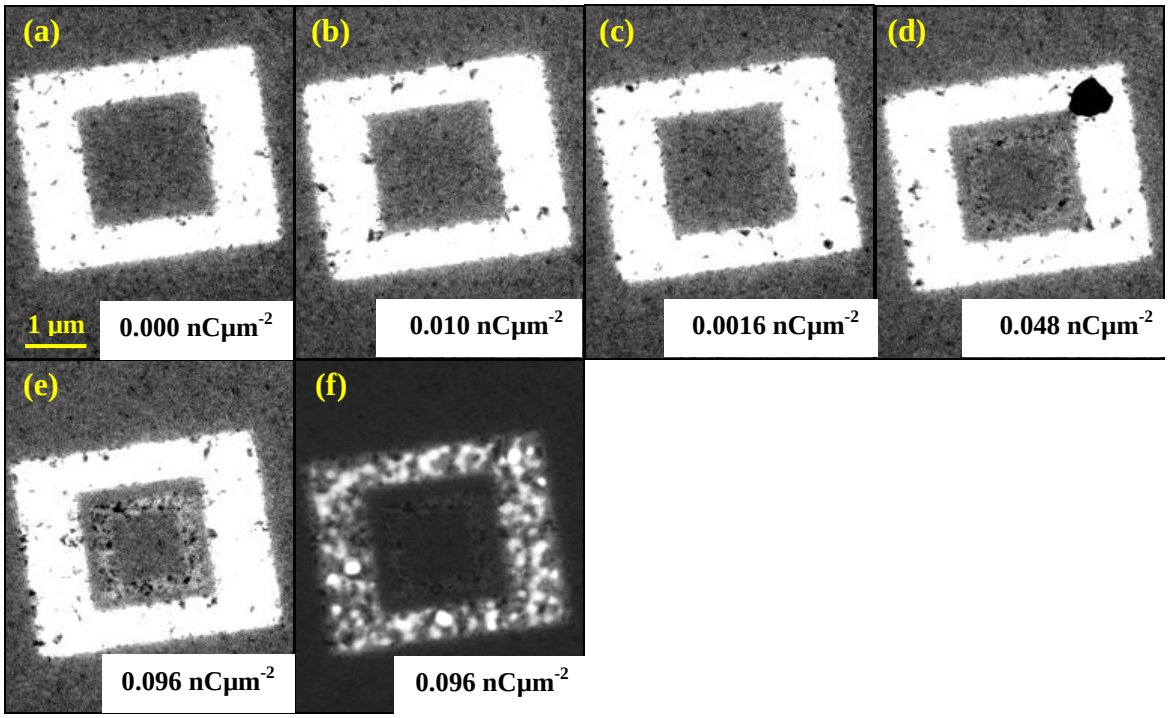

Figure 6.2: (a)-(e) low magnification bright field TEM images of 2×2 μm^2 irradiated elements with increasing doses (indicated) of the pattern shown in Figure 6.1(d), (f) is the same image as (e) with a lower contrast setting to highlight the remaining material in the trenches.

Higher magnification bright field TEM images of the elements shown in Figure 6.2 have been obtained and are shown in Figure 6.3. The unirradiated element, Figure 6.3(a), shows little evidence of grain growth throughout the entirety of the element in view. This is in contrast to the 500×500 nm^2 permalloy elements fabricated in chapter 5. In the elements discussed in chapter 5, grain growth of up to 35 nm could be observed at the edge of most elements for the permalloy on copper elements. The reduction in grain growth is most probably due to the remaining material in the trench allowing the energy of the beam to dissipate more easily. For the lowest, non-zero dose shown, there is little evidence of grain growth within the element (Figure 6.3(b)). By increasing the pattern irradiation dose to 0.0016 $nC\mu m^{-2}$ (Figure 6.3(c)), however, the outline of the pattern can be observed within the bright field image (indicated by a dotted red line). The higher magnification images shows grain growth of up to ~75 nm within the elements irradiated with the larger doses (Figure 6.3(d) and (e)).

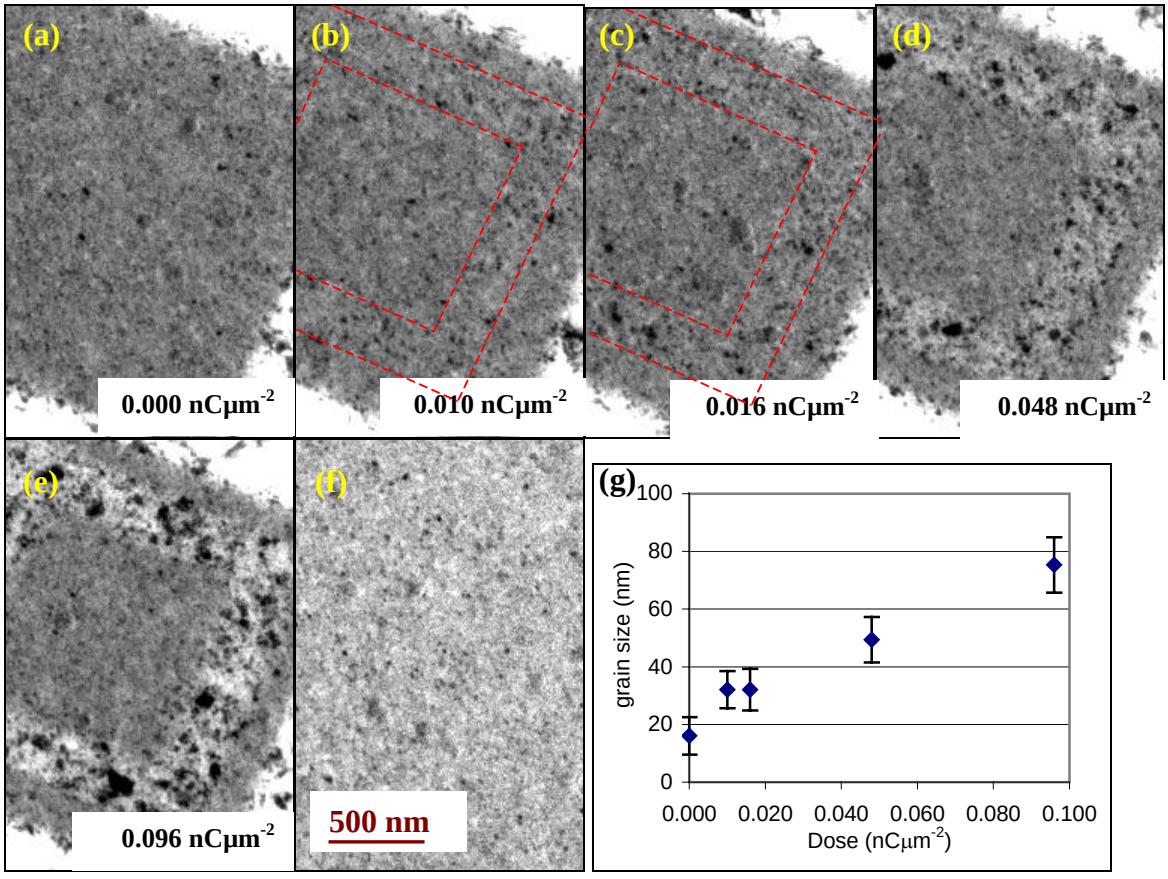

Figure 6.3: (a)–(e) high magnification images of Figure 6.2, (f) the as deposited film at the same magnification and (g) a plot of the average grain size against dose for the irradiated area of the elements.

From the bright field image of the highest dose (Figure 6.3(e)) the position of the pattern on the element can be measured. The registration and dimensions of the pattern are within 10 nm (1 pixel spacing) of the input pattern (250 nm wide trenches). Visible within the

unirradiated element and as deposited section of film (grain size (20 ± 7 nm)) are large grains. The cause of the large grain sizes is as yet unknown (they could be larger grains of material, contaminants on the film or redeposition of milled material). Compositional analysis through techniques such as electron energy loss spectroscopy (EELS) [5] or Auger electron spectroscopy (AES) [6] could be used to gain a better understanding of the grains.

As expected, due to the dimensions of the beam spot size being ~10 nm [4] and the doses being relatively small, not all of the patterns irradiated into the elements exhibit signs of grain growth (as is shown in Figure 6.4). For example, the one-dimensional diagonal cross (Figure 6.1(b)) shows no sign of grain growth in any bright field TEM imaging (Figures 6.4 (a)–(c)) even at the highest dose (Figure 6.4(c)). The Ga^+ irradiated lines, however, have an effect on the magnetisation within the element (as shown section 6.3).

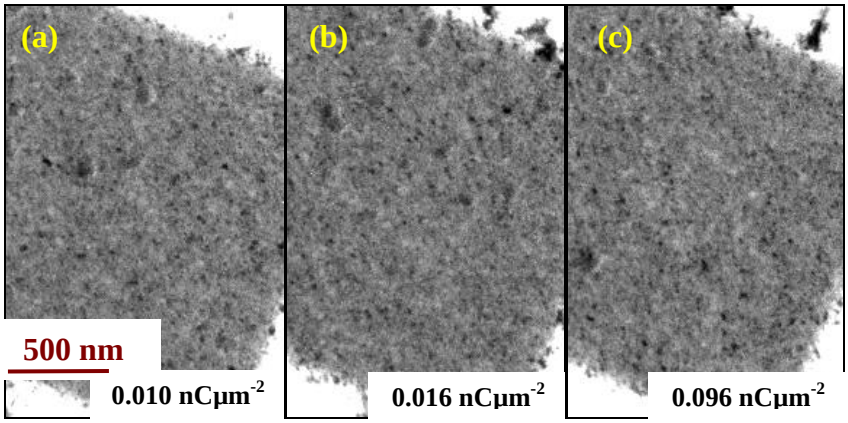

Figure 6.4: bright field TEM images of element irradiated with pattern Figure 6.1(b), the dose is indicated in the image.

6.2 The magnetic structure of an unirradiated and low dose elements

Fresnel imaging was used to view the irradiated and unirradiated elements in zero applied field. In the majority of irradiated elements, the behaviour is similar to the other unirradiated elements (such as those discussed in chapter 5). For example the irradiated and unirradiated elements shown in Figure 6.5, which form the single vortex structure in zero applied field. The similar behaviour persisted when cycled through an applied magnetic field. In the elements the magnetisation forms a C-state in an applied field of ~50 Oe along the easy axis. As the applied field is reduced the vortex state reforms at ~30 Oe. The vortex state then persists until it is expelled as the field in increased in the opposite direction, ~-50 Oe, and the reverse C-state is formed. A similar magnetisation path is followed as the applied field is reduced and increased in the opposite direction.

From the magnetisation cycles it can be observed that the majority of patterns irradiated into the elements (for the dose range of 0.001 to 0.096 nCμm^{-2}) have little to no effect on the magnetisation path. The exceptions are given in the subsequent sections and the relevant OOMMF simulations for the elements are discussed prior to the experimental detail.

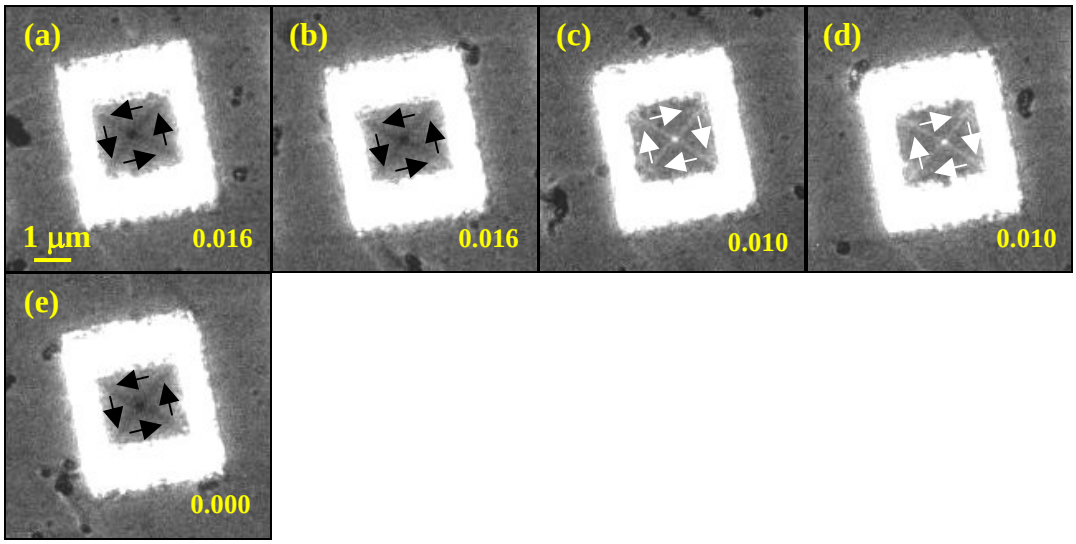

Figure 6.5: Fresnel images of the field free magnetic states of 2×2 μm^2 elements irradiated with the patterns in: (a) Figure 6.1(a), (b) Figure 6.1(b), (c) Figure 6.1(c), (d) Figure 6.1(d) and (e) unirradiated. The doses (nCμm^{-2}) are indicated. The single vortex state can be observed in all images, with the arrows indicating the direction of the magnetic induction within the domains.

6.3 The magnetic structure of an element irradiated with a line pattern

As a guide to the behaviour of the magnetisation within the experimental elements, as they were subjected to a cycled magnetic field, OOMMF simulations were performed using version 1.1b2. OOMMF version 1.1b2 [2] is an open source micromagnetic simulation package developed by NIST [7] and the details of the programme are described in section 1.4.2. A series of masks (similar to those used in section 4.4) were developed to examine the behaviour of the elements imaged, with the results presented along with the experimental results. As the OOMMF version 1.1b2 cannot calculate multiple layers with different magnetic properties it has been assumed that the irradiated areas have their magnetic properties reduced to zero and the unirradiated areas have the magnetic properties of permalloy with no intermixing with the copper layers. As shall be shown later this is not always be the case, in certain circumstances the Ga^+ concentration may not be sufficient to deaden the magnetic properties of the irradiated section. The pixel spacing

of the irradiated areas in the OOMMF simulations have been matched to the same width as that of the given Ga^+ beam spot size. As the magnetic structure of the elements irradiated by the 30 keV Ga^+ is often complex, DPC imaging has been implemented.

6.3.1 The diagonal cross pattern

A remanent state of the OOMMF simulation of a 2×2 μm^2, 20 nm thick permalloy element (the element is 20 nm thick as this is the thickness of the deposited magnetic layer) irradiated with a 10 nm wide diagonal cross is shown in Figure 6.6(a). This state is a vortex state with the core displaced from the centre due to the non-magnetic region and is most probably the ground state (the total simulated energy (2.3 kJm^{-3}), which is approximately half the C-type state (4.4 kJm^{-3}) shown in Figure 6.6(d)). The vortex is driven into the upper edge as the field is applied along an easy axis (as shown in Figure 6.6(b)). After the vortex has been expelled, the magnetisation within the element forms a C-type state, Figure 6.6(c). After the formation of a C-state, the simulated element differs from the experimental data shown in Figure 6.7 (such as not reforming the vortex until after remanence). One similarity between the simulated and experimental results is, as the applied field is reduced, the vortex core is off the central axis of the element; this is due to the influence of the non-magnetic section. Further detail cannot be obtained from the simulated states. The main reason for the difference could be the assumption made about the irradiated section being magnetically dead. In reality, the magnetic properties are thought to be reduced as observed by Kaminsky et al, [3].

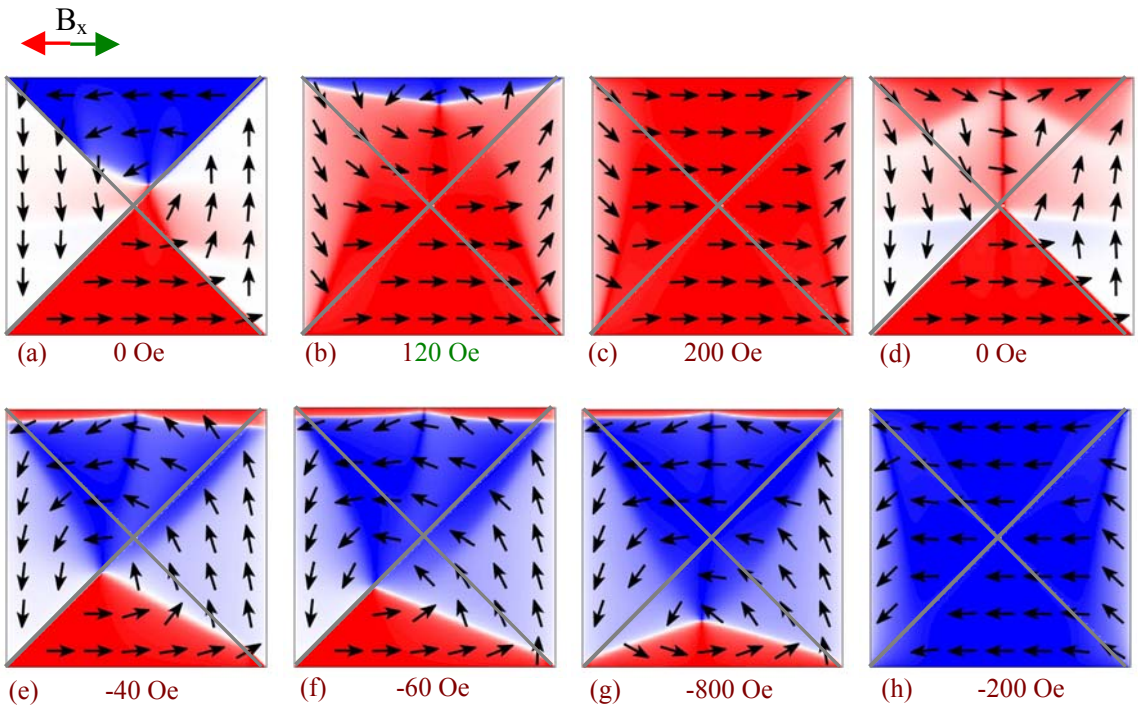

Figure 6.6: (a)–(h) OOMMF simulation of the irradiated pattern shown in Figure 6.1(a) (outlined in grey), cycled between an applied field of ± 500 Oe.

The behaviour of the magnetisation within the element irradiated with ~10 nm wide, one dimensional diagonal cross pattern (shown in grey is the nominal position in schematic accompanying the DPC images), with the highest dose (0.096 nCμm^{-2}) as the element has been cycled through an applied field is shown in Figure 6.7. As with the unirradiated element, in a sufficiently high applied magnetic field the magnetisation within the element is orientated in a C-state, Figure 6.7(a). A vortex that is off-centre forms in the lower quadrant of the element near the irradiated section as the applied field is reduced (as shown in Figure 6.7(b)). Here the irradiated section could possibly have altered the magnetic properties (such as a reduction in M_s, which has been observed in permalloy films irradiated with 30 keV Ga^+ [3]). This is expected to influence the energetics that govern the position and formation of the domain walls. It is hard to say for sure if the vortex core is in or near the irradiated section as it is not visible but the vortex core is local to the irradiated section. As the applied field is reduced to zero the vortex has moved towards the centre of the element (Figure 6.7(c)) but the exact position of the vortex core cannot be precisely determined, this is denoted by the hollow circle in Figure 6.7(c). As the applied field is increased in the opposite direction, the vortex core moves to the opposite quadrant in a discontinuous motion (Figure 6.7(d)). The element then proceeds to form a C-state as the applied field is increased further to –65 Oe and the vortex is then expelled. The element follows the same magnetisation path when a reverse field is applied, from –65 to 65 Oe.

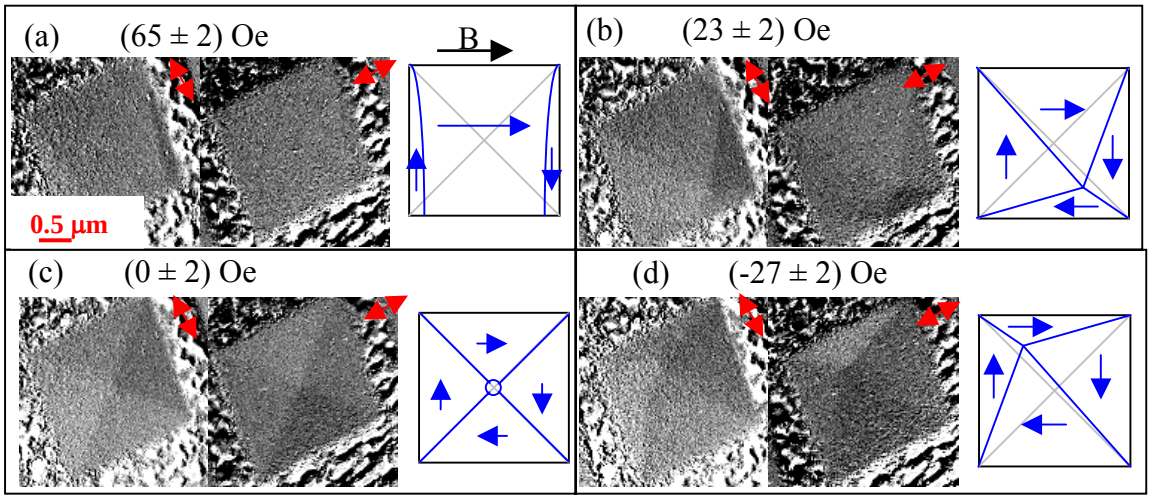

Figure 6.7: (a)–(d) DPC images and schematic of the magnetisation within an element irradiated using pattern nominally shown in the schematics with a dose of 0.096 nCµm^{-2} as a magnetic field is applied. Grey lines indicate FIB irradiated sections, blue indicates the direction of magnetic domains and domain walls and red arrows indicates the direction of sensitivity.

6.3.2 The horizontal/vertical cross pattern

From the input parameters of the 2×2 µm^2 element with a 10 nm wide horizontal/vertical cross, the two-dimensional OOMMF programme simulated initial remanent state has four magnetic regions that act as separate elements that influence each other through the thin non-magnetic region (Figure 6.8(a)). The influence of the elements through the non-magnetic region is similar to the trenches that have material remaining in them and their magnetic properties are not been destroyed (section 5.2.3), except in the trenches the influence is lessened due to distance. This state has a total energy density of 3.1 kJm^{-3}. As can be observed when a simulated field is applied to the element the four sections continue to act as four elements whose expulsion and formation events occur at the same fields due to the magnetostatic coupling. As shown in Figures 6.9 and 6.10 a real element fabricated in such a way differs significantly in its behaviour in an applied field.

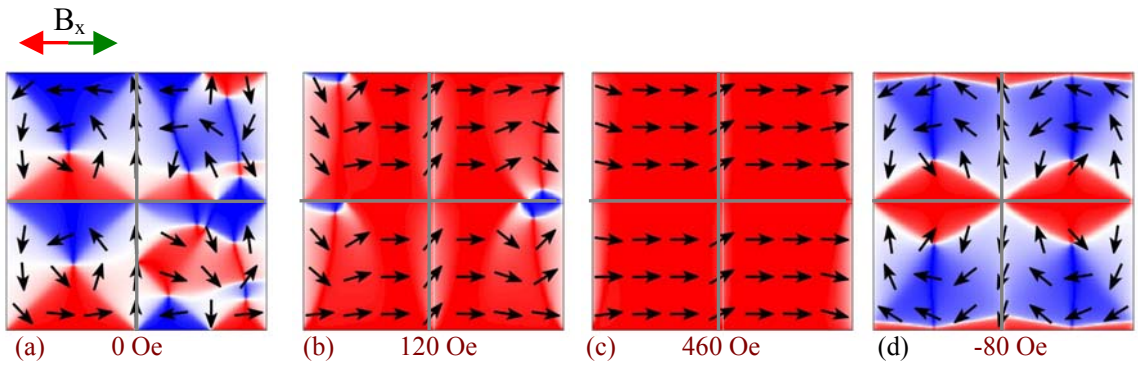

Figure 6.8: sample of OOMMF simulation of the pattern shown in Figure 6.1(b) (outlined in grey) cycled between an applied field of ± 500 Oe.

The magnetisation path for an element that has been irradiated with a ~10 nm horizontal/vertical cross using the highest dose (0.096 $nC\mu m^{-2}$) as it cycled through an applied magnetic field is shown in Figures 6.9 and 6.10. Figure 6.9 is of the magnetisation within the element as the applied field is cycled from ~65 Oe to ~-69 Oe and Figure 6.10 is of the same element as the applied field is cycled back to ~65 Oe. In a sufficiently high applied magnetic field the magnetisation is in a near uniform state with slight rotation at the ends of the element perpendicular to the applied field (Figure 6.9(a)). As the applied field is reduced, the element enters a multi-domain near flux closure state probably due to the influence of the irradiated section (Figure 6.9(b)). A further reduction of the applied field allows the flux closure structure to form (Figure 6.9(c)). The irradiated section influences the domain walls and does not allow the vortex to move continuously through the element. Instead as the applied field is increased there is a discontinuous jump from one side of the horizontal line to the other after remanence (Figures 6.9(d) and (e)). As the applied field is increased to a large enough value in the opposite direction the vortex is expelled and a near uniform state is formed, Figure 6.9(e).

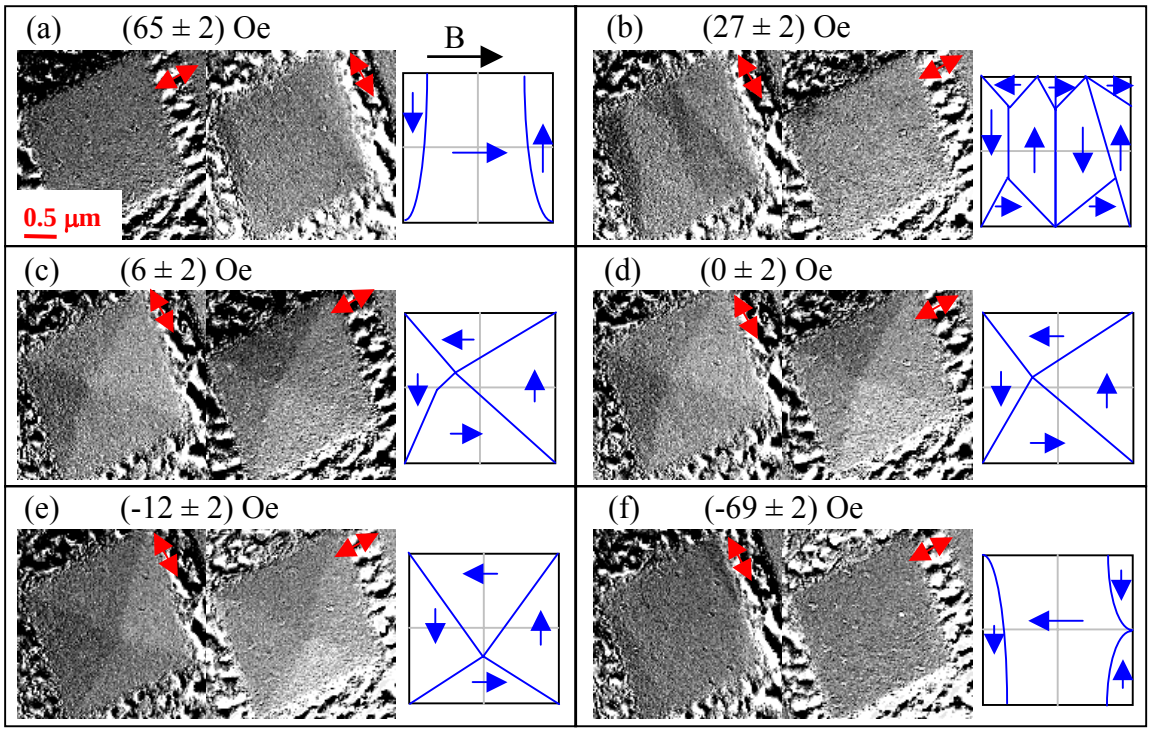

Figure 6.9: DPC images, with schematic of the magnetisation, of an element irradiated with the horizontal/vertical cross pattern using the 0.096 nCμm^{-2} dose for the first half of the magnetisation cycle. Grey lines indicate FIB irradiated sections, blue indicates the direction of magnetic domains and domain walls and red arrows indicates the direction of sensitivity.

As the applied field is decreased, the magnetisation within the element that is in a near uniform domain (Figure 6.10(a)) forms a multi-domain state (Figure 6.10(b)). Figure 6.10(a) is the same state as Figure 6.9(f) and is shown again for convenience. The multi-domain state is probably produced by the influence of the irradiated area. Upon reducing the applied field further, a four-domain state is observed (shown in Figure 6.10(c)). Instead of all four-domain walls converging to a point to form a single vortex core, a cross-tie wall (section 1.3.1) is formed centred in the irradiated section (highlight in green). When the field is reduced to zero a single core four-domain vortex state forms (Figure 6.10(d)), although the core is slightly off-centre (as with Figure 6.9(d)). An increase in the field in the opposite direction expels the vortex to form a C-state (Figure 6.10(e)) after the vortex has moved with a discontinuous motion to the opposite side of the horizontal irradiated line, as with Figure 6.9(e).

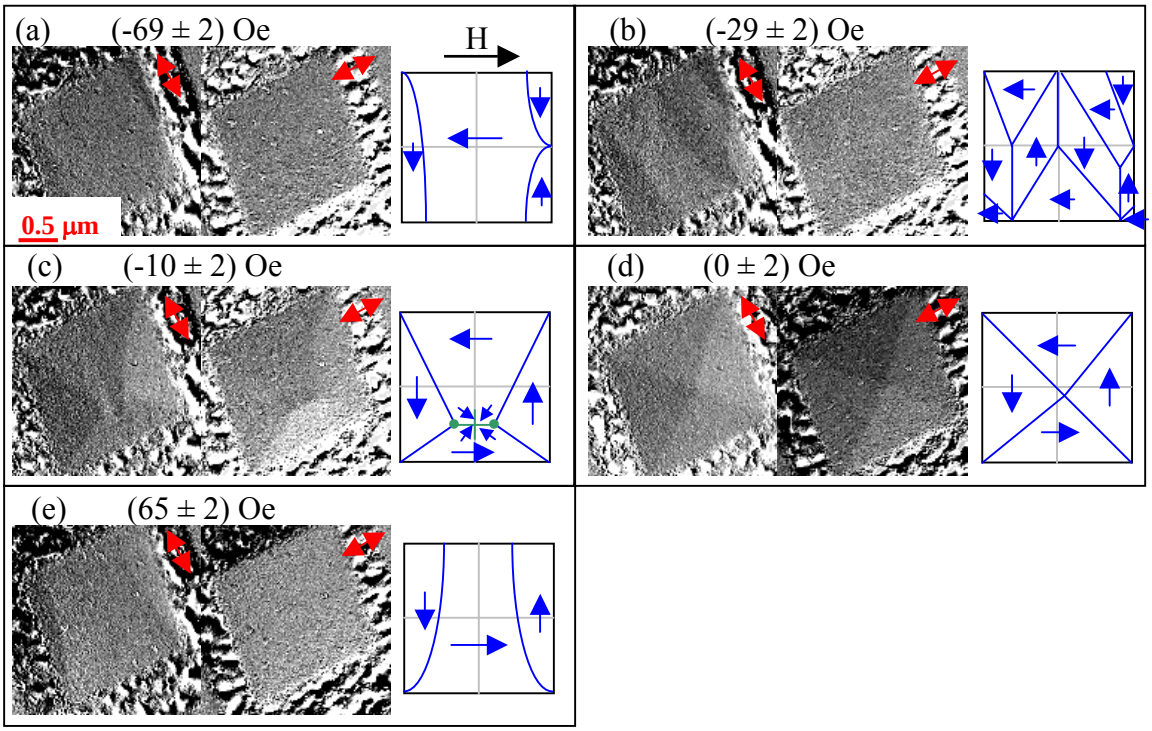

Figure 6.10: (a)–(e) DPC images, with schematics, of a 2×2 μm^2 element irradiated with the horizontal/vertical cross pattern using the 0.096 nCμm^{-2} dose for the second half of a magnetisation cycle. Grey lines indicate FIB irradiated sections, blue indicates the direction of magnetic domains and domain walls, red arrows indicates the direction of sensitivity and green the cross-tie wall.

The magnetic properties of the irradiated sections do not appear to be magnetically dead as previously thought. The formation of domain walls and a cross-tie structure in the irradiated areas is proof of this. If the irradiated sections were magnetically dead then magnetic domain walls could not form. In light of this, the use of the three-dimensional version of the OOMMF programme would be beneficial. The three-dimensional version of OOMMF allows the user control over the number of magnetic materials present, the properties of the materials, the thickness of the cell size; this is in addition to the abilities of the two-dimensional programme.

6.4 The magnetic structure of an element irradiated with an area pattern

6.4.1 Elements irradiated with a 500×500 nm² square in the centre

The OOMMF simulation of the 2×2 μm² element with a non-magnetic area of dimensions 500×500 nm² at the centre reveals that the magnetisation has formed a flux closure structure (similar to the vortex state) with the core in the non-magnetic region when allowed to relax in zero applied field, Figure 6.11(a). Upon the application of a magnetic field, the magnetisation path predicted by the simulation differs significantly from that that is observed experimentally (Figures 6.12 and 6.14) and is therefore not discussed further. Again this is due to the irradiated section not being magnetically dead as is assumed for the simulations.

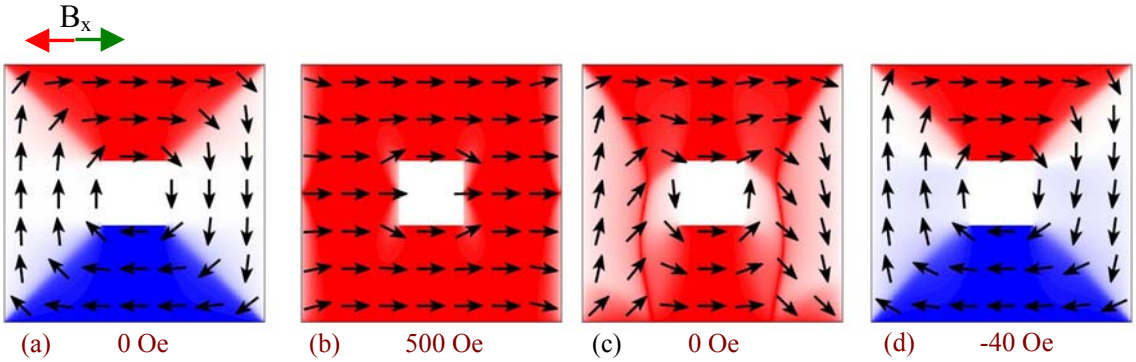

Figure 6.11: OOMMF simulation of the pattern shown in Figure 6.1(c) cycled between an applied field of ±500 Oe.

DPC images of the a 2×2 μm² element irradiated with a 500×500 μm² square at the centre using the 0.096 nCμm^{-2} dose of Ga^+ as the element is cycled through a magnetic field are shown in Figures 6.12 and 6.14. In a large magnetic field the magnetisation within the irradiated element forms an S-state, as seen in Figure 6.12(a). As the applied field is decreased the magnetisation forms a multidomain flux closure state, Figure 6.12(b). At this applied field, the irradiated area in the centre of the element influences the magnetisation to adopt a multidomain flux closure state. On the left side of the element the magnetisation has formed a cross-tie wall (in green). As the applied field is increased in the opposite direction, the irradiated element forms the four-domain flux closure structure, with the vortex core displaced off-centre, Figure 6.12(c). It is suspected that the irradiated area has some magnetic properties and not magnetically dead as assumed for the simulation. As a result the domain walls pass through the irradiated section, although this

is masked in the DPC images by the physical contrast. A further increase in the applied field drives the vortex core towards the lower edge of the element, Figure 6.12(d). Here the element is in a four-domain flux closure state. A reason for this could be the irradiated area within the element splitting the four domain walls that converge to form the vortex core. Increasing the field further acts to expel the four-domain structure and the magnetisation within the element forms a C-type state, Figure 6.12(e).

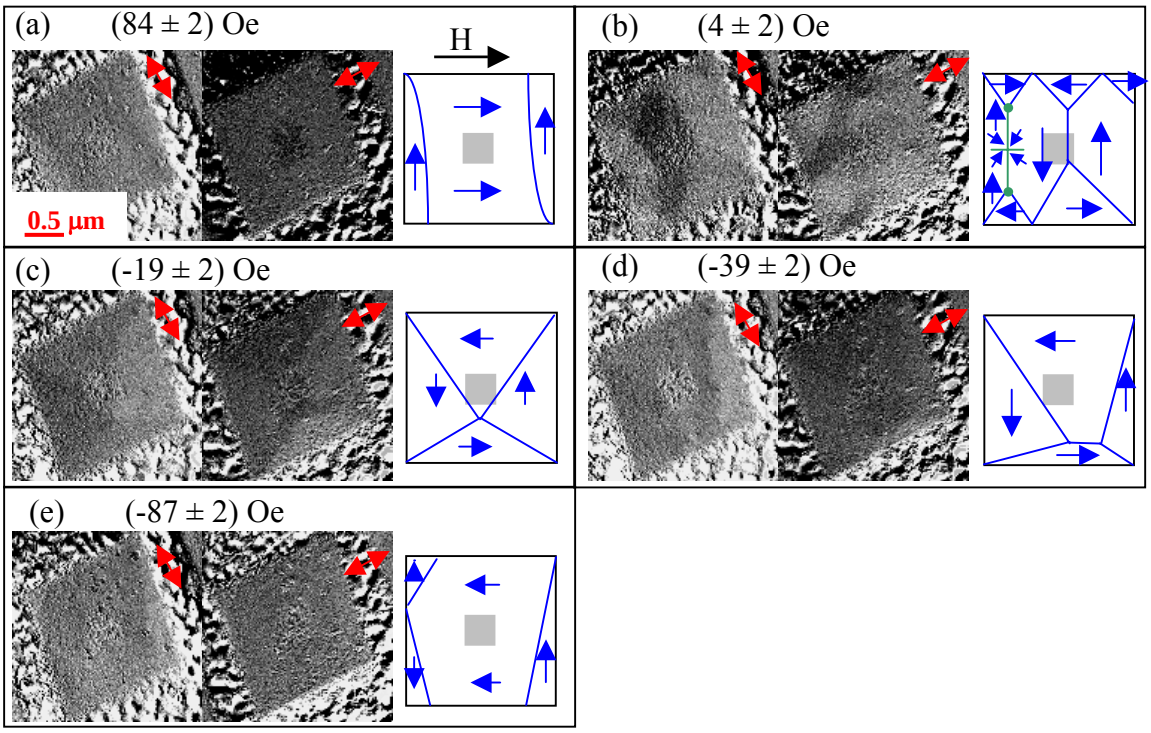

Figure 6.12: DPC images for the first half of the magnetisation cycle, with schematic of magnetisation, of an element irradiated with the pattern shown using the 0.096 nCµm^{-2} dose. Grey lines indicate FIB irradiated sections, blue indicates the direction of magnetic domains and domain walls, red arrows indicates the direction of sensitivity and green the cross-tie structure.

A higher magnification DPC image of the multi-domain state in Figure 6.12(b) in the area in and around the irradiated section is shown in Figure 6.13. The in-plane components of the integrated magnetic induction are shown in Figures 6.13(a) and (b); a schematic of the induction is shown in Figure 6.13(c) and the sum image is shown in Figure 6.13(d). Due to the size of the crystallites in the irradiated region (grain growth due to the Ga^+ beam) they mask the magnetic contrast in the difference images (Figures 6.13(a) and (b)). This highlights one of the limitations concerning this technique discussed in section 3.3. The higher magnification sum image does not show the same irregular edge structure as is observed in chapter 5. The main reason for the more regular structure is the milled depth, in chapter 5 the irregular edge structure is greatest for the FIB lithographed

elements with the highest doses. Conversely for elements fabricated from lower doses, little roughness is observed, as is the case with the irradiated areas here.

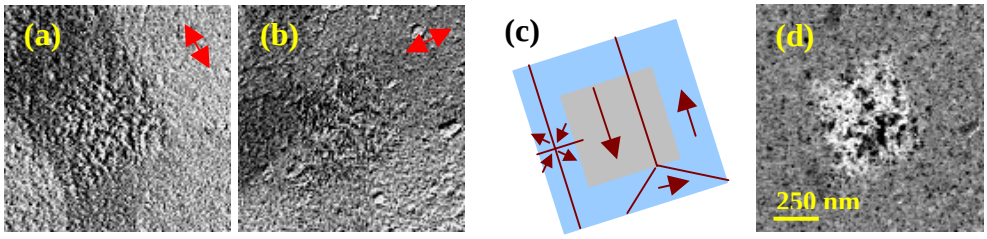

Figure 6.13: (a) and (b) higher magnification DPC images of Figure 6.12(b), with schematic (c). Blue represents the unirradiated film, grey the irradiated section burgundy the magnetic domain wall and direction and red the direction of sensitivity in the image. Included is the sum image (d).

Upon decreasing the magnetic field applied to the 2×2 μm^2 element with the magnetisation disturbed in a S-type state shown in Figure 6.12(e) (for convenience shown again as Figure 6.14(a)) the magnetisation within the element enters a multidomain state, Figure 6.14(b). Visible within the multidomain state is a cross-tie structure (outlined in green). As the field is reduced to zero, a single vortex state forms, Figure 6.14(c), although the core is observed to be in the irradiated area, similarly to the simulation shown in Figure 6.11(a). As the field is increased in the opposite direction a four-domain state is observed, Figure 6.14(d). A further increase in the applied magnetic field expels the four-domain state leaving the magnetisation in an S-state, Figure 6.14(e).

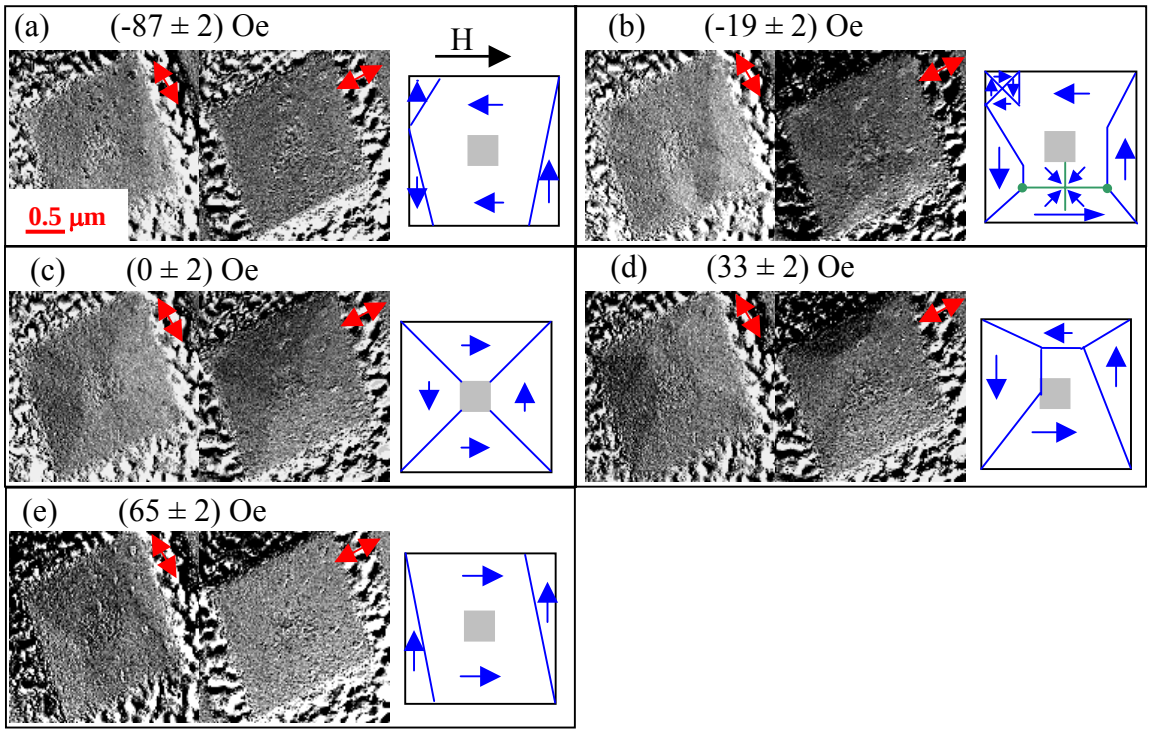

Figure 6.14: DPC images for the second half of the magnetisation cycle, with schematic of magnetisation, of an element irradiated with the pattern in Figure 6.1(c) using the 0.096 nCµm^{-2} dose. Grey lines indicate FIB irradiated sections, blue indicates the direction of magnetic domains and domain walls, red arrows indicates the direction of sensitivity and green the cross tie structure.

In zero applied field, Figure 6.14(c), the vortex core cannot be accurately determined. A Fresnel image of the element in zero applied field, Figure 6.15, however, shows the core to be outside the irradiated area. Again the large crystalline structure in the irradiated area obscures the magnetic contrast in the image. Although the non-magnetic contrast masks the path of the domain walls as they infringe on the irradiated area in the Fresnel image, it could be suggest that the domain walls travel through the irradiated area. This infers that the area is not magnetically dead and it is magnetostatically coupled to the non-irradiated section.

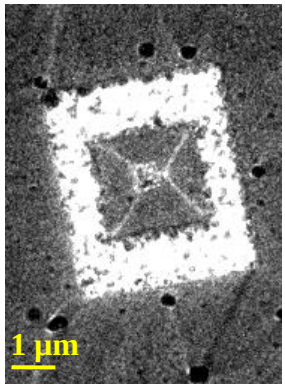

Figure 6.15: Fresnel image of the remanent state imaged by DPC in Figure 6.14(c).

6.4.2 Elements irradiated with interconnecting trenches

An OOMMF simulated magnetic field free state for the 2×2 μm^2 element irradiated with a series of 250 nm wide connecting trenches appear as two multidomain regions separated by a non-magnetic region, Figure 6.16(a). The outer section in the simulation appears to reverse through the formation of head to head domains [8] (Figures 6.16(b) and (c)), which are observed experimentally (Figures 6.17 and 6.17). The inner section also exhibits properties that are observed experimentally (the vortex formation and annihilation Figures (6.16(b), (c), (f) and (h)). The experiment also predicts the two-stage reversal for the inner and outer section, although the magnitudes of the event fields differ to those observed experimentally.

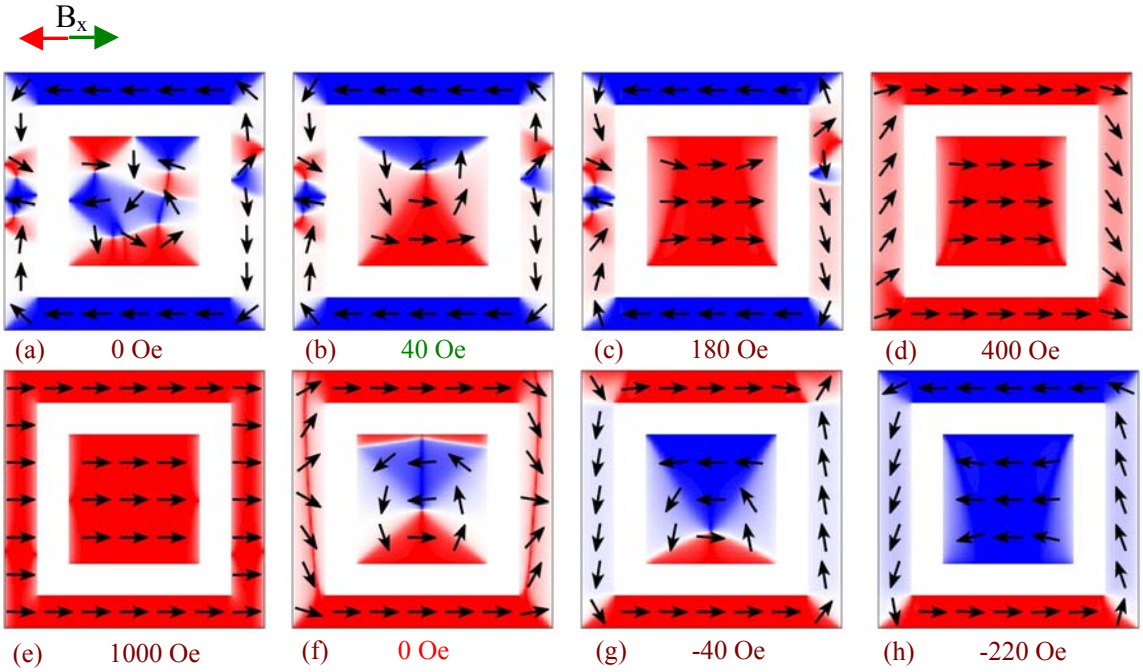

Figure 6.16: OOMMF simulation of the pattern shown in Figure 6.1(d) cycled between an applied field of ± 1000 Oe.

A 2×2 μm^2 element irradiated with a series of connecting trenches 250 nm wide using the highest dose (0.096 nCμm^{-2}) has been cycled through a magnetic field and DPC images of key magnetic points are shown in Figures 6.17 and 6.18. In a large enough magnetic field the magnetisation within the inner section of element is fully saturated in direction of the field but the outer element forms an onion state [9], Figure 6.17(a). Upon decreasing the field the magnetisation of the area of the element inside the irradiated section forms a C-type state, Figure 6.17(b). In the outer area faint contrast, which could be attributed to the onion state can be observed (although it is hard to tell with the physical contrast that is generated).

A further decrease in the applied field allows the inner section of the element to overcome the energy barrier and form a four-domain flux closure structure, Figure 6.17(c). Again, in the outer section the element appears to be in the same onion structure. After the applied field has been decreased to zero and increased in the opposite direction, Figure 6.17(d), the magnetisation within the inner section of the element forms an S-state, while the magnetisation in the outer element starts to reverse and a head to head wall is observed (although the detail is obscured). The vortex expulsion in the inner section and beginning of reversal the outer section with the head to head vortices (Figure 6.17(d)) is evidence of a two-stage reversal within the element. A further increase in the applied field orders the magnetisation within the inner section in the direction of the applied field with the outer section in the reverse onion state, Figure 6.17(e).

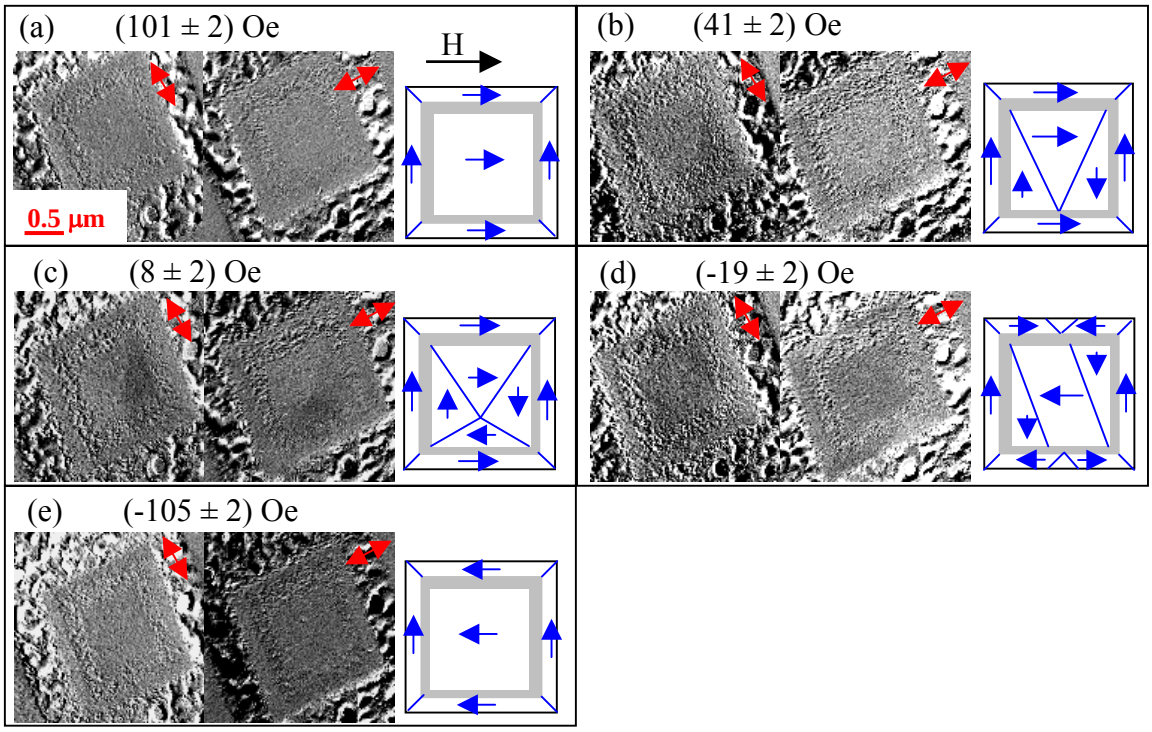

Figure 6.17: DPC images for the first half of the magnetisation cycle, with schematic of magnetisation, of an element irradiated with the pattern shown using the 0.096 nCµm^{-2} dose. Grey lines indicate FIB irradiated sections, blue indicates the direction of magnetic domains and domain walls and red arrows indicates the direction of sensitivity.

As the applied field is decreased from the saturation field (Figure 6.18(a)), the magnetisation of the inner section of the element forms a flower state and the outer section remains in an onion state, Figure 6.18(b). Again, for convenience the image of the element in the applied field (Figure 6.17(e)) is shown in Figure 6.18(a). A further decrease in the applied field is sufficient to allow the magnetisation to form the four-domain flux closure in the inner section of the element, Figure 6.18(c), notice the vortex forms off-centre. The

off-centre position and proximity to the lower irradiated edge suggest influence from the outer section or a pining site which allows the formation on this edge as opposed to the upper edge where the previous vortex was expelled. The magnetisation in the outer section starts to form head to head domains prior to the reversal of the outer section. At remanence the vortex in the inner element is still off-centre and more domains have formed in the outer section, Figure 6.18(d). The magnetisation within the element reverses by entering an S-state in the inner section and through domain rotation in the outer section of the element, Figure 6.18(e). An increase in the applied field further saturates the magnetisation within the inner section to the direction of the applied field and the outer section switches to the reverse onion state, Figure 6.18(f).

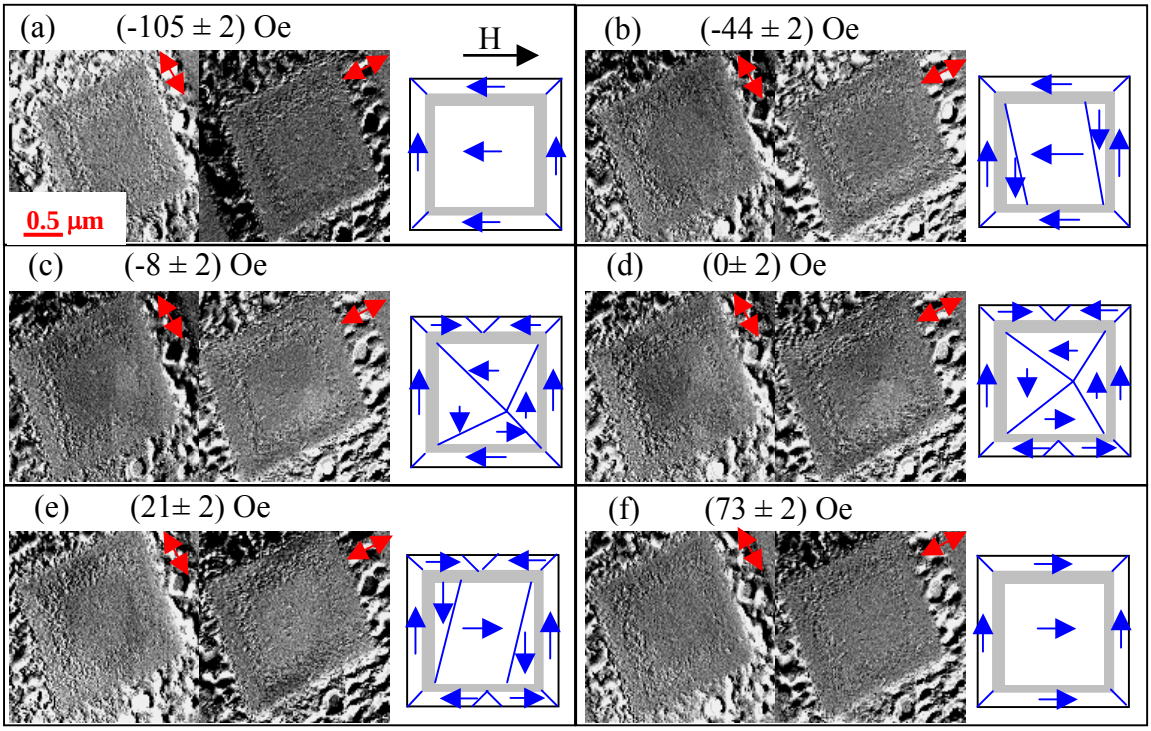

Figure 6.18: DPC images for the second half of the magnetisation cycle, with schematic of magnetisation, of an element irradiated with the pattern shown using the 0.096 nCµm^{-2} dose. Grey lines indicate FIB irradiated sections, blue indicates the direction of magnetic domains and domain walls and red arrows indicates the direction of sensitivity.

A 2×2 µm^2 element irradiated with the same pattern discussed in Figures 6.17 and 6.18 using the second highest dose (0.048 nCµm^{-2}) displays different magnetic characteristics when cycled through an applied magnetic field. DPC images of the element at important events as the element is cycled through the applied field are shown in Figures 6.19 and 6.20. The magnetisation within the element appears to be saturated in the direction of the applied field when in a sufficiently large applied field, Figure 6.19(a). As the applied field is decreased domains begin to form within the element, Figure 6.19(b). The domain on the

right side of the element appears to cross the irradiated area and appears to be pinned to the lower irradiated edge. A further decrease in the applied field lowers the energy in the system sufficiently to allow the magnetisation within to form a four-domain flux closure structure, Figure 6.19(c). As the applied is reduced to zero the vortex returns to the centre of the element. Increasing the applied field in the opposite direction drives the vortex into the opposite edge of the element, Figure 6.19(e). The vortex core is off-axis with respect to the central axis of the element and has been pinned by the irradiated section. A further increase in the applied field in the opposite direction expels the vortex core and the magnetisation becomes saturated in the opposite direction, Figure 6.19(f). Here the irradiated section has little influence over the magnetisation in the element, except to pin it at certain applied field magnetitudes.

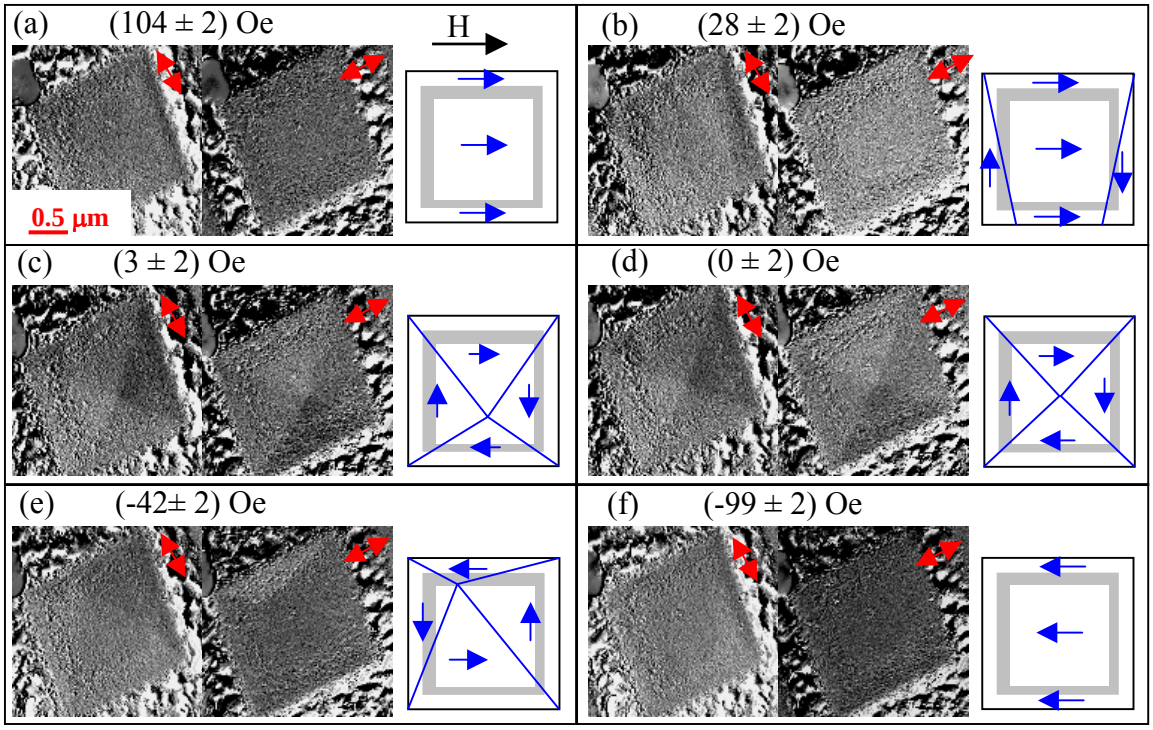

Figure 6.19: DPC images for the first half of the magnetisation cycle, with schematic of magnetisation, of an element irradiated with the pattern shown using the 0.048 nCµm^{-2} dose. Grey lines indicate FIB irradiated sections, blue indicates the direction of magnetic domains and domain walls and red arrows indicates the direction of sensitivity.

As the applied field that is used to saturate the magnetisation within the element in Figure 6.19(f) (for comparison shown as Figure 6.20(a)) is reduced to zero and eventually increased in the opposite direction the magnetisation follows a similar path to that shown in Figure 6.19, as shown in Figure 6.20. An exception is the formation of an intermediate state, Figure 6.20(c), before the formation of the four-domain flux closure state, Figure 6.20(d). In the intermediate state the domain walls have been influenced by the irradiated

section and the formation of the four-domain flux closure structure does not occur until the energy from the applied field is lowered by a sufficient quantity.

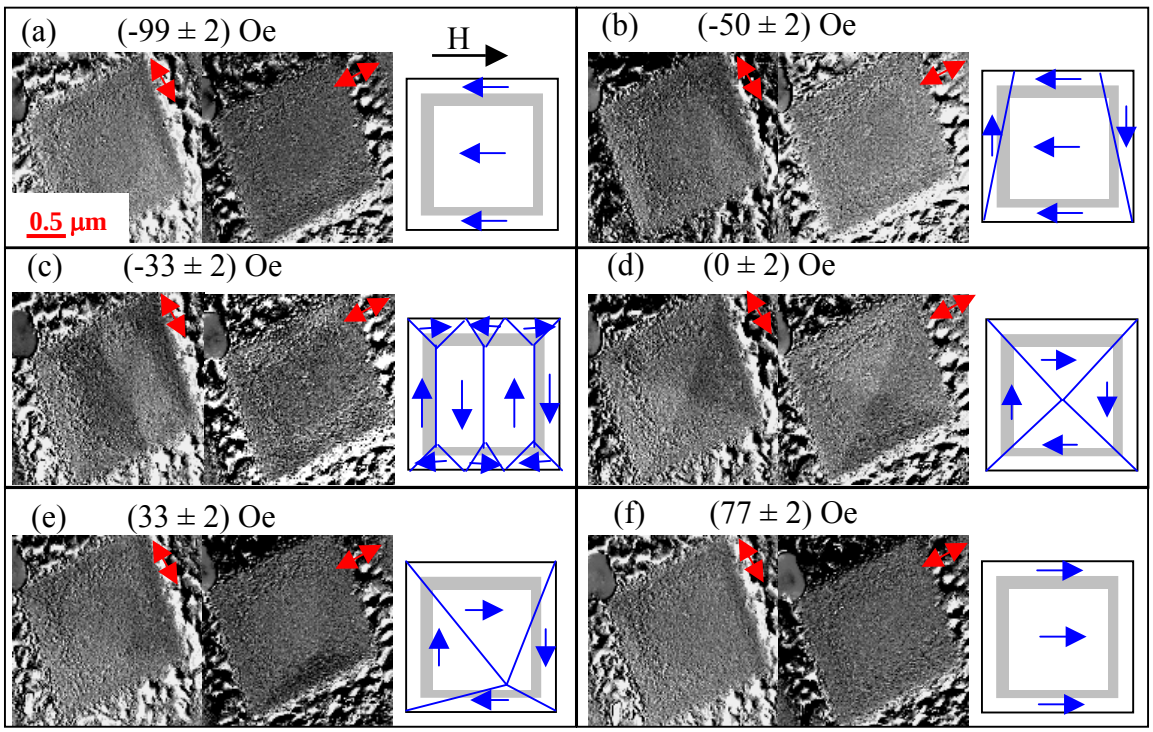

Figure 6.20: DPC images for the second half of the magnetisation cycle, with schematic of magnetisation, of an element irradiated with the pattern shown using the 0.048 nCµm^{-2} dose. Grey lines indicate FIB irradiated sections, blue indicates the direction of magnetic domains and domain walls and red arrows indicates the direction of sensitivity.

As can be observed in Figures 6.17–6.20, a change in dose alters the magnetisation path that is observed within two similar elements. When the 2×2 µm^2 element is irradiated with a lower dose (0.048 nCµm^{-2}), the magnetisation tends to form a continuous flux closure structure over the whole element that is only slightly influenced by the irradiated section (the irradiated section acts to pin the vortex core when the core is close to it). This is opposed to the element irradiated with the higher dose (0.096 nCµm^{-2}) where the irradiated area creates an element that has a two-stage reversal, one field for the inner section and a second higher field for the outer section.

6.5 Conclusions

Bright field images of all the irradiated 2×2 µm^2 elements that were fabricated by FIB lithography from 10 nm Cu/20 nm permalloy/5 nm Cu on a 50 nm thick, silicon nitride substrate reveal good clearance within the surrounding trenches. Alterations to the grain structure within the elements are only observed in elements irradiated with area patterns. Other patterns that have been irradiated into the elements do not show the grain growth

within the elements. Visible within the unirradiated areas of all of the elements are large grains that could be a result of either the deposition process or contaminants on the surface. Elemental mapping through EELS or AES or a similar technique would be beneficial to clarify the components of the elements and their quantities in the system.

Fresnel images of the majority of 2×2 μm^2 elements irradiated with a pattern behave in a similar fashion to the unirradiated elements. The elements form a four-domain flux closure structure similar to those discussed in chapter 5. The behaviour of these elements is again similar as a magnetic field is applied.

Only when the elements are irradiated with high doses (0.048 and 0.096 $nC\mu m^{-2}$) and with certain patterns can an effect on the magnetisation within the elements be observed. The irradiated areas act to: displace the vortex core (diagonal cross): form a cross-tie structure then collapse to a vortex with the core displaced (horizontal/vertical cross): disrupt the formation of the vortex core and trap the domain wall (irradiated area): segregate the magnetisation into coupled inner and outer elements (irradiated connecting areas): and trap domain walls as the vortex passes through the element (lower dose irradiated connecting trenches).

The OOMMF simulations of the irradiated elements are of limited use when used to describe the irradiated elements. In some cases the irradiated, magnetically dead, regions disrupt the whole element and forms a closely coupled series of elements. In others, the programme simulates observed remanent states but upon the application of a field deviates from that observed experimentally. The OOMMF simulations did predict the off-centre vortex core for the diagonal cross and the influence of the irradiated section on the vortex as the field was applied to the element. The simulations also predict the head to head domains in the outer section of the elements with interconnecting trenches and the resulting two stage reversal of the element. The differences in the simulated and experimental results are due to the assumptions made for the two-dimensional programme. Firstly that the irradiated section is magnetically dead: DPC and Fresnel images indicate that this may not be the case. Secondly the irradiated section is a well-defined region with an abrupt change: it has been shown in chapter 5 that the tails of the beam (believed to be Gaussian in nature) can influence areas that were supposed to be unirradiated. Thirdly, that the magnetic material used had the properties of unirradiated permalloy: as has been shown by experimentation, this is not always the case, intermixing can alter the properties of the magnetic materials. To overcome such problems the simulation could be run using the three-dimensional model of OOMMF that allows these problems to be incorporated into the simulation.

Bibliography

[1] McGrouther D., Chapman J.N., Vanhelmont F.W.M., J. Appl. Phys. 95(12) 7772.

[2] OOMMF simulation package available for download at NIST (URL active 16/02/06): http://math.nist.gov/oommf/

[3] Kaminsky W.M., Jones G.A.C., Patel N.K., Booji W.E., Blamire M.G., Gardiner S.M., Xu Y.B., Bland J.A.C., Appl. Phys. Lett. 78(11) (2001) 1589.

[4] FEI technical manual on operation of FIB microscope PN 20486-B.

[5] Williams D.B., Carter C.B., *Transmission electron microscopy"*, Plenum Press 1996, ISBN 030645324X.

[6] A brief description of Auger electron spectroscopy can be found at (URL active 2/9/2006): http://www.uksaf.org/tech/aes.html

[7] National Institute for Standard and Technology: http://math.nist.gov/

[8] Brownlie C, McVitie S., Chapman J.N.C., Wilkinson C.D.W., J. Appl. Physics 100 (2006) 033902.

[9] Uhlig T., Zweck J., Phys. Rev. Lett. 93(4) (2004) 047203-1.

7 The physical and magnetic structure of cobalt arrays fabricated by electron beam lithography

In this chapter, the results from a 50 nm thick, 10×10 μm^2 cobalt array composed of 270×270 nm^2 elements with a 400 nm period in both the x and y directions (defined in Figure 7.1), supported on 50 nm thick silicon nitride substrate are discussed. The purpose of studying such structures is to determine any superdomain structure relating to the magnetics of the array. The cobalt arrays have been fabricated by the electron beam lithography method (section 2.2) and deposition of the cobalt was by thermal evaporation (section 2.1.2). The physical and magnetic properties of the arrays have been investigated by bright field TEM imaging (section 3.2), Fresnel and differential phase contrast (DPC) imaging (discussed in section 3.3) with the results discussed in section 7.1. The Fresnel images obtained from the cobalt array have been digitised to analyse the level of ordering within and between the remanent states of the array and are discussed in section 7.2.

The OOMMF simulation package [1] (section 1.4.2) has been employed to model the magnetic state of the 270×270 nm^2 element and the behaviour of the magnetisation within the element as it is subject to an applied field. The OOMMF software has also been used to model the ground state and behaviour of reduced arrays (dimensions 4×4 μm^2) as they are cycled through an applied magnetic field. The resultant OOMMF states have also been used to calculate the stray field emanating from the element in different magnetic states, as well as the stray field interaction of the nearest neighbours, to try and determine any link between magnetic behaviour in the array and magnetostatic stray fields. The stray fields

have been calculated using a programme described in section 1.4.3, based on work by Beardsley [2] and McVitie et al, [3].

7.1 10×10 μm^2 cobalt arrays with 400 nm periodicity

A 50 nm thick cobalt array with overall dimensions of 10×10 μm^2 has been fabricated for elements with a 1:1 in-plane aspect ratio and 400 nm periodicity in both in-plane axes: the nominal dimensions of the individual elements are 270×270 nm^2.

7.1.1 Physical structure of 270×270 nm^2 cobalt elements

The 10×10 μm^2 cobalt array (henceforth known as the array) fabricated by EBL has been imaged using the bright field imaging technique discussed in section 3.2. The nominal dimensions of elements are expected to be 270×270 nm^2. A low magnification bright field TEM image is shown in Figure 7.1(a). In the low magnification image the squares appear to be well defined structures with regular gaps in both directions, for a more accurate measure of the element sizes however, higher magnification images are necessary, Figure 7.1(b). The low magnification image shows that the array is complete and intact, there are no elements missing or large areas of resist covering the array. Also shown in Figure 7.1 are the user defined x- and y-axes that are used for the orthogonal magnetisation cycles. From Figure 7.1(b) the elements appear to be square, although some appear to have some residual strands of resist still attached to the element, circled. The periodicity of the array also appears regular in this image.

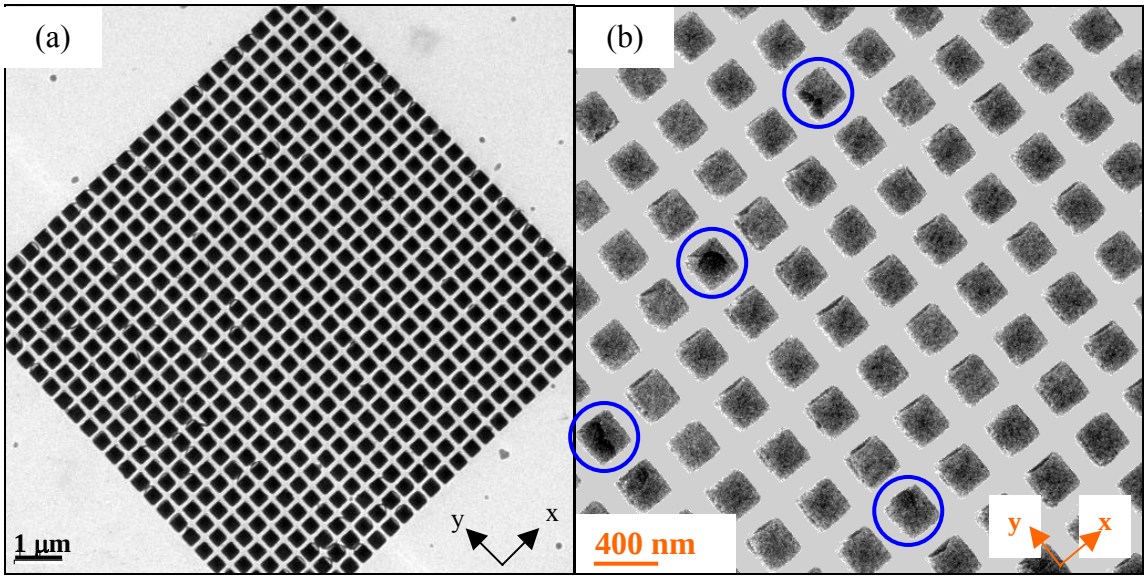

Figure 7.1: (a) low magnification and (b) higher magnification bright field TEM images of the 10×10 μm^2 array with elements of a nominal size of 270×270 nm^2 and a periodicity of 400 nm. Also shown are element with resist still attached (circled) and the user-defined axes.

The reduced dimensions of the elements within the array could, however, lead to texturing of the grains within the elements; this is where one crystalline orientation becomes the dominant orientation. Analysis of the crystalline structure within an element could be through analysis of the diffraction patterns at different tilt angles to determine if there is any texturing. The texturing, if any, may lead to anisotropy within the elements; if this is the case, then it would alter the energetics of the system and the micromagnetic simulations would have to be adjusted accordingly. As no analyse has been carried out on the texturing of the elements, then it is assumed for the remainder of the thesis that there is none. The texturing of the individual elements would be an interesting topic to study in greater detail.

From the analysis of several images similar to Figure 7.1(b) an estimation of the average element size in the x- and y-axis has been made. Averaging the orthogonal x and y directions (defined in Figure 7.1) over the entirety of the array, a difference between the x- and y-axes is observed. The average dimensions are similar to the expected dimensions, being (270 ± 4) and (276 ± 4) nm for the x- and y-axes respectively.

7.1.2 Magnetic structure of the array

Viewing the 270×270 μm^2 cobalt elements using both underfocus (Figure 7.2 (a)) and overfocus (Figure 7.2(b)) Fresnel imaging, two different levels of contrast are visible within the array. The light and dark contrast that is visible within the separate elements (that corresponds to different rotations of the vortices) reverse with the focus. One vortex rotation is clockwise and the other rotation is anticlockwise. In the underfocus image (defined as a weakened lens, as in [4]), the light contrast indicates a clockwise vortex rotation (Figure 7.2(e)) and the dark contrast indicates the anticlockwise vortex rotation (Figure 7.2(f)). This information is confirmed by DPC imaging of the array, shown in Figure 7.2(c) and (d).

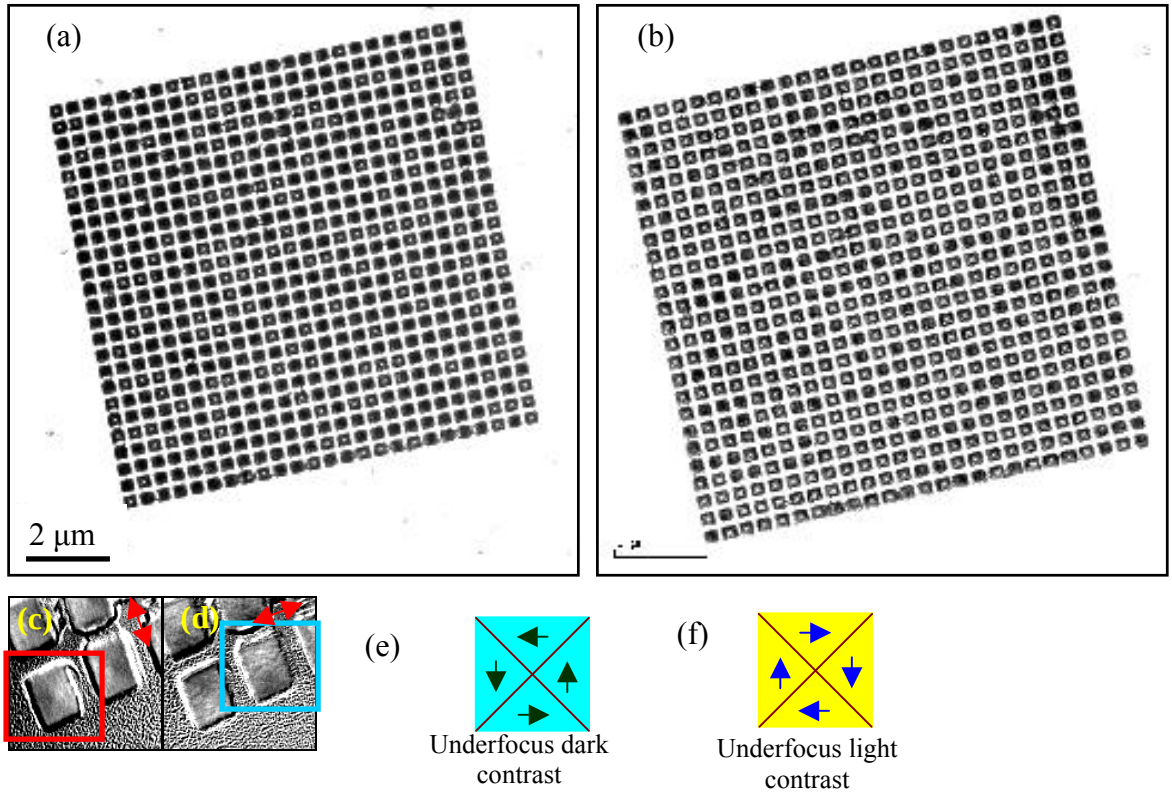

Figure 7.2: (a) underfocus and (b) overfocus Fresnel images of dark and light magnetic contrast within 10×10 µm^2 array. (c) and (b) DPC images of light (red box) and dark (blue box) contrast in a underfocussed Fresnel images. (e) and (f) are schematics of the rotation of the magnetisation within the elements.

We have found, through experiment, that the magnetic vortices within the cobalt elements in the array are formed and expelled over a range of fields, as shown in Figure 7.3. In a high applied magnetic field (~1150 Oe), the magnetisation within the elements is in C- state, Figure 7.3(a). As the field is reduced, two vortices with clockwise chirality (red boxes) form within two elements, Figure 7.3(b). A further reduction in the field allows twelve more clockwise vortices to form in the remaining elements, Figure 7.3(c). Cycled over ten fields, the vortex formation for the clockwise chirality begins at, on average, (690 ± 25) Oe and ends at (373 ± 24) Oe. As the applied field is reduced to zero, Figure 7.3(d), and then increased in the opposite direction a similar pattern of events is observed. At a large field (~-1200 Oe) the majority of the vortices are expelled with a few remaining, Figure 7.3(e). The remaining vortices are expelled with a slight increase in the field. Vortex expulsion, for vortices with clockwise chirality distributions, begins at, on average, (-1134 ± 23) Oe and ends at (-1264 ± 24) Oe. This spread in the formation and expulsion fields of the cobalt arrays is consistent with what has been previously been reported by Kirk et al, [5] and Kundrotatie et al, [6]. Kirk et al, found that the range at which cobalt arrays switch has a greater consistency than similar ones fabricated with permalloy. Kirk et al, also found that the range is approximately inversely proportional to the element width. Kundrotatie et al, found that the average switching field for cobalt

arrays is independent of the array spacing but the range of switching fields for the individual elements decreases with spacing due to interactions between the elements.

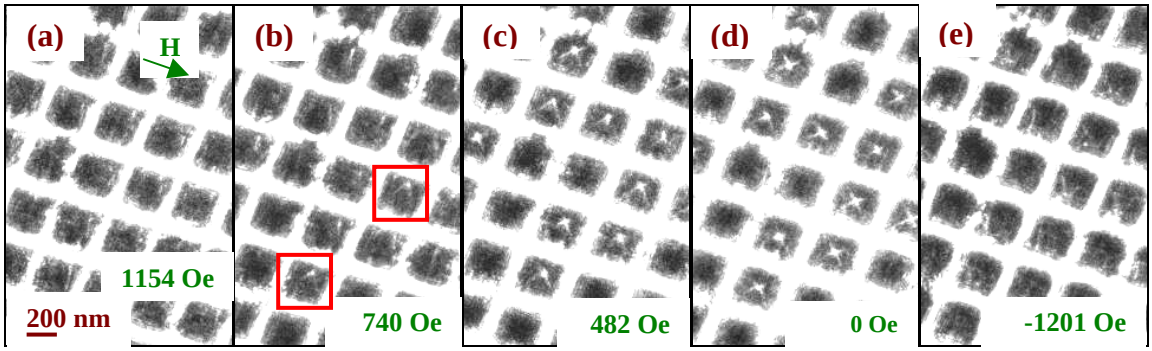

Figure 7.3: magnetic vortices forming and expelled in a selection of the array consisting of 270×270 nm^2 cobalt elements. Uncertainty in the field values are ± 21 Oe. The red boxes in (b) indicate the first elements to form vortices with a clockwise chirality.

Large magnetic fields (~0.7 T) have been applied to the array along both the x and y in-plane axes (as defined in Figure 7.4) in the CM20 TEM (described in section 3.1). As electrical contacts on the goniometer limit the tilt in one direction the full field can only be applied in one direction, as a result three separate procedures, described below, were employed to apply the full field in two opposite directions. The three procedures are used to evaluate the reproducibility of the magnetic states within the arrays. The specimen was mounted in a tilt and rotate rod to allow the fields to be applied.

i) The array is rotated from 0^o to 180^o about the x- or y-axis (as defined in Figure 7.4) with the array exposed to the full magnetic field (~0.7 T) in-plane (with no out-of-plane field) for each rotation. Fresnel images of the array were then taken at remanence for each rotation.

ii) The array is kept at 0^o in-plane orientation in the x- or the y-plane and then a field of ±~0.7 T was applied, with Fresnel images taken at remanence.

iii) (Similar to the second method and done for comparative purposes). The array is rotated to 180^o in-plane and remains there while a field of ±~0.7 T is applied and Fresnel images are taken at remanence.

In general the array was subjected to the three procedures for three complete cycles (a forward and reverse cycle) in both in-plane axes.

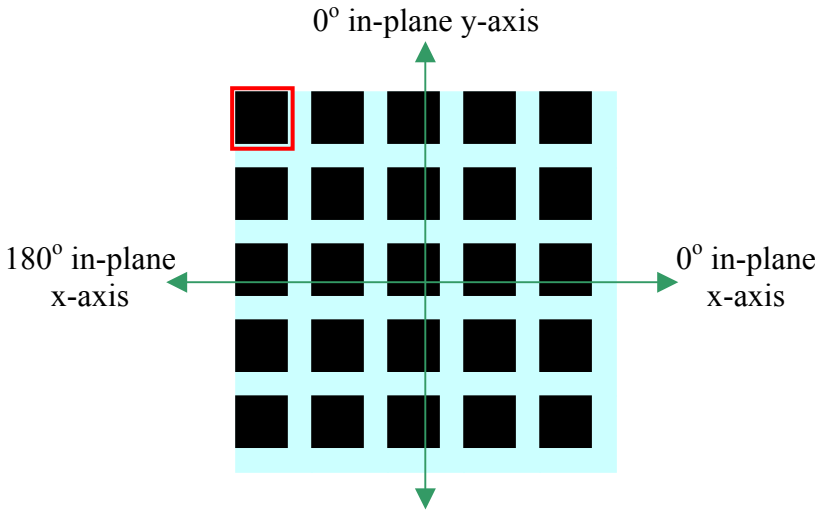

Figure 7.4: schematic of the direction of the applied of magnetic fields on the cobalt array, the red box indicates the (1, 1) position where all images are referenced from.

An example of the remanent states resulting from the second magnetisation method, described above, as it is applied along the y-axis is shown in Figure 7.5. In Figure 7.5(a), the red box has been moved to indicate the rotation of the image from earlier figures. In Figure 7.5(a) (the initial state), the magnetisation of the vortices within the array is predominantly of an anticlockwise orientation, with the distribution being ~80/20 in favour of anticlockwise vortex chiralities. After the first ~0.7 T magnetic field is applied in the y direction, the vortex chirality distributions reverses to become predominantly clockwise, the distribution changes to be 91/9. An image of this is shown in Figure 7.5(b). A further ~0.7 T magnetic field is then applied in the opposite direction (-y); the distribution becomes 90/10 in favour of the anticlockwise vortex rotation. An image of this is shown in Figure 7.5(c). The array adopts a similar state and distribution to the image shown in Figure 7.5(b) when the magnetic field is applied along the original direction. An image of the state is shown in Figure 7.5(d). It is the distributions of clockwise to anticlockwise ratios in these remanent states that form the basis of the analysis of the ordering within the remanent states in section 7.2.

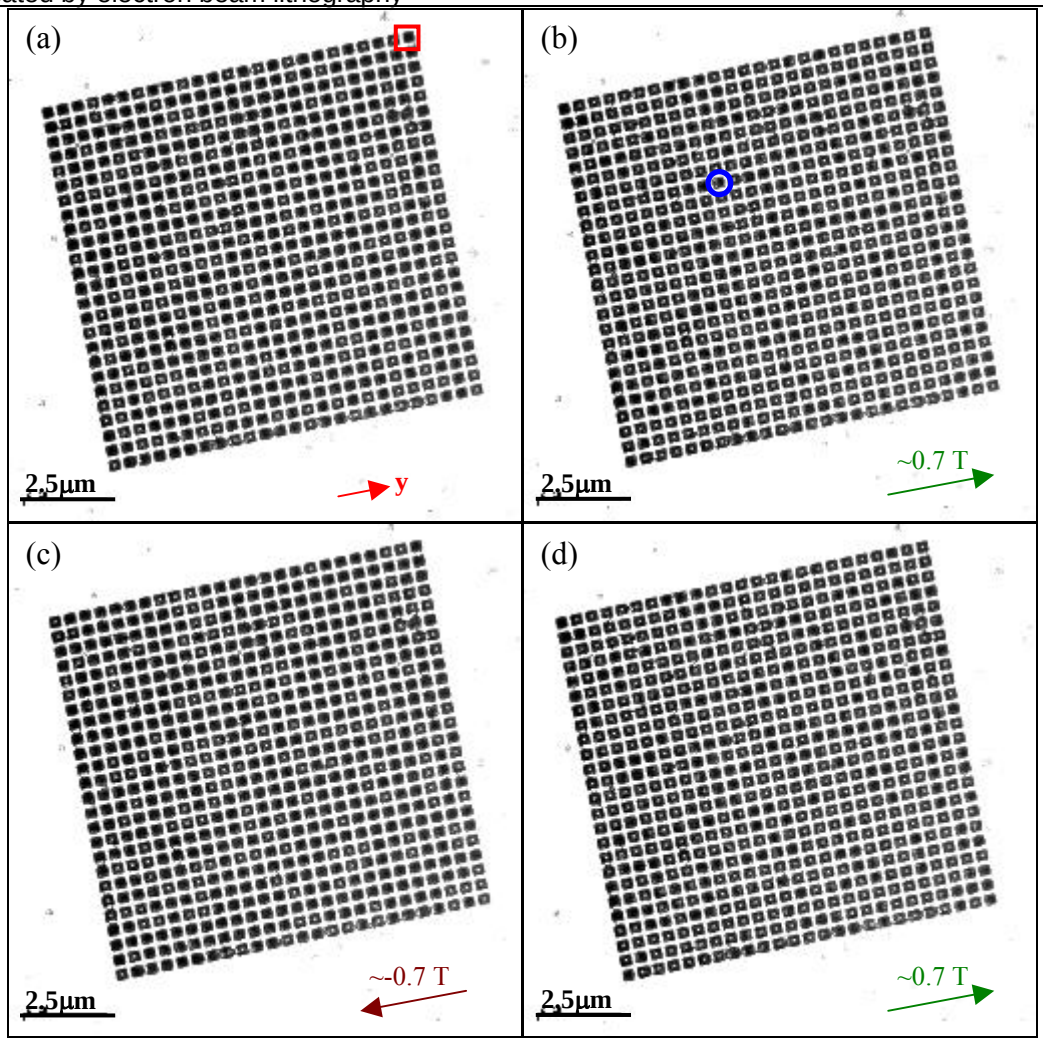

Figure 7.5:(a) low magnification Fresnel image of the initial state, (b) after being subjected to a magnetic field, (c) after being rotated by 180° in-plane and subjected to another magnetic field, (d) after being rotated by 180° in-plane again and being subject a magnetic field. Indicated in the image is the direction are of the field prior to that remanent field. The red box indicates the reference point of all digitised representations and the blue circle indicates a multiple vortex element.

The blue circle in Figure 7.5(b) indicates an element whose magnetisation is in a multiple vortex (a multivortex so to speak) state; that shall be explored further in section 7.4. As will be shown in section 7.4, these states have a preferential vortex direction and to simplify the analysis, these multiple vortex states have been assumed to be clockwise or anticlockwise depending on the dominant contrast.

7.2 Analysis of the magnetic distribution within the array

In order to assess any similarities within the magnetic vortex distribution of the different arrays and of the same array, a function, known as the correlation function, has been applied to the data. The correlation function, C, is defined in equation 7.1.

$$C = \frac{1}{N}\sum_{i}^{N} A_i B_i \qquad \textbf{(7.1)}$$

where i is an element in the arrays of A and B and N is the number of elements within the array. The arrays of A and B can either be two complete arrays at different remanent states of a cycle for cross correlation or reduced arrays in the same remanent state for auto correlation. Assigning the values of 1 to the clockwise rotation and –1 to the anticlockwise rotation of the vortices, the correlation of the magnetic vortex chiralities within the array can be assessed. Clockwise vortex rotation, as a result of the value assigned, appears as white contrast and anticlockwise vortex rotation appear as black. If there is complete correlation between both arrays then $C = 1$ and for complete anticorrelation $C = -1$.

The correlation function (equation 7.1) can be applied to a single array to determine the order within an array, this is known as the autocorrelation function, C_A. The autocorrelation function for a single array of *(n,n)* elements is determined by setting the autocorrelation array to run from *(1,1)* to *(n-m,n-o)* in *A* and *(1+m,1+o)* to *(n,n)* in *B*, where *m* and *o* are positives integers lying in the range between zero and *n* (*n* in itself being a positive integer). The value of *N* is decreased to reflect the fact that elements have been removed. For example, to determine the level of ordering within an array of *(5,5)* elements (shown in Figure 7.6) the autocorrelations for the horizontal, vertical and both diagonals (shown in Figure 7.7) can been measured over four integers. In the horizontal direction, *x*, the autocorrelation has been calculated from one row of separation (denoted *x+1*) to five rows of separation (denoted *x+5*). For one row, the autocorrelation arrays are taken from array *A* (red box in Figure 7.6(a) from *(1,1)* to *(4,5)*) to array *B* (blue box in Figure 7.6(a) from *(2,1)* to *(5,5)*), *N=20*. For five rows the autocorrelation arrays are taken from array A (red box in Figure 7.6(b) is *(1,1)*) and array B (blue box in Figure 7.6(b) is *(5 1)*), *N=5*.

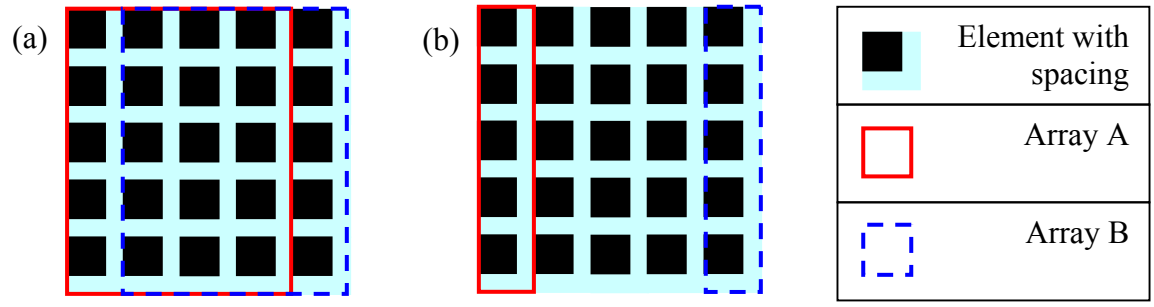

Figure 7.6: schematic of the autocorrelation arrays for (a) one spacing *(x+1)* and (b) five spacings *(x+5)* for a 5×5 element array. See key for colour details.

When $C_A = 1$, then the array can be said to have ferromagnet-like ordering (section 1.1). Conversely when the array has a C_A that alternates between -1 and 1 for odd and even spacing, then the array can be said to have antiferromagnet-like ordering (see section 1.2). If the average value of $C_A = 0$ for all autocorrelations then the array ordering is not well defined. The ordering could have moved towards a random distribution or a mixture of ferromagnetic like ordering and antiferromagnetic-like ordering.

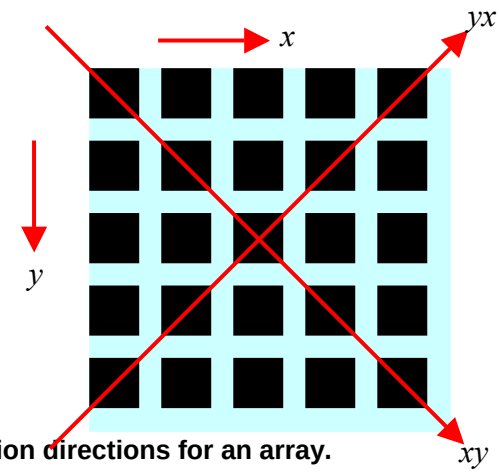

Figure 7.7: autocorrelation directions for an array.

Applying the correlation function to two separate remanent states of an array in a magnetising cycle can yield information about the distribution of vortex chirality within the arrays, this is known as the cross-correlation function, C_C. If $C_C = 1$ for the two arrays then the elements within the arrays can be said to be identical, where as is $C_C = -1$ then the elements within arrays can be said to be mirror states. If $0.5 \leq C_C \leq 1$ for two consecutive arrays in a magnetisation cycle then the two arrays have the majority of the same vortex chiralities at the same locations within the array. If $-0.5 \leq C_C \leq 0.5$ then there has been a shift in the distribution towards a more random magnetic distribution. If $-0.5 \leq C_C \leq -1$ the distribution the magnetic vortices within the array could be said to have predominantly reversed.

7.2.1 Saturation fields along the x- and y-axes of a 10×10 μm² array

An example of the digitised representations of the remanent states of a magnetisation cycle (the first magnetisation method, discussed in section 7.1.2) as the field was applied along the x-axis of the array is shown in Figure 7.8, denoted as cycle 1x. The initial remanent magnetic state (after the array had been exposed to a large magnetic field in the x-axis ~0.65 T) is shown in Figure 7.8(a); Figure 7.8(b) is the array after the first forward saturating magnetic field has been applied; Figure 7.8(c) is of the first reverse saturating magnetic field has been applied; this continues until the last representation (Figure 7.8(g)) which is after the third forward saturating magnetic field has been applied. Clockwise rotation vortices appear as white pixels and anticlockwise rotation appear as black. Also shown in Figure 7.8 for the digitised representations are the directions of the magnetic field applied prior to the formation of the remanent state. A comparison of the initial state, Figure 7.8(a) and the first remanent state after an applied magnetising field (known as 1F, Figure 7.8(b)) reveals little change in the distribution of vortices. Also visible in the digitised images are large areas of groupings of clockwise vortex chiralities and smaller groupings of anticlockwise vortex chiralities (domains so to speak). These domains are discussed in greater detail later in this section. Upon the application of a reverse saturation field (1R, Figure 7.8(c)) there is a reversal of the vortex chirality distribution, this is in addition to a reversal of the domains within the array. The vortex chirality distributions continue to reverse with the cycled field.

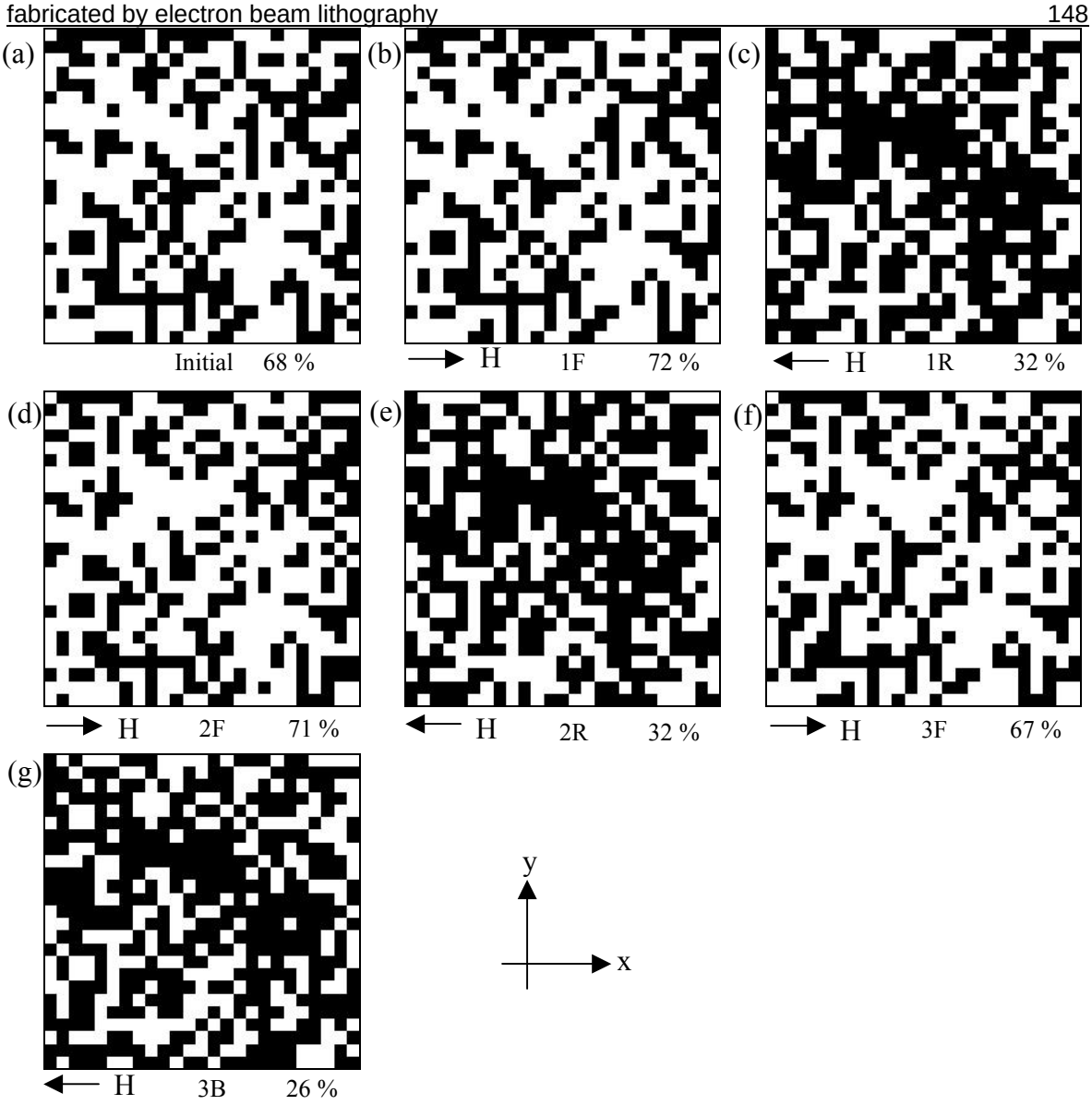

Figure 7.8: the digitised representations of the array subjected to saturation field cycle 1x from (a) intial to (g) the third reverse cycle. Shown below the image is the direction of the magnetic field applied prior to achieving this remanent state and the percentage of clockwise vortex chiralities.

The autocorrelation functions, applied along the two orthogonal easy axes (*x* and *y*, described in Figure 7.7), of cycle 1x are shown in Figures 7.9 and 7.10. From the autocorrelation plots against distance a non-zero autocorrelation function can be observed for both directions of the array. The low autocorrelation function indicates the presence of domains of similar chirality distributions that have limited sizes within the array, these domains are, however, short ranged (as can be observed within the digitised remanent representation, shown in Figure 7.8)). The autocorrelation function plots shown are representative of all the magnetisation cycles applied along the x-axis with slightly higher values measured for the y-axis.

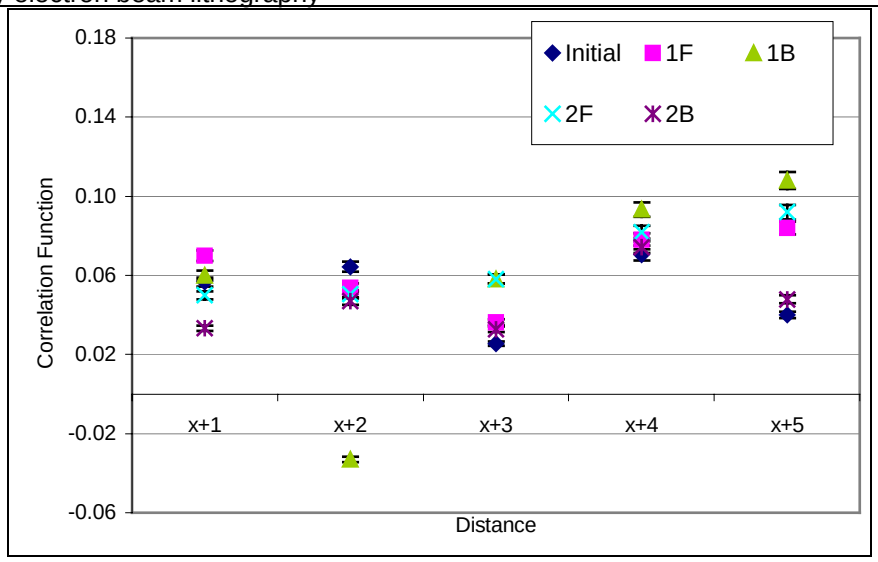

Figure 7.9: autocorrelation for the horizontal (*x* direction in Figure 7.7) of cycle 1x.

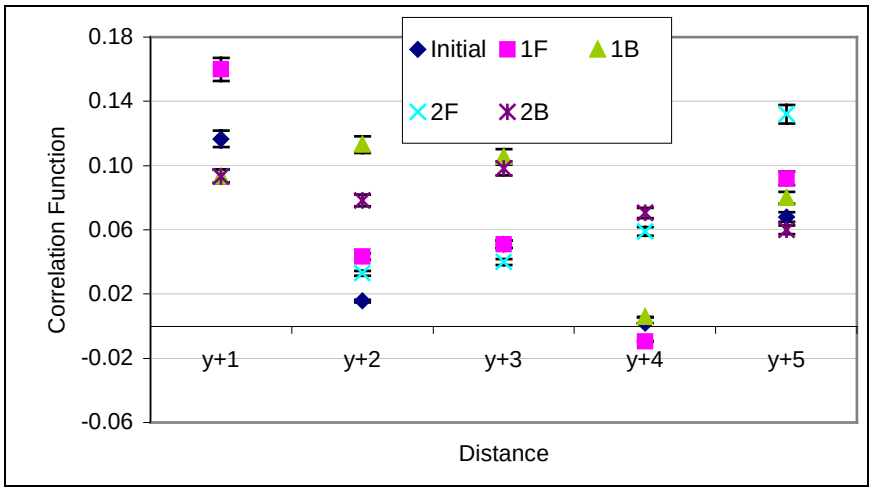

Figure 7.10: autocorrelation for the vertical (*y* direction in Figure 7.7) of cycle 1x.

An example of a digitised representation of a magnetisation cycle (similar to those applied along the x-axis) applied along the y-axis is shown in Figure 7.11, the cycle is denoted 1y. The states are represented in a similar fashion to that of cycle 1x (Figure 7.8). The initial state for cycle 1y (shown in Figure 7.11(a)) has a similar vortex distribution to that in cycle 1x, except with the anticlockwise being dominant. Previously the array had been subjected to a large field along the x-axis. As the saturation field is applied in the y–axis (shown in Figure 7.11(b)) the chirality distribution reverses to be in favour of the clockwise chirality. The vortex chirality distribution reverses as the applied field is cycled, similar to that shown in Figure 7.8. The y cycles do however have a larger split in the vortex chirality distributions than that observed in the x-axis cycles (~90/10%). A result of the larger chirality distributions is larger domains within the array compared to those of the x-axis cycles. The larger domains appear to reverse in nature with the direction of the

applied field and larger domains give rise to the slightly greater autocorrelation functions observed for the remanent states than for the x-axis.

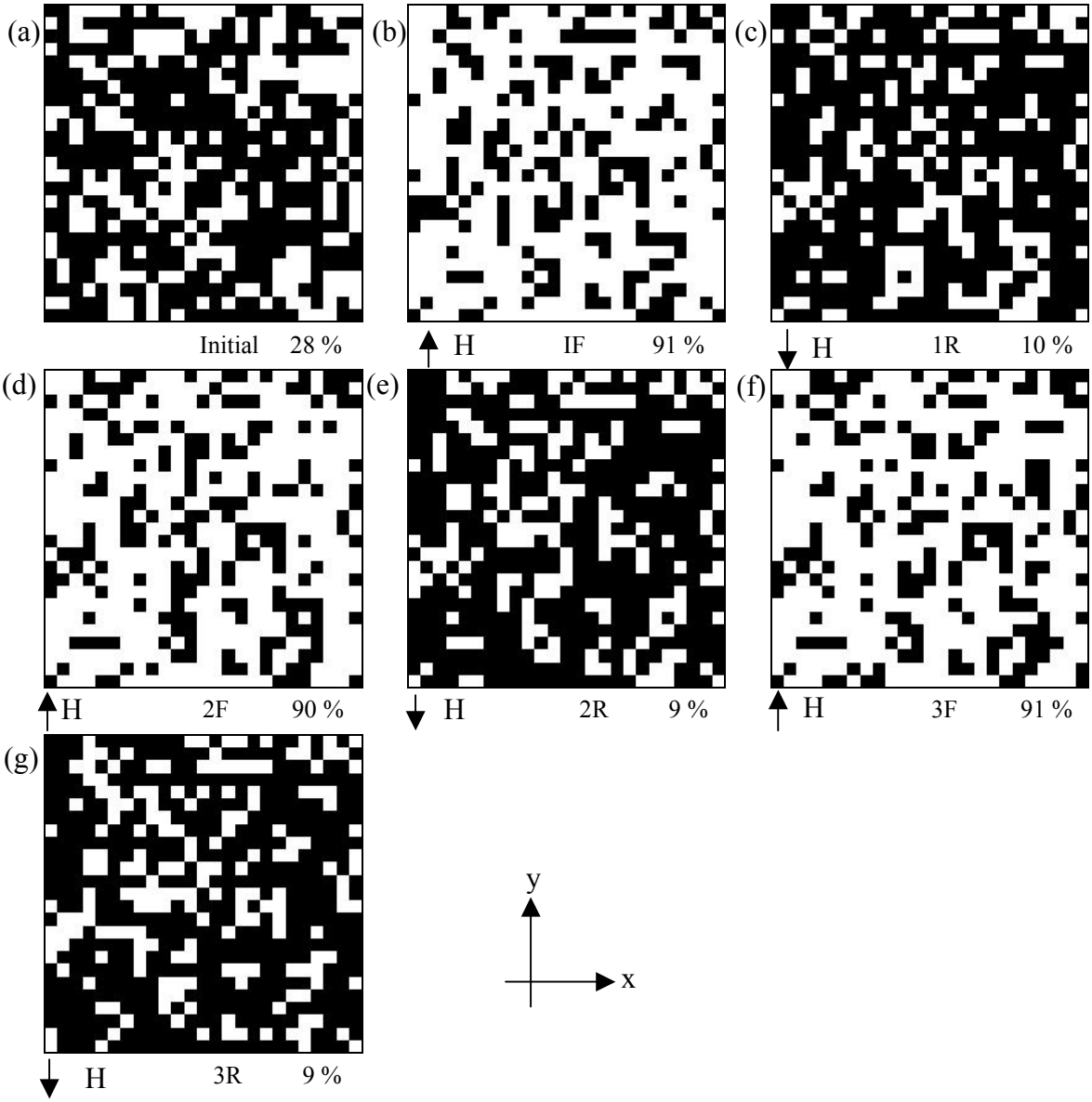

Figure 7.11: the digitised representations of the array subjected to saturation field cycle 1y from (a) intial to (g) the third reverse cycle. Shown below the image is the direction of the magnetic field applied prior to achieving this remanent state and the clockwise vortex chirality distribution.

A plot of the distribution of the clockwise vortex chiralities for the x- and y-axes loops is shown in Figure 7.12. Marked on the plot are the upper and lower average values (less the initial distributions) for the clockwise vortex distribution for both the x- and y-axes. The plot shows that the clockwise vortex chirality distribution has the greatest change in distributions as the applied field is cycled along the y-axis (blue dotted lines). The y-axis cycles also have a greater consistency (a spread of 2% is observed) in the vortex chirality distribution. The distribution of the clockwise vortex chiralities along the x-axis has been found to have larger spread of values, 8% for the upper x-axis and 4% for the lower x-axis.

The difference in the average clockwise vortex distribution between the x- (red dotted lines) and y-axes (blue dotted lines) suggests an anisotropy within the array. The slightly larger y-axis ((276 ± 4) nm compared to the (270 ± 4) nm for the x-axis) of the elements is the most probable source of the anisotropy, texturing of the crystallites could also account for it. To observe if there is any anisotropy within the film, the in-plane field could be applied along a diagonal of the array. If there is an associated anisotropy, the formation and expulsion of the vortex will occur off-axis of the diagonal. The direction the vortex takes will also give a qualitative result as to the direction of any anisotropy. Also visible in the plot shown in Figure 7.12 are out-of-phase points relating to cycles 3x and 3y, this is due to the nature of the applied field, see section 7.1.2.

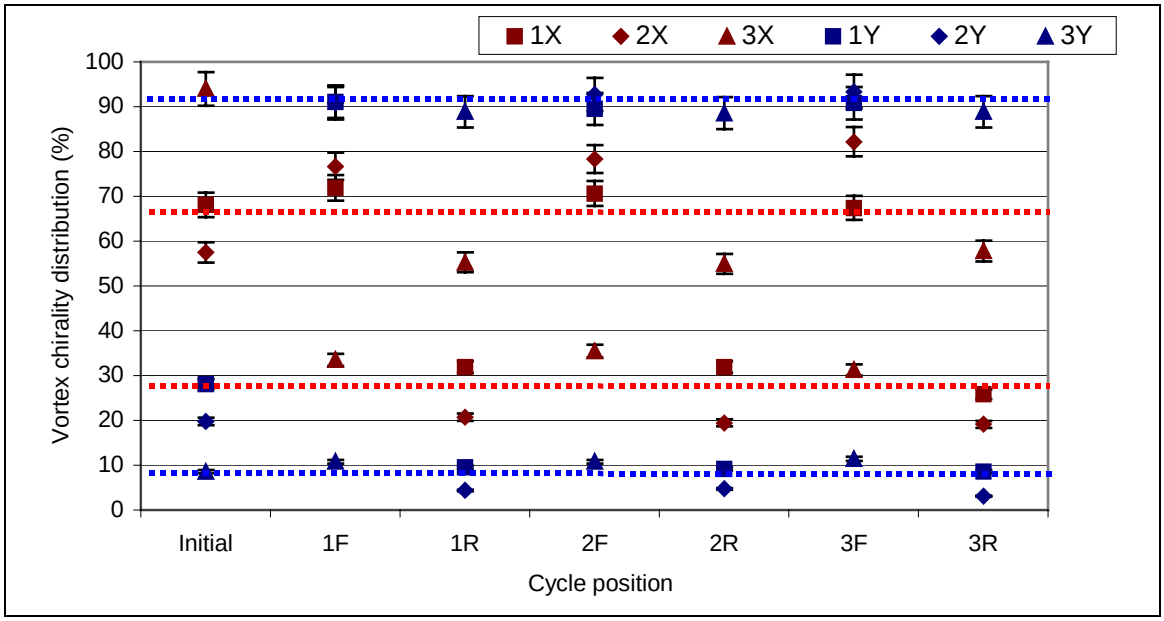

Figure 7.12: plot of the value of the clockwise vortex distributions for the magnetisation cycles (described in section 7.1.2), with average values shown. The red and blue dotted lines are the lower and upper averages values of the x- and y-axes cycles' respectively. An uncertainty of 4% is assumed for each.

7.2.2 The cross-correlation between remanent states in the magnetisation cycle

The cross-correlation functions between the remanent states in the individual magnetisation cycles (shown in the previous section) have been investigated, with the results discussed in this section. The cross-correlation functions between the consecutive remanent states are shown in Figure 7.13. The cross-correlation function for the magnetisation cycles is rarely above –0.6. The high negative cross-correlation function is what is to be expected if the vortex chiralities within arrays reverse with the direction of applied field (as is observed from the digitised representations). The cross-correlation

function here shows that the vortices within the arrays nearly completely reverse (a cross-correlation function of –1 would account for this). The magnetostatic interactions between the individual elements could be a reason for the partial reversal of the array (a subject to be explored in greater depth in section 7.3).

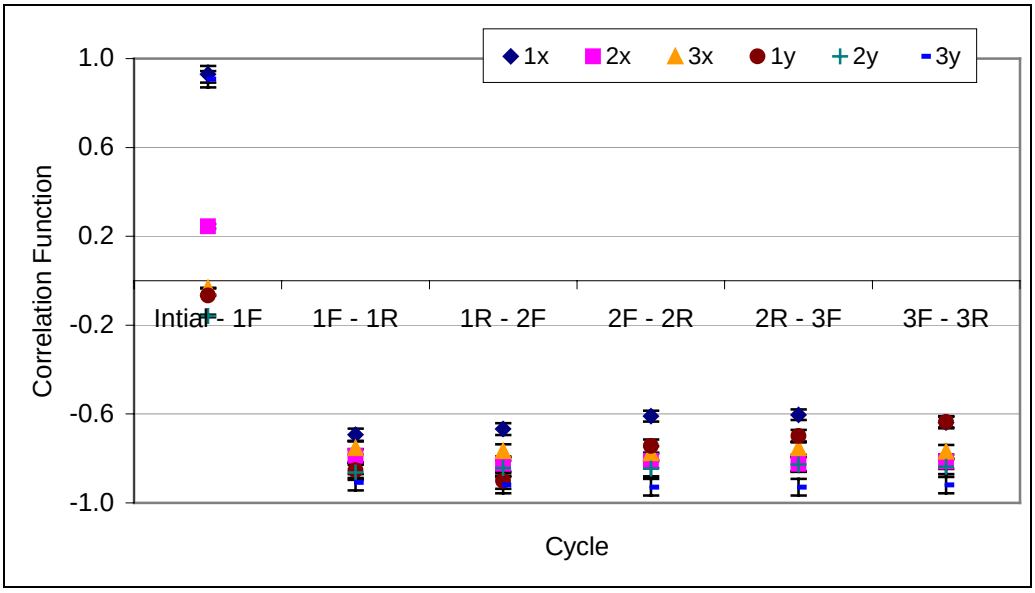

Figure 7.13: plot of the cross-correlation function against consecutive cycles for the magnetisation cycles of the two axes.

A plot of the cross-correlation function for the remanent states after the first field has been applied for each cycle (in other words the forward field, denoted F) has been produced (Figure 7.14). For the forward cycle the cross-correlation function is rarely less than 0.8. The high degree of cross-correlation between the arrays infers that there is some magnetic memory of the vortices within the array, a physical effect due to the interaction of the stray fields of the elements or of the fabrication process biasing the vortex chirality in the applied field could account for this.

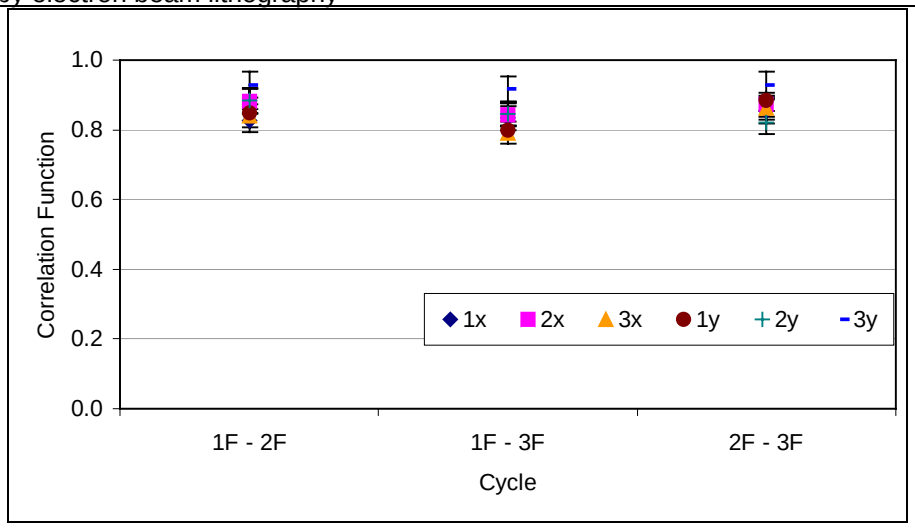

Figure 7.14: plot of the cross-correlation function against similar points on the forward magnetisation cycles for the two axes.

A similar plot to Figure 7.14 has been produced for the second field in the magnetisation cycle (in other words the reverse field, denoted R) and is shown in Figure 7.15. As with the cross-correlation function of the forward part of the cycle the cross-correlation function of the reverse is high and is rarely less than 0.7. The high cross-correlation function for the reverse part of the cycle again infers the existence of a domain like structure for the vortex chirality distributions.

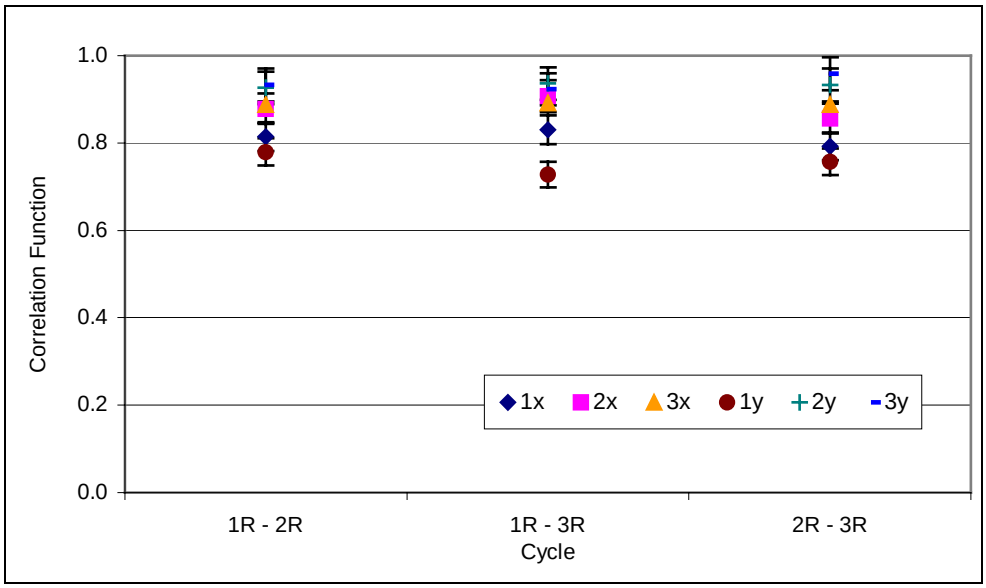

Figure 7.15: plot of the cross-correlation function against similar points on the reverse magnetisation cycles for the two axes.

7.2.3 Initial investigations into the effects of time and numerous cycles on the stability of the array

To test the stability of the vortex distribution within the array as it is subjected to repeated saturation fields, the array was subjected to the third magnetisation method described in section 7.1.2 along the x-axis for sixteen cycles (the number that could be successfully carried out in a day). The vortex chirality distributions for the beginning and end of the cycle are given in Figures 7.16(a) and (b) respectively. In the latter part of the cycle certain states were left for a period of ~60 min. to observe the stability of the array with time. No changes were observed in these states. As can be observed in the plots the array maintains an approximately constant value of ~76%/~24% (dotted lines in Figure 7.16) for the vortex chirality distribution over the course of sixteen magnetisation cycles. The constant values for the vortex distribution as the array is cycled over sixteen forward and reverse magnetisation cycles indicates stability within the array, with a great number of cycled fields.

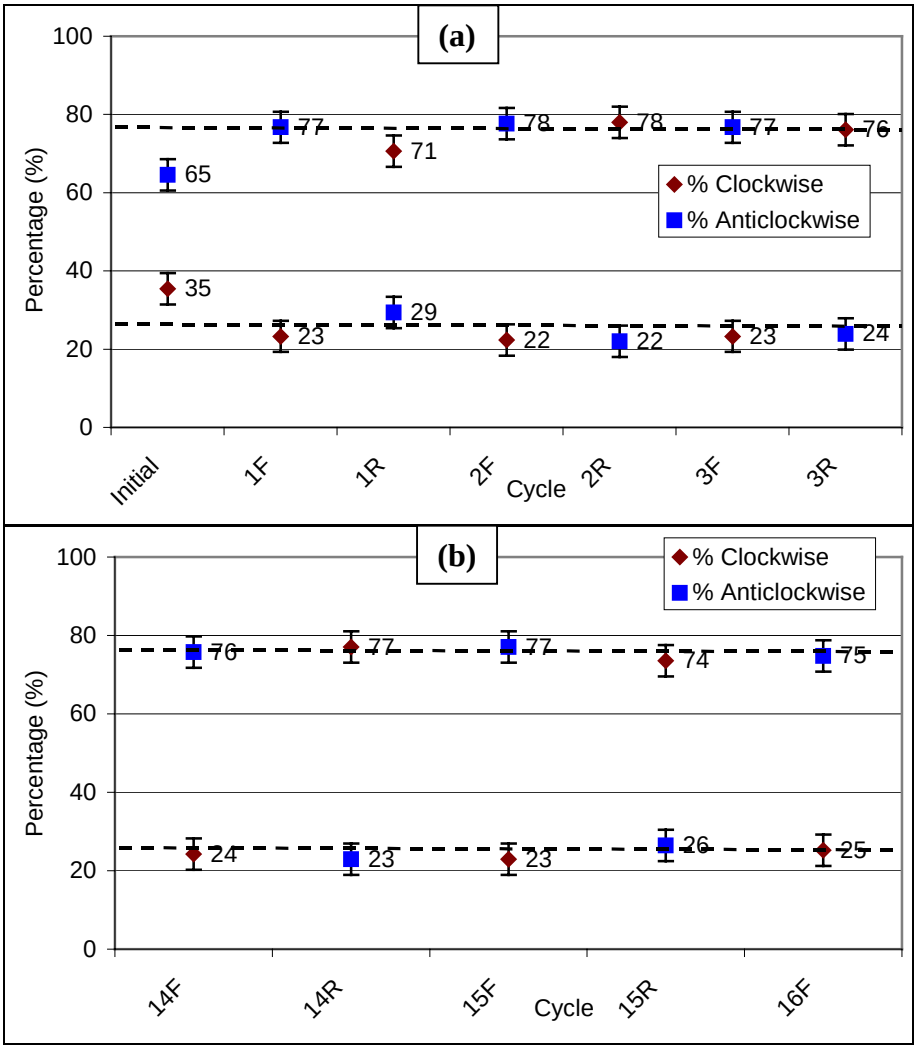

Figure 7.16: plot of vortex chirality distribution for (a) the first 3 cycles of 16, (b) the last 3 cycles of sixteen along the x-axis. The dotted lines represent the average values.

Using the cross-correlation function to compare the magnetisation cycle that has been taken over sixteen cycles (Figures 7.17 – 7.19), little difference can be observed between the cross-correlation at the beginning and end of the cycle can be observed. The similarity in the cross-correlation functions is an indication that the states in the array are stable over many magnetisation cycles.

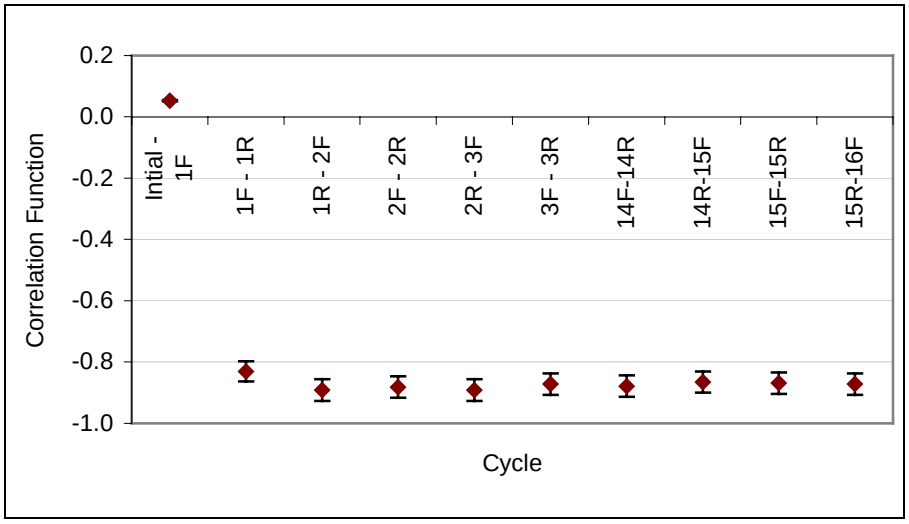

Figure 7.17: plot of the cross-correlation function against cycles over 16 cycles.

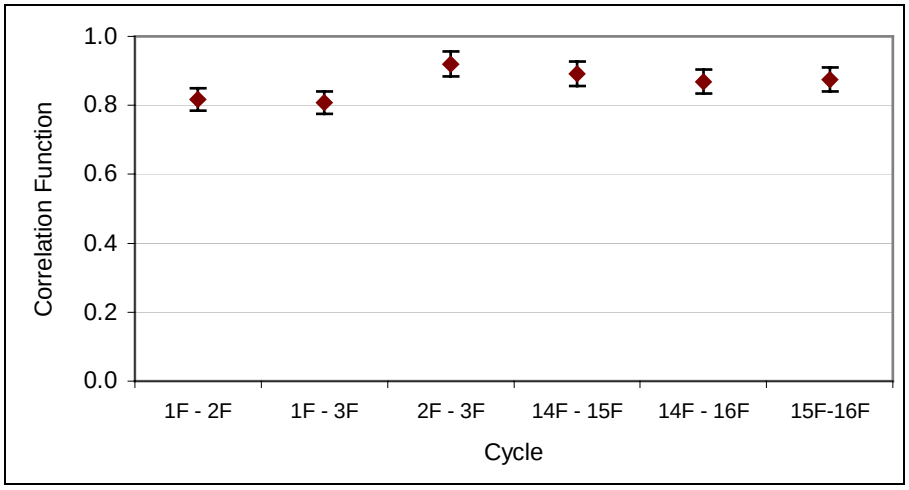

Figure 7.18: plot of the cross-correlation function against similar points on the forward magnetisation cycles over 16 cycles.

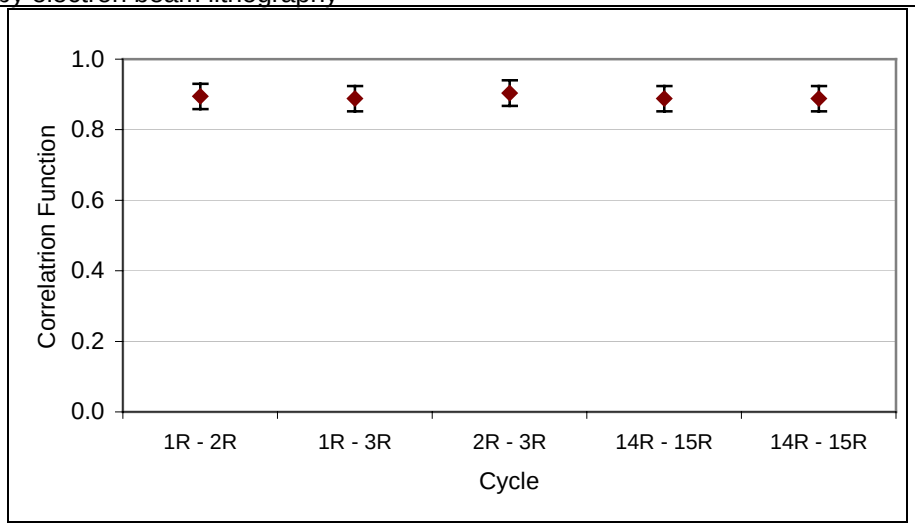

Figure 7.19: plot of the cross-correlation function against similar points on the reverse magnetisation cycles over 16 cycles.

To identify which elements had reversed between forward cycles and reverse cycles one image was subtracted from another, the elements that reverse chirality subsequently appear as black or white contrast on a grey background of unchanged elements. Shown in Figure 7.20 are the subtracted similar remanent states (1F – 2F for example) of the cycle discussed above. As can be observed from both the forward (Figure 7.20(a)) and the reverse (Figure 7.20(b)) images, the areas where the reversal of the vortex chirality of the elements appear to be random.

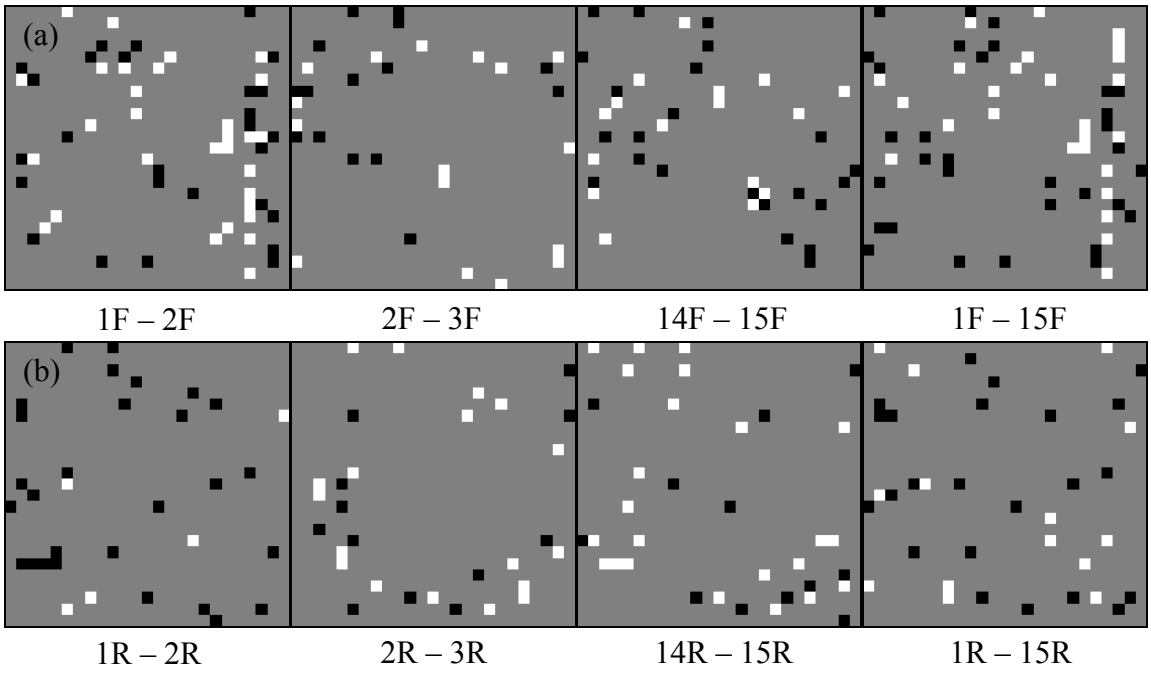

Figure 7.20: images showing the changes in remanent states of (a) the forward and (b) the reverse cycles.

The reversal of the vortices within the cobalt array has been shown to be anisotropic in nature with respect to the axes with which the field is applied. The anisotropy is most

probably due to the increased dimensions in one axis. As the applied field is cycled the vortices within the elements of the array cycle and small domains can be observed to form, the chirality of the vortices also appear to cycle with the field. Upon application of the cross correlation function to the consecutive states of the array a value of >-0.6 is calculated, this shows that the remanent states within the array almost reverse with the cycling field. Application of the cross correlation function to states on identical points of a cycle is again high (<0.7) this shows that the remanent states within the array are highly identical.

7.3 OOMMF simulation of cobalt elements

7.3.1 The ideal nanoscale cobalt element as modelled by OOMMF

OOMMF simulations have been performed for the ideal 270×270×50 nm^3 cobalt element and these indicate that several different possible states can exist at remanence, a selection of which are shown in Figure 7.21. The cell size for the simulated elements is 5 nm and the anisotropy of the polycrystalline cobalt was taken to be zero [7], all other simulation parameters are taken as the OOMMF recommended values. The x-, y- and z-axis component magnetisation (as defined in Figure 7.21) and the total energy density of the states are given in Table 7.1. From Table 7.1 the lowest energy states (the ground state) are the two single vortex states shown in Figures 7.21(a) and (b). These states are identical in terms of overall magnetic distribution and energy density and only differ in the rotation of the vortex, also discussed in section 4.3.3. It is these two states that are most frequently observed within the experimental array. The OOMMF package was also used to simulate other states such as the four-vortex state (Figure 7.21(c)), the double vortex state (Figure 7.21(d)), the flower state [8] (Figure 7.21(e)) and the onion state [9] (Figure 7.21(f)). The energy of these states is at least ~2.5 times the energy of the single vortex states (as shown in Table 7.1) and therefore the probability of the element adopting these configurations is low. As with the simulated 500×500×20 nm^3 permalloy elements discussed in section 4.3.3 the near uniform states (Figures 7.21(e) and (f)) have much higher energy densities than the flux closure structures (Figures 7.21(a)–(d)), as a result of there being no one well defined axes (shape anisotropy, section 1.5).

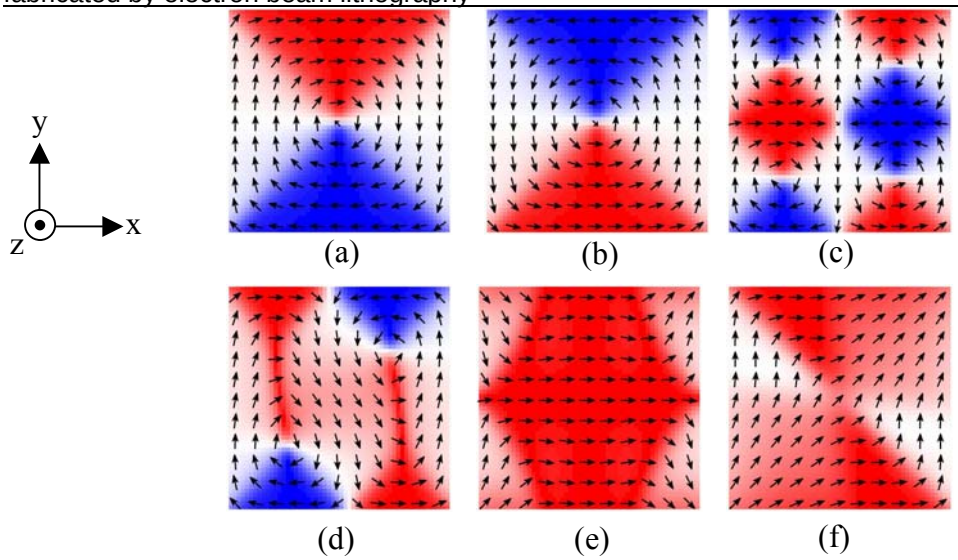

Figure 7.21: OOMMF simulated states of the magnetisation distribution within a 50 nm thick cobalt element with in-plane dimensions of 270×270 nm^2 in zero applied field: (a) is of the clockwise vortex, (b) is the anticlockwise vortex, (c) is the four-vortex state, (d) the double vortex, (e) the flower state and (f) is the onion state.

State	M_x/M_s	M_y/M_s	M_z/M_s	E_{TOT} (kJm^{-3})
(a) Vortex - clockwise	0.000	0.000	0.002	28.332
(b) Vortex - anticlockwise	0.000	0.000	0.002	28.332
(c) Four vortex state	0.000	0.000	0.004	76.378
(d) Double vortex	0.197	-0.020	0.001	77.501
(e) Flower state	0.854	0.000	0.000	136.098
(f) Onion state	0.636	0.636	0.000	138.135

Table 7.1: the magnetisation distributions and total energy densities of the OOMMF simulations shown in Figure 7.21 for a perfect 270×270×50 nm^3 cobalt element.

The lowest energy state (the vortex state, in Figure 7.21(b)) has been cycled through a simulated external applied field (± 2500 Oe) along the x-axis, with the first half of the loop shown in Figure 7.22. The magnetisation path differs from that observed in the larger 500×500×20 nm^3 permalloy elements discussed in sections 4.3.3 and 4.4 after the vortex is expelled, (Figures 7.22(a)–(c)). Here the applied field is increased to drive the magnetisation into a flower state (to erase the memory of the vortex chirality, Figure 7.22(d)). As the applied field is reduced the magnetisation adopts an S-state, Figure 7.22(e). With a further reduction in the applied field the magnetisation forms a double vortex state, Figure 7.22(f), which is consistent with the S-state. This state persists through remanence (Figure 7.22(g)) and reversal takes place through the creation of a metastable state that has two cross-tie structures present (Figure 7.22(h)) as the applied field is increased. The metastable state then collapses to the distorted two-vortex state after reversal (Figure 7.22(i)). The double vortex state forms an S-state (Figure 7.22(j)) after the vortices have been expelled with a further increase in the applied field. Note the lower

field at which the double vortex state is expelled (1180 Oe) compared to the single vortex state (1500 Oe), this is also observed in the simulated arrays, section 7.4. Again the magnetisation is driven to a flower state as the applied field is increased.

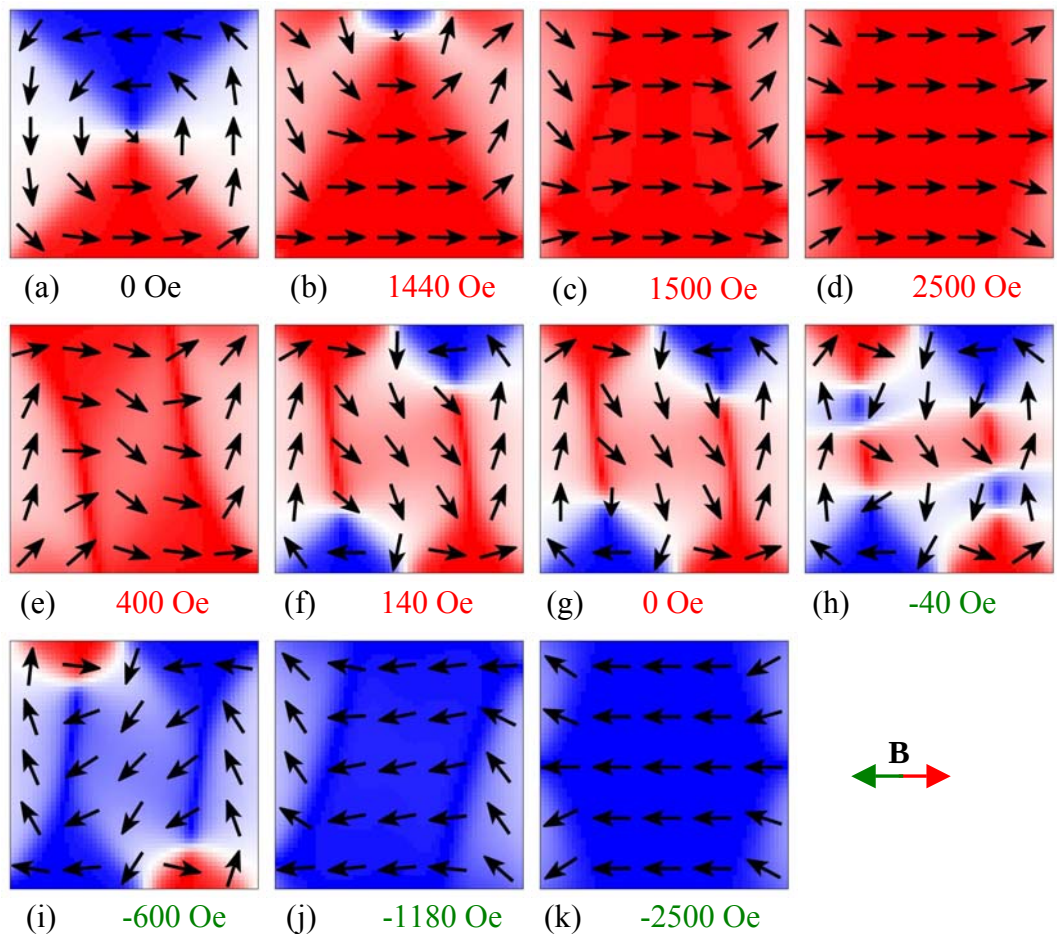

Figure 7.22: OOMMF simulation of the magnetisation distribution within a 50 nm thick 270×270 nm^2 cobalt element as it is subjected to an applied field of ±2500 Oe along the axis indicated.

7.4 OOMMF simulated 4×4 μm^2 arrays

Arrays of 50 nm thick cobalt elements with dimensions of 270×270×50 nm^3 and a period of 400 nm have been simulated using the OOMMF simulation package. The overall dimension for the arrays have been reduced to 4×4 μm^2 and the cell sizes have been increased to 10 nm to decrease the computation time of the simulations.

7.4.1 Fields applied along the x-axis of simulated 4×4 μm^2 arrays

A 10×10 array of perfectly ordered elements has been subjected to a simulated applied field using the OOMMF simulation package, with the important simulated field events shown in Figure 7.23. After the array has been relaxed from a random state, the array has

a ratio of clockwise to anticlockwise chirality distribution of 46/54, Figure 7.23(a). As a field is applied along the x-axis to the array (in the direction indicated in Figure 7.23), the vortices are driven into the edge of the elements, Figure 7.23(b). The vortices are expelled as the applied field is increased over a range of 200 Oe (with the bulk (59%) expelled at 1250 Oe, Figure 7.23(c)), the last vortices are expelled at 1450 Oe (Figure 7.23(d)). This is 50 Oe lower than the simulated isolated element (section 7.3). The applied simulation field is then increased to 2500 Oe to drive the magnetisation within the elements into a flower type state and thus erasing the vortex chirality memory of the array, as shown in Figure 7.23(e), similar to the individual element. Upon closer inspection of the elements within the array at 2500 Oe, the magnetisation in the outer elements has not formed a symmetrical flower type state. It is possibly through the influence of the magnetostatic stray fields of the surrounding elements (nearest neighbour effects, explored in greater detail in section 7.4.2), that the end domains within the corner elements become asymmetric, shown in Figures 7.24(a), (b), (d) and (e). This is compared to elements along the central axis of the array, Figure 7.24(c). The array could be said to have entered a global flower state as opposed to the individual elements.

As the applied field is reduced the magnetisation within the elements relax, in some elements the magnetisation forms a S-type state (28 S-states, circled in black) and in others a C-type state is formed, as is shown in Figure 7.23(f). As the simulated applied field is reduced, vortices form within the elements within the array over a field range of 400 Oe, with the nucleation points being at the edge perpendicular to the applied field (Figure 7.23(g)). Shown in Figure 7.23(h) is the formation of the majority of vortices, the vortices still to reform are along the domain boundary of the array and edge of the array. As the applied field is relaxed to zero two domains of clockwise and anticlockwise vortex chirality distribution have formed, Figure 7.23(i). Also visible are elements whose magnetisation has adopted a multivortex state. These multivortex states have an asymmetric direction allowing the vortex to be assigned a clockwise or anticlockwise label. Tracing back the multivortex state in Figure 7.23 it can be observed that they all form from a S-type state.

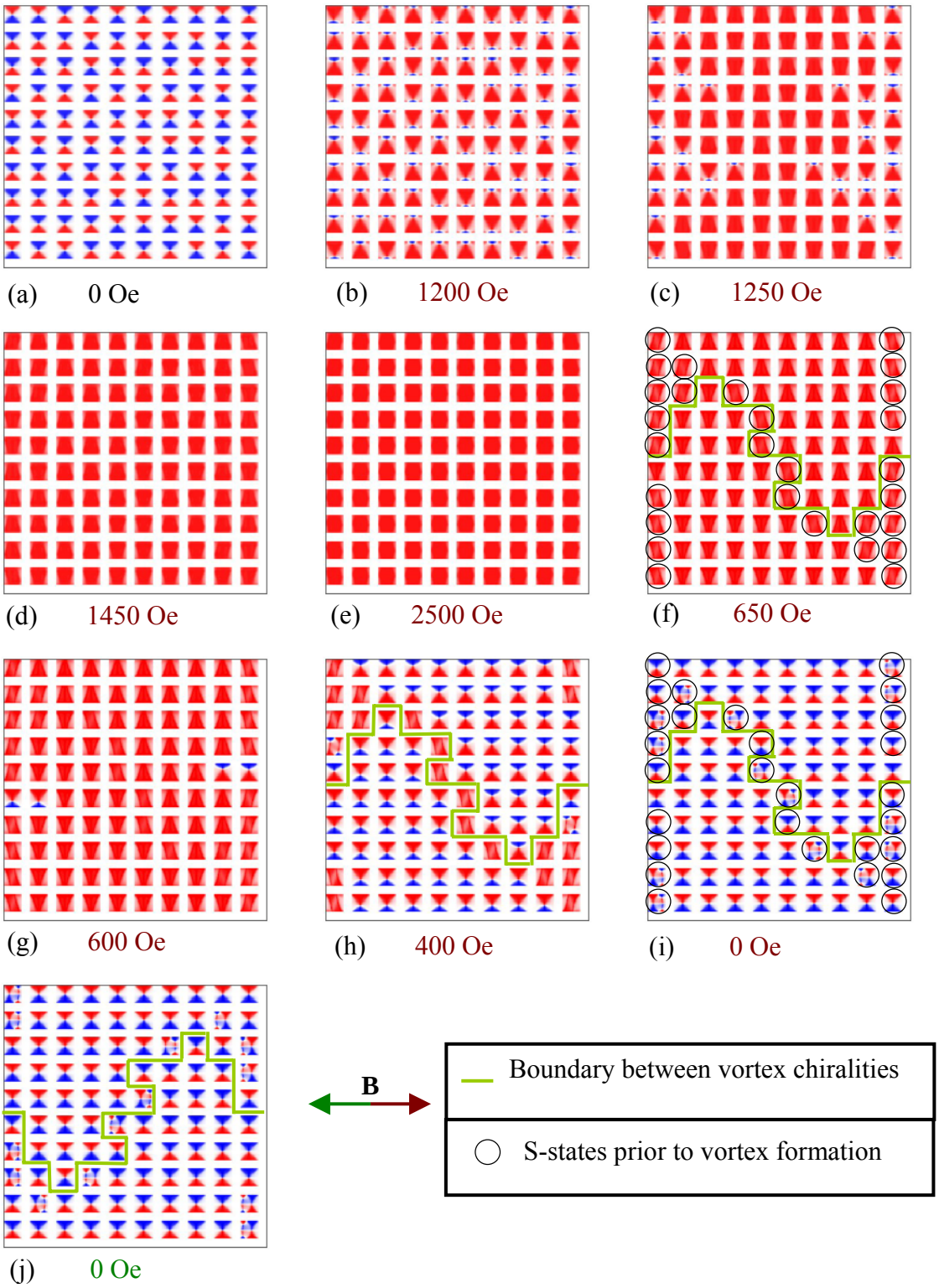

Figure 7.23: the OOMMF simulated expulsion and formation fields of the vortices within the cobalt elements of a perfect array, see text for details on the individual states.

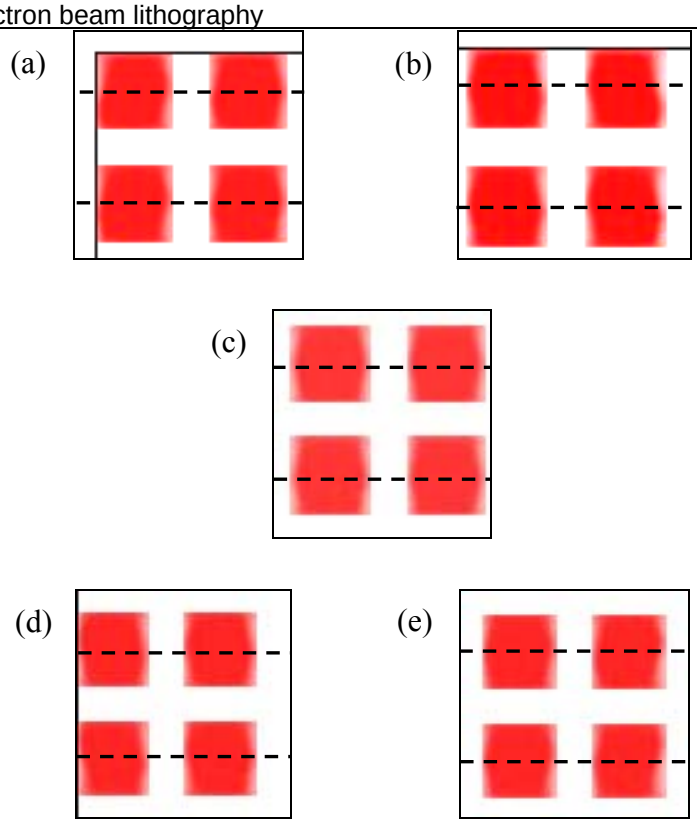

Figure 7.24: enlarged OOMMF simulations of the array in a flower type state at the (a) top left and (b) top right corner: (c) the centre; and (d) bottom left and (e) bottom right corners.

In the remanent state (Figure 7.23(i)) two "domains" can be clearly observed within the reduced array (separated by a boundary shown in green). In the remanent state there is a 50/50 split (14 of which are double vortices) in the vortex chirality distribution (approximating the multivortex states to either clockwise or anticlockwise chirality distribution). As the simulated applied field is increase to 2500 Oe in the opposite direction the magnetisation within the array follows a similar pattern as before, with the exception of the expulsion of the multivortex states at lower fields than the single vortex states. This is observed in the simulation of an isolated element in a cyclic applied field, Figure 7.22. The magnetisation, again, follows a similar path as the simulated applied field is reduced to zero. The remanent state is shown in Figure 7.23 (j). Here, due to the ideal structure of the array this remanent state is symmetrical about the lower edge of the previous remanent state, shown in Figure 7.23(i).

Analysis of the initial remanent state, shown in Figure 7.25(a), reveals a low autocorrelation function that fluctuates around zero in both x- and y-axes (indicated in Figure 7.25). In comparison the remanent states after a forward (Figure 7.25(b)) and reverse (Figure 7.25(c)) field has been applied yield high autocorrelation functions (>0.4 for up to a pixel spacing of four) in the x-axis indicating the large domains that can be observed visually in Figures 7.25(b) and (c). Initially the autocorrelation function in y-axis

is high (>0.5 for up to a pixel spacing of two) but after a pixel spacing of two, the autocorrelation function falls away rapidly (from 0.5 to 0.2 to 0.0 and finally to –0.4). Again this is due to the domain structure that can be observed visually in Figures 7.25(b) and (c).

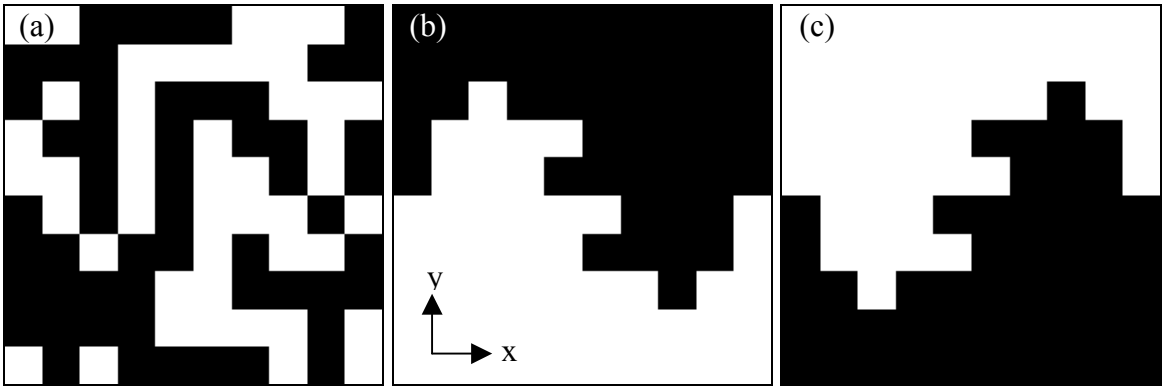

Figure 7.25: digitised representation of the (a) initial, (b) forward and (c) reverse remanent states of OOMMF simulation of the perfect array.

The cross-correlation function has also been applied to the remanent states of the perfect array simulation. The cross-correlation functions of the initial (Figure 7.25(a)) to forward (Figure 7.25(b)) and the initial to reverse (Figure 7.25(c)) remanent states are low (-0.16 and 0.00 respectively) revealing little ordering between the states. Between the forward and reverse states however, where digital images show the domains within array to reverse, the cross-correlation function for the elements is –0.36. This shows that the elements within the array don't have to reverse chirality for the array to reverse states. The ordering of the perfect array arises from the array flower state observed in high field (Figure 7.23(e)) and the subsequent nucleation of the vortices for the edge perpendicular to the applied field, Figure 7.23(g). The array simulated by the OOMMF programme is similar to the experimental array, in that there is the formation of the domain-like structures that can be defined by the vortex chirality. These domains reverse with the applied field. The simulated array, however, predicted two domain-like structures that are almost symmetrical along the direction of the applied field. The simulations, also, do not show the imbalance in the vortex chirality distributions that are observed in the experimental array. One of the main reason for the discrepancies between the experimental and simulated arrays could be the high symmetry of the simulated system.

The high degree of symmetry of the array shown in Figure 7.23 meant that the same magnetisation path and remanent states are observed as the field was applied along the y-axis, with the exception of the remanent states being rotated through 90^{o} in-plane. The boundary between the clockwise and anticlockwise domains is also rotated. The

experimental results (shown in section 7.2) show a difference between the orthogonal in-plane axis and not the similar results of the ideal OOMMF simulations. A reason for the difference between the experimental and OOMMF simulations could be the high degree of symmetry assumed for the simulation that is not achieved during the fabrication of the arrays. To break the symmetry of the array a mask was generated with elements that had been randomly moved by 0 or ±1 pixel in the x- or y-axes to be inputted to the OOMMF simulation, giving five possible displacements. The mask with the randomly moved elements (each pixel corresponds to 10 nm in real space) is shown in Figure 7.26(a). To make the movements truly random a grey scale representation of 100 pixels (one element equals one pixel) was generated using the Gatan Digital Micrograph programme (shown in Figure 7.26(b)) with each displacement (0, ±x, ±y) assigned a contrast range.

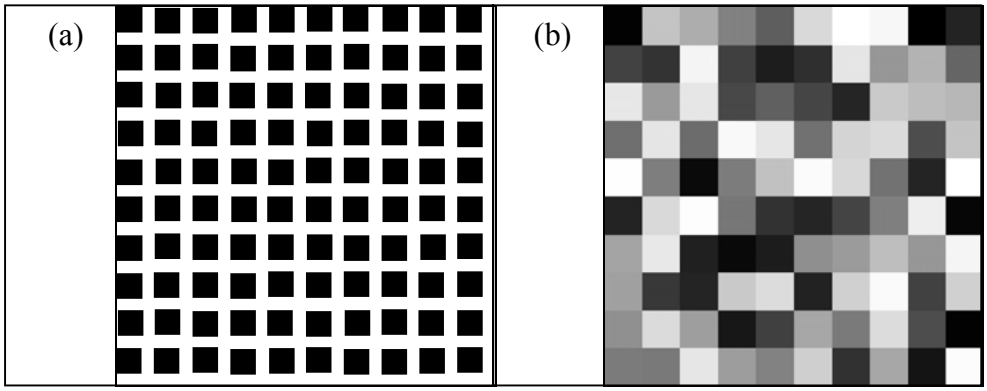

Figure 7.26: (a) the mask image inputted to the OOMMF package with random displacements of the elements used to break the symmetry of the system, (b) the randomly generated image used to displace the elements.

Upon relaxing the array of the randomly perturbed elements (henceforth known as the random array) from a random state, the elements were found to adopt an uneven split of clockwise and anticlockwise distributions (53/47% in favour of the anticlockwise chirality), shown in Figure 7.27(a). As a magnetic field is applied to the random array the vortex cores move towards an edge that is parallel to the applied field, shown in Figure 7.27(b). A further increase in the applied field to 1200 Oe starts the expulsion of the vortices within the elements, Figure 7.27(c), with the bulk of the vortices being expelled at 1250 Oe. The remaining vortices in the random array are expelled over the next 250 Oe, Figure 7.27(d). The range of expulsion fields is 50 Oe greater for the random array than for the perfect array. As with the perfect array, the field applied to the random array was increased to 2500 Oe to force the elements into a flower type state (Figure 7.27(e)). As with the perfect array, the outer elements have an off-centre flower type state with respect to the element axis, giving the random array the similar global flower state to the perfect array.

As the applied field is reduced the magnetisation within the elements relaxes and C- and S-states (35 S-states, circled in black) form in the elements prior to vortex formation, Figure 7.27(f). Nucleation of the vortices starts at 700 Oe with a single element at the edge perpendicular to the applied field (shown in Figure 7.27(g)). As the field is decreased over the next 200 Oe more vortices reform within the elements of the array and the nucleation of vortices is asymmetric, Figure 7.27(h). What is noticeable in Figure 7.27(h) compared to the perfect array at a similar stage, is a greater formation of anticlockwise than clockwise vortices and a clockwise vortex forming within what would appear (at this early stage) to be an anticlockwise domain. As the applied field is reduced by a further 200 Oe (Figures 7.27(i)) multivortex state appear in the array, the multivortex states appear to be more numerous than in the perfect array. A summary of the expulsion and formation fields for both arrays is shown in Table 7.2, with statistics for the number of S-state and multivortex states also shown. As the field is reduced to zero the two domains that appeared in the perfect array are not as visible within the random array, Figure 7.27(j). The distribution of vortex chiralities within the arrays has changed to be in favour of the anticlockwise vortices (a 62/38 split, with 23 multivortex states in the array), unlike the perfect array where an even split was observed.

Array	Expulsion			Formation		
	Start (Oe)	Finish (Oe)	Range (Oe)	Start (Oe)	Finish (Oe)	Range (Oe)
Perfect	1250	1450	200	600 (28)	200 (14)	400
Random	1200	1450	250	700 (35)	150 (23)	550

Table 7.2: table of the formation and expulsion fields for the perfect and random arrays simulated by OOMMF. In brackets in the start of formation column is the number of S-states prior to formation and in the end of formation column is the number of multivortex states. Uncertainty in each field step is ±50 Oe.

The increased multivortex state is due to the increased number of S-type states within the array. S-type states, which appear to be favoured in this array compared to the perfect array, can also form a single vortex within the element. Of the thirty-five S-states, twelve form single vortices and twenty-three form multivortices. In both arrays no C-state forms a multivortex state as would be expected from the end domain configuration. The multivortices form at the edge of the array and in clusters. It appears that the perturbation of the elements and, hence, the magnetostatic stray fields that emanate from them biases the array towards S-type states prior to vortex formation.

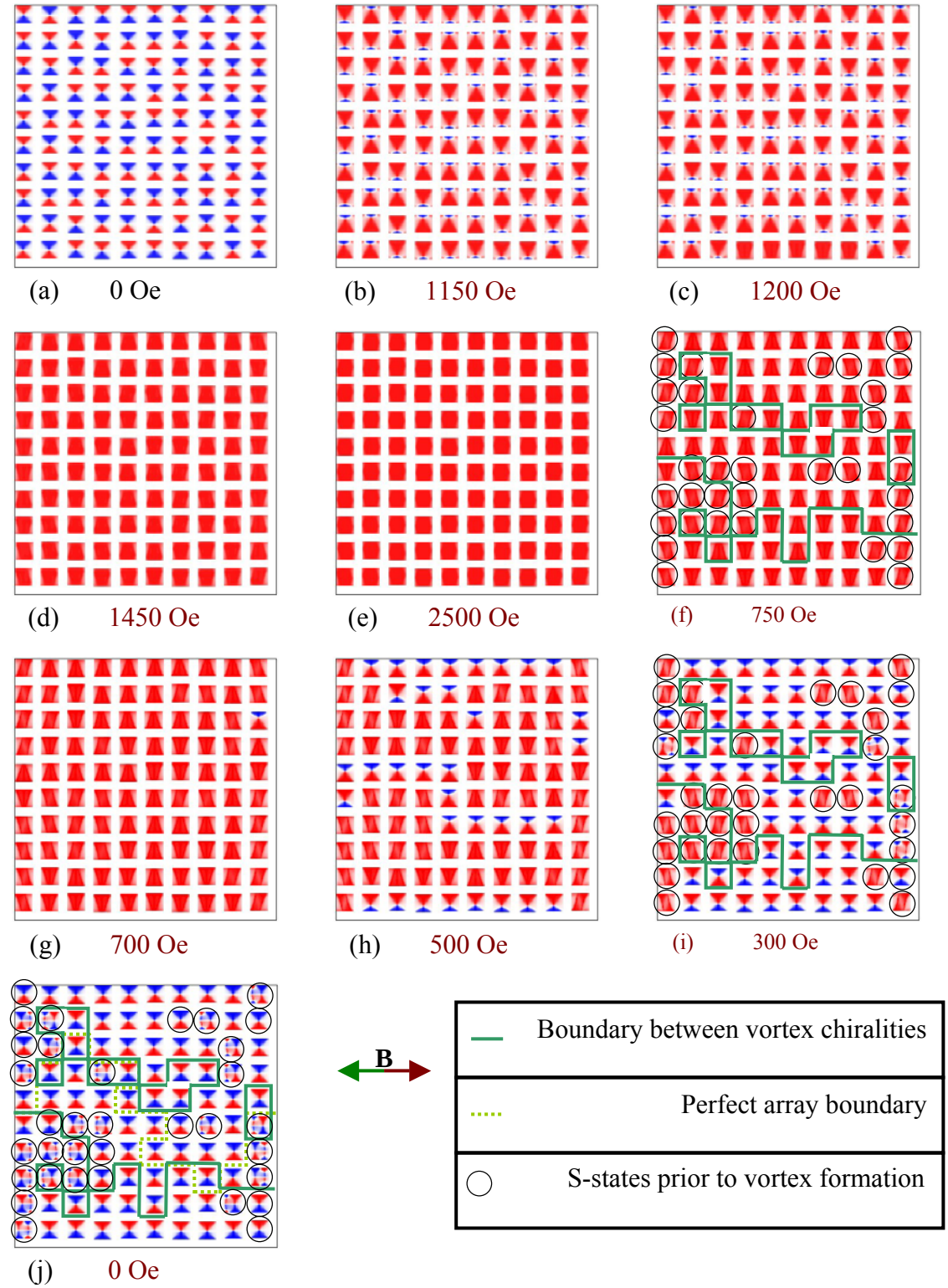

Figure 7.27: the simulated expulsion and formation fields of the vortices within the cobalt elements of a reduced array with random pertubation in the position of the elements, see text for details on the individual states.

As the field is applied in the opposite direction the expulsion and formation of the vortices occurs in a similar manner to that shown in Figure 7.27, with the exception of the multivortex states being expelled at lower fields than the single vortex states. The remanent state for the array as a field is applied in the opposite direction to the state shown in Figure 7.27(j) is shown in Figure 7.28. This remanent state appears to be a mirror to the

previous state. Also shown in Figure 7.28 are the borders of the anticlockwise vortex chirality domains (black lines), overlaying this is the similar distribution of the clockwise vortex chirality domains in the pervious remanent state (Figure 7.27(j), dotted green lines). From the two domain traces there appears to be a nearly complete reversal of the vortices. The vortex chirality distribution is almost a mirror as well, with a 61/39 split (with 18 multivortex states) in favour of the clockwise vortex chirality distribution.

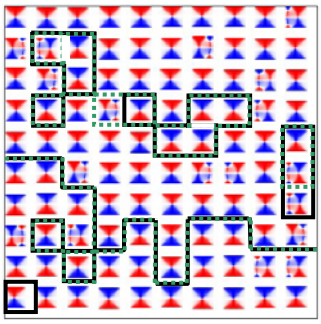

Figure 7.28: the remanent state of the random array after it has been exposed to a magnetising field in the opposite direction starting from the state shown in Figure 7.27(i).

As with the perfect array the autocorrelation function of the initial remanent state (Figure 7.29(a) for the random array is low and fluctuates around zero. In comparison the autocorrelation function of the forward (Figure 7.29(b)) and reverse (Figure 7.29(c)) remanent states have x-axis autocorrelations that are rarely <0.3, indicating a greater degree of ordering (although not as high a degree as the perfect array). Again, as with the perfect array, the y-axis autocorrelation is high for one pixel spacing (<0.3) but decreases rapidly to zero after one pixel. The slightly lower autocorrelation functions highlight the different domain structures of the two simulated arrays.

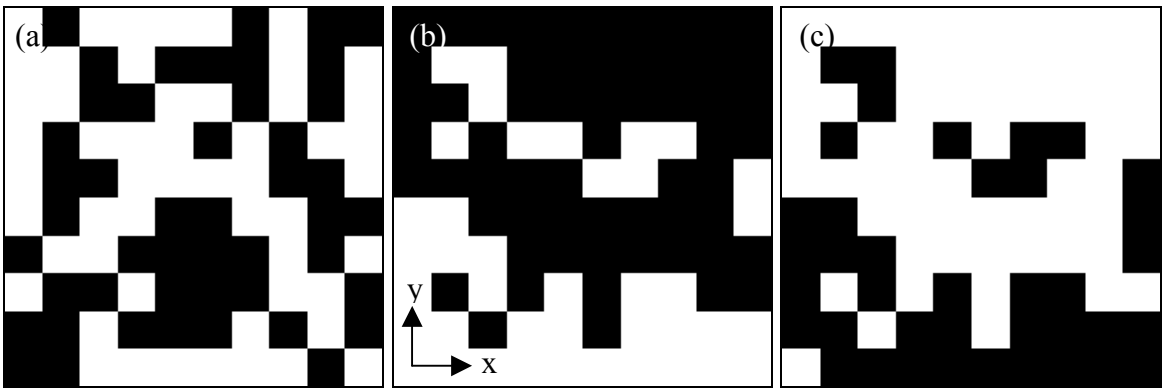

Figure 7.29: digitised representation of the (a) initial, (b) forward and (c) reverse remanent states of OOMMF simulation of the random array.

The cross-correlation function between the initial (Figure 7.29(a)) and forward (Figure 7.29 (b)) and the initial and reverse (Figure 7.29(c)) states is approximately zero inferring

that there are no major similarities or differences between the states. The cross-correlation function between the forward and reverse remanent states is –0.94 (close to complete reversal of all vortex chiralities within the array) showing also an almost complete reversal of the remanent state.

It appears from the simulations of the perfect and the random arrays that the position of the individual elements within the array (be it an edge, a displacement from the perfect position or both) contributes to the distribution of the vortex chiralities and the number of multivortex states that appear within the array. Although there is still a high degree of ordering in the remanent states, the random arrays shows some similarities when compared to the experimental results, section 7.2. Another simulation that could be run to find a better fit for the experimental data could be one with a dimension of the elements one pixel along one axis greater. To better understand why breaking the perfection of the array influences the distribution of vortex chiralities, simulations of the effects of stray field produced by the flower, C- and S-type states on their nearest neighbours have to be studied, the results of which are discussed in the next section (section 7.4.2).

7.4.2 Simulated stray field distribution surrounding elements

From the OOMMF simulations of the elements shown in section 7.4.1, it is possible to approximate the stray field distribution surrounding elements in different section of the array for the flower, C- and S-states using the method described in section 1.4.3. The calculation of the stray field distributions in the element for the various states will allow an estimation to be made on how the various states affect the surrounding magnetisation. This may allow for a reasonable estimation to be made as to how the various remanent states arise in the array. For example the flower type state (Figure 7.30) produced when the simulated cobalt element is subjected to a field of 1720 Oe in the direction shown has been used to calculate stray field distributions within the array prior to the formation of C- and S-type states. The OOMMF simulated state shows a symmetrical distribution of the magnetisation around the central axis of the element (indicated in Figure 7.30).

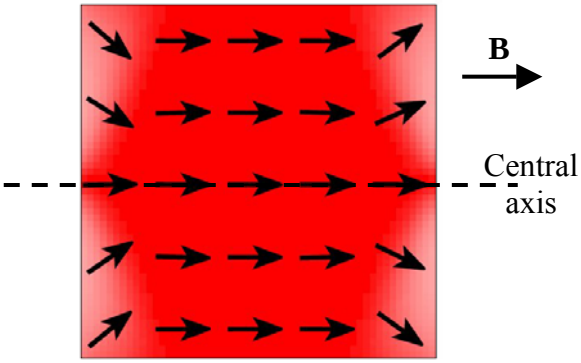

Figure 7.30: OOMMF simulated flower type state in an applied field of 1720 Oe applied along the direction shown.

The Gatan Digital Micrograph programme has been implemented (through scripting) to create 2×2 and 3×3 arrays of elements with one removed (Figures 7.31(a) and (b) respectively) of the flower, C- and S- magnetisation states, from this arrangement the stray field in the corner and bulk of the arrays can be estimated. The stray field, H, here is a relative fraction of the saturation magnetisation, M_S. For OOMMF M_s for cobalt is 1.4 MAm^{-1} (~17600 Oe). Line traces averaged over the width of the element can then be taken at the position of the element in both of the orthogonal in-plane directions and the stray field at the corner or in the bulk of the array can then be estimated.

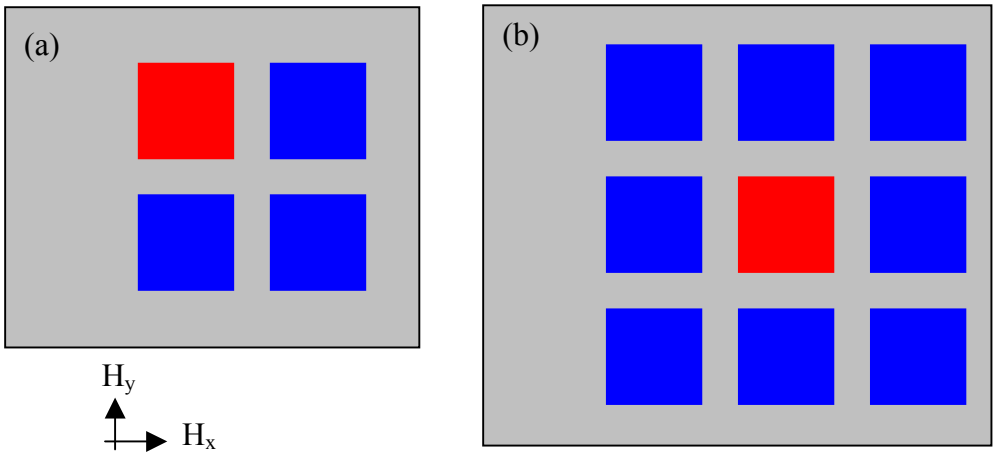

Figure 7.31: schematic of the images used to estimate the average field within the removed element of (a) the corner and (b) the bulk of an array for the flower, C- and S-state. grey is the background, blue the contributing elements and red the removed element. The axes indicate the direction of the stray field averaged over the width of the elements.

For an array of elements which are in symmetrical flower states, the field distributions of the elements surrounding a corner element are given, Figure 7.32. The average line trace of the space where the corner element is expected to be shows a stray field of ~440 Oe at the edge nearest the element in the direction applied field. In comparison, in the direction perpendicular to the field the stray field contribution is lower (~100 Oe Figure 7.32(b)). From the stray field calculation for the element at the corner of the array when the

magnetisation of the surrounding elements is in a flower type state, it can be observed that the component stray field due to the parallel and perpendicular elements influence the magnetisation within the corner element to adopt the asymmetric distribution observed for the perfect array (section 7.4) and the creation of S-type states. Hence the creation of the multivortex states and reversal of vortex chirality distributions can occur. A similar distribution is observed for the C-state at the corner of an array.

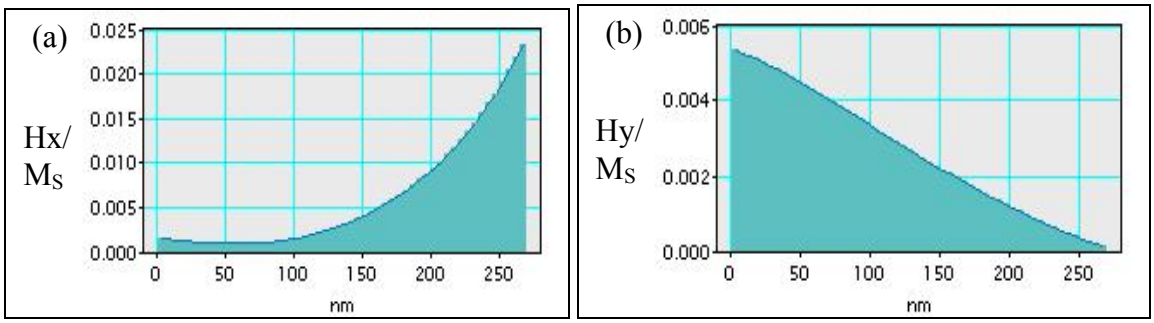

Figure 7.32: the average in-plane components of the stray field distribution in the removed corner element (a) parallel to and (b) perpendicular to flower state of the other elements.

Stray field calculations, both parallel and perpendicular to applied field directions, for an element in the bulk of the array show that the stray field within the element is parabolic about the centre (as shown in Figure 7.33). The symmetrical parabolic nature of the fractional stray field has no influence on the magnetic stray field in the bulk. This is only true however if the spacing between the elements is equal and the flower type states are symmetrical around the central axis. In the asymmetric magnetisation distribution case, there will be an asymmetric stray field distribution. Similar observations can be made about the distribution of the stray field emanating from the C-type state when simulations have been produced from the OOMMF output for the bulk elements in an array.

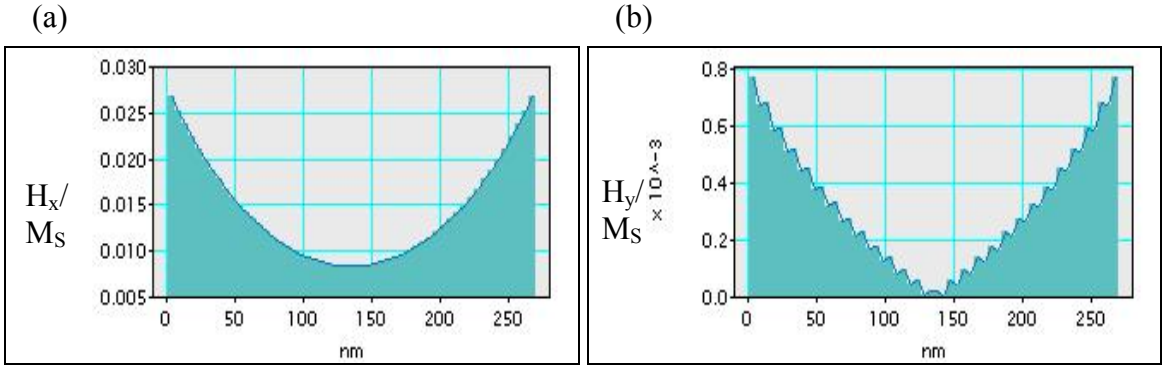

Figure 7.33: the average in-plane components of the stray field distribution in the removed bulk element (a) parallel to and (b) perpendicular to flower state of the other elements.

The average stray field distribution for elements at the corner of an array whose magnetisation is in an S-type state are similar to the flower and C-type state for the

elements parallel to the applied field, as shown in Figure 7.34(a). Stray field emanating from the elements perpendicular to the applied field however have a different distribution, shown in Figure 7.34(b). Initially the corner element senses a field of ~88 Oe, this field falls away, however after ~210 nm the stray field sensed by the element rises to ~35 Oe. The asymmetry of the stray field here could result in the magnetisation within the element being distorted and hence forming either a multivortex state or reversing the chirality of the vortex. The asymmetry of the stray field is due to the lack of symmetry in the S-state.

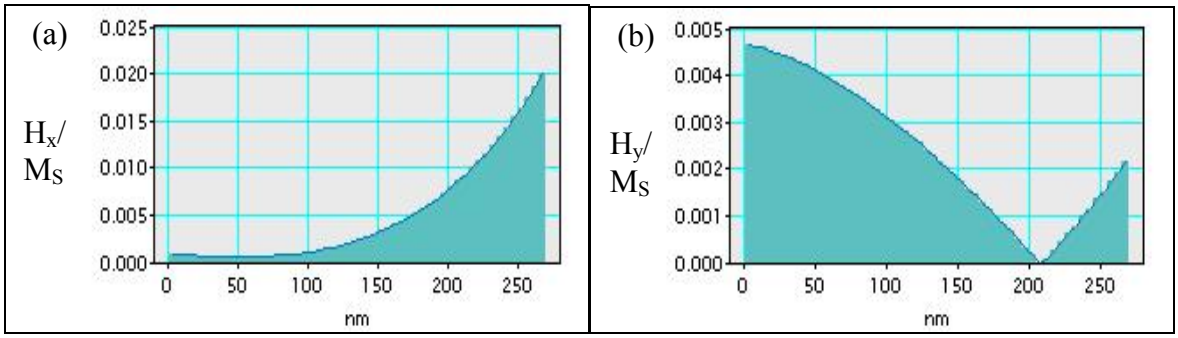

Figure 7.34: the average in-plane components of the stray field distribution in the removed corner element (a) parallel to and (b) perpendicular to S-state state of the other elements.

A similar phenomenon to the corner element is observed within an element in the bulk of the array. The average stray field distribution in the direction parallel to the applied field within the removed element space is symmetrically parabolic about the centre, as shown in Figure 7.35(a). The average stray field within the removed element space for the direction perpendicular to the applied field is not symmetrical, Figure 7.35(b) (with a stray field of ~53 Oe at the edge of the element and ~80 Oe at the other edge). From the line trace a shift of ~10 nm can be observed from the centre of the element. The asymmetrical stray field distribution is again due to the asymmetrical magnetisation distribution of the S-state. The asymmetric stray field contribution could be high enough to influence and distort the magnetisation within the element.

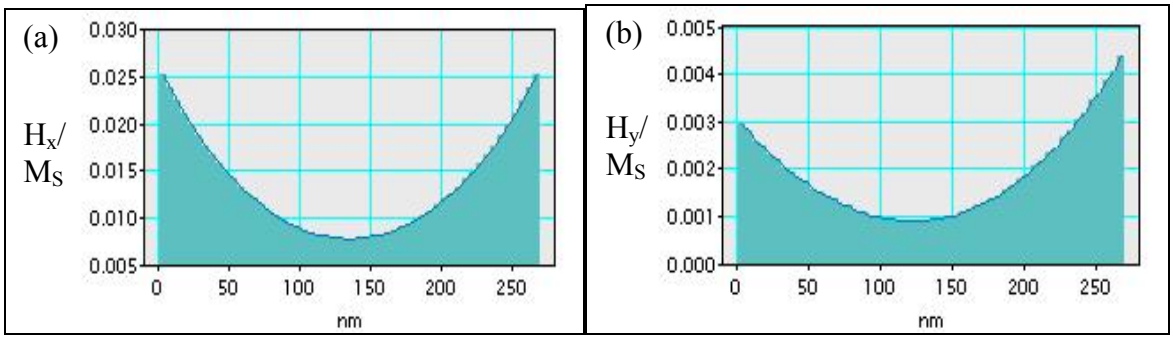

Figure 7.35: the average in-plane components of the stray field distribution in the removed bulk element (a) parallel to and (b) perpendicular to S-state state of the other elements.

The stray field calculations of the OOMMF simulated flower C- and S- magnetisations states within 3×3 and 2×2 arrays (bulk and corners of a larger array respectively) shows that the stray field distribution from the flower state is asymmetric (that arises from the magnetisation distribution within the element), this alters the distribution of the magnetisation within the elements in the bulk and hence progress through to the corners. The asymmetric magnetisation from the flower state gives rise to the array flower state. From the array flower state S-states form within the array. The S-states themselves produce a very asymmetric stray field that influences all the elements surrounding the element. The stray field calculations show that the stray field interaction of the elements within the array is the one of the most probable reasons for the domain-like remanent states that arise within the array.

7.5 Conclusions

Bright field TEM images of the nominal 270×270×50 nm^3 cobalt elements within the array reveal good clearance with respect to the patterning resist and that the array is whole and intact. Higher magnification bright field images reveal that the average in-plane dimensions of the elements are approximately square ((270 ± 4)×(276 ± 4) nm^2). The higher magnification images also reveal elements with residual strands of resist attached.

Fresnel images of the array reveal two main levels of magnetic contrast within the elements, light and dark contrast. By comparing the same section of the array using DPC imaging immediately after Fresnel imaging, it has been established that the light contrast when viewed in elements in underfocussed Fresnel imaging mode is generated by clockwise rotation of the magnetisation within the elements. Dark contrast is a result of anticlockwise rotation of the magnetisation. The formation and expulsion of the vortices within the element occur at a range of fields. The formation of vortices begins at (690 ± 25) Oe and ends at (373 ± 24) Oe, giving the vortex formation a range of ~317 Oe. The expulsion of vortices begins at (-1134 ± 23) Oe and ends at (-1264 ± 24) Oe, giving a range of ~130 Oe.

From the magnetisation cycles applied to the array, information was obtained about the behaviour of the elements within the array. It has been found that, in general, there is greater uniformity in the distribution of the vortex chirality as the field is applied in the y-axis as opposed to the x-axis and there is an increase in the vortex distributions in the y-axis. A reason for the greater uniformity could be due to the increase in the y dimension of the elements, this could increase the magnetostatic interaction between the elements as

the field is applied in this direction. The change in the y dimensions could be a consequence of a deposition or write effect from the EBL process. Texturing of the crystallites due to the reduced dimensions could also account for anisotropy. Analysis of the crystalline structure within an element could be through analysis of the diffraction patterns at different tilt angles to determine if there is any texturing. To observe if there is any anisotropy within the film, the in-plane field could be applied along a diagonal of the array. If there is an associated anisotropy, the formation and expulsion of the vortex will occur off-axis of the diagonal. The direction the vortex takes will also give a qualitative result as to the direction of any anisotropy. Applying the correlation functions to the remanent states of the magnetisation cycles shows that the array reverses state upon the application of consecutive saturation fields. The nature of the domains (clockwise and anticlockwise vortex chiralities) is found to reverse with the field. The saturation fields have also been applied to the array over the course of sixteen cycles and in a couple of instances a time period of ~60 mins has elapsed between the application of one field and the next field to observe the stability of the array. For the increased number of cycles there appears to be little change in the remanent states, inferring stability within the system over many cycles. Similarly there appears to be little change within the array with respect to time.

The domain like structures observed within the remanent states, as well as the high cross-correlation functions for cycles, indicates a supermagnetic domain type of array. As the remanent states do not appear to vary greatly for magnetic fields applied along the same axis from different initial states and for different cycles, this indicates a history in the supermagnetic domain that is intrinsic to the properties of array and not the applied field or magnetic history of the array.

The OOMMF simulation of an ideal 270×270×50 nm^3 cobalt element shows that the four-domain vortex clockwise or anticlockwise state has the lowest energy and hence is the ground state; with near-uniform states having the highest remanent energies. As with the simulations of permalloy squares in chapters 4 and 6, the OOMMF simulations cannot reform a single vortex state as the field is cycled: instead the simulation reforms a multivortex state and reverses through rotation of the domains. A reduced array of 10×10 elements has also been simulated in the presence of an applied field. For a perfect array it was found that the vortices are expelled over a range of 200 Oe as the applied magnetic field is raised to 2500 Oe to erase the memory of the individual element within the array. As the applied field is reduced, prior to vortex formation, S-states are observed in the array; the S-states in turn facilitate the formation of multivortex states within some

elements (but not all S-states form multivortex states). The vortices form within the array over a range of 400 Oe. This is consistent with experimental results. After the vortices have reformed, the array appears to form two domains of different chiralities with multivortex states at the domain boundaries and the edge of the array. These domains (with a 50/50% split) reverse upon application of a reverse saturation field. The symmetry of the state could arise due to the symmetry of the array and this is confirmed when a similar magnetising field is applied along the y-axis and a similar state is observed.

The symmetry of the remanent state of the array is broken when the symmetry of the array is broken. A mask of the elements that have been randomly perturbed confirms this. As the random array is cycled through an applied field the vortex chiralities do not form two domains in the remanent states. There is an increased number of S-states in the random array (compared to the perfect array) prior to vortex formation. This in turn increases the number of multivortex states observed at remanence. The random array is similar in nature to the fabricated array. It would be interesting to study simulations of arrays with elements perturbed by 1 or 2 pixels randomly in the x and y direction, in addition to an array where one dimension of the elements had been increased by one pixel. It would also be interesting to simulate an array of elements that have been altered by removing random pixels along their edges. Although the last simulation would be a time consuming simulation, both in the creation of the mask and the computation of the simulation. Both the auto and cross-correlation functions have been applied to the simulated arrays. We have found that the presence of well-ordered domains increases the autocorrelation functions in the direction of the applied field. Perpendicular to the applied field, however, the autocorrelation function falls off after a pixel spacing of two due to domain structure. The cross-correlation function of the perfect array, for the forward and reverse fields, reveals that although the domains reverse, not all the vortices reverse. This is contrary to the random array where the cross-correlation function is ~-1, showing reversal of the vortices, and there is an almost complete domain reversal. The states predicted by the OOMMF simulation package are not observed experimentally, even briefly during a transition state, as the remanent states are a direct result of the saturated state.

Reconstructions of the stray field emanating from elements whose magnetisation is either in a flower, C- or S-state surrounding a bulk or corner element yields insights into the influences of stray field affecting the elements. When the array is in the flower type state, the stray field is symmetrical in bulk, where as at the corner there is an increase/decrease (dependent on the orientations of the flower type states) of the stray field. This is true for

the C-type state as well. When the element is surrounded by S-type states, however, there is an asymmetrical stray field distribution that arises regardless of the element's position in the array. It is thought that the asymmetrical stray field distributions of the S-state result in the formation of the multivortex states that are observed as well as help facilitate the reversal of the magnetic vortex chiralities.

Bibliography

[1] OOMMF simulation package available for download at NIST (URL active 16/02/06): http://math.nist.gov/oommf/

[2] Beardsley I.C., IEEE Trans. Mag. 35(1) (1989) 671.

[3] McVitie S., White G.S., Scott J., Warin P., Chapman J.N., J. Appl. Phys. 90(10) (2001) 5220.

[4] Williams D.B., Carter C.B., *"Transmission electron microscopy"*, Plenum Press 1996, ISBN 030645324X.

[5] Kirk K.J., Chapman J.N., McVitie S., Aitchison P.R., Wilkinson C.D.W., Appl. Phys. Lett. 75(23) (1999) 3683.

[6] Kundrotatie A., Chapman J.N., Rahman M., IEEE Trans. Mag. 39(5) (2003) 2672.

[7] Dunin-Borkowski R.E., McCartney M.R., Kardynal B., Smith D.J., Scheinfein M.R., Appl. Phys. Lett. 75(17) (1999) 2641.

[8] Rave W., Hubert A., IEEE Trans. Mag. 36(6) (2000) 3886.

[9] Uhlig T., Zweck J., Phys. Rev. Lett. 93(4) (2004) 047203-1.

8 Conclusions and Future Work

Electron beam lithography (EBL) is primarily used for the fabrication of devices that have dimensions on the micron and sub-micron scale. These devises range from waveguides with a period of 23 nm [1] to T and Γ gates for metal-semiconductor field effect transistors used in the semiconductor industry [2]. EBL is also used to fabricate ferromagnetic elements [3, 4] that are used as components for magnetic random access memory (MRAM) [5] devices. MRAM is a new type of memory has been developed as a direct replacement for standard semiconductor RAM [6]. The advantage of MRAM over RAM is a reduced power consumption necessary when used, although areal density of memory bits, at present, limits the technology. It has been calculated by Cowburn [7] that the areal footprint of the device ultimate limits resolution of elements within an MRAM device, this is due to the superparamagnetism properties of the magnetic material. The true limit of the devices, however, is the ability to successfully read and write to the element. Reduced element sizes are also of particular interest in the read/write process of hard disk drives (HDD). As the track size of the memory bit width is reduced and the areal density is increased, the ability to read/write such areas also has to be reduced so as not to have the stray magnetic field of the head infringe on neighbouring bits. Recent advances have further increases the areal density of the HDDs to 100 Gb/inch^2, four times the previous best [8]. The increase is due to the bits being magnetised perpendicular to the film surface, this is as opposed to the traditional method of parallel magnetised bits. The perpendicular magnetisation storage devices are also reported to have greater thermal stability than their parallel counterparts. One of the limiting factors with this technology is the grain size of the recording media.

An alternative method of fabrication of such devices by focussed ion beam (FIB) lithography is the subject of this thesis, with the conclusions drawn form the work presented below. Any future work that could be carried out as a result is also presented along side the relevant section. Although the FIB microscope is a relatively new fabrication tool, it has been developed as a milling tool for the creation of cross-section for transmission electron microscope (TEM) imaging [9], for example. This method involves the milling of areas in front and behind the region of interest. The region of interest is then lifted out and deposited on a support such as holey carbon film or a copper grid. More recently the FIB microscope has been used to implant ions into areas of magnetic films and the resultant changes in magnetic properties have been measured [10, 11, 12]. Some work has been performed on micron sized element fabricated by FIB lithography [13, 14]; although the magnetisation characterisation of such elements has been through magneto-optical Kerr effect (MOKE) measurements, see section 3.3.3. The milling of the isolating trenches in the elements in such cases is into bulk substrates as there is no need to greatly control the milled depths and as a result the sputter rates had to be verified for the permalloy elements discussed in this thesis.

8.1 Preliminary results for the fabrication of nanoscale elements

The basis of the work discussed in chapter 4 was to establish the conditions for the fabrication of permalloy elements that are milled out of 20 nm thick permalloy film (on a 50 nm thick silicon nitride substrate) by FIB lithography. To establish the effects of the beam on such a film, trenches with an area of 1×1 μm^2 were milled into the film for varying doses and beam currents, they where then imaged using the atomic force microscope (AFM) and transmission electron microscope (TEM) described in chapter 3. The various beam currents produce trenches that increase in depth as the dose is increased. The edge profiles of such trenches were found to have a gradient between 250 and 500 nm wide associated with them. It is thought this gradient is related to the beam profile that is believed to be Gaussian in nature. Non-uniform milling was also observed within the trenches, especially at higher doses, this is evidence of the preferential milling of certain grain orientations.

Grain growth of the permalloy crystallites was observed within the trenches by bright field TEM imaging. The grain size increased with dose, reaching a plateau at higher doses. Upon correction of the doses to account for the milling of the aperture, a similar increase in the grain growth for the 12 and 102 pA beam currents was observed with an increase in

dose. Also observed, was a variation in the spread of grain sizes as the dose was increased. The variation in the spread of sizes is linked to the preferential milling mentioned previously. The increase in the total dose of the tails of the Ga^+ beam was observed as the beam current is increased form 12 to 102 pA. From the initial results of the gallium milling of a permalloy thin film, it has been decided to fabricate the permalloy elements using a nominal dose range of 0.03–0.11 $nC\mu m^{-2}$ and to use the nominally sized 10 pA beam current.

To determine the exact gradient of the boundary between the milled section and remaining material, FIB sharpened AFM tips could be used to achieve higher resolution surface maps. Also by using the FIB sharpened tips, a more detailed map of the remaining islands in the milled regions can be obtained and, therefore, a more accurate depth (and hence average depth) profile can be obtained for each dose and beam current. Further analysis of the trenches by elemental mapping techniques such as electron energy loss spectroscopy (EELS) and Auger electron spectroscopy (AES) could be used to determine the levels of Ga^+ implantation into the trenches and surrounding area. Electron beam diffraction could also be used to determine if the trenches and surrounding area is still polycrystalline.

The objected orientated micromagnetic framework (OOMMF) simulation programme was used to simulate possible initial configurations of the magnetisation within the elements and how they behave in a magnetic field is applied along the easy axis. Several possible states were modelled for the perfect element 1000×200 nm^2, the two lowest identical energy states were the C- and S-state. The other simulated states collapsed to either the C- or S-type state after a field was applied along the easy axis, dependent on the orientation of the end domains. The simulated coercivity of the elements was found to be 400-440 Oe with the square hysteresis loop simulated that was predicted for the element.

The magnetic ground state of the 500×500 nm^2 permalloy element was simulated to be the four-domain flux closure state that is observed experimentally. As a magnetic field is applied to this state the vortex moves to the edge of the element, as happens experimentally although the expulsion occurs at a higher field. As the field is reduced, however, the vortex does not reform, as expected from experiments, instead the element reverses in a manner similar to that of the 1000×200 nm^2 element. there are several reasons for this, one is the high degree of symmetry input to OOMMF. To combat this, elements with their symmetry broken were simulated. The magnitude of the vortex expulsion field of the roughened elements fluctuates with respect to the ideal element. It is found that the

roughened elements also do not reform the vortex state; they form either a C- or S-type state instead. A comparison of the energies shows that the C- and S-type states are larger than the vortex state. alterations of the symmetry does not greatly effect the magnetisation path, other reason why the vortex does not reform in the system could be: i) the vortex formation energy barrier is too great for the OOMMF simulation to overcome for these elements, ii) the field step size could be too large to allow the reformation of the vortex, iii) the convergence value of the $|\mathbf{M} \times \mathbf{H}|$ term could be too large and therefore allowing the metastable C-state to exist, iv) the cell size could be too large or v) a mixture of the previous facts. An investigation of these areas may help establish better simulations.

The OOMMF simulations illustrate the topic of shape anisotropy influencing of the magnetisation of the element as discussed in section 1.5. The simulations highlight the difference between the two chosen shape, the 1000×200 nm^2 element has the near uniform ground state and the 500x500 nm^2 element has the flux closure ground state.

8.2 The characterisation of nanoscale elements fabricated by electron beam lithography and focussed ion beam milling

In chapter 5 elements fabricated by EBL and FIB lithography were discussed. The elements fabricated by EBL have an edge roughness comparable to the as deposited grain sizes (~8 nm) with rounding of the corners approximately one quarter to a third the beam spot size (~80 nm). In comparison the average size of the grains within the FIB lithography fabricated elements vary with dose and composition. For high doses there is grain growth of up to ~32 nm, although this is for permalloy on copper and the grain growth is limited mainly to the edge of the element. For the permalloy-only sample a grain growth of up to ~25 nm is observed over the entire element for doses >0.11 $nC\mu m^{-2}$. For doses of 0.11 $nC\mu m^{-2}$ and lower, grain growth was confined to the edge of the element. It is thought that the grain growth is induced by the energy in the tails of the Ga^+ beam infringing on the element and the secondary events produced by the Ga^+ beam. Within the trenches milled to create the elements, preferential milling can be observed. This is confirmed by AFM profiles of the elements and surrounding area. The surface profiles measured by the AFM show that there is an increase in the average depth of the trenches with dose. From the surface profiles the average sputter rates of the materials have been calculated. For the 20 nm thick permalloy layer deposited on 50 nm thick SiN a sputter rate of (0.15 ± 0.05) $\mu m^3 nC^{-1}$ was calculated; after the permalloy was milled away on the

silicon nitride specimen an average sputter rate of (0.42 ± 0.05) $\mu m^3 nC^{-1}$ was calculated. A slight difference in the sputter rate of the two samples was attributed to the 4 nm copper layer.

As with the trenches discussed in chapter 4, a better understanding of the material could be obtained by elemental mapping using EELS and AES imaging, especially to determine the alloying of the remaining material in the trenches samples. Likewise electron beam diffraction analysis would be beneficial in the characterisation of the structural properties of the trenches.

In general the magnetisation of both the 1000×200 nm^2 and the 500×500 nm^2 elements fabricated using doses <0.04 $nC\mu m^{-2}$ from the FIB lithography samples behave in a similar fashion to the elements fabricated by EBL, although the fields at which these events take place are lower in magnitude. All the experimental fields are lower than those of the OOMMF simulated elements. The lower field magnitudes are probably due to the influence of the surrounding continuous thin film in the FIB lithographed elements and increased roughness and grain sizes of the real elements. In certain cases the magnetisation within the 500×500 nm^2 elements proceeds through a metastable twin vortex state from the C-type state to single vortex state. The intermediate twin vortex state probably arises due to the element roughness and the influence of the surrounding film. The vortex chirality is, as a result, reversed in all such cases. The extent of the influence of stray field emanating from the surrounding film on the elements could be estimate using the programme described in section 1.4.2. By setting the component of magnetisation in the film to lie parallel to the easy axis of the element this would give the largest stray field that impinged on the element.

In the case of the lower dose elements (<0.04 $nC\mu m^{-2}$) it appears that these elements are more topographical features of the film than isolated elements given the average depth in the trenches being 12 nm. As a result the magnetostatics of the films and the trenches reduce the event fields dramatically for the elements. For the 500×500 nm^2 elements, the magnetostatics effects hinder the formation of the magnetic vortex structure within the element and pin the vortex core to an edge if it does form. The three dimensional model of the OOMMF programme (section 1.4.1) could be used to model several scenarios to observe any influence of the surrounding film on the elements: i) the element is complete detached from the surrounding film: ii) the element is a topographical feature of a thin film (created by milling) where the connecting trenches have the same magnetic properties as the film and element and iii) the trench connecting the element and film has altered

magnetic properties. The OOMMF calculated magnetisation states from each scenario could also be used to calculate the stray field distribution of the film and element.

Although the elements fabricated by EBL still have better definition, with respect to edges and grain sizes, than those fabricated by FIB lithography, improvements in the machinery could lead to improvements in the elements. For example, in section 4.2 it was shown that a finer beam decreases edge roughness of trenches. The problem with a lower beam current being used to sharpen the edges (and decrease the tails of the beam) is the increased milling time. Using a combination of beam currents requires realignment of the beam between beam current changes. The accuracy of stage movements does not allow for good registration between stage movements and TEM windows are too fragile to image using the Ga^+. The new dual beam FIB microscope (a FIB microscope that has a Ga^+ and e^- source) will allow elements fabricated using multiple beam currents to be fabricated on TEM membranes. The use of this technology may allow for better clearing of the trenches and more regular edge structure giving an element of similar quality to that fabricated by EBL with decreased fabrication times.

8.3 The characteristics of gallium ion irradiated, square, micron sized ferromagnetic elements

In chapter 6 FIB lithographed 2×2 μm^2 elements that had been irradiated with different patterns for a range of doses have been discussed. Bright field images of all the irradiated 2×2 μm^2 elements that were fabricated by FIB lithography from 10 nm Cu/20 nm permalloy/5 nm Cu on a 50 nm thick, silicon nitride substrate reveal good clearance within the surrounding trenches. Alterations to the grain structure within the elements are only observed in elements irradiated with area patterns. Other patterns that have been irradiated into the elements do not exhibit grain growth within the elements. Visible within the unirradiated areas of all of the elements are large grains that could be a result of either the deposition process or contaminants on the surface. Elemental mapping through electron EELS or AES or a similar technique would be beneficial to clarify the elements and their ratios within such areas.

Fresnel images of the majority of 2×2 μm^2 elements irradiated with a pattern behave in a similar fashion to the unirradiated elements. These elements form a four-domain flux closure structure similar to those discussed in chapter 5. The behaviour of these elements is, again, similar as a magnetic field is applied.

Only when the elements are irradiated with high doses (0.048 and 0.096 $nC\mu m^{-2}$) and with certain patterns can an effect on the magnetisation within the elements be observed. The sections areas act to: displace the vortex core (diagonal cross): form a cross-tie structure then collapse to a vortex with the core displaced (horizontal/vertical cross): disrupt the formation of the vortex core and trap the domain wall (irradiated area): segregate the magnetisation into coupled inner and outer elements (irradiated connecting areas): and trap domain walls as the vortex passes through the element (lower dose irradiated connecting trenches). Altering the dimensions of the elements would alter the magnetic properties; the same patterns could be milled into elements with an in-plane aspect ratio of 5:1 to observe the changes in the magnetisation. A change in the buffer layer (4 nm copper) and capping layer material with, for example, tantalum may change the magnetic properties of the elements again.

The OOMMF simulations of the irradiated elements are of limited use when used to describe the irradiated elements. In some cases the irradiated, magnetically dead, regions disrupt the whole element and form a closely coupled series of elements. In others, the programme simulates observed remanent states but upon the application of a field deviates from that observed experimentally. The OOMMF simulations did predict the off-centre vortex core for the diagonal cross and the influence of the irradiated section on the vortex as the field was applied to the element. The simulations also predict the head to head domains observed in the outer section of the elements with interconnecting trenches and the resulting two stage reversal of the element. The differences in the simulated and experimental results are due to the assumptions made for the two-dimensional programme. Firstly that the irradiated section is magnetically dead: Differential phase contrast (DPC) and Fresnel images indicate that this may not be the case. Secondly the irradiated section is a well-defined region with an abrupt change: it has been shown in chapter 5 that the tails of the beam can influence areas that were supposed to be unirradiated. Thirdly, the magnetic material used had the properties of unirradiated permalloy: as has been shown by experimentation, this is not always the case, intermixing can alter the properties of the magnetic materials. To overcome such problems the simulation could be run using the three-dimensional model of OOMMF that allows these problems to be incorporated into the simulation.

8.4 The physical and magnetic structure of cobalt arrays fabricated by electron beam lithography

The ordering of vortex chiralities within a 10×10 μm^2 cobalt array have been discussed in chapter 7. Bright field TEM images of the nominal 270×270×50 nm^3 cobalt elements within the array reveal good clearance with respect to the patterning resist and that the array is whole and intact. Higher magnification bright field images reveal that the average in-plane dimensions of the elements are approximately square ((270 ± 4)×(276 ± 4) nm^2). The higher magnification images also reveal elements with residual strands of resist attached.

Fresnel images of the array reveal two main levels of magnetic contrast within the elements, light and dark contrast. It has been established that the light contrast when viewed in elements in underfocussed Fresnel imaging mode is generated by clockwise rotation of the magnetisation within the elements and the dark contrast is a result of anticlockwise rotation. The formation and expulsion of the vortices within the element occur at a range of fields. The formation of vortices begins at (690 ± 25) Oe and ends at (373 ± 24) Oe, giving a range of ~317 Oe. The expulsion of vortices begins at (-1134 ± 23) Oe and ends at (-1264 ± 24) Oe, giving a range of ~130 Oe.

From the magnetisation cycles applied to the array, information was obtained about the behaviour of the elements within the array. It has been found that, in general, there is greater uniformity in the distribution of the vortex chirality as the field is applied in the y-axis as opposed to the x-axis and there is an increase in the vortex distributions in the y-axis. A reason for the greater uniformity could be due to the increase in the y dimension of the elements, this could increase the magnetostatic interaction between the elements as the field is applied in this direction. The change in the y dimensions could be a consequence of a deposition or write effect from the EBL process. Texturing of the crystallites due to the reduced dimensions could also account for anisotropy. Analysis of the crystalline structure within an element could be through analysis of the diffraction patterns at different tilt angles would determine if there is any texturing. To observe if there is any anisotropy within the film, the in-plane field could be applied along a diagonal of the array. If there is an associated anisotropy, the formation and expulsion of the vortex will occur off-axis of the diagonal. The direction the vortex takes will also give a qualitative result as to the direction of any anisotropy. Applying the correlation functions to the remanent states of the magnetisation cycles shows that the array reverses state upon the application of consecutive saturation fields. The nature of the domains (clockwise and

anticlockwise vortex chiralities) was found to reverse with the field. The saturation fields have also been applied to the array over the course of sixteen cycles and in a couple of instances a time period of ~60 mins has elapsed between the application of one field and the next field to observe the stability of the array. For the increased number of cycles there was little change in the remanent states, inferring stability within the system over many cycles. Similarly there appears to be little change within the array with respect to time. The domain like structures observed within the remanent states, as well as the high cross-correlation functions for cycles, indicates a supermagnetic domain type of array. The remanent states do not appear to vary greatly for magnetic fields applied along the same axis from different initial states and for different cycles, this indicates a history in the supermagnetic domain that is intrinsic to the properties of array and not the applied field or magnetic history of the array.

The OOMMF simulation of an ideal 270×270×50 nm^3 cobalt element shows that the four-domain vortex clockwise or anticlockwise state has the lowest energy and hence is the ground state; with near-uniform states having the highest remanent energies. As with the simulations of permalloy squares in chapters 4 and 6, the OOMMF simulations cannot reform a single vortex state as the field is cycled: instead the simulation reforms a multivortex state and reverses through rotation of the domains. A reduced array of 10×10 elements has also been simulated in the presence of an applied field. For a perfect array it was found that the vortices are expelled over a range of 200 Oe as the applied magnetic field is raised to 2500 Oe to erase the memory of the individual element within the array. As the applied field is reduced, prior to vortex formation, S-states are observed in the array; the S-states in turn facilitate the formation of multivortex states within some elements (but not all S-states form multivortex states). The vortices form within the array over a range of 400 Oe. This is consistent with experimental results. After the vortices have reformed, the array appears to form two domains of different chiralities with multivortex states at the domain boundaries and the edge of the array. These domains (with a 50/50% split) reverse upon application of a reverse saturation field. The symmetry of the state could arise due to the symmetry of the array and this is confirmed when a similar magnetising field is applied along the y-axis and a similar state is observed.

The symmetry of the remanent state of the array is broken when the symmetry of the array is broken. A mask of the elements that have been randomly perturbed confirms this. As the random array is cycled through an applied field the vortex chiralities do not form two domains in the remanent states. There is an increased number of S-states in the random array (compared to the perfect array) prior to vortex formation. This in turn

increases the number of multivortex states observed at remanence. The random array is similar in nature to the fabricated array. It would be interesting to study simulations of arrays with elements perturbed by 1 or 2 pixels randomly in the x and y direction, in addition to an array where one dimension of the elements had been increased by one pixel. It would also be interesting to simulate an array of elements that have been altered by removing random pixels along their edges. Although the last simulation would be a time consuming simulation, both in the creation of the mask and the computation of the simulation. Both the auto and cross-correlation functions have been applied to the simulated arrays. We have found that the presence of well-ordered domains increases the autocorrelation functions in the direction of the applied field. Perpendicular to the applied field, however, the autocorrelation function falls off after a pixel spacing of two due to domain structure. The cross-correlation function of the perfect array, for the forward and reverse fields, reveals that although the domains reverse, not all the vortices reverse. This is contrary to the random array where the cross-correlation function is ~-1, showing reversal of the vortices, and there is an almost complete domain reversal. The states predicted by the OOMMF simulation package are not observed experimentally, even briefly during a transition state, as the remanent states are a direct result of the saturated state.

Reconstructions of the stray field emanating from elements whose magnetisation is either in a flower, C- or S-state surrounding a bulk or corner element yields insights into the influences of stray field affecting the elements. When the array is in the flower type state, the stray field is symmetrical in bulk, where as at the corner there is an increase/decrease (dependent on the orientations of the flower type states) of the stray field. This is true for the C-type state as well. When the element is surrounded by S-type states, however, there is an asymmetrical stray field distribution that arises regardless of the element's position in the array. It is thought that the asymmetrical stray field distributions of the S-state result in the formation of the multivortex states that are observed as well as help facilitate the reversal of the magnetic vortex chiralities.

Bibliography

[1] Lister K. A., Casey B.G., Dobson P.S., Thoms S., Macintyre D.S., Wilkinson C.D.W., Weaver J.M.R., Microelec. Eng. 73-74 (2004) 319.

[2] Chen Y, Macintyre D., Thoms S., J. Vac Sci Tech B 17(6) (1999) 2507.

[3] Lui X., Chapman J.N., McVitie S., Wilkinson C.D.W., Appl. Phys. Lett 84(22) (2004) 4406.

[4] Schneider M., Liszkowiski J., Rahm M., Wegscheider W., Weiss D., Hoffmann H., Zweck J., J Phys D: Appl Phys 36 (2003) 2239.

[5] For information on MRAM see: http://www.mram-info.com/introduction (active as of 12th August 2007).

[6] MRAM developed by freescale semiconductor company see: http://www.freescale.com/webapp/sps/site/overview.jsp?nodeId=015424 (active as of 12th August 2007).

[7] Cowburn R.P., J. Appl. Phys. 93(11) (2003) 9310.

[8] IBM web site detailing the perpendicular magnetic storage device: http://domino.research.ibm.com/comm/pr.nsf/pages/news.20010518_whitepaper.html (active as of 12th August 2007).

[9] Kato N.I., J. Elec. Micros. 53(5) (2004) 451.

[10] Kaminsky W.M., Jones G.A.C., Patel N.K., Booij W.E., Balmire M.G., Gardiner S.M., Xu Y.B., Bland J.A.C., Appl. Phys. Lett 78(11) (2001) 1589.

[11] Woods S.I., Ingvarsson S., Kirtley J.R., Hamann H.F., Koch R.H. Appl. Phys. Lett. 81(7) (2002) 1267.

[12] McGrouther D., Chapman J.N., Vanhelmont F.W.M., J Appl Phys 95(12) (2004) 7772.

[13] Xiong G., Allwood D.A., Cooke M.D., Cowburn R.P., Appl. Phys. Lett. 79(21) 2001 3461.

[14] Park C.-M., Bain J.A., IEEE Trans Mag. 38(5) (2002) 2337.